MBE-grown semiconductor nanostructures with electronic and photonic confinement

Jensen, Jacob Riis; Hvam, Jørn Marcher; Langbein, Wolfgang Werner

Publication date:
2000

Document Version
Publisher's PDF, also known as Version of record

Abstract

In this thesis the realization of semiconductor nanostructures in the InAlGaAs material system with molecular beam epitaxy (MBE) is described, as well as the characterization of their optical properties. First, the growth conditions used for different materials and surfaces are given, and the general capabilities of the MBE-systems are demonstrated, with respect to growth of structures with varying thicknesses / alloy compositions, and the synthesis of alloys, so-called digital alloying.

In the first main part of the thesis a group of low-dimensional structures are described, the so-called quantum wells, wires and dots. For quantum wells in the InAlGaAs material system, a detailed analysis is presented of the influence of surface segregation during growth, and it is shown how the measured energy levels and linewidths may be calculated with very high precision. Furthermore, the limits of strain in multi quantum wells are deduced, that determine when dislocations will be formed. It is also demonstrated how T-shaped quantum wires with enhanced confinement energies are realized by overgrowing InAlGaAs quantum wells with a GaAs quantum well. Finally, the growth of quantum dots in both InAs, InGaAs and InAlGaAs is described, and it is shown how structures with very uniform quantum dots at energies near the visible red part of the spectrum may be realized.

The second main part of the thesis deals with the growth of optical microcavities, where the light is strongly interacting with a quantum well and so-called polariton resonances are formed. It is shown how particularly narrow, tunable resonances may be achieved, by a combination of a low cavity energy gradient across the samples and a narrow exciton resonance in a broad quantum well where the density of free carriers is particularly low. Next, the polariton energies and linewidths are measured and analysed as a function of detuning and temperature. It is demonstrated that a coupled-harmonic oscillator model yields a good agreement with the energies, but the analysis of the linewidths requires that the absorption in the quantum well is also taken into account, which is demonstrated in a microcavity with a reduced light-matter interaction. For the polariton with the lowest eigenenergy, it is shown that the probability for scattering on lattice vibrations or free carriers is reduced. Finally, the secondary emission from a microcavity is measured and analysed, where a good qualitative agreement with theories for Rayleigh scattering is found, and the so-called polariton bottleneck is observed.

Resumé

I denne afhandling beskrives fremstillingen af halvleder nanostrukturer i InAlGaAs materialesystemet ved hjælp af molekylstråle epitaksi (MBE), og karakteriseringen af deres optiske egenskaber. Først gennemgås de anvendte dyrkningsbetingelser for forskellige overflader og materialer, og MBE-anlæggets generelle egenskaber demonstreres med henblik på dyrkning af strukturer med varierende lagtykkelser / legeringssammensætninger og syntetisering af legeringer, såkaldte *digitale legeringer*.

I det første hovedafsnit af afhandlingen beskrives en gruppe lav-dimensionale strukturer, såkaldte kvantebrønde, kvantetråde og kvanteprikker. For kvantebrønde i InAlGaAs systemet præsenteres en grundig analyse af indflydelsen af overflade segregation under dyrkning, og det vises hvordan de målte energiniveauer og liniebredder derefter kan beregnes med meget stor nøjagtighed. Desuden bestemmes grænserne for strain i multikvantebrønde, der afgør hvornår dislokationer bliver dannet. Det demonstreres også hvordan T-formede kvantetråde med forøgede bindingsenergier kan fremstilles ved overdyrkning af InAlGaAs kvantebrønde med en GaAs kvantebrønd. Endelig beskrives dyrkningen af kvanteprikker både i InAs, InGaAs og InAlGaAs materialesystemerne, og det vises hvordan strukturer med meget uniforme kvanteprikker og energier nær den synlig røde del af spektret kan fremstilles.

Det andet hovedafsnit af afhandlingen omhandler dyrkningen af optiske mikrokaviteter hvor lyset vekselvirker stærkt med en kvantebrønd og såkaldte polariton resonanser dannes. Det vises hvordan særligt smalle, tunbare resonanser kan opnås, ved at kombinere en lav gradient af kavitetens resonans energi henover prøverne med en smal exciton resonans i en bred kvantebrønd hvor tætheden af frie ladningsbærere er særligt lav. Herefter måles og analyseres polaritonernes energier og liniebredder som funktion af detuning og temperatur. Det vises at en koblet, harmonisk oscillator model giver en god beskrivelse af energierne, men en forståelse af liniebredderne kræver at absorptionen i kvantebrønden også tages i betragtning hvilket bl.a. demonstreres i en mikrokavitet med reduceret lys-stof vekselvirkning. For polaritonen med den mindste egenenergi vises det desuden at den har en reduceret sandsynlighed for spredning på gittervibrationer og frie ladningsbærere. Endelig, måles og analyseres den sekundære emission fra en mikrokavitet, hvor en god kvalitativ overensstemmelse med teorier for Rayleigh spredning er fundet, samt den såkaldte polariton flaskehals er eksperimentelt påvist.

Preface and Acknowledgements.

This thesis is part of the requirements for the Danish Ph.D.degree. It reports on scientific research carried out from September 1997 to September 2000. In this period I have been enrolled as a ph.d.-student at The technical University of Denmark, first at Mikroelektronik Centret (until 1998) and later at Research Center COM.

A large part of the work has taken place at III-V Nanolab, at the Ørsted Laboratory, University of Copenhagen, where the samples have been grown using molecular beam epitaxy. Another large fraction of the work has taken place in the optics laboratories at The Technical University of Denmark.

First of all I wish to thank my supervisor, Prof. Jørn M.Hvam, for giving me the opportunity to do research in his group within the fields of semiconductor growth and optics. Secondly, I am very grateful to my second supervisor, Dr. Wolfgang Langbein, for creative inspiration on sample design and for his valuable help with the optical characterisation. Likewise, I would like to thank Dr. Claus B. Sørensen for patiently teaching me how to do MBE-growth, and for his instructions on many practical details of sample processing.

Furthermore, I have enjoyed and benefitted from fruitful collaborations with Dr. Paola Borri, Dr. Dan Birkedal, Dr. John Erland and Dr. Hannes Gislason, and I would like to thank Dr. Sergey I. Bozhevolnyi, Dr. Leigh Smith, Dr. Jesper Mørk, and Dr. Svend Bischoff for many enlightening discussions.

I greatly acknowledge the help and inspiration from all my colleage ph.d.-students at Mikroelektronik Centret and Research Center COM, especially Kristjan Leosson, Francis P. Romstad, Sune Højfeldt, Kresten Yvind, Ingibjorg Magnusdottir, Niels Asger Mortensen, and Kristinn Johnsen. Their friendly attitude has contributed to a pleasant daily atmosphere in the office and in the lab.

Finally, I am very grateful to my girlfriend Ditte, who has been very patient with me and given me all her love during the hard times of the project.

Jacob Riis Jensen
Lyngby, 25/9-2000

List of publications.

Publications in international journals.

1. J. R. Jensen, J. M. Hvam, and W. Langbein, "*Optical properties of InAlGaAs quantum wells: Influence of segregation and band bowing*.", Jour. Appl. Phys. **86** (5), 2584 (1999).

2. K. Leosson, J. R. Jensen, W. Langbein, and J. M. Hvam, "*Exciton localization and interface roughness in growth-interrupted GaAs/AlAs quantum wells*", Phys. Rev. B **61** (15), 10322 (2000).

3. W. Langbein, K. Leosson, J. R. Jensen, J. M. Hvam, and R. Zimmermann, "*Instantaneous Rayleigh scattering from excitons localized in monolayer islands.*", Phys. Rev. B **61** (16), R10555 (2000).

4. J. Erland, S. Bozhevolnyi, K. Petersen, J. R. Jensen, and J. M. Hvam, "*Second-harmonic imaging of quantum dots.*", Appl. Phys. Lett. **77** (6), 806 (2000).

5. K. Leosson, J. R. Jensen, J. M. Hvam, and W. Langbein, "*Linewidth statistics of single InGaAs quantum dot photoluminescence lines.*", phys. stat. sol. (b) **221**, No. 1, 49-51 (2000).

6. J. R. Jensen, W. Langbein, P. Borri, and J. M. Hvam, "*Ultranarrow polaritons in a semiconductor microcavity*", Appl. Phys. Lett. **76** (22), 3262 (2000).

7. P. Borri, J. R. Jensen, W. Langbein, and J. M. Hvam, "*Direct evidence of reduced dynamic scattering in the lower polariton of a semicondcutor microcavity.*", Phys. Rev. B **61** (20), R13377 (2000).

8. P. Borri, W. Langbein, U. Woggon, J. R. Jensen, and J. M. Hvam, "*Microcavity polariton linewidths in the weak disorder regime*", Phys. Rev. B **63** (3), 35307, (2001).

Publications outside the work reported here

9. P. Borri, W. Langbein, U. Woggon, J. R. Jensen, and J. M. Hvam, "*Biexcitons or bipolaritons in a semiconductor microcavity?*", Phys. Rev. B **62** (12), R7763 (2000).

10. J. Erland, V. Mizeikis, W. Langbein, J. R. Jensen, and J. M. Hvam, *"Stimulated secondary emission from semiconductor microcavities"*, Phys. Rev. Lett. **86** (25), 5791, (2001).

Conference contributions.

1. J. R. Jensen, J. M. Hvam, and W. Langbein, "*InAlGaAs/AlGaAs quantum wells: line widths, transition energies and segregation*", Microelectronic Engineering, 51-52 (2000), p.257-264. (Conference of low-dimensional Structures and Devices (LDSD), Antalya, Tyrkey 1999).

2. J. R. Jensen, W. Langbein, and J. M. Hvam, "*Enhanced confinement energy in strained asymmetric T-shaped quantum wires*", Journal of Crystal Growth, vol.227-228, p. 966 (2001). (The eleventh international conference on Molecular Beam Epitaxy (MBE-XI), Beijing, China 2000).

3. J. Erland, W. Langbein, J. R. Jensen, and J. M. Hvam, *"Seeding dynamics of nonlinear polariton emission from a microcavity"*, CLEO/QELS, San Francisco, 2000.

4. K. Leosson, J. Erland, J. R. Jensen, and J. M. Hvam, "*Exciton dephasing in single InGaAs quantum dots*", CLEO/QELS, San Francisco, 2000.

5. L. M. Smith, K. Leosson, J. Erland, J. R. Jensen, J. M. Hvam, and V. Zwiller, "*Excited state dynamics in* $In_{0.5}Al_{0.04}Ga_{0.46}/\ Al_{0.08}Ga_{0.92}As$ *self-assembled quantum dots"*, abstract book, p. 62 of International Conference on Semiconductor Quantum Dots, Munich, Germany, 2000.

Table of contents

Chapter 1

Introduction

This thesis reports on molecular beam epitaxial (MBE) growth of semiconductor nanostructures, and their optical properties.

MBE is one of several ways of growing crystalline semiconductors, that also include metal-organic chemical vapour deposition (MOCVD) and liquid phase epitaxy (LPE). For basic research both in electronics and optics, MBE has been the favourite choice due to the higher purity and higher precision of interfaces and alloy compositions that may be obtained compared to other growth methods. Two important examples of structures where these unique properties are necessary are high mobility two-dimensional electron gases and the recently developed quantum cascade lasers [1]. Due to recent developments in the MBE-technology the throughput and cost-effciency has been considerably improved, so MBE-grown structures are presently used also in large-scale commercial production, e.g. of hetero-bipolar transistors (HBTs), high electron mobility transistors (HEMTs) and high power lasers at 980 nm [2, 3].

The work reported here concerns growth of structures for different basic research activities within semiconductor optics in the Optoelectronics Group at Mikroelektronik Centret and later the III-V Semiconductor Components and Materials Competence Area at Research Center COM. A common denominator of the project has been the realization, understanding and improvement (or tailoring) of structures with electronic and photonic confinement. These goals have been pursued by exploring both the properties of the MBE-system itself and the properties of the full quaternary material system availible in our MBE, InAlGaAs. The scope of the work has ranged from growth to basic optical characterisation, determining the energy levels and line widths, but for some of the structures the optical properties have been further investigated.

More specifically the results reported here fall under two main areas. The

first is the realization of low-dimensional structures, quantum wells, wires and dots, allowing a comparison between structures grown using quaternary InAlGaAs and the more conventional ternary compounds, InGaAs and AlGaAs. The second is the growth of planar microcavity structures with very narrow polariton resonances, and the optical characterisation of their properties.

The thesis is organized as follows. In chapter 2 a basic treatment of semiconductor optics is given comprising mostly the topics related to this work. Chapter 3 describes MBE-growth of thin films, their different morphologies and growth on an atomic scale. A number of "tricks" that may be used during growth are also demonstrated, such as growth interrupts, intentional thickness and composition variations, and digital alloying. In chapter 4 the growth and characterisation of nanostructures based on InAlGaAs is described and compared to similar ternary structures. Chapter 5 treats the design and growth of planar microcavities and the line widths and energies of the polaritons are compared for samples with different inhomogeneous broadenings and strengths of the light-matter coupling. Finally, in chapter 6 the main results are summarized and conclusions are drawn.

Chapter 2

Basic semiconductor optics

2.1 Introduction.

In this chapter an overview of semiconductor optics is given, focussing on the properties relevant for this work. The treatment here is based on Ref. [4, 5, 6] unless other references are specifically given. In the first part the material properties, band structure and electronic excitations of bulk and low-dimensional structures are described, whereas the second part deals with the propagation of light in semiconductor structures.

2.1.1 Band structure and exctions in bulk crystals.

The so-called III-V semiconductors consist of elements from group-III and group-V of the periodic table. The *binary* materials contain one element from each of the two groups, while in *ternary* and *quaternary* alloys one or two more elements have been added. The Arsenide-based semiconductors crystallise in the zinc-blende structure, shown in Fig.2.1, and the lattice constants of the binary InAs,GaAs and AlAs materials used here are given in Table 2.1.

Also shown in In Fig.2.1 is the band structure of GaAs, a prototype of a III-V semiconductor. The bands are filled up to zero energy, and since the highest filled state is at the same k-vector, k=0, as the lowest unfilled state the band gap is *direct*. Both GaAs and InAs are direct band gap semiconductors, while AlAs is *indirect* since the lowest unoccupied state is at $k \neq 0$.

Most semiconductor optics deals with transitions between the three higest filled bands, the valence bands, and the lowest unfilled band, the conduction band. In bulk, the two upper valence bands are degenerate at k=0, and referred to as the heavy-hole and light-hole bands. The third band is the

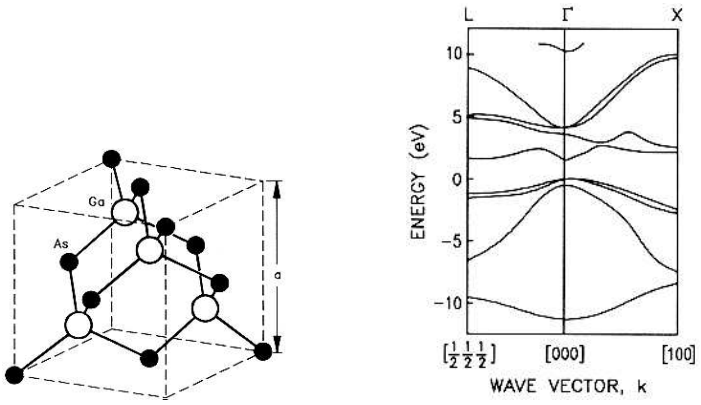

Figure 2.1: Left: The zinc-blende crystal structure of Arsenide-based III-V semiconductors. Right: The band structure of GaAs.

so-called split-off band, which is shifted to lower energies by an amount V_{so}, see Table 2.1.

The valence and conduction bands are classified in terms of their total angular momentum, J, and the projection of the total angular momentum, m_J, which are good quantum numbers for the electronic states. Due to spin, each band is two-fold degenerate, with ($J=\frac{1}{2}$, $m_J=\pm\frac{1}{2}$) for the conduction band, ($J=\frac{3}{2}$, $m_J=\pm\frac{3}{2}$) for the heavy-hole band, ($J=\frac{3}{2}$, $m_J=\pm\frac{1}{2}$) for the light-hole band and ($J=\frac{1}{2}$, $m_J=\pm\frac{1}{2}$) for the split-off band. The split-off band will not be treated further here.

To a very good approximation, the dispersion of the conduction band is isotropic and parabolic around k=0, that is

$$E_{cond}=\frac{\hbar^2}{2m_e}k^2 + E_g \tag{2.1}$$

where k is the magnitude of the k-vector, $\overline{k}=(k_x,k_y,k_z)$, and E_g is the band gap. The heavy and light-hole bands are anisotropic and their dispersions are given by

$$E_{hh} = -\frac{\hbar^2}{2m}\left\{\gamma_1 k^2 - \left[4\gamma_2^2 k^4 + 12\left(\gamma_3^2-\gamma_2^2\right)\left(k_x^2k_y^2+k_x^2k_z^2+k_y^2k_z^2\right)\right]^{1/2}\right\} \tag{2.2}$$

$$E_{lh} = -\frac{\hbar^2}{2m}\left\{\gamma_1 k^2 + \left[4\gamma_2^2 k^4 + 12\left(\gamma_3^2-\gamma_2^2\right)\left(k_x^2k_y^2+k_x^2k_z^2+k_y^2k_z^2\right)\right]^{1/2}\right\} \tag{2.3}$$

where γ_1, γ_2 and γ_3 are the so-called Luttinger parameters. The effective electron mass and the Luttinger parameters are also given in Table 2.1.

The elementary excitation of the electronic system in a bulk semiconductor crystal is the so-called exciton, consisting of an electron in the conduction

Parameter	GaAs	AlAs	InAs
Lattice constant (Å)	5.6503	5.6611	6.0583
Stiffness constant, $C_{11}(\times 10^{10}\text{Pa})$	11.88	12.02	8.329
Stiffness constant, $C_{12}(\times 10^{10}\text{Pa})$	5.38	5.70	4.526
Stiffness constant, $C_{44}(\times 10^{10}\text{Pa})$	5.94	5.89	3.959
Relative electron mass, m_e/m_0	0.0667	0.15	0.0248
Luttinger parameter, γ_1	7.1	3.76	19.7
Luttinger parameter, γ_2	2.02	0.9	8.37
Luttinger parameter, γ_3	2.91	1.42	9.29
Hydrostatic deformation potential, a_g (eV)	-8.233	-8.110	-6.080
Shear deformation potential, b_v (eV)	-1.824	-1.7	-1.8
Split-off band shift, V_{so} (meV)	340	275	380

Table 2.1: Material parameters for the binary semiconductors GaAs, AlAs and InAs, from Ref.[35].

band bound to a hole in the valence band via the Coulomb interaction. This is conceptually similar to a hydrogen atom and the exciton binding energy, E_x, and exciton Bohr radius, a_{Bx}, may then be expressed in terms of the Rydberg energy, Ry=13.6 eV, and the Bohr radius, a_B=0.53 Åas

$$E_x = \left(\frac{m_R}{\epsilon_R^2}\right) \text{Ry} \tag{2.4}$$

$$a_{B,x} = \left(\frac{\epsilon_R}{m_R}\right) a_B \tag{2.5}$$

where ϵ_R is the relative permittivity of the semiconductor, and m_R is the ratio of the reduced effective exciton mass to the free electron mass. For bulk GaAs, E_x=4.2 meV and a_B=14 nm. The band gap, E_g, usually refers to the energy difference between a free particles in the valence and conduction bands. That is, the total energy of an exciton at rest is given by E_g-E_x, corresponding to the energy of a photon emitted when an exciton recombines.

2.1.2 Uniform deformation of a bulk crystal.

Under a mechnical deformation of a semiconductor crystal the bands are shifted. Assuming a uniform deformation, the stress and strain tensor ele-

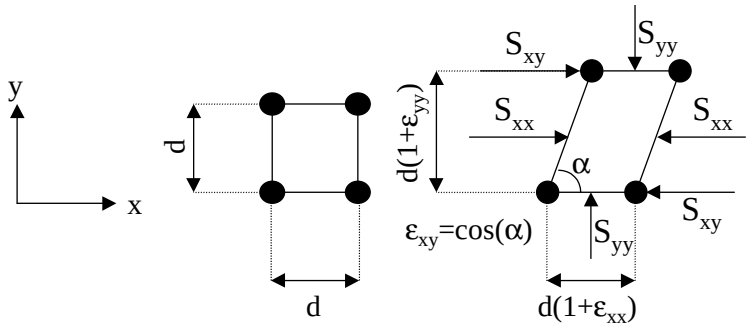

Figure 2.2: Left: Orientation of coordinate system. Middle: Undeformed cubic crystal. Right: Deformed cubic crystal, indicating the effect of the stress and strain tensor elements.

ments are constant, and given by

$$\begin{bmatrix} S_{xx} \\ S_{yy} \\ S_{zz} \\ S_{xy} \\ S_{xz} \\ S_{yz} \end{bmatrix} = \begin{bmatrix} C_{11} & C_{12} & C_{12} & 0 & 0 & 0 \\ C_{12} & C_{11} & C_{12} & 0 & 0 & 0 \\ C_{12} & C_{12} & C_{11} & 0 & 0 & 0 \\ 0 & 0 & 0 & C_{44} & 0 & 0 \\ 0 & 0 & 0 & 0 & C_{44} & 0 \\ 0 & 0 & 0 & 0 & 0 & C_{44} \end{bmatrix} \cdot \begin{bmatrix} \epsilon_{xx} \\ \epsilon_{yy} \\ \epsilon_{zz} \\ \epsilon_{xy} \\ \epsilon_{xz} \\ \epsilon_{yx} \end{bmatrix} \tag{2.6}$$

where the symmetry reduces the number of independent elements of the stiffness tensor to three, C_{11}, C_{12} and C_{44}. In Fig.2.2 the stress and strain tensor elements are illustrated for the deformation of a two-dimensional cubic crystal with lattice constant d.

In the special case where the crystal strain is equal in the x- and y-directions, ϵ_{xx}=ϵ_{yy}, the influence on the band structure is described by two parameters, the hydrostatic and shear energy shifts, ΔE_H and ΔE_S, given by [41]

$$\Delta E_H = a(\epsilon_{xx}+\epsilon_{yy}+\epsilon_{zz}) \tag{2.7}$$
$$\Delta E_S = b(\epsilon_{xx}-\epsilon_{zz}) \tag{2.8}$$

where a and b are the hydrostatic and shear deformation potentials, see Table 2.1. In the limit where the shear energy is small compared to V_{so} the gaps between the conduction band and the heavy-hole and light-hole bands are

$$E_{hh} = E_g+\Delta E_H-\Delta E_S \tag{2.9}$$
$$E_{lh} = E_g+\Delta E_H+\Delta E_S \tag{2.10}$$

where E_g is the band gap in the absence of strain. Hence, the volume deformation leads to the same shift of the two band gaps, while the shear

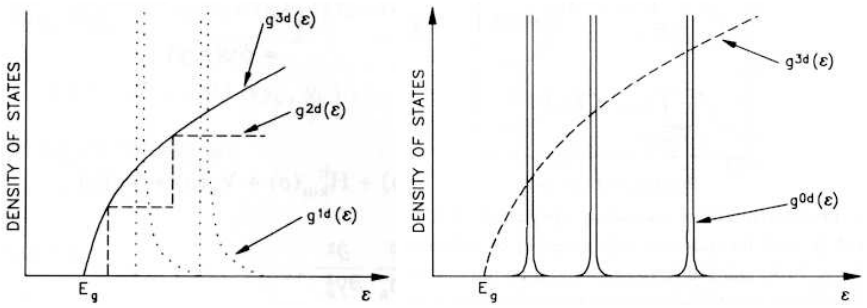

Figure 2.3: Comparison of the density of states for at bulk semiconductor ($g^{3d}(\epsilon)$), a quantum well ($g^{2d}(\epsilon)$), a quantum wire ($g^{1d}(\epsilon)$) and a quantum dot ($g^{0d}(\epsilon)$), from [5]. E_g is the band gap and ϵ is the energy.

component splits the heavy and light-hole bands. For compressive strain ($\epsilon_{xx} > 0$) $E_{hh} < E_{lh}$, and vica versa for tensile strain. The shear part of the deformation only shifts the valence bands, while ΔE_H is distributed between the two bands, with $\approx 90\%$ in the conduction band.

2.1.3 Semiconductor alloys.

For a semiconductor alloy, the values of one of the parameters in Table 2.1 may be found using a weighted average of the values for the binary materials (Vegard's law). To make the treatment of the electron and hole masses consistent, the Luttinger parameters and the *inverse* electron masses should be interpolated.

However, for the band gaps experimentally obtained relations exist for the ternary AlGaAs and InGaAs that go beyond the linear interpolation, given by [41, 22]

$$\mathrm{E}(\mathrm{Al}_x\mathrm{Ga}_{1-x}\mathrm{As}) = 1.519{+}1.36\mathrm{x}{+}0.22\mathrm{x}^2 \quad (2.11)$$

$$\mathrm{E}(\mathrm{In}_x\mathrm{Ga}_{1-x}\mathrm{As}) = 1.519{-}1.584\mathrm{x}{+}0.475\mathrm{x}^2 \quad (2.12)$$

for unstrained material at low temperatures, (T≈10K).

2.1.4 Low-dimensional structures.

Combining different semiconductors in the same structure leads to a spatially varying band gap that influences the energies and the motion of electrons and holes. If the band gap modulations take place on a length scale comparable to or shorter than the exciton Bohr radius, the confinement leads to a quantisation of the exciton levels. These so-called nanostructures are classified according to the number of motional degrees of freedom. That is,

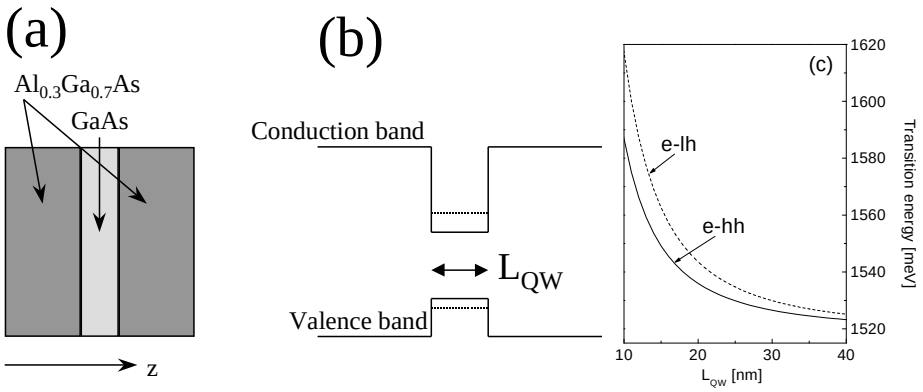

Figure 2.4: a): Layer structure of quantum well. b): Square well potential of quantum well. c): Energies of the heavy-hole and light-hole transitions in a quantum well with infinite barriers.

in two-dimensional (quantum wells), one-dimensional (quantum wires) and zero-dimensional (quantum dots) structures, the excitons are free to move in a plane, along a line or cannot move. In the absence of Coulomb interactions, the density of states above the band edge of a low-dimensional structure is constant for a quantum well and to proportional to $E^{-1/2}$ for a quantum wire, while for a quantum dot the density of states is delta-function like, as illustrated in Fig.2.3. So as the dimensionality of a structure decreases, the density of states increases at the band edge. This is in fact one of the major motivations for research in low-dimensional structures since it has been predicted to lead to improved device performance, e.g. lower treshold current density and larger temperature stability in laser diodes [7].

As an illustration of some of the important differences between bulk and low-dimensional structures, the quantum well will be treated here. It is typically realized by growing a layered structure consisting of e.g. $Al_{0.3}Ga_{0.7}As$, GaAs and $Al_{0.3}Ga_{0.7}As$, as shown in Fig.2.4a. Because of the different band gaps, the AlGaAs layers act as barriers for the GaAs layer, and the electron and hole eigenstates may be obtained from the Schrödinger equation

$$H\Psi = \left[-\frac{\hbar^2}{2m}\nabla^2 + V(z)\right]\Psi \tag{2.13}$$

where V(z) is assumed to be a square well potential, as illustrated in Fig.2.4b. In Fig.2.4c the energy of the band gaps are plotted as a function of the GaAs layer thickness, and it is noted that because of the different hole masses in the confinement direction, the quantisation energy of the heavy-hole is always smaller than for the light-hole.

In general the exciton binding energy is expected to increase as the dimen-

sionality decreases, because the confinement potential "pushes" the electron and hole closer to each other, increasing the Coulomb energy. For the quantum well here, the heavy-hole and light-hole excitons have different binding energies, the light-hole exciton binding being larger than the heavy-hole by 1-2 meV [79]. The exact value of the binding energy depends on both the thickness of the well and the material composition in the barrier, with typical values of 8-10 meV for the heavy-hole exciton in a $\approx$ 10 nm well [79].

2.2 Light-matter interaction.

Inherently, MBE grown samples are layered structures where the alloy composition changes in the growth direction but is practically uniform in the plane of the wafer. The optical properties of such stratified media are elegantly described by the so-called transfer matrix method (TMM), which will be reviewed here after treating electromagnetic waves in uniform media.

2.2.1 Electromagnetic waves in a uniform medium.

An electromagnetic wave propagating in a uniform medium is described by the wave equation

$$\nabla^2\overline{\mathrm{E}} - \frac{1}{\mathrm{c}^2}\frac{\partial^2}{\partial \mathrm{t}^2}\overline{\mathrm{E}} = \frac{1}{\mathrm{c}^2}\frac{\partial^2}{\partial \mathrm{t}^2}\overline{\mathrm{P}} \tag{2.14}$$

where $\overline{\mathrm{E}}$ is the electric field strength, and c is the speed of light in vacuum. Eq. 2.14 basically states that the electric field induces a polarisation in the medium, the nature of which influences the wave propagation. In the linear regime the polarisation of an isotropic medium is proportional to the electric field, and may be written

$$\overline{\mathrm{P}}(\omega) = \chi(\omega)\overline{\mathrm{E}}(\omega) \tag{2.15}$$

where the susceptibility, $\chi(\omega)$, is a scalar. In this case Eq. 2.14 has plane wave solutions of the form

$$\overline{\mathrm{E}} = \overline{\mathrm{E}}_0 \exp[\mathrm{i}(\mathrm{kz} \pm \omega \mathrm{t})] \tag{2.16}$$

for propagation along the z-axis, where k is the wave vector. In the general case, the susceptibility has both a real and an imaginary part, and it is related to the relative dielectric function of the material, $\epsilon(\omega)$, usually written in the form

$$\epsilon(\omega) = 1 + \chi(\omega) = \epsilon'(\omega) + \mathrm{i}\epsilon''(\omega). \tag{2.17}$$

The solution of Eq.2.14 then yields the following expression of the real and imaginary part of the wave vector, k=k'+ik", where the explicit dependence on frequency has been dropped and n is the refractive index.

$$k' = \frac{\mathrm{n}\omega}{\mathrm{c}} \tag{2.18}$$

$$k'' = \frac{\omega}{2\mathrm{cn}}\epsilon'' \tag{2.19}$$

$$\mathrm{n}=\sqrt{\frac{1}{2}\left(\epsilon'+\sqrt{(\epsilon')^2+(\epsilon'')^2}\right)} \tag{2.20}$$

The real part of the wave vector determines the phase velocity of light in the medium whereas the imaginary part describes the absorption since the power density of the electromagnetic wave in Eq. 2.16 has a decay length of α^{-1} =1/2k". In essence, the polarisation in Eq. 2.15 is given by the microscopic properties of the material, and once known it determines the propagation of the macroscopic electromagnetic field, as given by the wave vector k.

Of particular interest here is the susceptibility of an ideal excitonic resonance at ω_x given by

$$\chi(\omega)=\frac{Ne^2 f_x}{2m\omega_x}\frac{1}{\omega_x\text{-}\omega\text{-}i\gamma'} \tag{2.21}$$

The parameters N, f_x and γ' are the exciton density, oscillator strength and homogeneous linewidth. The homogeneous linewidth is the sum of the radiative linewidth, Γ, and the non-radiative linewidth, γ, where the latter describes the additional dephasing of the exciton caused by scattering on e.g. phonons, free carriers or other excitons. Γ is proportional to the oscillator strength and to the square of the dipole matrix element between the exciton and the crystal ground state, $|d_{cv}|^2$ [8], that is Γ is essentially a measure of the coupling strength between the photons and the excitons.

2.2.2 Electromagnetic waves in a stratified medium.

To calculate the electromagnetic field in a stratified medium with TMM, the structure is split into simpler elements, such as interfaces, dielectric layers and quantum wells. At each element the field amplitude of the incident, transmitted and reflected waves on both sides are related to each other by a matrix equation

$$\begin{bmatrix} \mathrm{E}^+_{i+1} \\ \mathrm{E}^-_{i+1} \end{bmatrix} = \overline{\mathbf{M}}_i \cdot \begin{bmatrix} \mathrm{E}^+_i \\ \mathrm{E}^-_i \end{bmatrix} \tag{2.22}$$

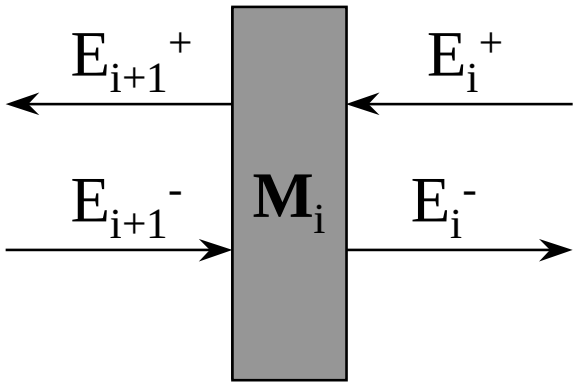

Figure 2.5: Illustration of the directions of the incident, reflected and transmitted waves on either side of an element in a stratified structure.

ensuring that the waves are solutions to Maxwells equations. The fields are propagated from right to left, as illustrated in Fig.2.5, and $\overline{\mathbf{M}}_i$ is the transfer matrix of the i'th element. The transfer matrix of a structure containing many elements is then given by

$$\overline{\mathbf{M}}_{tot}=\overline{\mathbf{M}}_{i-1}\overline{\mathbf{M}}_{i-2}....\overline{\mathbf{M}}_2\overline{\mathbf{M}}_1 \tag{2.23}$$

which leads to the general equation

$$\begin{bmatrix} \mathrm{E}_i^+ \\ \mathrm{E}_i^- \end{bmatrix} = \begin{bmatrix} \mathrm{M}_{11} & \mathrm{M}_{21} \\ \mathrm{M}_{12} & \mathrm{M}_{22} \end{bmatrix}_{tot} \cdot \begin{bmatrix} \mathrm{E}_1^+ \\ \mathrm{E}_1^- \end{bmatrix} \tag{2.24}$$

that relates the field amplitudes on either side of a structure to each other. All optical properties of the full structure is contained in M_{11}, M_{12}, M_{21} and M_{22}, and the amplitude reflection and transmission coefficients for light incident on the first element are then given by

$$\mathrm{r}=\frac{\mathrm{E}_1^-}{\mathrm{E}_1^+}=\frac{\text{-}\mathrm{M}_{21}}{\mathrm{M}_{22}} \tag{2.25}$$

$$\mathrm{t}=\frac{\mathrm{E}_i^+}{\mathrm{E}_1^+}=\frac{\det(\mathrm{M}_{tot})}{\mathrm{M}_{22}} \tag{2.26}$$

Furthermore, if the electric fields are known on one side, the transfer matrices may be used to propagate the field through the structure to find its value at any point inside.

Assuming normal incidence on the layers of the stratified medium, the transfer matrices are given in the following. For an interface between two dielectrics with refractive indices n_1 and n_2 it is

$$\overline{\mathbf{M}}_{int}=\begin{bmatrix} \frac{1}{2}(1+\frac{n_1}{n_2}) & \frac{1}{2}(1-\frac{n_1}{n_2}) \\ \frac{1}{2}(1-\frac{n_1}{n_2}) & \frac{1}{2}(1+\frac{n_1}{n_2}) \end{bmatrix} \tag{2.27}$$

where n_1 (n_2) is the index on the left (right) side of the interface. For a dielectric layer of thickness d, where the wave vector is k, the transfer matrix is [81]

$$\overline{\mathbf{M}}_{diel}=\begin{bmatrix} \exp(ikd) & 0 \\ 0 & \exp(-ikd) \end{bmatrix} \tag{2.28}$$

Finally for a heavy-hole exciton in a quantum well it is given by

$$\overline{\mathbf{M}}_{QW}=\frac{1}{\omega-\omega_x+i\gamma}\begin{bmatrix} \exp(ikL_{QW})(\omega-\omega_x+i\gamma-i\Gamma) & -i\Gamma \\ i\Gamma & \exp(-ikL_{QW})(\omega-\omega_x+i\gamma+i\Gamma) \end{bmatrix} \tag{2.29}$$

where L_{QW} is the quantum well thickness.

In appendix 1 the computer code for the program "stratify" is given, which calculates the reflectivity and transmission coefficients of an arbitrary structure containing these three elements.

Chapter 3

MBE growth

3.1 Introduction.

The MBE technique was developed in the late 1960s, and is presently used both in industry and research for growth of semiconductor structures with high precision, high purity and high uniformity [9]. In MBE, the atoms needed for growth are supplied by thermal evaporation from solid or liquid elemental sources. Under ultra high vacuum (UHV) conditions, the atoms are ballistically transported to the sample surface in the form of molecular beams. Epitaxy refers to the situation where the atoms stay on the surface to form their own arrangement (epi=on, taxy=arrangement), in contrast to catalysis where the atoms desorp after a surface reaction [10].

The capabilities in growth of a specific semiconductor material system ultimately set the limits of the optical and electrical properties that can be achieved in a heterostructure. Some limits are set by the equipment which is used for the growth, e.g. the uniformity of the layer thickness, and some are set by the physics of the material system itself, e.g. the band gaps that can be achieved or the restricted range of alloys that can be combined due to different lattice constants.

In this chapter the growth of the InAlGaAs material system with MBE is described. The focus is put only on the topics relevant for the work in this thesis, and no general overview is intended. In the first two sections the principles of crystal growth, independent of the MBE-system, is treated both from a macroscopic and a microscopic point of view, by considering the thermodynamic phases of a grown layer and the surface reactions on the atomic level. The next section describes the practical use of our MBE-system, the geometry of the sources, and typical growth parameters. In the final section, a couple of advanced growth techniques are described and experimentally demonstrated, that have been used to make the design and

growth of structures more flexible with as many variable material parameters as possible in the same sample.

3.2 Thermodynamics of thin films.

Since all Arsenide-based III-V semiconductors crystallize in the zinc-blende structure, thin grown layers usually adapt to the structure and lattice constant of the GaAs substrate, which is referred to as *pseudomorphic* growth (pseudo=false, morphology=structure) [10]. If the grown semiconductor has a different bulk lattice constant than the substrate it is uniformly strained in the beginning, but as growth proceeds a critical thickness, h_c, is reached where the misfit is accommodated by a change of the layer structure. In this section a thermodynamic approach is taken to describe the critical thickness and the two important mechanisms of strain relaxation by generation of misfit dislocations or by forming coherently strained islands.

3.2.1 Free energy of a uniform layer.

Fig.3.1 illustrates a layer of semiconductor B with a thickness of t, which is pseudomorphically grown on the [001]-surface of a semiconductor A. Since the grown layer adopts the lattice constant of the substrate and the angles between the crystallographic axis remain 90 degrees, five of the strain tensor elements, Eq.2.6, in the grown layer are directly given by

$$\epsilon_{xx} = \epsilon_{yy} = \frac{d_A - d_B}{d_B} \tag{3.1}$$

$$\epsilon_{xy} = \epsilon_{xz} = \epsilon_{yz} = 0 \tag{3.2}$$

where d_A and d_B are the bulk lattice constants of the two materials. The case of $\epsilon_{xx} < 0$ ($\epsilon_{xx} > 0$) corresponds to compressive (tensile) strain in the grown layer. The in-plane strain of the grown layer leads to a deformation in the growth direction, given by

$$\epsilon_{zz} = -2\frac{C_{12}}{C_{11}}\epsilon_{xx} \tag{3.3}$$

where C_{11} and C_{12} are stiffness constants of material B [11]. The sign of Eq. 3.3 implies that in-plane compressive (tensile) strain leads to a expansion (contraction) of material B in the growth direction.

The surface energy of the grown layer, γ_B, is the cost per unit area of creating the surface from a bulk crystal by cleavage. The value of γ_B depends on the crystallographic orientation of the surface, and generally has a local

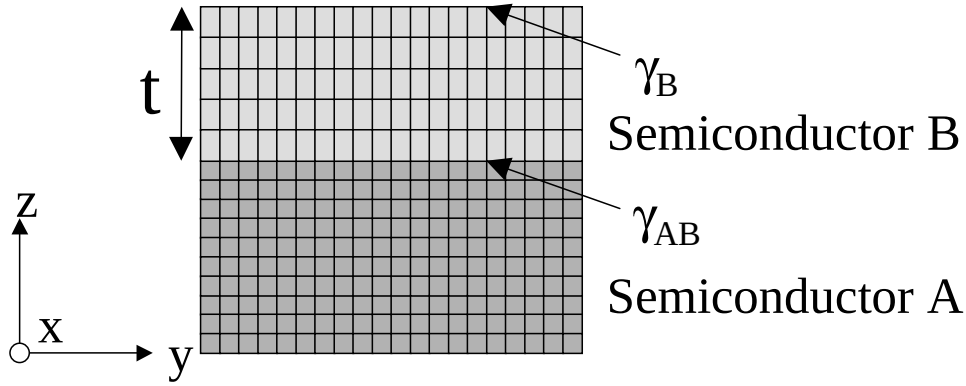

Figure 3.1: Pseudomorphically grown layer of semiconductor B with thickness t on a substrate of semiconductor A.

minimum for high symmetry directions [10]. Likewise, the interface energy, γ_{AB}, corresponds to the interface energy of the materials A and B, but the exact value is not important here and it has only been included for the sake of a qualitative discussion.

Adding the bulk strain and the surface contributions, the total free energy per unit area of the grown layer is given by

$$E_{epi} = tC_0\epsilon_{xx}^2 + \gamma_B + \gamma_{AB} \tag{3.4}$$

where $C_0 = C_{11} + C_{12} - 2C_{12}^2/C_{11}$ [12]. In Table 2.1, the stiffness constants discussed here are given for the three binary semiconductors used in this work.

3.2.2 Surface morphology.

The total energy of the uniform layer given in Eq. 3.4 is a good basis for understanding the possible surface morphologies that may occur during growth, and the parameters that govern them. In the ideal case of *lattice matched* growth, only the surface energies in Eq. 3.4 remain, and it is relavant to compare E_{epi} with the surface energy of the substrate, γ_A. In the cases where $\gamma_B + \gamma_{AB} < \gamma_A$ growth of flat layers on the substrate is favourable, often referred to as the Frank-Van der Merwe (or layer-by-layer) growth mode. In the opposite case, $\gamma_B + \gamma_{AB} > \gamma_A$, flat layers are energetically unfavourable leading to clustering on the surface - the socalled Volmer-Weber growth mode. Finally, the Stranski-Krastanow growth mode may occur for $\gamma_B + \gamma_{AB} \approx \gamma_A$, where the deposited layer first wets the substrate and then forms islands on top of this so-called wetting layer. In the semiconductor system used here

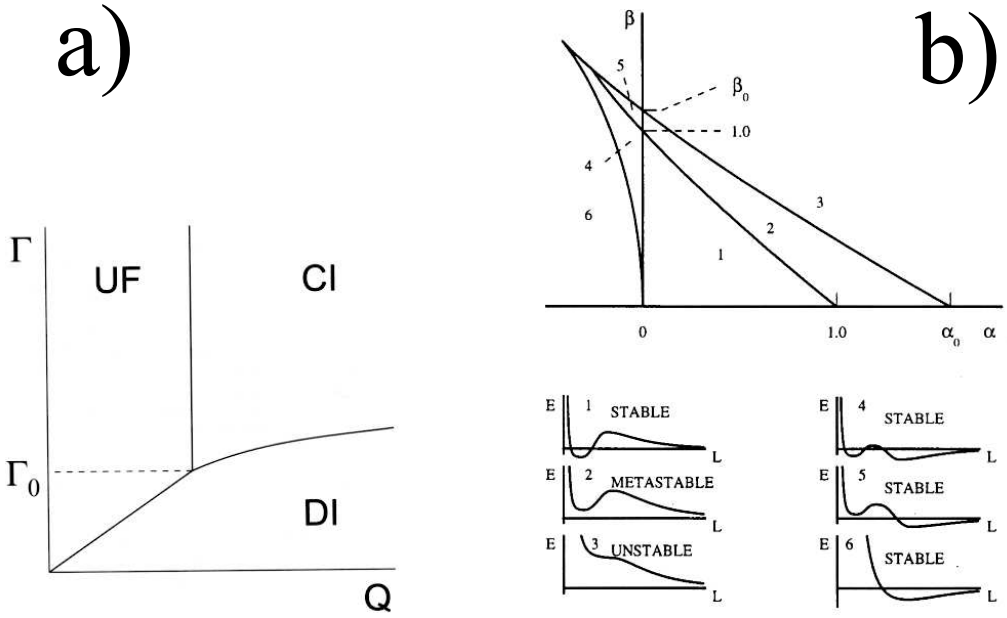

Figure 3.2: a): Phase diagram for the three different surface morphologies, uniform film (UF), dislocated islands (DI) and coherent islands (CI) [14]. b): Detailed phase diagram for coherently strained islands [13].

layer-by-layer growth is obtained for the growth of $Al_xGa_{1-x}As$ on a GaAs substrate, which in practise may be regarded as lattice matched because of the nearly identical lattice constants of AlAs and GaAs.

In the case of *lattice mismatched systems*, e.g. $In_xGa_{1-x}As$ on GaAs, Eq. 3.4 yields the total energy for $t \leq h_c$. Further growth of the layer leads to a phase transition, with a change of free energy that may be expressed as $\Delta E_{elastic}+\Delta E_{morph} < 0$, where $\Delta E_{elastic} < 0$ is the change of elastic energy due to strain relaxation. In the case of dislocation formation $\Delta E_{morph}=E^{disl}_{inter}$ is the cost of forming a dislocated interface, whereas in the case of coherent island formation $\Delta E_{morph} = \Delta E_{surf}$ is the change of surface energy [14].

In fact, the ratio $\Gamma = E^{disl}_{inter}/\Delta E_{surf}$ determines which of the two morphologies are preferred, and it is possible to construct a phase diagram, Fig. 3.2a, that distinguishes between a uniform film (UF), coherent islands (CI) and dislocated islands (dislocated film) (DI) as a function of Γ and the amount of deposited material, Q [14]. In the $In_xGa_{1-x}As$/ GaAs system it was found that for coherent island formation to occur in MOCVD (Metal Organic Chemical Vapour Deposition) grown structures a value of $x \geq 0.33$ is required, otherwise a dislocated film results above the critical thickness. [15].

3.2.3 Misfit dislocations.

In the case of dislocation formation, the critical thickness is obtained by equating the strain force of the grown layer to the line tension of a misfit dislocation, which yields the relation

$$\epsilon\text{-}\epsilon_{fric}=\frac{1\text{-}0.25\upsilon}{4\pi(1+\upsilon)}\left(\frac{\mathrm{b}}{\mathrm{h}_c}\right)\left[\ln\left(\frac{\mathrm{h}_c}{\mathrm{b}}\right)+1\right] \tag{3.5}$$

where $\upsilon=C_{12}/(C_{11}+C_{12})$ is Poisson's ratio, b=4Å is the size of the Burges vector for the dislocation here and $\epsilon=\epsilon_{xx}$ is the amount of in-plane strain[47]. The term ϵ_{fric} accounts for a frictional strain that works against the formation of dislocations [46], explaining the observation that for low values of ϵ strained layers with very high values of h_c have been achieved [45] [47].

In section 4.2.5 the generation of misfit dislocations will be discussed further, where limiting values of ϵ_{fric} for InAlGaAs structures are derived from experiments.

3.2.4 Coherently strained islands.

To form the phase of coherently strained islands the uniform film breaks up into a three dimensional structure, consisting of islands that typically form pyramids with low index facets. Part of the deposited material forms a wetting layer between the substrate and the islands corresponding to Stranski-Krastanow growth, and the break-up takes place without generation of dislocations. These islands, e.g. formed by growing $In_xGa_{1-x}As$ on GaAs are particularly interesting because when they are capped with GaAs they effectively confine the electrons and holes in zero-dimensional structures of high optical quality, so-called *quantum dots*, that have properties similar to individual atoms.

A detailed treatment of the surface structure yields a number of different phases of coherently strained islands depending on certain control parameters α and β [12] [13]. The phase diagram is shown in Fig.3.2b for pyramid-shaped islands in a square lattice, in additon to plots showing the dependence of the island energy on the size for each of the phases. The parameter α is proportional to the change of surface energy in the island formation, and although the surface area increases it may actually be negative due to a strain induced reduction of the surface energy. The parameter β increases with the amount of deposited material used for forming the islands, that is the total amount of deposited material minus the part of it used for the wetting layer. Phases 1,4,5 and 6 correspond to stable arrays of islands with an optimum size, L_{opt} that minimizes the energy. In the phases 2 and 3, the

energy is minimized for L$\rightarrow \infty$, corresponding to so-called Ostwald ripening where the average island size increases with time while the density decreases, due to coalesence of islands.

Experimentally, it has been found that the growth of 4 ML of InAs in a normal As_2-background pressure leads to a stable periodic array of coherent islands with an optimum size of L$\approx$140Å, but when the As_2-background pressure is lowered, Ostwald ripening occurs. This is succesfully explained by the phase diagram in Fig.3.2b as a change of the surface free energy from α <0 to α >0 while β is constant, moving the system from phase 4 to 3 [12] [13]. However, recent investigations show that kinetic effects also need to be considered in more accurate models of the island formation [17] than the equilibrium model given here.

3.3 Growth on an atomic scale.

While the thermodynamic approach considered above yields the different equilibrium phases of the surface morphology during growth, it does not describe the processes on a microscopic scale. Knowledge of these processes is important, in order to choose the optimal growth rates, beam fluxes and substrate temperature, and additionally they influence the structure of the interface between two alloys. Here, the basic atomic processes taking place during MBE-growth of GaAs on the GaAs [001]-surface are first considered, which are assumed to be representative of MBE-growth of most III-V semiconductors [18]. Second, exchange processes between different alloys are described, that account for surface segregation and leads to interfaces that are not abrupt.

3.3.1 Surface reactions.

For typical growth temperatures with a background As_2 pressure the GaAs [001]-surface forms a (2×4) reconstruction, where the top layer is terminated by As dimers forming rows in the [$\bar{1}$10]-direction, as illustrated in Fig.3.3. In the case of GaAs growth, Ga atoms are incorporated into the surface with a sticking coefficient assumed to be one. As_2 on the other hand, is physisorbed to the surface, and only in the presence of Ga sites with vacant As sites next to them is the chemisorption of As_2 possible where the Ga-As bond is formed. The As_2 molecules in the physisorbed reservoir may also desorp back into the vacuum. Hence growth is completely controlled by the flux of the group-III elements when the flux of the group-V elements is high enough to keep the physisorped reservior filled. This is accomplished with a V/III flux

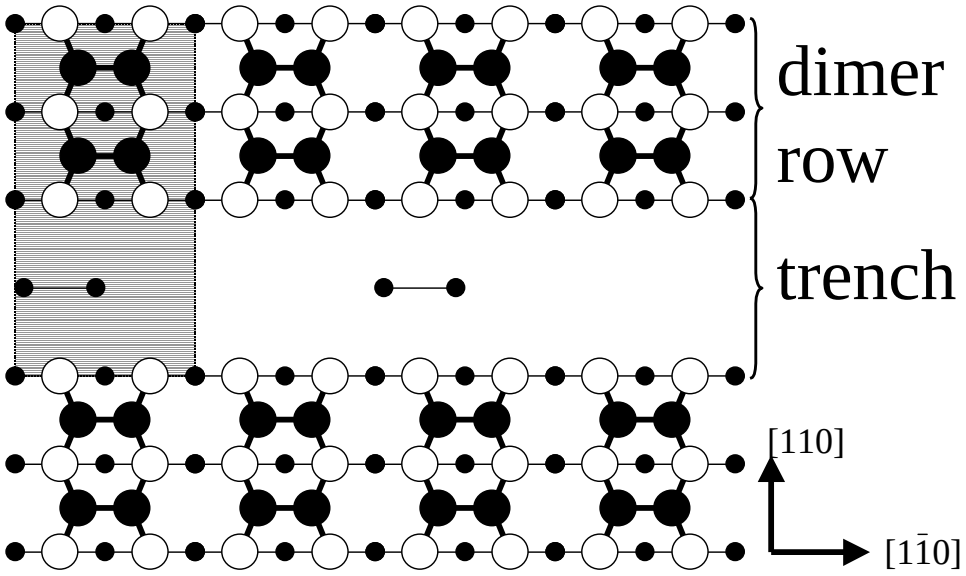

Figure 3.3: Drawing of the top three monolayers in the (2×4) reconstruction of a As-rich [001]-GaAs surface. Big (small) filled circles are As-atoms in the first (third) layer from the top, and open circles are Ga-atoms in the second layer. The shaded box indicates the unit cell.

ratio of 7-8 for growth on the GaAs [001]-surface. If the flux of the group-III elements is too high, the surface eventually becomes Ga rich, and terminated with Ga dimers. In this case further deposition of group-III elements lead to the formation of metal clusters on the surface with detrimental effects on the optical and electrical properties.

When a group-III element is incorporated into the surface, it hops, or migrates, between many different lattice sites, before it eventually forms a Ga-As bond in a chemisorption event. Hence, the flux rate of group-III atoms should be low enough to allow them to find the (local) minimum energy position on the surface. The surface migration of the group-III atoms may be enhanced by raising the substrate temperature, but if it is too high

Surface	Alloy	V/III ratio	T_{sub}	Max. growth rate
(001)	AlGaAs	8-10	595-625° C	1 μm/h
(001)	InAlGaAs	8-10	500-520° C	1 μm/h
(110)	AlGaAs	$\approx$ 20	470°C	0.5 μm/h

Table 3.1: Growth conditions used here for different material systems and surface orientations.

desorption of group-III atoms significantly reduces the growth rate.

The growth conditions used here for different surfaces and alloys as given in Table 3.1. The growth of InAlGaAs requires a lower substrate temperature than for AlGaAs, because of the higher In-desorption rate. For the [110]-surface, which is non-polar, the low incorporation rate of As_2 is compensated for by a combination of a high V/III flux ratio, a low substrate temperature and a slow growth rate [38].

Starting from the As_2 terminated (2×4) surface reconstruction it has recently been shown that after deposition of a fraction of a monolayer of Ga, GaAs islands with a height of a single monolayer are formed after nucleation on the As dimer rows [19]. In the ideal layer-by-layer growth mode, the number and size of the islands then increase until approximately half a monolayer has been deposited, after which the islands coalesce and a terrace free surface is eventually obtained at the completion of the monolayer. In this picture, the step density on the surface increases until approximately half a monolayer has been grown, and then decreases to zero after growth of exactly one monolayer. However, experimental and numerical investigations have shown that this growth mode is only obtained in the beginning, whereas a steady state surface topography is reached after the deposition of several monolayers, where the density of terrace steps is constant and growth proceeds by step propagation. This corresponds to the average migration length being shorter than the average distance between terrace steps [18]. As will be demonstrated in section 3.5.1, the surface recovers the topography with a low density of terraces if a growth interrupt is introduced.

3.3.2 Surface segregation.

The sharpness of the interface between two alloys influences the optical properties of semiconductor structures, e.g. the energy levels and inhomogeneous broadening of excitons in quantum wells. In the plane of the interface the sharpness is ultimately set by the surface topography as described in the previous paragraph. On the other hand, the sharpness in the growth direction is determined by the tendency of the elements in the two alloys to float to the surface, referred to as surface segregations. While this effect is negligible in AlGaAs alloys, and GaAs/ AlGaAs interfaces are very abrupt, In has a pronounced tendency of floating on the surface [24][28]. Thus, when growing an $In_xGa_{1-x}As$ quantum well with GaAs barriers, the In-content is only gradually increasing after the first interface and gradually decreasing to zero after the second interface.

On the microscopic scale, shown in Fig.3.4, surface segregation in e.g. $In_xGa_{1-x}As$ results from an exchange proces of a Ga atom in the surface

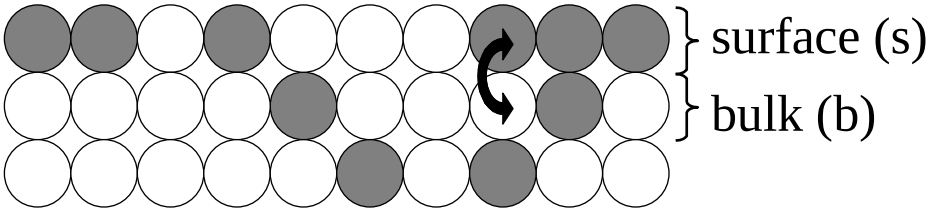

Figure 3.4: Illustration In surface segregation, as an exchange proces in the group-III sublattice, making the surface layer (s) more In-rich (grey cicles).

atomic layer (s) with an In atom in the bulk monolayer underneath (b), in which the system gains an amount of chemical energy E_s and an elastic energy E_{elas} due to strain. The chemical energy is related to the binding energies between group-III and group-V elements[26][24], and reflects that in the lowest energy configuration the most strongly bound group-III element is in the bulk layer because of the fewer bonds of a surface atom compared to a bulk atom. The lowest elastic energy configuration is obtained when the largest atom is in the layer with the least compressive strain.

To simulate the composition profile of an InAlGaAs structure influenced by surface segregation during growth, a model was build based on the three possible segregation processes[35]

$$\mathrm{Ga(b) + Al(s)} \longleftrightarrow \mathrm{Ga(s) + Al(b)} \tag{3.6}$$

$$\mathrm{In(b) + Ga(s)} \longleftrightarrow \mathrm{In(s) + Ga(b)} \tag{3.7}$$

$$\mathrm{In(b) + Al(s)} \longleftrightarrow \mathrm{In(s) + Al(b)} \tag{3.8}$$

with chemical energies E_{s1}, E_{s2} and E_{s3} respectively. The elastic energy term may be neglected for the first proces because the GaAs and AlAs lattice constants are practically identical.

If the bulk (surface) molefractions of In, Al and Ga are x_b (x_s), y_b (y_s) and z_b (z_s), the elastic energies in the last two processes are given by[25]

$$E_{elas} = \frac{1}{2} c^3 \Delta^2 (x_b - x_s) \left[J + \frac{3}{2} \delta J (x_b + x_s) \right] \tag{3.9}$$

where c is the lattice constant of the GaAs substrate, Δ ($\approx 7\%$) is the lattice mismatch between InAs and GaAs/ AlAs, and J = $12.3 \cdot 10^{10}$Pa (J+δJ = $7.9 \cdot 10^{10}$Pa) is the value of $C_{11}+C_{12}-2C_{12}^2/C_{11}$for GaAs/ AlAs (InAs). Using the reactions 3.6 to 3.8, the segregated composition profile of an InAlGaAs structure may be modelled layer-by-layer. If the initial molefractions of the bulk layer are known, and the initial molefractions of the surface layer

are set by the source fluxes, the equilibrium molefractions of the two layers may be found from the law of mass action, using the conservation relations $x_b+y_b+z_b=1$, $x_s+y_s+z_s=1$, $x_s+x_b=$const., $y_s+y_b=$const. and $z_s+z_b=$const. The equilibrium molefractions obtained for the surface layer, are then used as the bulk molefractions in the simulation of the next layer.

In appendix 2, the computer code for the program "segsimul" is given that calculated the composition profile given the nominal profile and the segregation energies. In section 4.2.1, results from this model will be described and compared with experiments.

3.4 MBE growth in practice.

3.4.1 Preparations for growth.

The MBE-system used here is a Varian Modular GEN II, shown schematically in Fig.3.5 where the upper case letters label the parts that will be described in the following. The substrates used for growth are commercially available, *epi-ready*, 2 inch GaAs wafers. The thickness is typically 500μm $\pm$25 μm, with a maximum miscut angle to the [001]-direction of 1°. In the flow bench, (A), the wafers are mounted on sample holders that are attached to a trolley. Typically four wafer are introducted in the MBE-system in each loading.

The trolley is inserted into the *entry-exit* chamber (B), which is pumped down to a pressure of $\approx 10^{-6}$ Torr and degassed for 4 hours at 200°C. During degassing the water vapour is removed, and a final pressure of $< 10^{-8}$ Torr is reached. Through the valve (C) the trolley is moved into the *buffer* chamber (D), where the wafers are prepared for growth. With the manipulation arm (E) a sample holder is moved from the trolley onto the high temperature degassing station (F), where each sample is heated up to 400°C for 1-4 hours, in order to remove residual gasses inside the wafer. A background pressure of $\approx 10^{-11}$ Torr can be obtained in the buffer chamber, increasing to $> 10^{-8}$ Torr during the degassing. To avoid contamination, the valve to the growth chamber (G) is not opened until the pressure in the buffer chamber gets below $2 \cdot 10^{-10}$ Torr after degassing.

With the manipulation arm (H), the sample holder is introduced into the growth chamber and fastened on a substrate holder, the socalled CAR (continuous azimuthal rotation) (I). The CAR is turned so the wafer surface faces the sources (J). The backside of the source flange is shown in the inset in Fig.3.5 where the positions of the sources are indicated. The sources are heated up to a temperature given by the desired beam flux, typically 180°C for As, 800°C for Ga and Al, and 600°C for In. A cracker cell at the end of the As-source decomposes As_4-molecules evaporated from solid As into

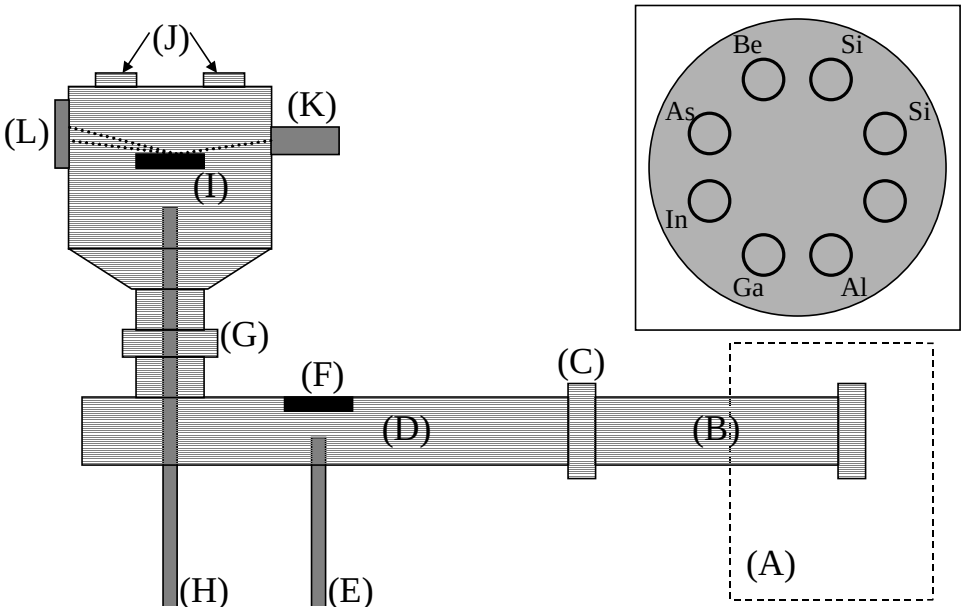

Figure 3.5: Schematic top-view of the MBE-system. (A): Flow bench, (B): Entry-exit chamber, (C): Valve, (D): Buffer chamber, (E): Transfer arm, (F): high temperature degassing station, (G): Valve, (H): Transfer arm, (I): CAR-station, (J): Sources, (K): Electron gun, (L): Flourescent screen. Inset: Side-view of source flange with positions of the individual elemental sources.

As_2-molecules, at a temperature of 700°C. Since the group-III elements are liquids at the operating temperatures they are positioned at the bottom of the flange pointing upwards to the sample. The flux from the sources can be turned on and off by pneumatically activated shutters, either manually or from a computer.

3.4.2 RHEED calibration and growth.

A very important tool for characterizing the sample surface and determining the growth rates, is the socalled reflection high energy electron diffraction (RHEED) pattern. This is formed by the diffraction of 15 keV electrons from the electron gun (K), in Fig.3.5, on the sample surface under a small angle, and is imaged on the flourescent screen (L). Prior to growth, oxides are removed from the wafer surface by heating it up to a high temperature of ≈640°C in a background pressure of As_2 for a few minutes. Formation of the As_2 stabilized (2×4) surface reconstruction is then visible in the RHEED pattern, showing elongated spots when the electron beam is incident along

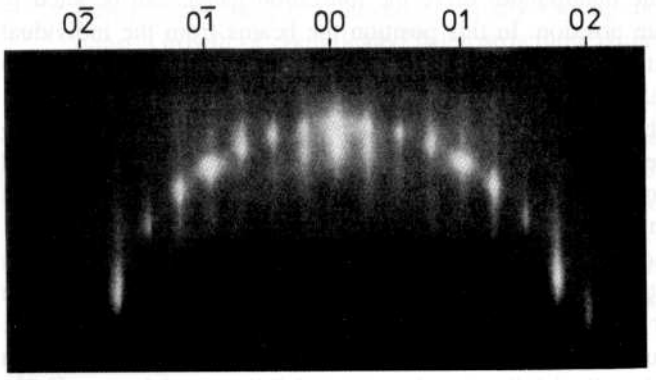

Figure 3.6: Typical RHEED diffraction pattern from the GaAs (2×4) reconstructed surface in the [$\bar{1}$10] direction. From Ref.[9].

the high symmetry directions [110] and [$\bar{1}$10], see Fig.3.6. The spots correspond to diffraction orders of the electrons in the crystal lattice, and in between bright integer order spots weaker fractional order spots are seen, corresponding to the two or four times longer periodicity of the reconstruction. When growth is initiated oscillations in the specular reflection are clearly seen, corresponding to the growth of a single monolayer for each period. The oscillations are damped and disappear after several monolayers (>10), and a constant specular reflection intensity remains which is lower than the initial value. This corresponds to the transition from layer-by-layer growth to step propagation, as described in section 3.3.1, since the RHEED specular intensity is in essence a measure of the density of terrace steps on the surface. The oscillations are utilized to make a precise calibration of the growth rates of the binary compounds and the group-III molefractions in the alloys. Usually, the growth rates are measured separately on a calibration wafer before introducing the wafer on which the desired structure is grown. The substrate temperature, T_{sub}, should be the same for the calibration and the growth, because the growth rates depend on T_{sub} due to the temperature dependence of group-III desorption. Note that the values of T_{sub} given here are the real surface temperature measured with a pyrometer. Due to heat loss, the set point of the thermocouple, T_{TC}, should be higher, and a relation of $T_{sub}=0.78 \cdot T_{TC}+56.4$ was found [38].

During growth the As_2-source is kept open, and growth is controlled by opening and closing the group-III sources, as described in section 3.3.1. For ternary and quaternary alloys the molefractions of the group-III elements are determined by their relative fluxes. At the end of every growth, the surface is capped by a thin layer of GaAs, usually about 10 nm, in order to protect the surface from oxidation in an ambient environment.

After taking out the wafers, some kind of postprocessing is carried out, depending on the particular application of the grown sample. For most of the measurements described in this work the wafer is simply cleaved into 5 mm square pieces that are easily mounted on the cryostat holders used for optical characterization.

The standard optical characterisation techniques of photoluminescence and reflection will not be described in detail here. Only in section 4.3.3 and section 5.3.1 this characterization will be described in further detail, where a special setup was used.

All samples in this thesis are labelled HCØxxx similar to the standard labelling at the III-V Nanolab. (HCØ stands for Hans Christian Ørsted, who discovered electromagnetism, purified Aluminum and founded the Technical University of Denmark!)

3.5 Advanced growth techniques.

In this section a collection of growth "tricks" are presented, that have been used frequently in the work here, e.g. to improve the sharpness of quantum well interfaces, to vary the layer thickness and composition across the wafer or to facilitate the use of several different alloys in the same sample. The main motivation for using these techniques is either to economize on the number of growths, or to be able to vary a parameter continuously (layer thickness or composition) under constant growth conditions.

3.5.1 Growth interruption.

The effects of growth interruptions (GI) were studied in a series of samples, HCØ500-503 , as reported in Ref. [20] [21]. Only the influence of GI on the exciton lineshape will be described here. All four samples were grown under identical growth conditions, that is a substrate temperature of 625°C, a maximum AlGaAs growth rate of 1 μm/h and a V/III flux ratio of 8-10. In each sample three GaAs quantum wells with $Al_{0.35}Ga_{0.65}As$ barriers were grown without wafer rotation. In HCØ503 no GI was used, in HCØ501 (HCØ502) a 120s GI was introduced at the first (second) interface of the quantum wells, and in HCØ500 a 120s GI was used at both interfaces. Fig.3.7 shows the PL spectra at T=50K of a quantum well with a nominal thickness of 7 nm in the four samples.

Comparing the top and bottom spectra in Fig.3.7, it is seen that when GI is used at both quantum well interfaces, the exciton lineshape splits into two narrow lines in contrast to one broad line when no GI is used. This is

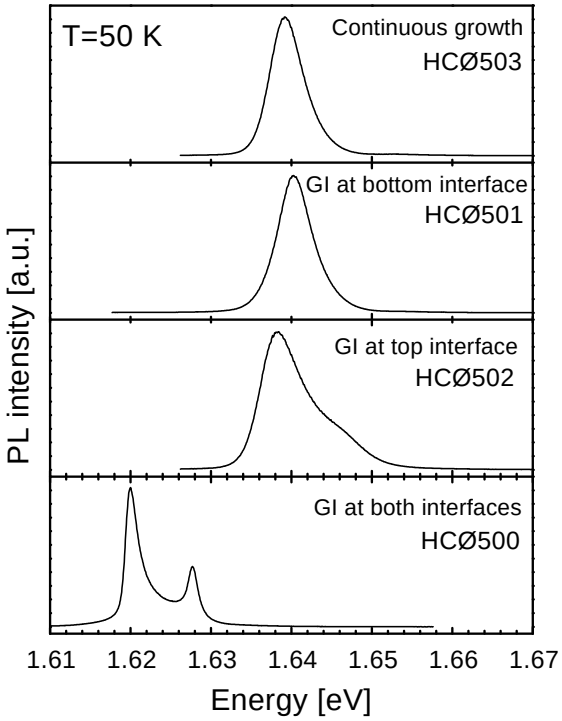

Figure 3.7: PL-spectra at T=50K of the 7 nm quantum well in samples HCØ500-503. For each spectrum it is indicated at which interface(s) a growth interrupt was used.

a consequence of the surface reaction kinetics as described in section 3.3.1. During continuous growth the surface is not in equilibrium and many small islands are present, but when growth is interrupted the islands coalesce into fewer and larger islands that differ in height by exactly one monolayer. The exciton Bohr radius, a_B, acts as a probe of the size, l, of the monolayer flat islands at the interfaces. If $l<a_B$, as in HCØ503, the exciton effectively averages over the monolayer fluctuations at the interface yielding a broad structureless PL-peak, whereas if $l>a_B$, as in HCØ500, the exciton experiences an atomically flat interface which is evidenced in the PL spectrum as two sharp peaks corresponding to quantum well thicknesses differing by one monolayer.

The PL-spectra of HCØ501 and HCØ502 show that interrupting the growth only at the top interface has a larger influence on the lineshape than an interrupt at the bottom only, and in the former case a broad double peak structure is already seen. This indicates that the actual formation of large monolayer flat islands is due to the top interface only, whereas the bottom interface contributes with smaller potential fluctuations that may be further reduced by the growth interrupt.

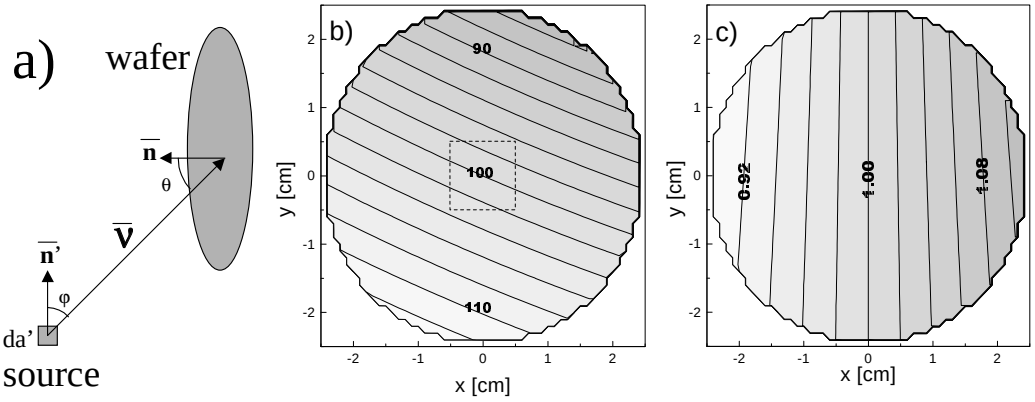

Figure 3.8: a): Geometry of source and sample, with definitons used in Eq. 3.10. b): Relative thickness variation across wafer for growth of GaAs. c): Relative alloy composition variation across wafer for growth of AlGaAs, expressed as the ratio between the Al and the Ga molefraction.

Hence, GI at both interfaces of a quantum well can be used to obtain narrow PL-peaks at discrete energies, corresponding to thicknesses of an interger numbers of monolayers. A growth interrupt of 120s is short enough not to incorporate impurities that degrade the optical properties noticeably, and sufficient to achieve islands larger than the exciton Bohr radius.

3.5.2 Thickness gradient.

A practical problem in thin film growth concerns the uniformity of the layer thickness. The material flux from a source typically decreases like r^{-2}, where r is the distance from the source, which means that close to the source a flat surface experiences a non-uniform flux distribution, while far away the flux is uniform but small. Consider an infinitesimal surface area of the source, da′, with surface normal $\overline{n}'$ and areal evaporation rate E, see Fig.3.8a. The flux dF impinging on a point on the sample surface with position vector $\overline{v}$ relative to the source and a surface normal $\overline{n}$, is then given by [9]

$$dF = \frac{(\overline{n}' \cdot \overline{v})(-\overline{n} \cdot \overline{v})}{\pi(\overline{v} \cdot \overline{v})^2} E da' = \frac{\cos\varphi \cdot \cos\theta}{\pi |\overline{v}|^2} E da' \qquad (3.10)$$

If the coordinates of the Ga-source relative to the sample surface in our MBE system are used, and the source is approximated by a point source, the thickness variation shown in Fig.3.8b is obtained. The thicknesses are given relative to the center thickness, and the resulting variation is nearly linear in the direction of the largest gradient with a slope of $\approx 5\%\text{cm}^{-1}$. This slope

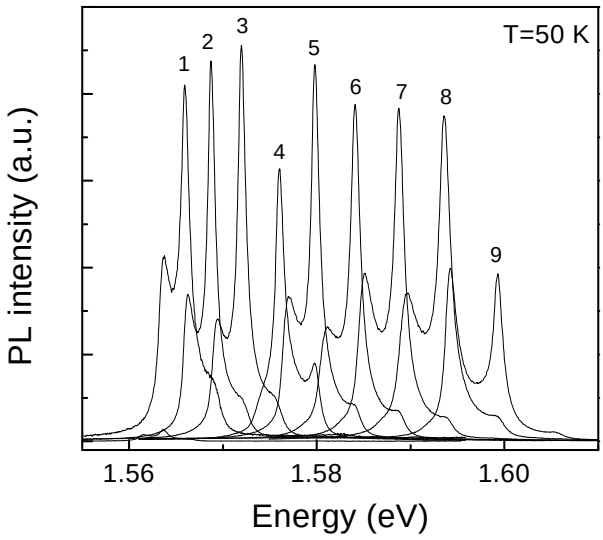

Figure 3.9: PL-spectra across the wafer of HCØ500, for a growth interupted quantum well with a nominal thickness of 10 nm.

is in agreement with the thickness variation experimentally obtained from counting the number of discrete exciton lines across the growth interrupted sample HCØ500, shown in Fig.3.9, where the wafer rotation was stopped during growth of the well. The thickness in the middle of the wafer corresponds to 10 nm and the nine PL-peaks correspond to a thickness difference of 2.5 nm across the 2 inch wafer diameter, or a slope of $\approx 5\%\text{cm}^{-1}$ as obtained above.

Since the thickness gradient is nearly linear it may be efficiently eliminated by azimuthal rotation of the wafer during growth. From experiments on rotated quantum wells, it was found that effects of non-uniformity are only seen in areas 2-3 mm from the growth edge. Fig.3.8b also shows that for the RHEED calibration the electron beam should hit the sample in the middle in order to obtain the average growth rate experienced during growth with sample rotation. If high precision is needed this may be accomplished by bonding a 1 cm square piece of GaAs to the middle of the calibration wafer, which can then be used as a "marker" for centering the electron beam, as indicated with the dashed square, see Fig.3.8.

Alternatively, the linear thickness gradient may be utilized for structures with special functionalities, for instance a tunable microcavity as described in section 5.2.4. Furthermore, the different positions of the group-III sources may be used in combination with the thickness gradient to grow structures with spatially varying alloy compositions. This is illustrated in Fig.3.8c for AlGaAs, where the spatial variations of the relative growth ratio is shown.

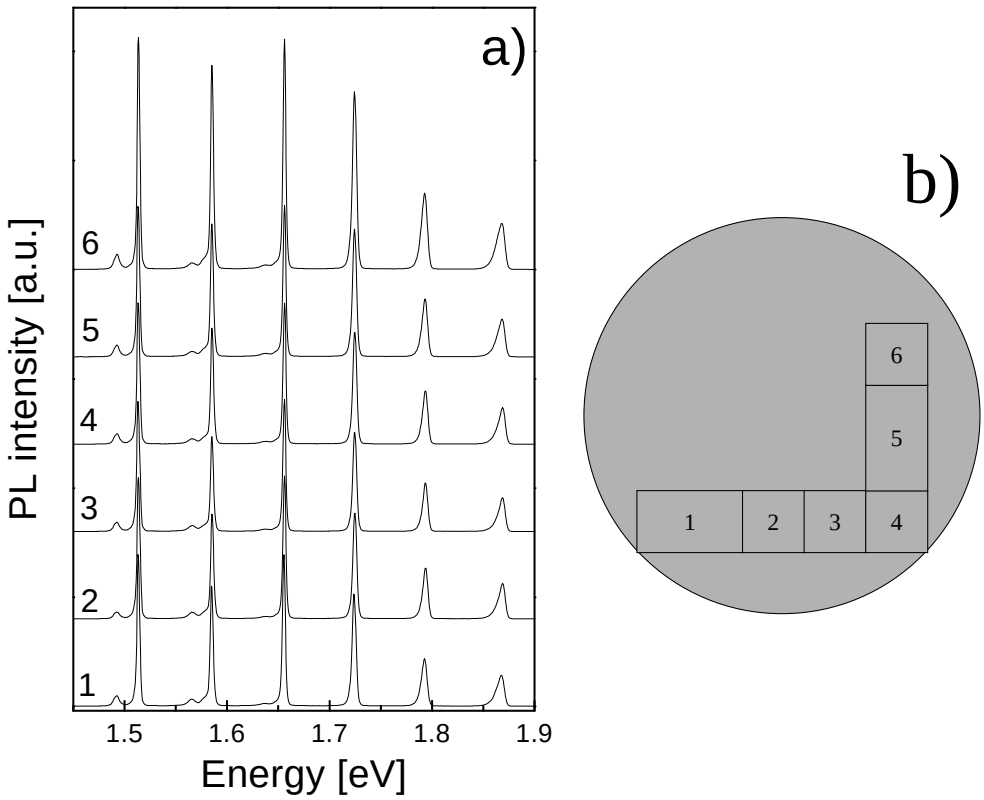

Figure 3.10: a): PL-spectra at T=11K for six different positions, 1-6, on sample HCØ575. b): The six sample pieces cut from the wafer, corresponding to position 1-6 in a).

The possibility of having different alloy compositions in the same layer on one wafer is very advantageous, for instance for the growth of quantum dot structures where the relation between the alloy composition and the transition energies is not known in detail, see section 4.4.2. In this way, the effect of different alloy compositions can be probed in one growth instead of growing several samples until the desired quantum dot energies are achieved.

3.5.3 Digital alloying.

Growth of the typical barrier alloy $Al_{0.30}Ga_{0.70}As$ is usually accomplished by setting the growth rates of AlAs (GaAs) to 0.30 μm/h (0.70 μm/h). In an advanced structure it is often necessary to have several different alloy compositions, which may then be achieved by changing the temperature of the Ga or Al source during growth. However, changing the temperature is a slow process that typically takes 15 minutes before the source is stabilized,

so for several different alloy compositions in the same structure changing the source temperature is not an acceptable solution. Instead, a superlattice consisting of alternating layers of e.g. $Al_xGa_{1-x}As$ and GaAs may be used to realize an *average* alloy composition of $Al_yGa_{1-y}As$ (y<x). In such a digital alloy the relative thicknesses of the two layers determine the value of y, and the period, Λ, of the layers should be chosen much shorter than the length scale of the excitation that probes the digital alloy. That is, if the digital alloy is designed for a specific refractive index the period should fulfill $\Lambda \ll \lambda/n$, where λ is the vacuum wavelength of the light and n is the refractive index. Likewise, if it is designed for a specific band gap one has $\Lambda \ll a_B$, where a_B is the exciton Bohr radius.

Assume that the Al and Ga sources are set to grow $Al_xGa_{1-x}As$ barriers, but somewhere in the structure an $Al_yGa_{1-y}As$ layer (y<x) is needed. This may be achieved by keeping the Ga shutter open during growth of this layer, while the Al-shutter is only periodically opened corresponding to a duty cycle t_{duty} of

$$t_{duty} = \frac{y}{1-y} \cdot \frac{1-x}{x} \tag{3.11}$$

In this case the average growth rate of the digital alloy, GR_{DA}, is given by

$$GR_{DA} = t_{duty} \cdot GR_{Al} + GR_{Ga} \tag{3.12}$$

where GR_{Al} (GR_{Ga}) is the growth rate of AlAs (GaAs). To achieve the most uniform digital alloy possible across a wafer, the opening time of the Al-shutter in each period should be synchronised to match an integer number of wafer rotations. Here, a rotation speed of 60 rpm was used, and an opening time of an integer number of seconds.

The capabilities of digital alloying was experimentally tested, in sample HCØ575 containing five 50 nm wide $Al_yGa_{1-y}As$ layers with y=0, 0.05, 0.10, 0.15, 0.20, 0.257 where x=0.257. The growth parameters for each of the digitally alloyed layers are shown in Table 3.2, and it is noted that the thickest period is 5.42 ML corresponding to 1.5 nm, which is small compared to the bulk exciton Bohr radius. A rotation speed of 60 rpm was used corresponding to the growth times of AlGaAs which are an integer number of seconds. In Fig.3.10a, the photoluminescence (PL) spectrum of the structure at T=10K is shown for the six different places on the wafer shown in Fig.3.10b. The six peaks correspond to the band edges in the quantum wells, and we note that the uniformities of the digital alloys are very good, with no detectable spectral shift of the band edge along two perpendicular directions on the wafer. The spectral position of the measured band edges as a function of the

y	t_{duty}	d_{GaAs} [ML]	t_{GaAs} [s]	d_{AlGaAs} [ML]	t_{AlGaAs} [s]	N_{lay}	E_{gap} [meV]
0	0	177	225.6	0	0	1	1514
0.05	0.152	4.37	5.58	1.05	1.0	33	1585
0.10	0.321	1.66	2.12	1.05	1.0	65	1656
0.15	0.510	1.50	1.92	2.11	2.0	49	1724
0.20	0.723	0.90	1.15	3.16	3.0	44	1793
0.257	1	0	0	177	167.6	1	1868

Table 3.2: Growth parameters for the six layers of the digitally alloyed sample HCØ575. y: average Al-molefraction, t_{duty}: Al-shutter duty cycle, d_{GaAs}/t_{GaAs}: thickness/growth time of GaAs layer, d_{AlGaAs}/t_{AlGaAs}: thickness/growth time of AlGaAs layer, N_{lay}:number of periods in digital alloy, E_{gap}: measured transition energy.

molefraction y, was fitted to a line yielding the relation

$$E_{gap}(Al_yGa_{1-y}As) = (1515.9 \pm 1.6) + (1379.7 \pm 10.1) \cdot y \tag{3.13}$$

This is very close to the experimentally obtained relation for bulk AlGaAs [22], and hence proves the capability of "synthezising" AlGaAs alloys by digital alloying.

The growth of the quaternary $In_zAl_yGa_{1-y-z}As$ material may be treated in a similar way assuming the Ga and Al-fluxes are set to grow $Al_xGa_{1-x}As$ (y<x). Then the $In_zAl_yGa_{1-y-z}As$ may be grown as a digital alloy where the In and Ga-shutteres are kept open and the Al-shutter is open periodically. The growth rate of GR_{In} and the duty cycle of the Al-shutter is given by

$$GR_{In} = \frac{z}{1-y-z} \cdot GR_{Ga} \tag{3.14}$$

$$t_{duty} = \frac{y}{1-y-z} \cdot \frac{1-x}{x} \tag{3.15}$$

and likewise the average growth rate of the digital alloy is

$$GR_{DA} = t_{duty} \cdot GR_{Al} + GR_{Ga} + GR_{In} \tag{3.16}$$

The same synchronization of the growth time of the Al-containing layer and the rotation period as discussed for the ternary alloy should be maintained.

In section 4.2.4 the characterization of digitally alloyed $In_zAl_yGa_{1-y-z}As$ multi quantum wells with $Al_xGa_{1-x}As$ barriers will be described, and a comparison is made with continuously grown InAlGaAs structures.

Chapter 4

Nanostructures based on quaternary InAlGaAs

4.1 Introduction.

As described in section 2.1.4, reducing the dimensionality of semiconductor nanostructures leads to an increasing density of states at the band edge, with the prospect of new physical properties and improved device performance. In the practical realization of low dimensional structures, the choice of semiconductor alloys is very important since it determines the layer thickness that may be grown, the sharpness of the interfaces and the position of the band edge. For MBE-growth on GaAs, the most common material choices are InGaAs/ GaAs or AlGaAs/ GaAs, but occasionally combinations of the ternary alloys are also used, including InAlAs. However, the full quaternary InAlGaAs alloy is rarely used, and very few of its properties are available in standard references [85].

The present chapter deals with the growth and optical properties of quantum wells, quantum wires and quantum dots based on quaternary InAlGaAs alloys, as reported in Ref. [35] [77] [70] [71] [74] [75] [23]. For each of these dimensions, an experimental comparison will be made with similar structures based on binary or ternary alloys, in this way making a direct comparison with the quaternary alloys possible.

4.2 InAlGaAs quantum wells.

Starting with the two-dimensional structure, a detailed analysis of InAlGaAs quantum wells is first presented, with emphasis on the composition profile when surface segregation is taken into account and the modelling of the

measured transition energies and linewidths. Secondly, a series of digitally alloyed multi quantum wells (MQWs) is compared with the continuously grown structures. Finally, the conditions for avoiding misfit dislocations in InAlGaAs MQWs are experimentally investigated.

4.2.1 Composition profile of InAlGaAs quantum wells.

As described in section 3.3.2, In shows a tendency of segregating to the surface, leading to interfaces that are not abrupt. Here, the calculated composition profiles are shown, in order to compare the different alloy systems.

The most important parameters for finding the equilibrium of the exchange reactions, Eq. 3.6-3.8, are the chemical energies, which are not well known from measurements and depend strongly on the growth conditions. Experimentally, it has been found that $E_{s3} > E_{s2} > E_{s1}$ [24] [31] [33], showing that the tendency of In segregation is always stronger than Ga segregation in AlGaAs. However, it was also found that segregation depends more strongly on temperature than the Boltzmann factor, exp(-E_s/kT), entering the law of mass action [30][29][26], suggesting a chemical energy that increases with temperature. The growth model in section 3.3.2 has been compared with a detailed Monte Carlo simulation[26], showing a good agreement at the normal growth temperatures of In-containing structures (T_{sub} $\approx$520°C) where thermodynamic equilibrium is reached [32], and underlining the necessity of taking the strain energy term in Eq.3.9 into account. The comparison also concludes that E_s only should be considered as a fitting parameter valid at the specific growth conditions, and the apparently strong temperature dependence is in fact due to kinetically limited diffusion on the surface. As described in the next section the values E_{s1}=0.17 eV, E_{s2}=0.34 eV and E_{s1} =0.52 eV were found for the growth conditions used here [35].

Using these values, Fig.4.1 compares the simulated composition profiles of an 8 nm GaAs/ $Al_{0.3}Ga_{0.7}As$ quantum well and three 8 nm $In_xGa_{1-x}As$/ GaAs quantum wells (x=0.05, 0.10 and 0.20), with and without segregation. For the GaAs/ $Al_{0.3}Ga_{0.7}As$ well, the composition profile with segregation is not much different from the nominal profile, and most of the change of the Al-molefraction at the interfaces takes place within one monolayer. On the other hand, at the first interface of the $In_xGa_{1-x}As$/ GaAs quantum wells the In-molefraction reaches 90% of the x-value after 7, 8 and 9 MLs, and at the second interface it decays to 10% of the x-value after 7, 9 and 12 MLs. The rise and decay lengths decrease with increasing In-molefraction because of the increasing influence of the elastic energy term, that tends to equilibrate the In-molefraction in the surface and bulk layers. The decay length at the second interface corresponds to 20-35 Å, in good agreement

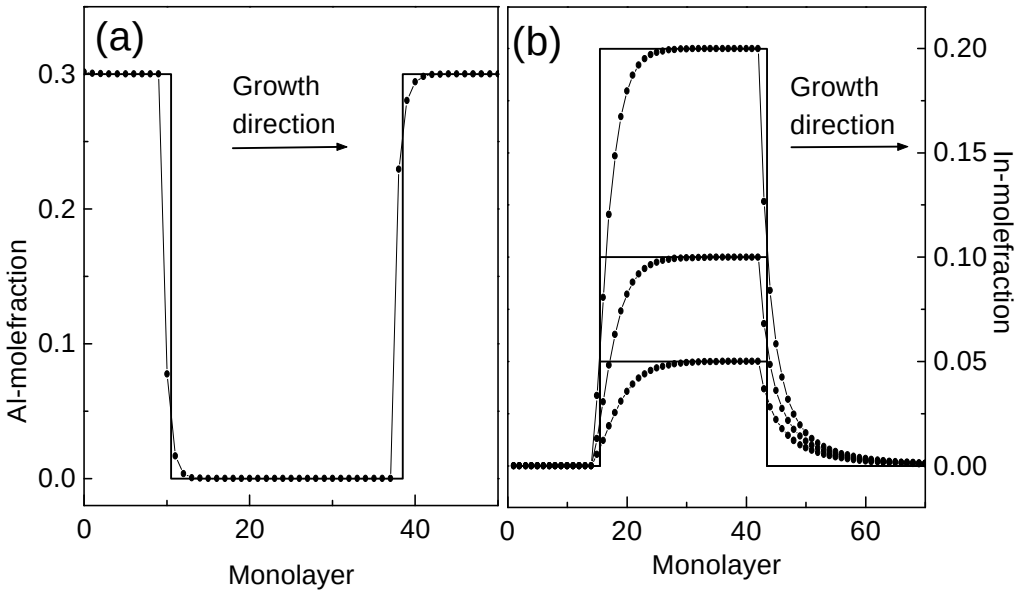

Figure 4.1: a): The solid line (solid line with circles) show the nominal (segregated) composition profile of an 8 nm GaAs/ $Al_{0.3}Ga_{0.7}As$ quantum well. b): The solid lines (solid lines with circles) show the nominal (segregated) composition profile of three 8 nm $In_xGa_{1-x}As$/ GaAs quantum wells, with x=0.05, 0.1 and 0.2.

with SIMS measurements [29].

In Fig.4.2 the simulated composition profile of an $In_{0.15}Al_{0.255}Ga_{0.595}As$/ $Al_{0.3}Ga_{0.7}As$ quantum well is shown. These molefractions are typical for the work here. The rise and decay lengths, defined in the same way as above, are 4 (3) at the first (second) interface for Al and 8 (10) at the first (second) interface for Ga and In. This difference is expected due to the low tendency of Al-segregation. Hence, the model shows that for InAlGaAs quantum wells, the Al composition profile is close to the nominal profile, and the In and Ga profiles are very similar to pure ternary InGaAs quantum wells.

4.2.2 Energy levels of InAlGaAs quantum wells.

For a systematic experimental analysis of InAlGaAs quantum wells, three samples were grown, HCØ548-550, each containing several quantum wells [35]. The first sample was used to find the value of the chemical energy E_{s2} corresponding to the growth conditions used here. The second was used to calibrate the In-source flux as a function of temperature, and the third contains the actual InAlGaAs quantum wells. For all samples a substrate temperature of 515°C, a V/III flux ratio of ≈ 8 and a wafer rotation speed

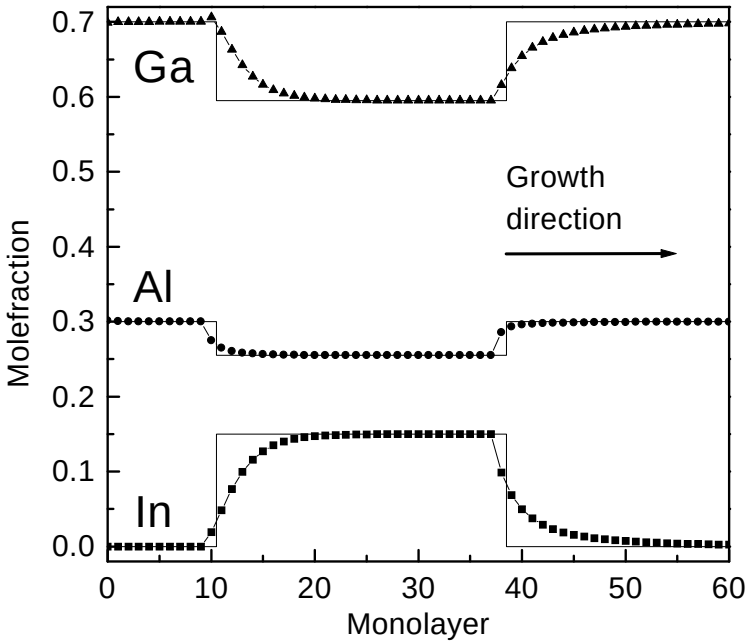

Figure 4.2: The solid lines (solid lines with symbols) show the nominal (segregated) composition profile of Al, Ga and In in an 8 nm $In_{0.15}Al_{0.255}Ga_{0.595}As$ quantum well with $Al_{0.3}Ga_{0.7}As$ barriers.

of 20 rpm were used. To model the transition energies the segregation model described in the previous section was used to calculate the composition profile of grown structures. For each monolayer the band structure parameters were then obtained from the molefractions, that is the effective masses and the position of the band edges, which was then used to solve the Schrödinger equation in a six-band k·p model, using a previously developed computer code [40]. In this calculation the Coulomb interaction is not included, so the exciton binding energy must be subtracted from the eigenvalues afterwards.

In the first sample, HCØ549, 8 InGaAs quantum wells were grown with a nominal In-molefraction of 0.10 and quantum well thicknesses of 1, 2, 3, 5, 7, 10, 20 and 40 nm. In Fig.4.3 the PL-spectrum at T=10K is shown on the right, and the measured transition energies are shown on the left as a function of well width. First, a corrected In-molefraction of x_{corr}=0.092 was found using a square well potential for the thickest quantum well, where surface segregation does not influence the transition energy. Next, the value of the chemical energy E_{s2}=0.34 eV was fitted to yield the best overall agreement with all the quantum well transition energies, using a well width dependent exciton binding energy [41]. The measured and calculated values are compared in Fig.4.3, showing an average deviation of a few meV. In Fig.4.3

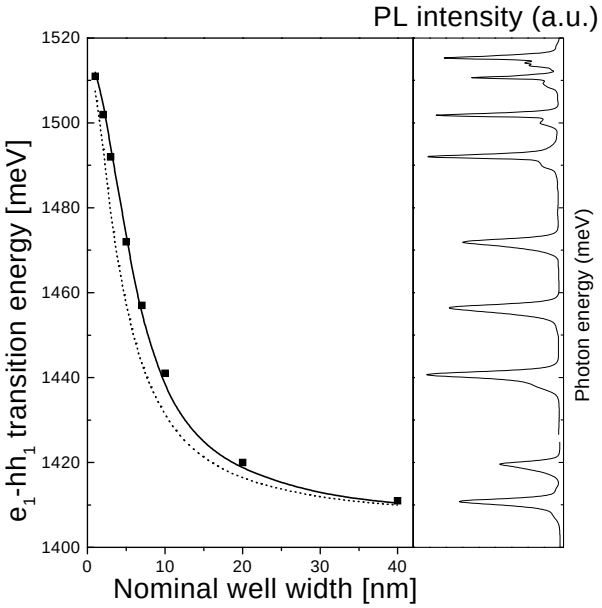

d_{nom} [nm]	x_{nom}	meas. $E_{e\text{-}hh}$ [meV]	calc. $E_{e\text{-}hh}$ [meV]
1.0	0.1	1511	1512
2.0	0.1	1502	1505
3.0	0.1	1492	1494
5.0	0.1	1472	1474
7.0	0.1	1457	1463
10.0	0.1	1441	1438
20.0	0.1	1420	1418
40.0	0.1	1411	1410

Figure 4.3: Right in figure: PL-spectrum at T=10K for HCØ549. Left in figure: The squares show the measured transition energies. The solid (dashed) lines show the calculated transition energies as a function of well width, for a segregation potential (square well potential). Table: Measured and calculated values of the transiton energies in HCØ549.

the calculated transition energies are plotted as a function of well width, for composition profiles with and without segregation. Clearly, including the effect of segregation improves the overall agreement, and it is especially important for the intermediate quantum well thicknesses. At large thicknesses the electron and hole wave functions have small amplitudes at the interfaces, and hence are not influenced much by the exact shape of the quantum well potential here. For narrow wells, the wavefunctions penetrate deeply into the barriers and averages over the quantum well potential, so changes in the shape of the potential do not influence the transition energies much.

The second sample, HCØ548, contained six 5 nm wide $In_xGa_{1-x}As$/ GaAs quantum wells with nominal molefractions of x=0.05, 0.10, 0.15, 0.20, 0.25, 0.30. The sample was used to calibrate the In-source flux as a function of temperature, which is difficult with RHEED for several reasons. Generally, the RHEED intensity oscillations are weaker for growth of InGaAs than for AlGaAs, and at high In fluxes relatively few monolayers of InGaAs can be grown before the critical thickness is reached. Furthermore, if the electron beam does not hit the center of the wafer the RHEED calibration does not yield the exact growth rate obtained for growth with wafer rotation, see section 3.5.2.

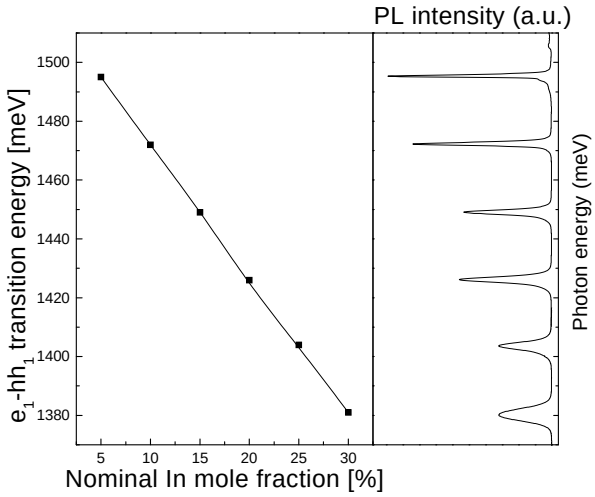

d_{nom} [nm]	x_{nom}	meas. $E_{e\text{-}hh}$ [meV]	calc. $E_{e\text{-}hh}$ [meV]
5.0	0.05	1495	1495
5.0	0.10	1472	1472
5.0	0.15	1449	1449
5.0	0.20	1426	1425
5.0	0.25	1404	1403
5.0	0.30	1381	1381

Figure 4.4: Right in figure: PL-spectrum at T=10K for HCØ548. Left in figure: Measured and calculated transition energies for the best fit of the In-source flux. Table: Measured and calculated values of the transiton energies in HCØ548.

In Fig.4.4 the measured PL-spectrum at T=10K is shown on the right, and on the left the measured and calculated transition enegies are shown for the best fit of the In-source flux. For the calculations the value E_{s2}=0.34 eV found above was used, and the exciton binding energy was taken from Ref.[41]. In agreement with the Clausius-Clapeyron relation, it was assumed that the In-source flux is proportional to exp(-α/T), where T is the absolute temperature and α is a fitting parameter. In 4.4 the values measured and calculated transition energies are compared, yielding a deviation of one meV or less.

Comparing the measured energies of the nominally identical 5 nm $In_{0.1}Ga_{0.9}As$/ GaAs quantum wells in HCØ548 and HCØ549, shows that the reproducibility of the growth conditions is so good that no difference can be observed with PL.

In HCØ550, five 8 nm InAlGaAs quantum wells were grown, referred to as QW1-QW5, with $Al_{0.17}Ga_{0.83}As$ barriers. For the wells In was added without using digital alloying, yielding a quaternary alloy which may be written as $In_x(Al_{0.17}Ga_{0.83})_{1-x}As$ to indicate that the relative molefractions of Al and Ga are the same in the whole structure. The nominal In-molefractions, x=0.05, 0.10, 0.15, 0.20 and 0.25 were obtained by varying the In-source temperature. The PL-spectrum of HCØ550 at T=10K, see Fig.4.5, shows five well defined peaks with similar shapes but differing widths, indicating a good sample quality without strain relaxation. In addition to the e-hh transition

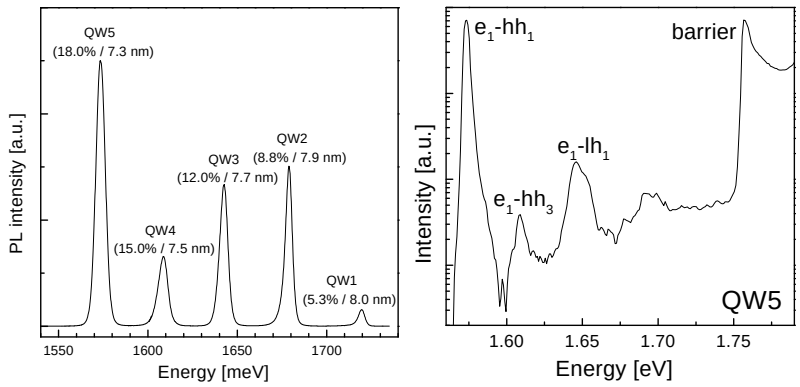

Figure 4.5: Left: PL-spectrum of HCØ550 at T=10K, corresponding to the e-hh transition in QW1-QW5. At each peak the corrected values of the well width and In-mole fraction are given. Right: PLE-spectrum of QW5 at T=10K, with assignments of the peaks.

energies obtained from PL, the e-lh transition energies were also measured using photoluminescence excitation spectroscopy (PLE), see Fig.4.5. In this plot e_1-hh_1 (e_1-lh_1) refers to the transition between the first level in the conduction band and the first level in the heavy-hole (light-hole) band. Since the quantisation energies of the second and third levels are much lower for the holes than for the electrons, due to the larger hole mass, and since e_1-hh_2 is forbidden by symmetry [5], the peak in between is assigned to the e_1-hh_3 transition.

To model the measured e-hh and e-lh transition energies, the In-source calibration and the value of E_{s2} obtained above was used to calculate the composition profile of the quantum wells. The values of E_{s1} and E_{s3} needed to model the segregation in the quaternary system were derived from E_{s2}, using the experimentally determined ratio of approximately 1:2:3 between the energies [25][31]. Since the nominal In-source flux differed from the calibrated In-source flux obtained from HCØ548, the nominal thicknesses and In-molefractions in QW1-QW5 were corrected as indicated in Fig.4.5 and Table 4.1. The binding energies were assumed to be 7 (8) meV for the heavy (light) hole exciton.

The best fit to the transition energies, see Table.4.1 was obtained using the following empirical relation for the unstrained $In_x(Al_yGa_{1-y})_{1-x}As$ bandgap

$$E_{gap}(In_x(Al_yGa_{1-y})_{1-x}\ As)=1.519+1.36y+0.22y^2-1.584x+0.475x^2+0.55xy \quad (4.1)$$

In the limits $x\rightarrow 0$ and $y\rightarrow 0$ this relation becomes the experimentally well

Label	L_{nom} [nm]	x_{nom}	L_{corr} [nm]	x_{corr}	E^{meas}_{e-hh} [meV]	E^{calc}_{e-hh} [meV]	E^{meas}_{e-lh} [meV]	E^{calc}_{e-lh} [meV]
QW1	8.0	0.05	8.0	0.052	1719	1720	1742	1734
QW2	8.0	0.10	7.9	0.088	1679	1679	1717	1709
QW3	8.0	0.15	7.7	0.120	1643	1643	1694	1689
QW4	8.0	0.20	7.5	0.150	1609	1609	1674	1670
QW5	8.0	0.25	7.3	0.180	1574	1578	1650	1652

Table 4.1: Measured (meas) and calculated (calc) values of the transition energies in QW1-QW5 of HCØ550. L_{nom} (L_{corr}) and x_{nom} (x_{corr}) are the nominal (corrected) quantum well thicknesses and In mole fractions respectively.

determined band gap relation of AlGaAs [22] and InGaAs [41], see section 2.1.3, and the last term proportional to xy is the lowest order correction due to the simultaneous presence of Al and In. The measured barrier bandgap of QW1-QW5, obtained from the PLE measurements, was in very good agreement with Eq.4.1 for x=0 and y=0.17.

4.2.3 Linewidth analysis.

In Table 4.2, the measured full width at half maximum (FWHM) of the PL-peaks in HCØ550 are given. In a simple model of the linewidths of InAlGaAs quantum wells the width is assumed to be the Gaussian sum of three independent contributions

$$\Delta E_{FWHM}=\sqrt{\Delta E_x^2+\Delta E_y^2+\Delta E_{wwf}^2} \tag{4.2}$$

where ΔE_x and ΔE_y are due to alloy fluctuations of In and Al, and ΔE_{wwf} is due to fluctuations of the width of the quantum well. The alloy fluctuations may be described statistically as a standard deviation of e.g. the In-molefraction within the volume of the exciton [42]

$$\Delta E_x=2\sqrt{2\ \ln 2}\sqrt{\frac{x(1-x)}{N}}\frac{\partial E_{gap}}{\partial x} \tag{4.3}$$

where x is the mean In-molefraction, N is the number of group-III atoms within the exciton volume and $\partial E_{gap}/\partial x$ is the partial derivative of the alloy bandgap. To calculate the exciton volume $V=\pi a_0^2 L_z$ was used, where a_0=13 nm is the in-plane Bohr radius and L_z is the FWHM of the wave function in the growth direction. A similar relation was used for Al.

Label	ΔE^{meas}_{FWHM} [meV]	ΔE_x [meV]	ΔE_y [meV]	ΔE_{wwf} [meV]	ΔE^{calc}_{FWHM} [meV]
QW1	3.5	1.75	2.93	0.77	3.50
QW2	3.9	2.19	2.94	1.43	3.93
QW3	4.6	2.58	3.06	2.31	4.62
QW4	5.4	2.93	3.20	3.08	5.32
QW5	6.0	3.19	3.29	3.85	5.99

Table 4.2: Measured and calculated linewidths of QW1-QW5 at T=10K.

To describe the broadening due to well width fluctuations the derivative of the e-hh transition energy with respect to the well width was calculated, $\partial E_{e-hh}/\partial L$, and an effective size of the effective well width fluctuations, ΔL_{eff}, was used,

$$\Delta E_{wwf} = \frac{\partial E_{e-hh}}{\partial L} \Delta L_{eff}. \tag{4.4}$$

A very good fit to all the measured well widths was obtained with ΔL_{eff}=1.1 ML as shown in Table 4.2, where the magnitudes of the three individual contributions are also given. We note that the variation of ΔE_y is negligible because the Al-molefraction is almost constant in the wells.Due to the square root dependence in Eq. 4.3 ΔE_x increases sublinearly with the In-molefraction. On the other hand, the contribution from well width fluctuations increases almost linearly with the In-molefraction, and changes from being the least significant contribution in QW1 to the most significant in QW5.

It should be emphasized that the linewidth analysis here is a very simplified approach, and for instance does not consider the effect of partially localized excitons that may result in a more narrow lineshape than the potential distribution [43]. However, it is sufficient to estimate the relative magnitude of the contributions to the lineshape, and to conclude that the linewidths are determined purely by random statistical effects. That is, clustering of the group-III elements may be excluded as well as partial relaxation of the strain, which leads to much broader linewidths [44].

4.2.4 Digitally alloyed InAlGaAs MQWs.

A number of InAlGaAs MQWs were grown for making T-shaped quantum wires, that will be described in the following sections. For these structures high barriers were needed, typically of $Al_{0.3}Ga_{0.7}As$, but at the same time it

Sample	Well material z,y	L_{QW} [nm]	E_{e-hh}^{meas} [meV]	E_{FWHM} [meV]	E_{e-hh}^{calc} (ΔE) [meV]
HCØ583	0.15,0.16	10.6	1591	15.5	1650(59)
HCØ584	0.10,0.145	20.1	1558	20	1633(75)
HCØ587	0.10,0.145	17.6	1591	4.6	1638(47)
HCØ588	0.10,0.11	17.9	1537	3.7	1589(52)
HCØ589	0.10,0.18	17.9	1644	4.4	1686(42)
HCØ626	0.15,0.15	8.8	1606	5.1	1652(46)
HCØ627	0.20,0.18	8.2	1632	7.9	1667(35)

Table 4.3: Nominal quantum well In(z)- and Al(y)-mole fractions, quantum well thickness, L_{QW}, measured e-hh energy, E_{e-hh}^{meas}, measured e-hh linewidth, E_{FWHM}, and calculated e-hh energy, E_{e-hh}^{calc}, (deviation from measurement, ΔE) of the InAlGaAs MQWs investigated here. All samples were grown with $Al_{0.3}Ga_{0.7}As$ barriers.

should be possible to choose the In- and Al-molefractions in the well independently. To avoid changing the source temperatures several times during growth, this was accomplished by using digital alloying as described in section 3.5.3. In Table 4.3 the In and Al-molefractions and quantum well thicknesses are given for these structures. All samples were grown with a substrate temperature of 500°C, a V/III flux ratio of 8-10 and the wafer rotation was synchronized to the growth time of the InAlGaAs layer in the digital alloy.

The energy and linewidth of the e-hh transition was measured with PL at T=10K, and in Table 4.3 these values are compared to the calculated values using the model in the previous section and a constant exciton binding energy of 7 meV. Especially for HCØ583 and HCØ584 the difference is very large and the spectra are broad, which is explained by a clearly visible strain relaxation due to misfit dislocations. For the rest of the samples, the calculated values are all ≈40-50 meV higher than the measured values indicating a systematic origin of the difference. Two important differences between these samples and the samples HCØ548-HCØ550 described in section 4.2.2 should be emphasized, that may explain this deviation. First, the growth rates for the samples in Table 4.3 were obtained from the RHEED oscillations, that is no calibration samples were grown to check the In and Al-molefractions. Secondly, digital alloying was used in these samples to obtain the desired molefractions in the quantum well. As mentioned in section 3.5.2, RHEED calibrations yield the wrong molefractions and growth rates if the electron beam is not centered on the sample, and in fact for small variations of Δy=0.015 and Δx=-0.015 Eq. 4.1 leads to an increase of the bandgap of ≈45 meV. Because the RHEED calibration is more difficult for the growth rate of InAs than for AlAs and GaAs, most of the uncertainty is

Sample	L_b [nm]	N	ϵ_{eff} [%]	d* [nm]	Growth
HCØ583	25	41	0.32	1460	relaxed
HCØ584	25	25	0.32	1128	relaxed
HCØ587	50	10	0.19	680	pseudo
HCØ588	50	10	0.19	680	pseudo
HCØ589	50	10	0.19	680	pseudo
HCØ626	50	10	0.16	588	pseudo
HCØ627	100	10	0.11	1082	pseudo

Table 4.4: Barrier thickness, L_b, number of wells, N, effective strain, ϵ_{eff}, total thickness, d*, and growth morphology of the InAlGaAs MQWs investigated here.

probably related to the In molefraction. Furthermore, the frequent shutter operations during growth of the digital alloy may cause deviations of the molefractions from the nominal values if the opening and closing times are different. Although the measurements in section 3.5.3 do not indicate this problem, changes of the shutter speeds over time have not been checked.

However, since the linewidths of the InAlGaAs MQWs in Table 4.3 are very similar to the ones of HCØ550, see Table 4.2, it may be concluded that digital alloying leads to a distribution of the group-III elements which is experimentally indistinguishable from continuously grown alloys. Additionally, the almost constant difference between the calculated and measured e-hh transition energies show that it is realistic to grow digitally alloyed InAlGaAs MQWs with energy levels differing at the most by ≈ 10 meV from the designed values - if the exact origin of the systematic deviation is known.

4.2.5 Misfit dislocations in InAlGaAs MQWs.

A potential problem of growing strained MQWs, is that the accumulation of elastic energy leads to formation of misfit dislocations even if the individual quantum well does not exceed the critical thickness. For structures with multiple quantum wells, it has been shown that the governing parameters are the effective (average) strain, ϵ^*, and the total thickness, d*, given by

$$\epsilon^* = \frac{L_{QW}\epsilon_{QW} + L_b\epsilon_b}{L_{QW}+L_b} \tag{4.5}$$

$$d^* = (L_{QW}+L_b)N \tag{4.6}$$

where L_{QW} (ϵ_{QW}) and L_b (ϵ_b) are the thickness (strain) of the quantum wells and the barriers, and N is the number of periods in the structure[45]. The

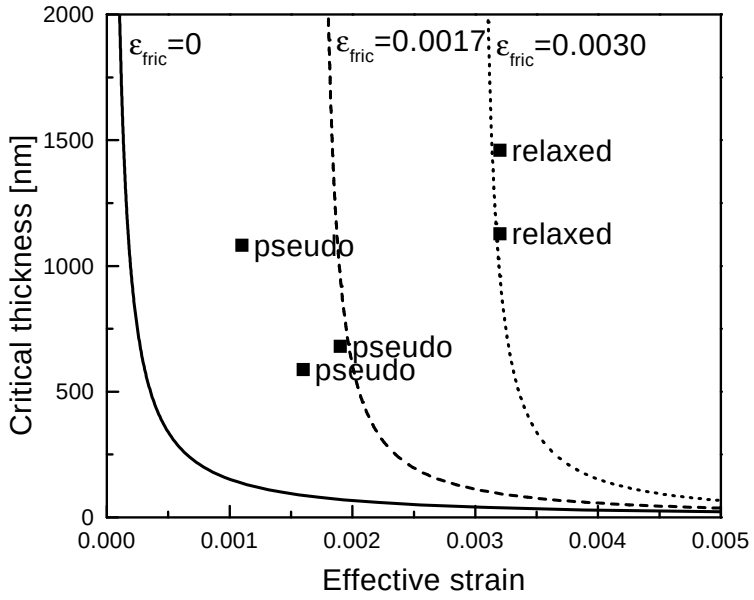

Figure 4.6: Plot of effective strain and total thickness (solid squares) of the InAlGaAs MQWs investigated here, indicating the surface morphology for each set of values. The solid, dashed and dotted lines show the calculated relation between critical total thickness and effective strain for ϵ_{fric}=0, 0.0017 and 0.0030.

condition for generation of misfit dislocations is then the same as for a single quantum well, see Eq. 3.5, with the well thickness and strain replaced by d^* and ϵ^*.

For the MQW structures grown here ϵ_b=0 since the barriers are lattice matched to the substrate. The values of ϵ^* and d^* are given in Table 4.4 and plotted in Fig.4.6, indicating whether the quantum wells were pseudomorphically grown (pseudo) or the elastic strain was relaxed by forming misfit dislocations (relaxed).

Using the values b=4 Å and υ=0.33 for Poisson's ratio[47], the dependence of critical total thickness, d_c^*, on the effective strain is plotted in Fig.4.6 for three different values of ϵ_{fric}. Clearly, for ϵ_{fric}=0 misfit dislocations should be present in all the samples grown here, in contrast to observations. The dashed and dotted lines correspond to the minimum and maximum values of ϵ_{fric} deduced from the samples here. The minimum value of ϵ_{fric}=0.0017 is in good agreement with the value of ϵ_{fric}=0.0015 found for growth of $GaAs_{0.95}P_{0.05}$ on GaAs substrates [47].

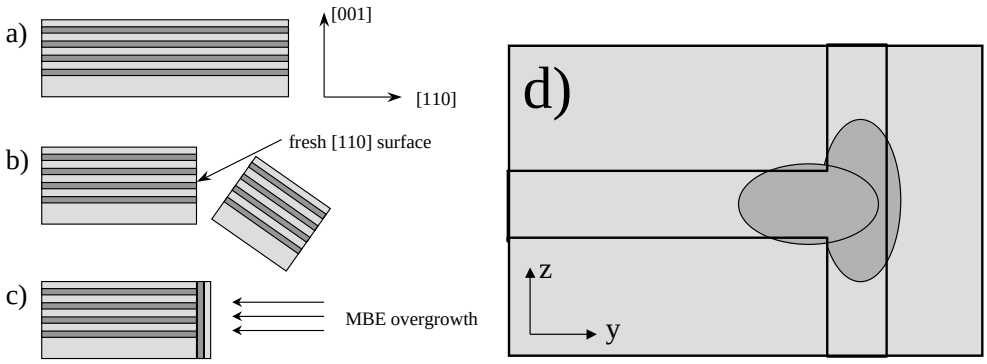

Figure 4.7: a): Orientation of MQW structure used for cleavage. b): Cleavage under UHV conditions, leaving a clean [110]-surface. c): Overgrowth on the [110]-surface. d): Schematic illustration of the T-wire wavefunction, spreading out into both the MQW and OGW structures.

4.3 InAlGaAs quantum wires.

4.3.1 Background.

One of the most promizing and well controlled ways of making quantum wire structures, is the socalled cleaved edge overgrowth method. Originally proposed in 1985 [49] and experimentally demonstrated in 1992 [48], it consists of an [001]-oriented multi quantum well (MQW) structure which is cleaved along a [110]-plane under UHV conditions, and overgrown by a single quantum well (OGW). This procedure is schematically shown in Fig. 4.7a-c, and the final structure is referred to as a T-wire (TWR). The transition energy of the overgrown well, E_{OGW}, is matched to the transition energy of the MQWs, E_{MQW}, and at the T-shaped intersection a new state is formed with an energy $E_{TWR} < E_{MQW}$, E_{OGW}. Since this state is bound in the yz-plane, and free to move only in the x-direction, it is a quantum wire state.

The mechanism of binding is purely quantum mechanical [48], which is seen from the Hamiltonian in the yz-plane

$$H\Psi = \left[\frac{-\hbar^2}{2m^*}\nabla^2 + V(y,z) \right] \Psi \qquad (4.7)$$

where m^* is the effective mass of either the electron or hole, and V(y,z) is the variation of the bandgap in the yz-plane. At the T-shaped intersection the electron and hole can spread out their wavefunctions into both quantum wells, as illustrated in Fig.4.7d, in this way lowering the quantization energy in Eq. 4.7 that originates from the first term on the right hand side.

A frequent pursuit of TWR research has been to maximize the separation between the quantum wire energy and the lowest of the two quantum well energies, E_{MQW} and E_{OGW}, the so-called *confinement* energy, E_{conf}. To accomplish this, different T-wire structures have been proposed, which may be separated into symmetric and asymmetric geometries.

In the symmetric structures the MQWs and the OGW consist of the same well material and the maximum confinemet is achieved for $E_{MQW}=E_{OGW}$, which requires the OGW to be a little thinner than the MQWs, because of the larger hole mass in the [110]-direction[52]. The absolute value of E_{conf} is influenced by scaling the structure, and for GaAs/ $Al_{0.3}Ga_{0.7}As$ quantum wells it was found experimentally that the thinner the quantum wells the larger is E_{conf}, because E_{conf} increases with the quantization energy in the quantum wells [55]. Likewise, for increasing barrier heights E_{conf} also increases as demonstrated by using either GaAs/ AlAs[55][54][56] or $In_xGa_{1-x}As$/ $Al_{0.3}Ga_{0.7}As$[51][58] quantum wells instead of GaAs/ $Al_{0.3}Ga_{0.7}As$.

It was demonstrated both theoretically and experimentally that higher confinement energies may be achieved in asymmetric structures compared to symmetric ones, and a record high E_{conf}=54 meV was obtained with 12 nm $Al_{0.14}Ga_{0.86}As$/ $Al_{0.3}Ga_{0.7}As$ MQWs and a 2.5 nm GaAs/ $Al_{0.3}Ga_{0.7}As$ OGW[63][61]. Also for the asymmetric TWRs, the maximum confinement energy is obtained for $E_{MQW}=E_{OGW}$.

Only a few quantum wire structures have been reported where confinement is influenced by the potential, V(y,z), in Eq. 4.7. In one structure, a GaAs quantum well with $Al_{0.3}Ga_{0.7}As$ barriers on *both* sides was overgrown on strained InGaAs/GaAs MQW[50]. The penetration of the strain field into the quantum wells was reported to modify the bandgap of the overgrown well through the deformation potential, giving rise to local minima in V(y,z) along the z-direction. In the $In_xGa_{1-x}As$/ $Al_{0.3}Ga_{0.7}As$ T-wire structures, the bandgap in the overgrown well is also modified in the z-direction due to strain, but this effect was estimated to be not more than a few meV [51].

The following sections describe the growth, characterization and analysis of a number of asymmetric, strained T-wire structures based on quaternary InAlGaAs MQWs with GaAs OGWs. With this material combination a novel T-wire structure is realized, where $E_{MQW}=E_{OGW}$ can be achieved and at the same time the overgrown well is only strained in the T-shaped intersection. The energy levels are compared both experimentally and theoretically with unstrained asymmetric T-wires.

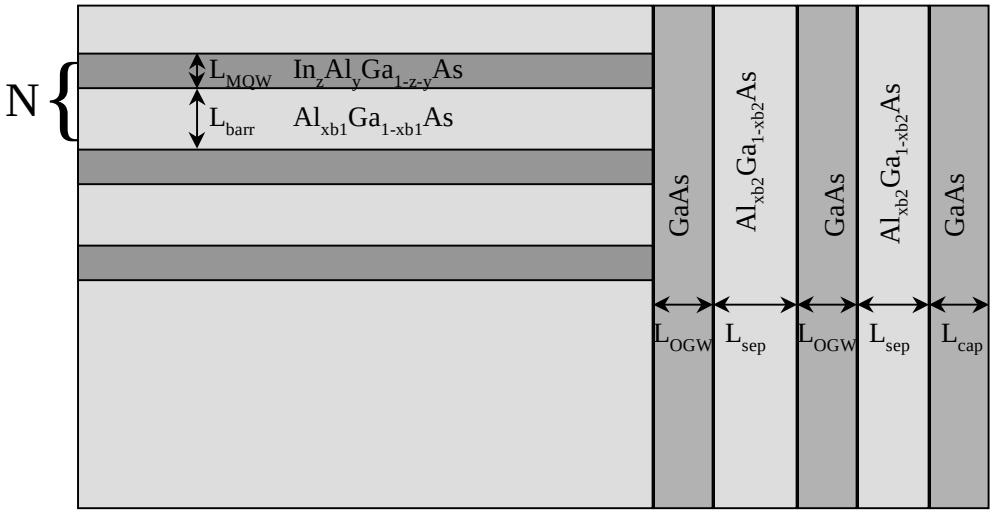

Figure 4.8: Schematic illustration of the composition and geometry of the TWRs studied here.

4.3.2 Growth of T-wires.

In Fig.4.8 a cross sectional view of the quantum wire structures used here is shown. First N periods of $In_zAl_yGa_{1-y-z}As$/ $Al_{xb1}Ga_{1-xb1}As$ quantum wells were grown on the [001]-surface, with well widths of L_{MQW} and separatios of L_{barr}, as described in section 4.2.2. After growth, the wafer was cut into four pieces along the diameters in the [110] and [1$\bar{1}$0] directions. Each piece was mechanically lapped to a thickness of $\approx$120μm using an emulsion of 9 μm sized aluminium-oxide grains in water, and subsequently an almost mirror-like surface was obtained by mechanical polishing with 0.3 μm sized grains. The lapped and polished pieces were then cut into smaller 4 mm $\times$ 7 mm samples, and a scratch was made on the surface perpendicular to the long edge, 4 mm from one of the short edges.

Before being loaded in the MBE system, the samples were cleaned three times in trichloroethane ($\approx$100°C), then in methanole ($\approx$80°C) and finally in demineralized water ($\approx$80°C). After drying in a flow of nitrogen gas the samples were attached on special holders using Ga-bonding. Each holder had space for 6-8 samples, that were mounted horizontally with the scratched surface facing upwards. Typically the samples were scratched on the polished surface and bonded on the grown surface, but the opposite configuration was also tried where the bonding to the polished surface was found to be equally efficient. After loading, the same procedure was followed for growth preparation as for ordinary wafers.

Immediately before growth, the samples were cleaved on the trolley in the buffer chamber, using the fingers of the transfer arm. The cleavage emanated from the position of the scratch, leaving a 4 mm $\times$ 4 mm piece on the sample holder with the cleaved surface facing outward, like the surface of an ordinary wafer during growth. Especially two factors were found to be important in order to obtain cleavage at the position of the scratch. First, the liquid Ga applied to the surface holder for bonding should have a smooth, mirror-like surface over the whole area which the samples were bonded to. If the surface was mat grey or solid particles were visible in the liquid Ga, the obtained bonding strenght was not always sufficient to keep the samples fixed to the holder during the cleavage. Second, the pressure and sharpness of the diamond scriber used to make the scratch should be set to the normal values used for scribing and cleaving pieces of a GaAs wafer. If the force from the scriber was reduced, cleavage was often difficult and the samples broke into small pieces. When paying attention to these conditions, cleavage at the position of the scratch was typically obtained on four out of five samples.

After cleavage, the sample holder was transferred to the growth chamber, and heated up to the growth temperature in 5 minutes after which the overgrowth was started. Hence, the total time from cleavage to overgrowth was typically <10 minutes, and during this time the pieces were kept either in the low pressure environment of the buffer chamber or in the background As_2-pressure of the growth chamber. In this way surface contamination was minimized, yielding a clean interface between the cleaved surface and the overgrown layers.

The overgrowth consisted of a GaAs quantum well of thickness L_{OGW} with an $Al_{xb2}Ga_{1-xb2}As$ barrier of thickness L_{sep}, see Fig.4.8. After the barrier a reference quantum well was grown, with a barrier layer of the same thickness L_{sep}. Finally, a GaAs cap layer of thickness L_{cap} was grown to avoid surface oxidation and to separate the quantum wells further from the surface. Due to the [110]-orientation of the cleaved surface, special growth conditions was used. The substrate temperature was set to 470°C, the AlGaAs growth rate was kept below 0.6 μm/h and the ratio of the As flux to the group-III flux was 18-20 [38, 37].

In Table 4.3.2 the growth parameters are shown for the quantum wire structures grown and characterized here. HCØ594, HCØ595, HCØ654 and HCØ655 are based on the InAlGaAs MQW structures described in the previous section, where the details of their design and growths can be found. HCØ613, HCØ615 and HCØ624 are AlGaAs MQW structures, grown using digital alloying for the well material.

Sample	L_{MQW} [nm]	N	MQW alloy z,y	xb1	L_{OGW} [nm]	L_{sep} [nm]	xb2	L_{cap} [nm]
HCØ594	17.9	10	0.10,0.18	0.30	3.0	30	0.32	80
HCØ595	17.9	10	0.10,0.18	0.30	3.5	30	0.32	150
HCØ654	8.8	10	0.15,0.15	0.29	5.0	30	0.30	150
HCØ655	8.8	10	0.15,0.15	0.29	4.2	30	0.30	150
HCØ613	18.0	50	0,0.063	0.31	4.2	30	0.35	100
HCØ615	24.0	50	0,0.03	0.31	6.3	30	0.29	100
HCØ624	16.0	50	0,0.082	0.31	3.0	50	0.32	80

Table 4.5: Alloy compositions and well thicknesses of the TWR structures investigated here. The definition of the parameters are given in Fig.4.8.

4.3.3 PL-measurements of T-wires.

For PL characterization at low temperatures a recycling He-cryostate with very high vibration stability was used. The samples were mounted to facilitate excitation and collection of light normal to the cleaved surface. For the excitation a He-Ne CW laser beam was focussed with a 60 mm focal length lens to a spot size of 20 μm on the sample surface. The same lens was used to collect the luminescence, which was dispersed in a grating spectrometer with a resolution of 100 μeV. The light emission was monitored with a CCD-camera, to make sure that the sample was always focussed during measurements.

With an xyz-translation stage, the sample holder could be moved to investigate the spatial variations of the PL-spectrum, as indicated in Fig.4.9. Movements in the z-direction was used to distinguish the origin of different PL-peaks in a similar way as the micro-PL measurements reported in Ref.[57]. Starting at arrow 1, where the substrate is below the overgrown layers, only luminescence from the overgrown reference well is seen (dashed lines). When the sample is moved in the z-direction to the edge where the MQWs intersect with the overgrown well, luminescence is seen both from the quantum wires, the MQWs and the reference well (solid lines). Since the quantum wire states are present only at this intersection, the luminescence shows a very strong dependence on the z-position which is used to identify them (marked with TWR). The luminescence of the MQWs is visible over a larger range of z-positions because they may also be excited by defocussed light deeper in the sample along the x-direction. Because the excitation is in the plane of the MQWs, they are efficiently excited and usually the strongest feature in the spectra. In Fig.4.9 and Fig.4.10 the PL-spectra at T=11K of the seven samples are shown, and the positions of the peaks are listed in

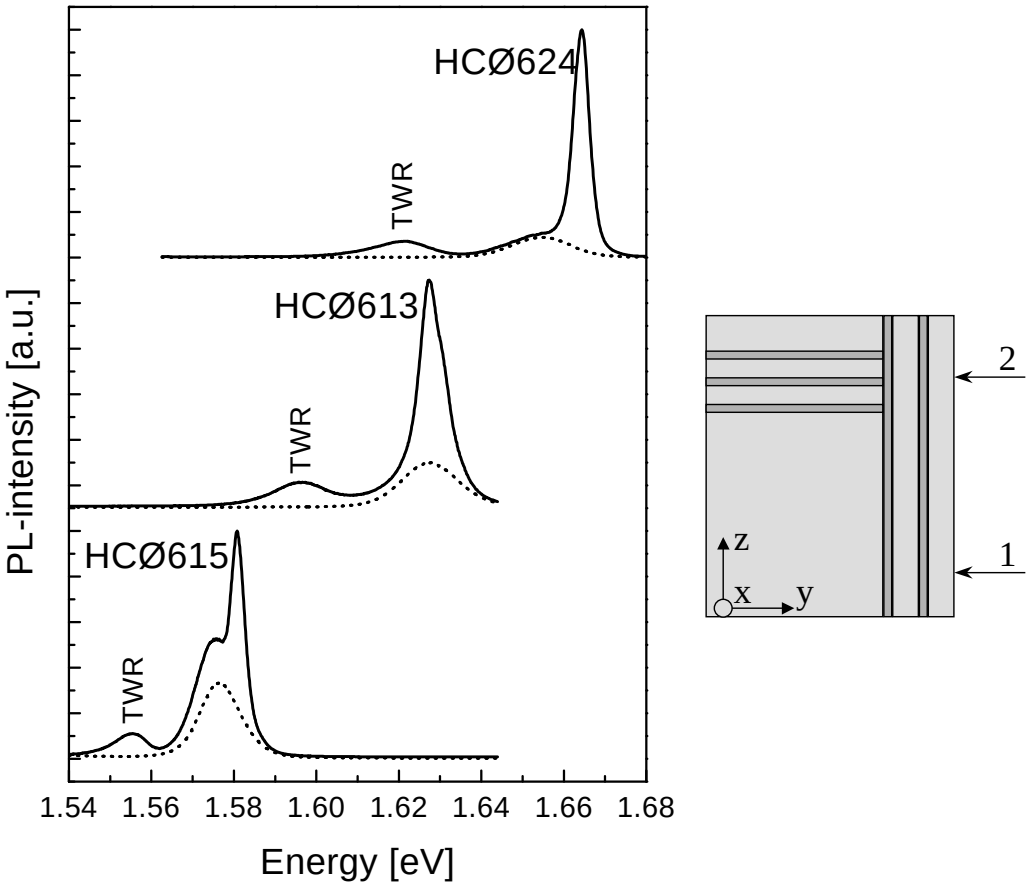

Figure 4.9: Left: PL-spectra of HCØ624, HCØ613 and HCØ615 at T=11K. The dahsed (solid) lines are the spectra obtained in region 1 (2) of the quantum wire structure shown in the right illustration.

Table 4.6.

In general, the PL efficiency was higher for the unstrained wires than for the strained. For HCØ613 and HCØ615 PL-spectra similar to the one shown in Fig. 4.9 were obtained on the majority of the cleaved samples, however for the strained wires in HCØ594, HCØ654 and HCØ655 the wire luminescence was always weaker than for the unstrained wires, and only clearly visible on the minority of the cleaved samples. The particularly intense TWR spectrum of HCØ595 compared to the other samples is not fully understood, but may be due to the spectral overlap of the high energy side of the TWR peak and the low energy side of the OGW peak, leading to a more efficient population of the TWRs. The qualitity of the wires was degrading for increasing In-molefraction in the MQWs, that is the wire luminescence was weaker for HCØ654/655 than for HCØ594/595, and in fact HCØ627 with a nominal In-

Figure 4.10: PL-spectra at T=11K of HCØ594 and HCØ595 (left), and HCØ654 and HCØ655 (right). The dashed (solid) lines correspond to the region 1 (2) in shown in Fig.4.9.

molefraction of 0.20 was also overgrown but no wire luminescence was found at all.

The thickness of the overgrown layers was also found to influence the strength of the luminescence, as reported in a previous study [62]. In a number of samples, not shown here, the reference quantum well was overgrown with a 50 nm barrier and a 20 nm GaAs cap. In these cases, neither the reference well nor the quantum wires were observed in the PL-spectra. However, for a total thickness of the barrier and cap layers of more than $\approx$100 nm, see table 4.3.2, the luminescence from the reference well was always observed. This effect may be explained by pinning of the Fermi level at the surface of the overgrowth, which leads to a bending of the band that penetrates into the structure, sweeping out the electrons or holes of the reference well and the T-wires if they are too close to the surface.

In Fig. 4.11, the temperature dependence of the quantum wire energy, the MQW energy and the intensity of the quantum wire luminescence is shown. Since the mechanism of confinement is independent of temperature, the difference between E_{MQW} and E_{TWR} is constant for increasing temperature. The integrated intensity of the luminescence in Fig.4.11c, shows the typical behaviour of the quantum wire samples measured here. For low temperatures the intensity increases with temperature, however beyond a certain value of

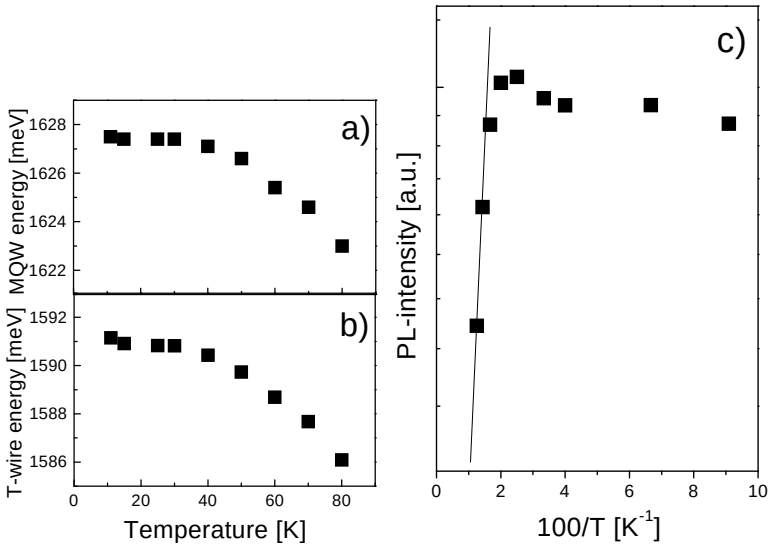

Figure 4.11: Temperature dependence of MQW (a) and TWR (b) energies. c): Integrated PL-intensity of the T-wire as a function of temperature. Y-axis is logarithmic.

$\approx$ 50K, the intensity drops steeply. On the logarithmic scale in Fig.4.11c, the decrease of the intensity is approximated by a line, with a slope corresponding to an energy of 15 meV. For 11K<T<50K, the behaviour is explained by the activation of localized excitons in the MQWs, which are then captured into the quantum wire states, increasing the population here. For T>50K the excitons in the T-wires are thermally excited to higher energy levels with a larger density of states, e.g. the OGW or the MQWs, thus reducing the population of the wires. In agreement with this picture, the activation energy of 15 meV is the same order of magnitude as the confinement energy.

4.3.4 Discussion of energy levels.

Although the T-wire structures characterized here are not all exactly matched, that is $E_{MQW} \neq E_{OGW}$, one may estimate the confinement energy in a similar matched structure by $E_{conf}=(E_{MQW}+E_{OQW})/2\text{-}E_{TWR}$, in agreement with systematic measurements of the T-wire energy in mismatched structures[55]. The confinement energies of the structures measured here are compared to calculations of the confinement energy[63] in Table 4.6, where the difference is also given. The calculations do not include the effects of strain. It is noted that for the unstrained structures, HCØ613, HCØ615 and HCØ624, the agreement is within 5.5-7 meV, which is mainly due to the Coulomb interaction not being included in the model. Hence, the difference should correspond approximately to the difference between the quantum well and

Sample	E_{MQW} [meV]	E_{OGW} [meV]	E_{TWR} [meV]	E_{conf} [meV]	E_{calc} (ΔE) [meV]
HCØ594	1644	1645	1606	38.5	28.5 (10)
HCØ595	1645	1629	1596	41	-
HCØ654	1603	1600	1574	27.5	16 (11.5)
HCØ655	1604	1617	1584	26.5	-
HCØ613	1627	1628	1596	31.5	26 (5.5)
HCØ615	1581	1577	1555	24.0	18 (6)
HCØ624	1664	1655	1621	38.5	31.5 (7)

Table 4.6: Measured transition energies of the multi quantum wells (MQW), overgrown well (OGW) and quantum wires (TWR) in the samples investigated here. Also given are the measured and calculated (from [63]) confinement energies and their difference, ΔE.

quantum wire exciton binding energies, in reasonable agreement with a measured exciton-binding energy of 12 meV [64].

The influence of strain can be estimated by comparing HCØ613 and HCØ595, that both consist of 18 nm MQWs and have almost equal values of E_{TWR} and E_{OGW}. However, in HCØ595 this is achieved with a transition energy of the MQWs 18 meV higher than in HCØ613, indicating an increase of the confinement energy of $\approx$9 meV due to the strain in HCØ595. Comparing the matched structure in HCØ594 with HCØ613 a 7 meV increase of the confinement energy is found, whereas only a 2.5 meV increase is predicted from the model. Hence, for HCØ594/595 we find a strain induced increase of the confinement energy of 4.5-9 meV.

For HCØ654/655 the ratio between the thickness of the MQWs and the OQW is $\approx$2, which is more symmetric than any of the other structures measured here. In a symmetric T-wire with slightly higher values of E_{MQW} and E_{OGW}, a confinement energy of 18 meV was found [55], yielding an upper limit of $\approx$10 meV to the strain induced increase of the confinement energy in HCØ654/655. On the other hand, if the measured confinement energy is compared to the calculated value and the same discrepancy is expected as in HCØ613/HCØ615, the strain induced increase of the confinement is $\approx$5 meV. That is, for HCØ654/655 we find an increase of the confinement of 5-10 meV, similar to HCØ594/595.

In contrast to the $In_xGa_{1-x}As$/ $Al_{0.3}Ga_{0.7}As$ T-wire structures [51][69] the OGWs in the structures here are only strained in T-shaped intersection with the InAlGaAs MQWs, because GaAs is lattice matched in all other areas of the cleaved surface. The source of the strain field is the larger lattice constant of the strained InAlGaAs layers in the z-direction, given by Eq. 3.3. When strain equilibration between the MQWs and the OGW is neglected, it

was shown that the strain tensor elements in the OGW are given by

$$\epsilon_{xx}=\epsilon_{yy}=\frac{\epsilon_{xy}}{2}=\frac{-C_{12}}{C_{11}+C_{12}+2C_{44}}\epsilon_{zz} \tag{4.8}$$

where $\epsilon_{zz}=(a_{SLS}-a_{GaAs})/a_{GaAs}$ is the misfit to the InAlGaAs layers[50]. For an In-molefraction of 0.1, a_{SLS} =5.7303 Å, ϵ_{zz}=1.36% and ϵ_{xx}=-0.25% is obtained which leads to a volume deformation of $\epsilon_{xx}+\epsilon_{yy}+\epsilon_{zz}$=0.86% in the OGW. The corresponding volume and shear deformation potentials lead to a shift of the bandgap of ΔE_{vol}=-71 meV and $\Delta E_{shear}=\pm 27$ meV. However, these values are very high compared to the measured changes of the confinement energy due to strain, suggesting that a more realistic strain field should be calculated in a continuum model.

4.4 Quantum dots.

The growth and characterization of quantum dots (QDs) described in this section, takes its starting point by investigating the growth conditions, using the well characterized binary InAs QDs. The growth and basic characterization of special quantum dot structures for single dot spectroscopy, second harmonic generation and time resolved measurements is then treated, where both ternary and quaternary alloys are used for the QD material.

4.4.1 Growth conditions probed by InAs quantum dots.

Four samples were grown, HCØ567-HCØ570, to investigate the influence of the substrate temperature and growth interrupts on the optical properties of the InAs-dots.

All samples were grown on [001]-oriented GaAs wafers. At a substrate temperature of 595°C a 500 nm GaAs buffer layers was grown, followed by a ten period 2 nm AlAs/ 2 nm GaAs superlattice and a 100 nm GaAs spacer layer. Then the substrate temperature was lowered to T_{sub} and 4 ML of InAs was deposited followed by a growth interrupt with a duration of t_{GI}. The quantum dots were covered with 10 nm GaAs before increasing the substrate temperature to 595°C and completing the cover layer with another 20 nm of GaAs. Finally, a ten period 2 nm AlAs/ 2 nm GaAs superlattice and a 50 nm cap layer was grown. The purpose of the superlattice is to flatten the surface during growth and trap surface segregating impurities. Furthermore, for excitation above the GaAs band gap the superlattices act as barriers for the excitons preventing them from diffusing out into the substrate instead of being captured into the quantum dots.

Sample	T_{sub}	t_{GI} [s]	E_{QD} [meV], (OD=0/1.0/2.0)	FWHM [meV], (OD=0/1.0/2.0)
HCØ567	480°C	0	1125/ 1125/ 1123	51/ 48/ 48
HCØ568	515°C	0	1185/ 1178/ 1175	117/ 114/ 102
HCØ569	515°C	10	1210/ 1204/ 1202	109/ 99/ 95
HCØ570	480°C	30	1134/ 1132/ 1132	63/ 59/ 56

Table 4.7: Substrate temperatures, growth interrupt times, QD peak positions and QD linewidths of the four InAs QD samples.

The samples HCØ567-HCØ570 were characterized with PL-measurements at T=11K. The spectra were obtained over two orders of magnitude, corresponding to power densities of 500, 50 and 5 W/cm^2, and in the following these values will be referred to as OD = 0, 1 or 2 corresponding to the strength of the optical density filter used to attenuate the excitation laser. In Table 4.7, the PL-peak positions and FWHM values are given for the four samples, as well as growth parameters T_{sub} and t_{GI}.

Comparing first the spectra of HCØ567 and HCØ568, shown on a logarithmic scale in Fig.4.12, it is clearly seen that the quantum dot peak is much broader for HCØ568. It is noted that, for increasing excitation power the peak in HCØ568 is blue shifted and broadens noticeably, while for HCØ567 the shift and the broadening is negligible. Even at low powers the peak in HCØ568 is blue shifted compared to HCØ567. These observations suggest that the quantum dots in HCØ568 are generally smaller and more dispersed in size than in HCØ567, and filling of the lowest lying states in HCØ568 accounts for the blue shift and broadening for increasing excitation power. In HCØ567 the high energy shoulder at OD=0 is also attributed to emission from excited states due to filling of the ground states.

Since the only difference between HCØ567 and HCØ568 is the value of T_{sub}, it is assumed that the rate of In desorption from the surface is significantly higher at T_{sub}=515°C than at T_{sub}=480°C leading to an effectively thinner deposition of InAs, and hence smaller and more dispersed dots.

Introducing a growth interrupt also leads to a blue shift, as seen when comparing HCØ570 to HCØ567 (Fig.4.13a) and HCØ569 to HCØ568 (Table 4.7), which is also explained by In desorption during the growth interrupt. The significantly larger blue shift in HCØ568/HCØ569 than in HCØ570/HCØ567 is due to the higher rate of In desorption at T_{sub}=515°C than at T_{sub}=480°C. In fact, the rather small blue shift in HCØ570 with a 30 second growth interrupt also shows the stability of the reconstructed surface at this temperature, and the absence of e.g. Ostwald ripening as discussed in section 3.2.4.

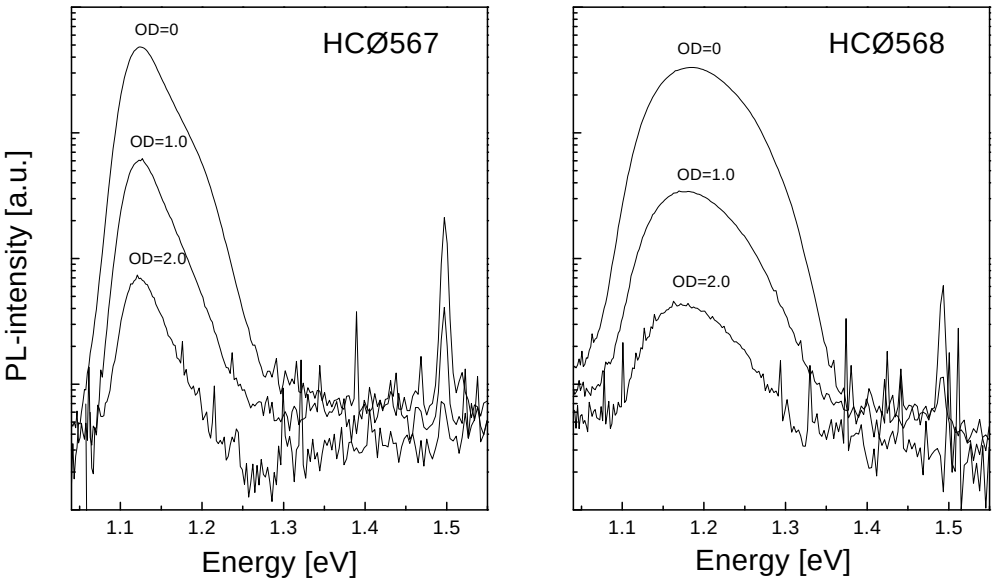

Figure 4.12: PL-spectra at T=11K of HCØ567 (left) and HCØ568 (right), over two order of magnitude of the excitation power.

Finally, the spectra of HCØ567 at T=11K and at T=293K are compared in Fig.4.13b. At room temperature the quantum dot peak is at 1042 meV, corresponding to the red shift of the InAs and GaAs band gaps. The FWHM of 44 meV is smaller than at low temperatures, which may be explained by a more efficient relaxation to the lowest lying states at room temperature, e.g. due to a larger population of phonons. The similar widths of the PL-peaks at low and high temperatures underlines the zero dimensional nature of the quantum dot states, where thermal broadening is negligible, which is why they are frequently referred to as "artificial atoms".

4.4.2 InGaAs QDs for single dot spectroscopy.

For InAs/ GaAs QDs with a narrow size distribution, like in HCØ567 described above, the average size and hence the peak transition energy is determined by the self-organization process, which is not easily modified by the growth parameters. Depending on the application other transition energies may be desired, which are achieved either by using an alloy for the the barrier material or for the dot material, or for both. For lower energies than the "standard" InAs/ GaAs QDs, an InGaAs cover layer may be used instead of GaAs [66, 67], and likewise for higher energies AlGaAs barriers may be used [68]. Here, $In_{0.5}Ga_{0.5}As$/ GaAs quantum dots grown for single dot spectroscopy will be described. Since the detector for these measurements is

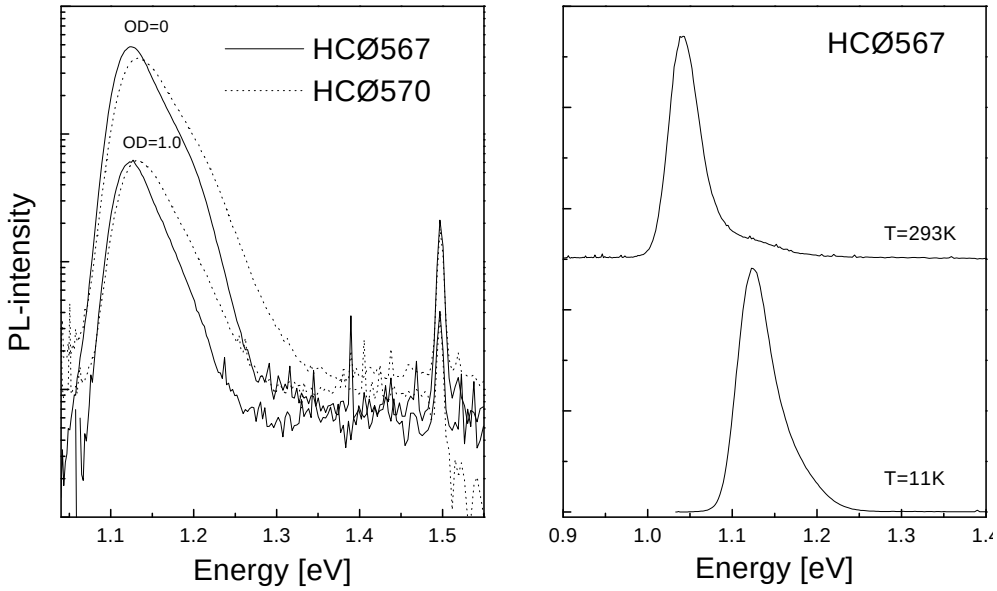

Figure 4.13: a): PL-spectra at T=11K of HCØ567 and HCØ570. b): PL-spectra at T=11K and T=293K of HCØ567.

a cooled Si CCD chip, the transition energies of these dots should be above the cut off energy of ≈1300 meV.

For the sample, HCØ593, a 500 nm thick GaAs buffer layer was grown on a [001]-oriented wafer, followed by an 8 nm AlAs barrier and 80 nm GaAs spacer at T_{sub}=595°C. The substrate temperature was then lowered to T_{sub}=500°C and the wafer rotation stopped. After a 20 nm GaAs spacer, 5 monolayers of $In_{0.5}Ga_{0.5}As$ were grown one at the time with an 8 second growth interrupt after each monolayer. The change from the 2D to the 3D growth mode was monitored using the RHHED pattern, which changed from a streaky to a spotty pattern. After the dot formation, a 20 nm GaAs cover layer was grown, T_{sub} was raised to 595°C, the wafer rotation was resumed, and the growth was completed by a 8 nm AlAs barrier layer and a 20 nm GaAs cap. The 8 second interrupt after each monolayer was introduced to decrease the average growth rate, which was reported to yield a good uniformity of the dots [72], and shift the transition energy up. Finally, at the substrate temperature T_{sub}=500°C some In desorption is expected according to the measurements in the previous section, however the RHEED pattern did not show any signs of change of the surface morphology during the growth interrupts, indicating a stable surface reconstruction, like in HCØ570, without Ostwald ripening.

Since the wafer rotation was stopped during growth of the QDs in HCØ593, a spatial variation of the alloy composition in the dots and the total thick-

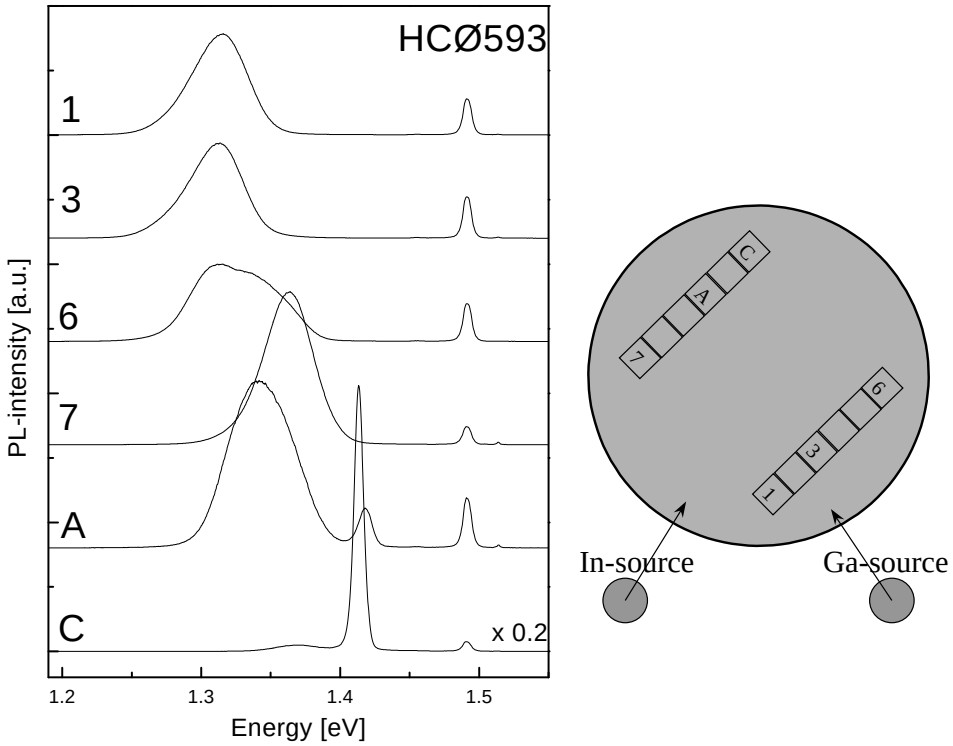

Figure 4.14: a): PL-spectra at T=11K for six different places on HCØ593. b): Position on the wafer of the six sample pieces measuered in a), relative to the Ga and In source.

ness of the deposited InGaAs layer is present in the sample. In Fig.4.14a, the PL-spectra at T=11K is shown for six different positions on the sample, as indicated in Fig. 4.14b. The samples C and A are on the "thin" side furthest away from the sources, while the samples 1 and 3 are on the "thick" side.

Sample C, which has the thinnest InGaAs layer, shows a sharp peak corresponding to an InGaAs quantum well with a thickness slightly lower than the critical thickness. The small peak on the low energy side indicates the formation of a small density of dots. On the other hand, sample A has a large broad peak at ≈ 1350 meV, corresponding to quantum dots, in addition to a small narrow peak at the energy of the quantum well in sample C. Thus, in sample A most of the InGaAs has formed dots. Close to the sources, samples 1 and 3 have very similar quantum dot peaks at 1315 meV with a width of 46-48 meV. The samples 6 and 7 have intermediate thicknesses of the InGaAs layer, but different molefractions due to their different positions relative to the sources. In the Ga-rich sample 6, this leads to a broad peak, that looks like a combination of the peaks in sample 1 and 3, and the peak in sample A. This structure is currently not understood.

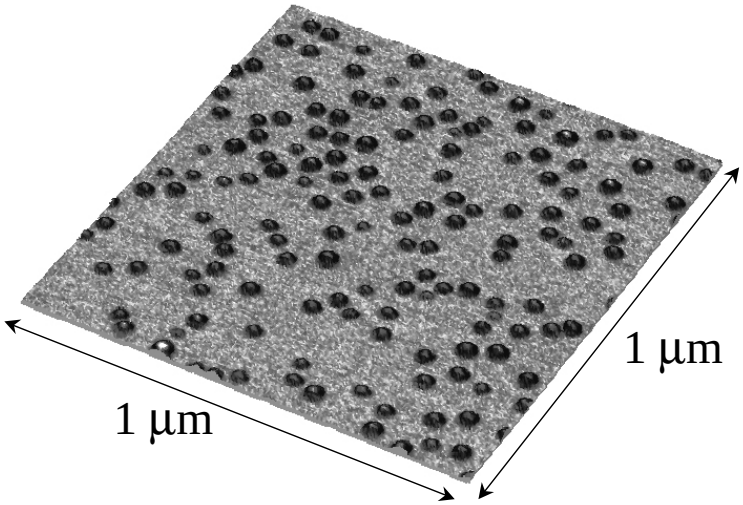

Figure 4.15: AFM scan of a sample similar to HCØ593, in which the quantum dots have not been capped.

Note that the peaks in sample 1 and 3 of HCØ593 have the same linewidth as the best InAs QD sample, HCØ567. This indicates that the size distribution of the $In_{0.5}Ga_{0.5}As$ QDs is similar to the InAs QDs, and that random alloy fluctuations do not play an important role for the linewidth.

Fig.4.15 shows an AFM scan of a sample similar to HCØ593 which has been grown without covering the dots. The uncapped sample was very stable under ambient conditions, and could be scanned for hours without measureable changes of the surface morphology. It is believed that the dot shape in a capped sample is very different from the measured shape in an uncapped sample, e.g. due to surface segregation during the capping [73], but the density is the same. Here, the measured average density is $2\times10^{10}\mathrm{cm}^{-2}$, in good agreement with reports on similar structures.

HCØ593 was used for single dot spectroscopy as reported in Ref. [70][71], where a distribution of single dot linewidths was found peaking at $\approx$50 μeV for T = 10 K. As the temperature was increased, a broadening of 0.4 μeV/K was found, which is 4-8 times lower than in InGaAs quantum wells.

4.4.3 Quaternary quantum dots.

To obtain higher QD energies than with the ternary $In_{0.5}Ga_{0.5}As$ alloy, two samples were grown with a quaternary alloy in the QDs. The substrate temperature, the V/III flux ratio, the stop of wafer rotation and the interrupts after each monolayer of the quantum dot material were identical to sample HCØ593 described above.

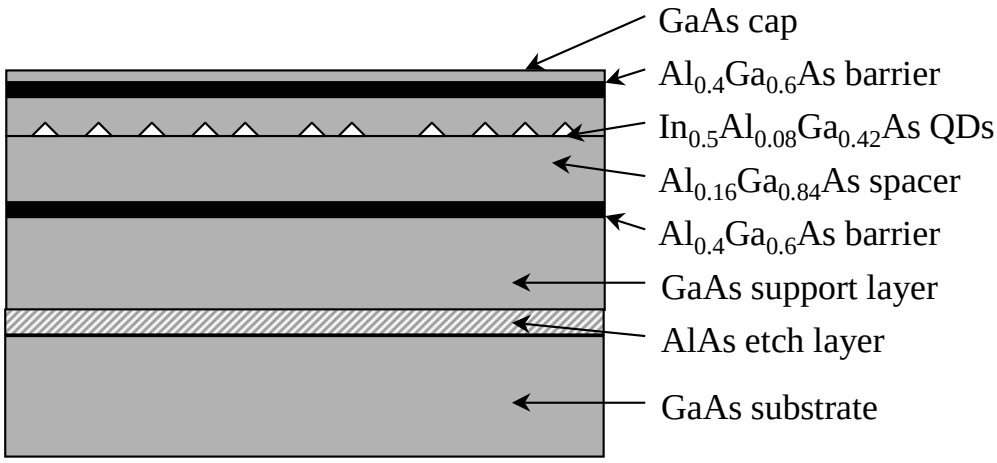

Figure 4.16: Growth profile of HCØ649. The layers role of the diffent layers is explained in the text.

For time resolved streak camera measurements, it was necessary to shift the energies to slightly higher values than the ones in HCØ593. This was accomplished in sample HCØ648 by growing a 100 nm $Al_{0.08}Ga_{0.92}As$ spacer layer with 6 ML $In_{0.5}Al_{0.04}Ga_{0.46}As$ for the quantum dots, covered by a 20 nm $Al_{0.08}Ga_{0.92}As$ layer. Each monolayer of the dots were grown as a kind of digital alloy, by depositing 0.5 ML of the barrier material, $Al_{0.08}Ga_{0.92}As$, and 0.5 ML of InAs. By adding Al to the spacer layer, the quantum dot energies were kept well separated from the spacer layer band gap. The spacer layer was bounded by 8 nm AlAs barriers to hinder the escape of excited electron-hole pairs. As reported in Ref.[23] the quantum dot energies in this sample were peaked at $\approx$ 1430 meV at T=10K, with a width of $\approx$ 50 meV.

For second harmonic spectroscopy, resonant excitation at room temperature of the quantum dots were required using a pulsed Ti:sapph laser with a minimum photon energy of $\approx$ 1380 meV (900nm). Furthermore, a very thin sample was needed to facilitate transmission measurements. To obtain QDs with ground states at E>1380 meV at room temperature, the sample HCØ649 was grown in a similar way as HCØ648, and the growth profile is shown in Fig.4.16. In HCØ649 $Al_{0.16}Ga_{0.84}As$ was used for the spacer layer and 6 ML $In_{0.5}Al_{0.08}Ga_{0.42}As$ for the quantum dots. The spacer was bounded by digitally alloyed $Al_{0.4}Ga_{0.6}As$ barriers. The whole structure was grown on a 50 nm AlAs etch layer and a 500 nm support layer.

After etching the sample in 10% HF the AlAs etch layer was removed, separating the upper layers from the substrate. The thin layers containing the quantum dots were then mounted by vax on a sapphire substrate[74]. The PL-spectrum at room temperature of the lift-off sample is shown in

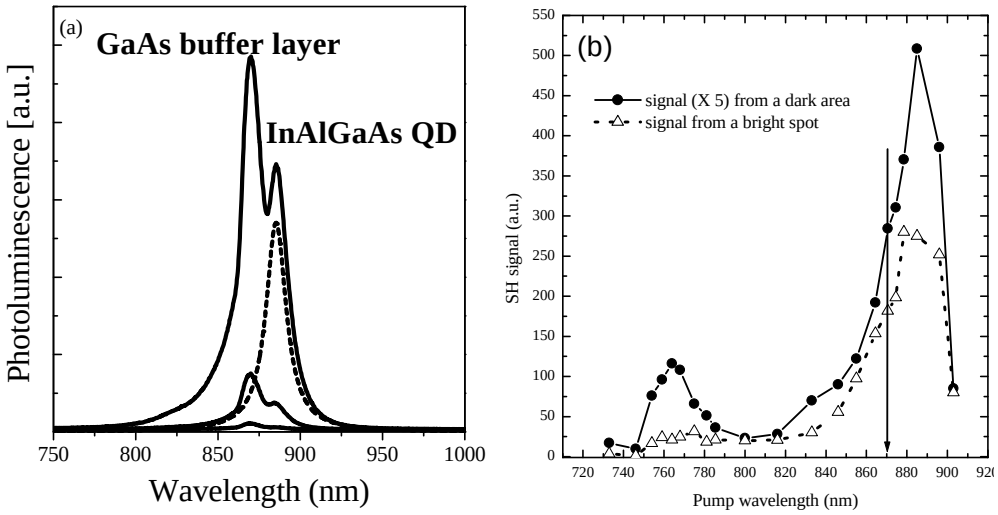

Figure 4.17: a): Room temperature PL spectrum of HCØ649, after lift-off and mounting on a sapphire substrate. b): Intensity of the second harmonic signal as a function of energy. Both Figures are reproduced from Ref.[74].

Fig.4.17a. A second harmonic signal was observed for excitation at the energy of the quantum dots, ≈1400 meV (885 nm), as well as at the energy of the $Al_{0.16}Ga_{0.84}As$ spacer layer, ≈1620 meV (765 nm) [74], as shown in 4.17b. Near field images showed spatial variation of the second harmonic signal depending on the excitation wavelength, which is interpreted as a signature of the quantum dot inhomogeneous broadening[75].

The width of the quantum dot peak in Fig.4.17b is ≈ 30 nm, corresponding to ≈ 50 meV. The peak energy of 1400 meV at room temperature corresponds to about 1490 meV at T=10K, assuming that the quantum dot energy shift is similar to GaAs. Comparing HCØ593, HCØ648 and HCØ649 then yields an approximately linear shift of the quantum dot energies of 180 meV when increasing the Al-molefraction from zero in $In_{0.5}Ga_{0.50}As$/ GaAs to 8% in the quantum dot layer of $In_{0.5}Al_{0.08}Ga_{0.42}As$/ $Al_{0.16}Ga_{0.84}As$. For this range of Al-mole fractions, no significant broadening of the quantum dot distribution is seen. In an alternative approach to growing quantum dots with transition energies of 1300-1500 meV, 1.8 ML InAs was used for the dots and $Al_xGa_{1-x}As$ as the surrounding material with x=0.6-0.8 [68]. For these dots the line widths were about 150 meV at room temperature, showing that the approach used here where Al is added both to the dots and the barriers yields a much better uniformity. Furthermore, the same transition energies may be obtained using much lower Al mole fractions, which is advantageous e.g. for quantum dot laser structures where a refractive index

contrast to the cladding layers with a high Al mole fraction is needed.

Chapter 5

Semiconductor microcavities

5.1 Introduction.

An atom inside a high quality optical cavity, may couple to the light field so the energy oscillates coherently between the excited atom and the photons. This so-called strong coupling regime is achieved when the probability for absorption by the atom is larger than for the photon to escape the cavity, either by transmission or background absorption [6].

In 1992 it was experimentally demonstrated that a similar system could be realized in a solid, using the excitonic resonance of a quantum well embedded in a microcavity (MC) [88]. The eigenstates of this combined system are the so-called *microcavity polaritons*, and their optical properties have been studied intensely since their discovery. As a possible application of microcavity polariton resonances, all optical switching has been suggested [78].

In this chapter the design and growth of microcavities is first described, giving a detailed treatment of each of its elements, the distributed Bragg reflector, the spacer layer and the quantum well inside. Next, the optical properties of the polaritons are investigated, focussing mostly on the energy levels and linewidths.

5.2 Design and growth of microcavities.

5.2.1 Distributed Bragg reflectors.

The principle of Bragg reflection is known both from solid state physics and optics, and simply means that propagation of a wave in a periodic potential may be forbidden in a certain frequency interval, *the band gap*, because of destructive interference from multiple back scattering. In a solid, the electron wave is propagating in the periodic Coulomb potential of the atomic nuclei,

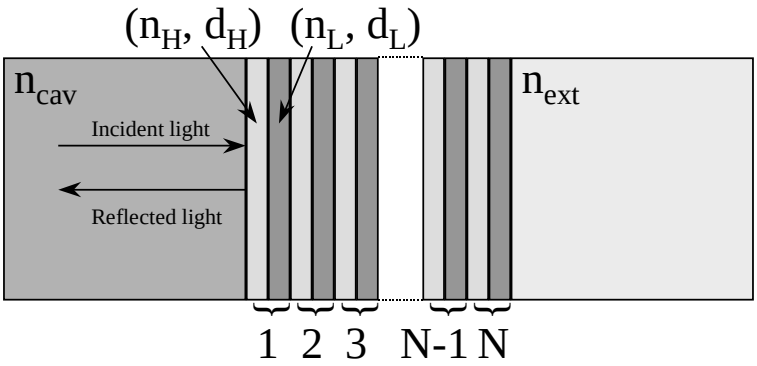

Figure 5.1: Schematic illustration of the light incident on a Bragg reflector. The parameters are explained in the text.

while in optics the periodic potential is a refractive index modulation. The latter may be achieved by growing a periodic structure of thin films with different refractive indices, which will be described in the following.

Consider a periodic structure of uniform layers, for instance grown by MBE, where each period consists of two layers with indices n_H and n_L ($n_H > n_L$), and thicknesses d_H and d_L. On the incident side of the structure the refractive index is n_{cav} and on the other side it is n_{ext}, see Fig.5.1. If the optical thicknesses of the layers are equal to a quarter of the wavelength of the light, $\lambda_0/4 = n_H d_H = n_L d_L$, propagation is strongly damped because a round trip in each layer corresponds to a phase shift of π, which leads to destructive interference. At this socalled *Bragg condition*, the intensity reflectivity, R, at normal incidence of the structure is given by

$$R = 1 - 4\frac{n_{ext}}{n_{cav}}\left(\frac{n_L}{n_H}\right)^{2N} \tag{5.1}$$

where N is the number of periods [81][80]. For such a distributed Bragg reflector (DBR), the reflectivity is high in a band of frequencies centered around the frequency matching the Bragg condition, and for N$\rightarrow \infty$ the fractional width of this socalled *stop band* is

$$\left|\frac{\Delta E}{E_0}\right| = \left|\frac{\Delta\lambda}{\lambda_0}\right| = \frac{4}{\pi}\arcsin\left(\frac{n_H - n_L}{n_H + n_L}\right) \tag{5.2}$$

where $E_0 = \frac{hc}{\lambda_0}$ is the center photon energy and ΔE and $\Delta\lambda$ are the widths of the stop band [82]. Equations 5.1 and 5.2 show that in order to achieve a high reflectivity with a few periods and a broad stop band, it is important to have a high refractive index contrast in the two layers. It is interesting to note that in the GaAs based material system used here, a maximum contrast of

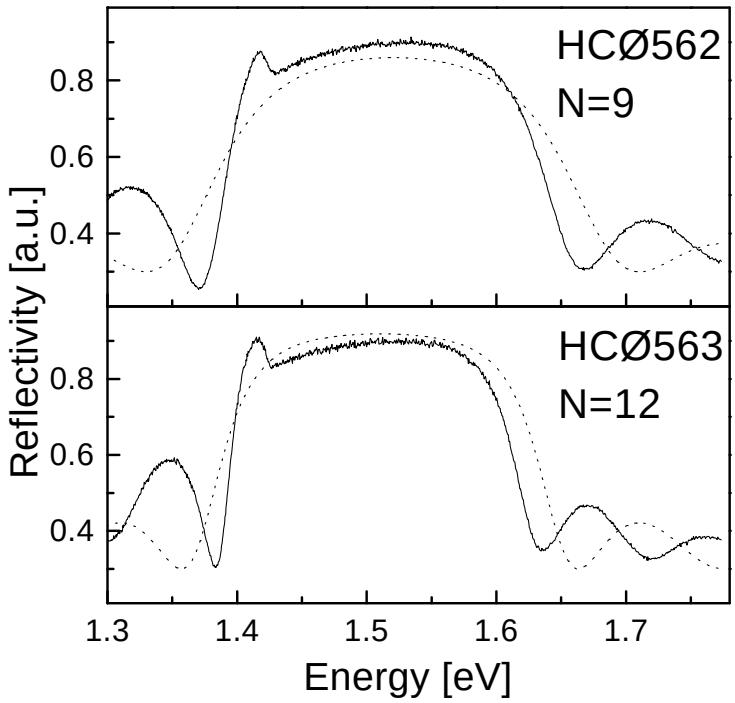

Figure 5.2: The measured (calculated) room temperature reflectivity spectra of HCØ562 (a) and HCØ563 (b) are given by the solid (dashed) lines. N is the number of periods in the DBRs.

n_{GaAs}/n_{AlAs} ≈3.6/3.0=1.2 can be obtained, which is significantly higher than in the technologically important InGaAsP/InP system where the maximum contrast is $n_{In_{0.55}Ga_{0.45}As}/n_{InP}$ ≈1.1 [85]. Hence, the AlGaAs system is better suited for DBR structures.

Two AlAs/ GaAs DBRs were grown, using standard growth conditions. Sample HCØ562 (HCØ563) contains 9 (12) periods, and the room temperature reflectivity spectra are shown in Fig.5.2. The stop band is visible from ≈ 1400 meV to ≈ 1600 meV, and the sharp drop of the reflectivity at 1425 meV is due to absorption at the GaAs band edge. The oscillations of the reflectivity on the high energy side of the stop band show that above the band gap the shape of the spectrum is still determined by the real part of the susceptibility. If the absorptive part was dominating, no structure would be expected.

Also shown in Fig.5.2 are the calculated reflectivity spectra using the matrix method described in section 2.2.2. It is noted that the measured spectrum seems "squeezed" compared to the calculated spectrum. However, in the broad spectral range probed here the dispersion of the refractive indices should be taken into account, which was assumed to be zero in the model.

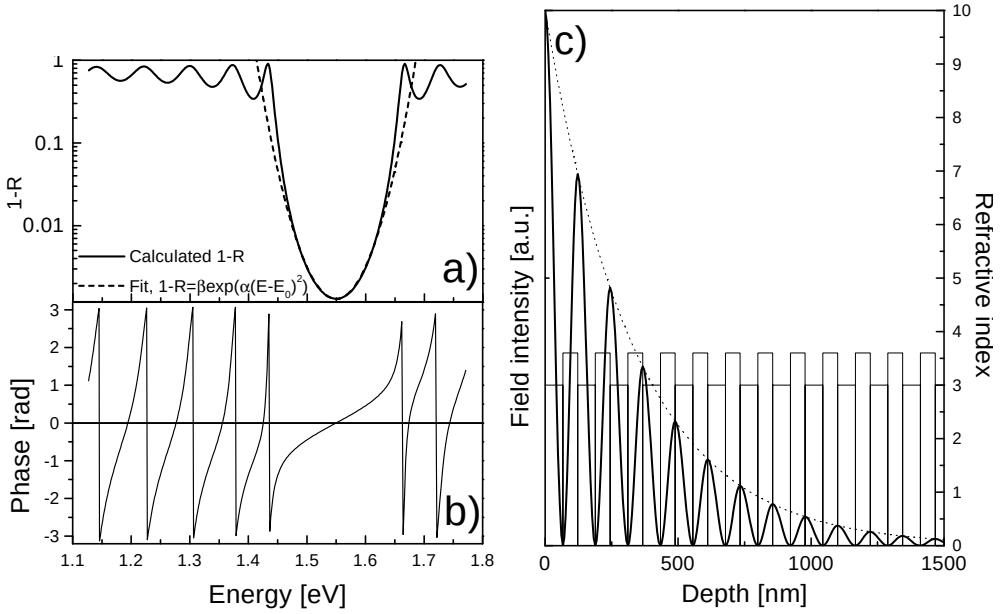

Figure 5.3: Calculated properties of a 18 period AlAs/GaAs DBR. a): The calculated (fitted) deviation of the intensity reflectivity from 1 is given by the solid (dashed) line. b): The phase change of the reflected light. c): The penetration of light into the DBR at the center of the stop band. The bold solid line is the field intensity and the thin line is the refractive index.

In fact, since ∂n/∂E>0 for GaAs and AlAs the side band modulations will change faster with energy than if the dispersion was zero, in agreement with the observations here.

5.2.2 Phase relations of DBRs.

In a narrow spectral range, where the dispersion of the refractive index is not important, the TMM model here can be used to illustrate some further properties of DBRs. In Fig.5.3a, the calculated deviation of the reflectivity from 1 is shown on a logarithmic scale for an AlAs/GaAs DBR with N=18, and n_{GaAs}/n_{AlAs}=3.6/3.0=1.2. The light is incident from a GaAs layer and the structure is bounded by air on the other side. The maximum reflectivity is 99.85% in agreement with equation 5.1, and the shape of the 1-R spectrum is well fitted to a parabola in a broad range of the stop band. Hence, empirically we can use the relation

$$R(E) = 1 - \beta \exp(\alpha(E - E_0)^2) \tag{5.3}$$

to describe the reflectivity in the stop band, which is the range of interest in most of the work here. β is obtained by comparison with equation 5.1, and α is related to the width of the stop band in the particular structure. In Fig.5.3b, the phase of the reflection is shown for the same structure. It is noted that the phase is zero at the center of the stop band, which generally holds if n_{cav} is higher than the refractive index of the first layer in the DBR, otherwise the phase is π. The phase changes linearly with the detuning from the center energy, which is equivalent to placing a mirror with a constant phase change at a distance L_τ behind the DBR interface [82]. L_τ is the *phase penetration depth*, but for historical reasons twice this distance, $L_{DBR}=2L_\tau$, is always used in the microcavity litterature [81] [80], given by

$$L_{DBR} = \frac{\lambda_0}{2}\frac{n_L n_H}{n_{cav}^2(n_H - n_L)} \tag{5.4}$$

where λ_0 is the center of the stop band. In the case of zero phase change at the center of the stop band, the energy dependence of the phase is therefore given by

$$\varphi(E) = \frac{n_{cav}L_{DBR}}{\hbar c}(E - E_0) \tag{5.5}$$

In the limit of $N\rightarrow\infty$, the phase penetration depth is identical to the *energy penetration depth*, L_E, which is defined as the thickness by which the medium on the incidence side should be extended to contain the same energy as is stored in the DBR[82]. The distribution of the field intensity inside the DBR is shown in Fig5.3c. for a light wave incident from the left. The exponential decay length of the intensity maxima is 335 nm, while equation 5.4 yields L_τ=278 nm. This difference is due to the lower average index in the DBR than n_{cav}, for which a larger physical distance is needed to obtain the same optical thickness.

5.2.3 Photonic cavities.

A photonic cavity can be realized by growing two DBRs on top of each other, separated by a spacer layer of thickness L_{cav} and refractive index n_{cav}. The condition for a resonance is that the phase change in a cavity round trip is an integer number of 2π, or alternatively an integer number of π for half a round trip, which may be expressed using equation 5.5

$$\varphi(E) + \frac{EL_{cav}n_{cav}}{\hbar c} = \frac{n_{cav}EL_{eff}}{\hbar c} - \frac{n_{cav}E_0L_{DBR}}{\hbar c} = \pi m \tag{5.6}$$

where $L_{eff}=L_{DBR}+L_{cav}$ is the *effective cavity length* and m is the order of the mode [82]. Equation 5.6 is only valid if E is inside the stop band where

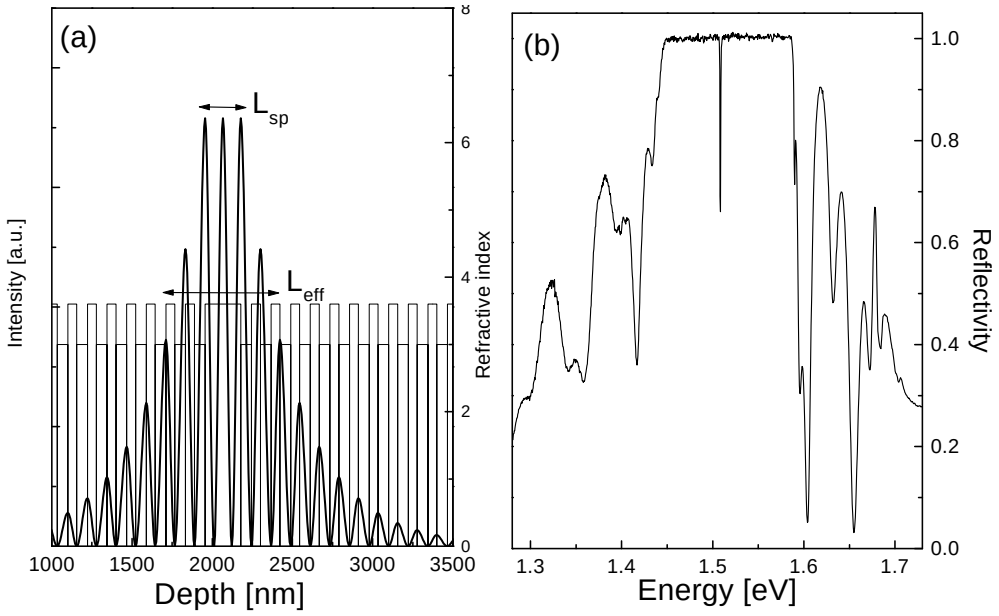

Figure 5.4: a): Calculated standig wave pattern in a λ-microcavity showing the difference between L_{sp} and L_{eff}. b): Measured broadband reflection spectrum of a λ-cavity. The bold and thin lines are the field intensity and refractive index respectively.

the linear phase relation holds, and it follows that for the resonance to be at the center of the stop band, E_0, the thickness of the spacer layer should be an integer number of half wavelengths, $L_{cav}=m\lambda_0/2n_{cav}$. In fact, the name *micro*cavity refers to the particular situation where the cavity length is on the order of the wavelength of light, typically m=2 or 3. In Fig.5.4a the calculated standing wave pattern for such a MC with m=2 is shown, also referred to as a λ-cavity since the optical thickness of the spacer layer is equal to the wavelength. A refractive index contrast of 1.2 was used, and the number of periods in the DBRs are 16 (25) on the left (right) side corresponding to the type of structure used in most of the work here. With λ_0=800 nm we have, L_{DBR}=556 nm, L_{sp}=222 nm and L_{eff}=778 nm, as indicated in Fig.5.4a. Note that $L_{eff} \approx 3.5L_{sp}$, in contrast to short cavities with metallic mirrors, where the effective cavity length is identical to the spacer layer thickness. The antinodes are placed at the interfaces between the spacer layer and the DBRs because the phase of the reflection from the DBRs is zero in the center of the stop band.

Fig.5.4b shows the measured broadband reflectivity spectrum of a typical photonic cavity structure used in this work. This particular structure consists of a λ-cavity with a 16 (25) period DBR on the top (bottom), and will be described in the following sections. The stopband of the DBRs is clearly

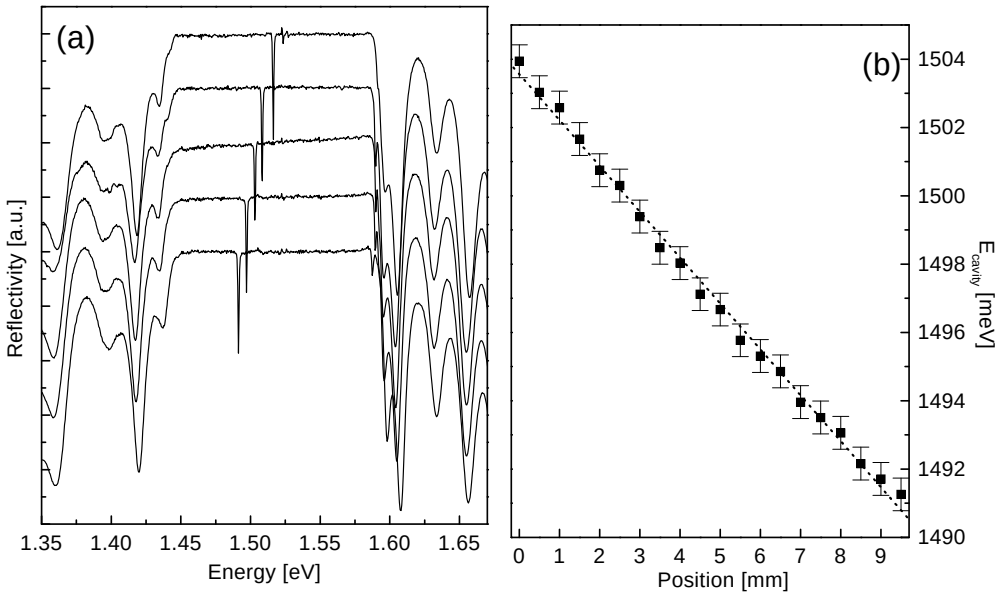

Figure 5.5: a): Broad band reflectivity spectra for different positions along the gradient of a wedged microcavity. b): Cavity resonance energy as a function of position on the wafer.

visible, and the dip corresponds to the photonic resonance. It is noted that the structure outside the stopband is more complicated than in a single DBR, but is well understood from TMM calculations as an interference effect between the top and bottom DBRs.

5.2.4 Wedged photonic cavities.

In real MC structures it is often desirable to be able to tune the photonic resonance with respect to another narrow (excitonic) resonance, and investigate their interaction. A controlled *spatial* variation of the cavity resonance energy may be achieved by intentionally wedging the microcavity, for instance by stopping the wafer rotation during growth. For the MBE system here, a thickness gradient of 25% is obtained across the wafer without rotation, see section 3.5.2, corresponding to a slope of the cavity resonance of 375 meV over 5 cm, or 7.5 meV/mm, if the resonance at the center of the wafer is 1.5 eV. With a typical probe spot size of 75 μm, an inhomogeneous broadening larger than 500 μeV is obtained which is usually much more than the homogeneous linewidth and may result in undesired stationary coherences [98]. However, the slope of the cavity resonance may be significantly reduced if only part of the structure is wedged [80]. If the thickness of the spacer layer is not exactly matched to the center of the stop band, it follows from

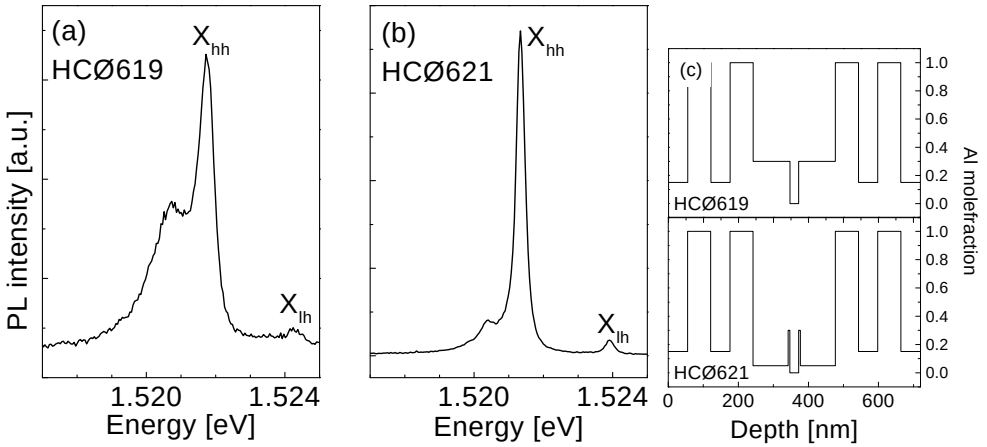

Figure 5.6: PL-spectum at T=11K of the quantum well in HCØ619 (a) and HCØ621 (b). In (c) the composition profile in the spacer layer of the two samples is shown.

equation 5.6 that the cavity resonance energy is

$$E_{cav} = \frac{L_{sp}E_{sp} + L_{DBR}E_0}{L_{eff}} \tag{5.7}$$

for m=2 and E_{sp}=hc/$n_{cav}L_{sp}$. In essence this relation states that the cavity resonance energy is a weighted average of the center energy of the stopband and the resonance energy of an ideal Fabry-Perot cavity of lenght L_{sp}. Hence, if only the spacer layer thickness is wedged and the wafer is rotated during growth of the DBRs, E_0 is constant and the gradient of cavity energy is reduced by a factor of $L_{sp}/L_{eff} \approx 1/3.5$ compared to a fully wedged structure.

In Fig.5.5a the measured broad band reflectivity spectrum is shown for different spatial positions of such a MC structure where only the spacer layer is wedged. It is clearly seen that the only spectral feature which differs significantly is the position of the reflectivity dip, whereas both the positions of the stop band and the structure outside the stop band is the same because of the spatially uniform DBRs. The measured slope of the cavity energy, shown in Fig.5.5b, is 1.35 meV/mm in reasonable agreement with the predicted reduction and sufficiently low to ensure that the inhomogeneous broadening within a spot size of 75 μm is much less than the homogeneous linewidth.

5.2.5 Quantum wells in photonic cavities.

To study the light-matter interaction in a microcavity a quantum well is grown in the spacer layer. In order to maximize the overlap between the quantum well and the optical field, it should be placed at an antinode of

the standing wave pattern, see Fig.5.4a. In a λ-cavity it is most practical to choose the center, but placing the quantum well next to one of the DBR interfaces will also give an almost maximum overlap.

The inhomogeneous linewidth of a quantum well is determined both by the alloy composition and the width of the well, as described in section 4.2.3. The narrowest excitonic lines are obtained when the inhomogeneous broadening is small, which may be achieved with a broad well of a binary material, such as a GaAs well with AlGaAs barriers. However, when embedded in a microcavity charging of the quantum well turns out to be a serious obstacle for achieving the same narrow linewidths as in an isolated quantum well [99].

The PL spectrum at T=11K of the uncoupled quantum well inside a MC, may be measured through the small but non-zero transmittivity of the top DBR at a position where the photonic resonance is tuned to much higher energies than the exciton resonance, typically >30 meV. This is shown in Fig.5.6a, for a 25 nm GaAs quantum well in a microcavity with an $Al_{0.3}Ga_{0.7}As$ spacer layer [100]. The peak on the low energy side of the quantum well transition is due to charged excitons, socalled trions, and the intensity of the line compared to the peak of the free exciton, X_{hh}, indicates a large free carrier density. It is expected that the background charge density from a large part of the microcavity structure will accumulate in the quantum well, since this is the lowest lying state. However, it was found that with a modification of the spacer layer band structure a significant reduction of the charge density was achieved, as shown in Fig.5.6b. In Fig.5.6c the region around the spacer layers of the two samples, HCØ619 and HCØ621, are compared. In HCØ619 the 25 nm GaAs quantum well is embedded in a spacer layer consisting only of $Al_{0.3}Ga_{0.7}As$, that act as a barrier. However, in HCØ621 only thin 5 nm $Al_{0.3}Ga_{0.7}As$ barriers are used and the rest of the spacer layer consists of $Al_{0.05}Ga_{0.95}As$ which was grown using digital alloying. Due to the lower lying states in the spacer layer outside the quantum well in HCØ621 compared to HCØ619, it is possible for the free carriers to tunnel out through the narrow barrriers of the quantum well in HCØ621 explaining the lower density here.

5.2.6 Layer profiles and growth conditions.

Based on the measurements and analysis described above and in the previous chapter on MBE growth, an optimized MC structure, shown in Fig.5.7, was developed to ensure a low cavity energy gradient, a reduced free carrier charging of the quantum well, narrow excitonic lines and as fast a growth as possible without changes of the source temperatures during growth.

The AlAs and GaAs growth rates were calibrated for growing $Al_{0.3}Ga_{0.7}As$

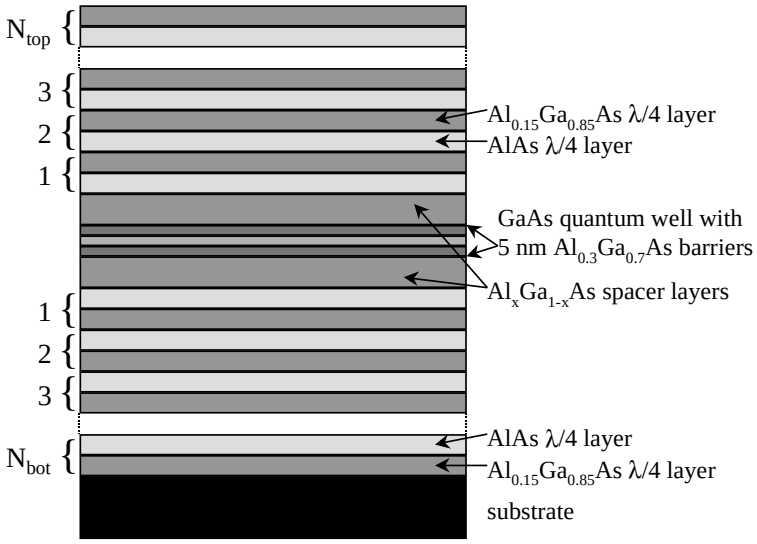

Figure 5.7: Growth profile of optimised microcavity structure. The structure is described in detail in the text.

at a speed of 1 μm/h and a substrate temperature of 625°C was used. The bottom DBR consists of N_{bot} periods of $Al_{0.15}Ga_{0.85}As$/AlAs, where the $Al_{0.15}Ga_{0.85}As$ alloy was grown using digital alloying. The particular Al-molefraction of this alloy was chosen to make sure that the band gap was well above the transition energy of the quantum well in the cavity while keeping the refractive index contrast in the DBR as high as possible. The spacer layer consists of a GaAs quantum well of width L_{QW} with 5 nm $Al_{0.3}Ga_{0.7}As$ barriers, and digitally alloyed $Al_xGa_{1-x}As$ to fill out the spacer layer to a optical thickness of λ. The wafer rotation was stopped only during growth of the $Al_xGa_{1-x}As$ spacer layers, whereas rotation was resumed during growth of the quantum well, to ensure a constant quantum well resonance across the wafer. The position of the wafer was monitored to make sure that the orientation of the thickness gradients of the $Al_xGa_{1-x}As$ spacer layers were the same on both sides of the quantum well. Finally, the top DBR consists of N_{top} periods of $Al_{0.15}Ga_{0.85}As$/AlAs, except for the last layer where 10-20 nm of the $Al_{0.15}Ga_{0.85}As$ was replaced with GaAs in order to cap the structure and avoid surface oxidation. The number of periods of the DBR was chosen so $N_{top} < N_{bot}$ to ensure a preferential emission of the cavity in the surface direction.

In Table 5.1, the exact values of the parameters are given for the six structures used here. The difference between HCØ621, HCØ634, HCØ641 and HCØ642 is mainly the quantum well thickness and position. HCØ596 is not a structure with optimized design, but is instead based on an InGaAs

Sample	L_{QW}	d_{qw} [nm]	pos	N_{bot}	N_{top}	x_{DBR}	x_{spacer}
HCØ596	0.15	10	anti	20	20	0	0
HCØ619	0	25	anti	25	16	0.15	0.3
HCØ621	0	25	anti	25	16	0.15	0.05
HCØ641	0	15	anti	25	16	0.15	0.06
HCØ642	0	10	anti	25	16	0.15	0.07
HCØ634	0	20	≈node	25	16	0.15	0.05

Table 5.1: Growth parameters of the μ-cavity samples investigated here. x_{qw} is the quantum well In-molefraction, L_{QW} is the quantum well thickness, pos indicates if the well is placed at the node or the antinode, N_{bot} (N_{top}) is number of periods in the bottom (top) DBRs, x_{DBR} is the Al-molefraction in the high index DBR layers, and x_{spacer} is the Al-molefraction in the AlGaAs spacer layers.

quantum well and a fully wedged cavity with AlAs/GaAs DBRs.

5.3 Linewidths and energies of microcavity polaritons.

5.3.1 Experimental steup.

Reflection measurements of polaritons in MCs require a careful consideration of the probe spot diameter, d_{spot}, and the opening angle of the beam incident on the sample, given by the numerical aperture (N.A.) of the setup. In the diffraction limit the two values are related through the Rayleigh criterion, $d_{spot}=1.22\lambda/(\text{N.A.})$. In order to avoid a significant inhomogeneous broadening of the bare cavity resonance d_{spot} should be as small as possible, but at the same time the spread of the in-plane wavevectors of the probe light, $k_{||}$, should be as small as possible because of the steep dispersion of the cavity resonance. For a cavity resonance of E_0 at $k_{||}=0$, the in-plane dispersion is given by

$$E(k_{||}) = E_0\sqrt{1+\left(\frac{k_{||}\lambda_0}{2\pi n_{cav}}\right)^2} \tag{5.8}$$

where $E_0=\hbar c/\lambda_0$[101]. If the cavity linewidth is γ_{cav} the spread of the in-plane wavevectors should fulfill $\gamma_{cav} > E(k_{||})-E(0)$, otherwise the measured cavity resonance will broaden on the high energy side. Clearly, both the requirements of a small probe spot and a small beam divergence cannot be

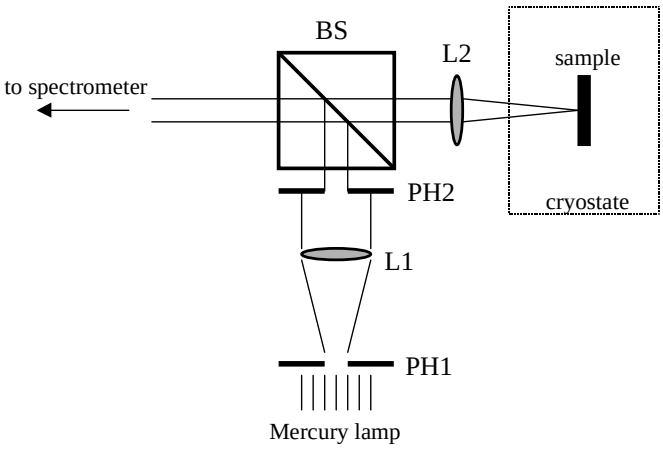

Figure 5.8: Setup used for reflectivity measurements of cavity polaritons at normal incidence. PH1 and PH2 are pinholes, L1 and L2 are lenses and BS is a beam splitter.

fulfilled at the same time and the best compromise must be found. In practise a setup was used with a variable N.A., where the N.A. was reduced until the measured linewidths reached a minimum.

In Fig.5.8 the experimental setup is shown. A pinhole (PH1) with a diameter of 300 μm is illuminated with light from a broad band source, and imaged onto the surface of the MC sample with a magnification of 0.2 (60 μm spot size), using a telescope with two lenses having focal lengths of 750 mm (L1) and 150 mm (L2). In the parallel beam path a pinhole (PH2) was used to reduce the opening angle of the light cone incident on the sample as described above. With a beam splitter (BS), the reflected light was separated from the incident light and passed to a grating monochromator where the dispersed light was detected with a cooled CCD chip.

The samples were cut into pieces having a typical size of 5 mm $\times$ 10 mm, with the thickness gradient dominantly oriented along the long side. In the cryostat, the samples were kept at temperatures down to T=11K and with micropositioners the whole sample holder could be translated in all three directions. In a typical measurement, the reflection spectrum of the sample was obtained for a number of equidistant positions along the thickness gradient on the sample, in this way probing the polaritons for different detunings of the cavity resonance with respect to the exciton resonance(s). The spectra obtained in such a range of measurements are shown in Fig.5.9, for 13 different probe spots, spaced by 1.5 mm on the sample.

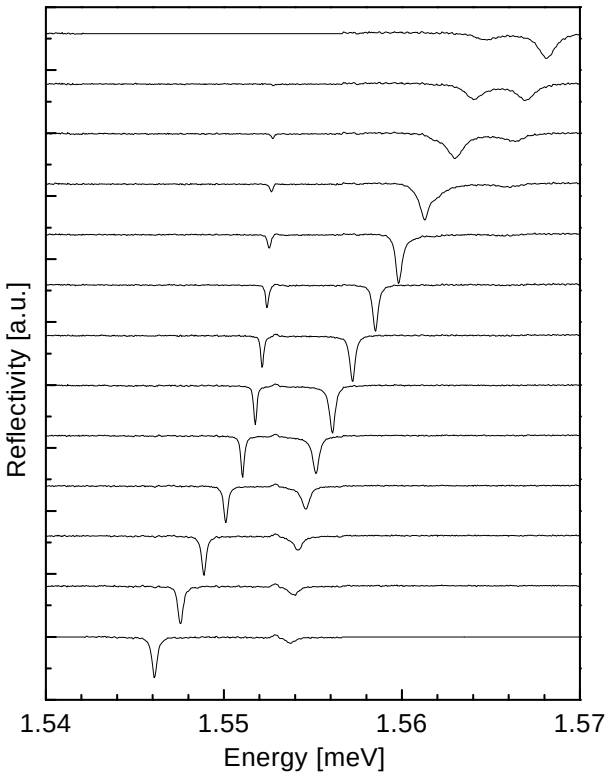

Figure 5.9: Reflectivity spectra of HCØ642 at T=11K, measured at 13 equidistant positions on the sample, spaced by 1.5 mm.

5.3.2 Data analysis.

The dips in the reflectivity spectra shown in Fig.5.9 correspond to the polariton eigenstates. For all the measurements reported in this chapter, they were fitted with Lorentzian lineshapes to obtain the polariton energies and linewidths. In general a Lorentzian shape was found to fit much better than a Gaussian shape.

The broadening function of the spectrometer was nearly Gaussian with a FWHM of γ_{spec}=95 μeV, unless differently stated. In order to correct for the instrumental resolution the fitted linewidth γ_{fit} was related to the polariton linewidth as $\gamma_{pol}=(\gamma_{fit}^2-\gamma_{spec}^2)^{1/2}$ which is only strictly valid for two Gaussian lineshapes, but a good approximation here because the Gaussian width is always much smaller than the fitted Lorentzian width.

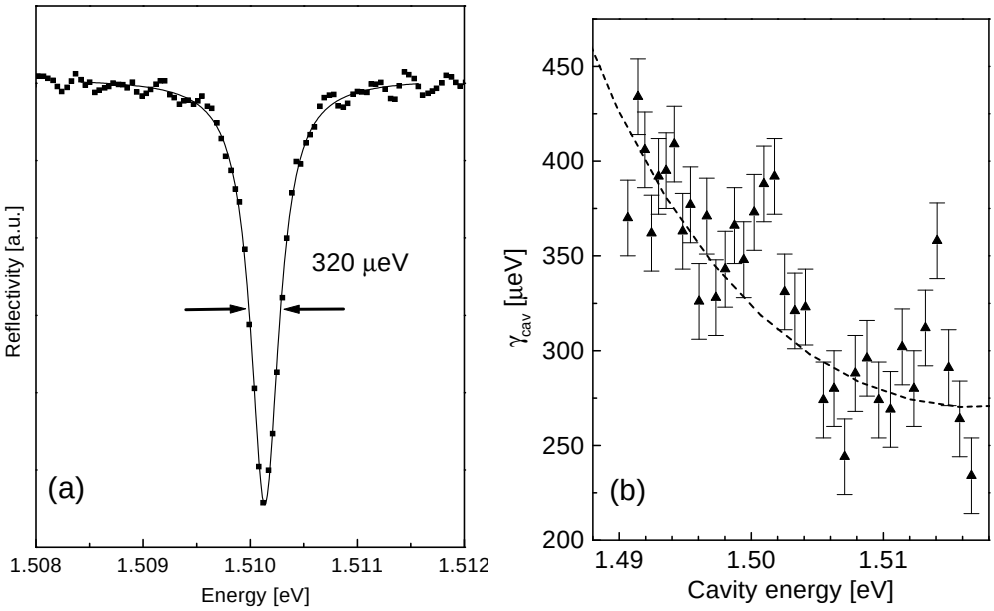

Figure 5.10: a): Measured (solid squares) and fitted (solid line) reflectivity dip from bare cavity resonance. b): Measured (solid triangles) and fitted (dashed line) values of the linewidth of the cavity resonance as a function its energy.

5.3.3 Bare cavity resonance.

When the cavity resonance is tuned well below the exciton resonance the concept of polaritons is not valid and only one reflectivity dip is seen corresponding to the bare cavity. In Fig.5.10a the measured bare cavity dip and the corresponding fit is shown for HCØ621. A fitted width of γ_{fit}=320 μeV was obtained, corresponding to γ_{pol}=300 μeV when corrected for the instrumental resolution, which was γ_{spec}=110 μeV here. Assuming this linewidth to be homogeneously broadened, it corresponds to a field intensity decay time of $\tau=\hbar/\gamma$=2.2 ps, or an average number of round trips in the cavity of $c\tau/2n_{cav}L_{eff}$ $\approx$120. In the absence of absorption, the photon life time is only due to the small transmission probability, and may be expressed as [80]

$$\tau = \frac{n_{cav}L_{eff}}{c(1-R)} \tag{5.9}$$

corresponding to R=99.6% for the values here.

The narrowest linewidth obtained so far for MBE grown cavities, γ =120 μeV [84], was found to be approximately a factor of two higher than the value obtained from TMM calculations. This discrepancy was ascribed to a small curvature of the cavity thickness across the probe spot, whereas contributions from background absorption and mirror roughness was found to have a

negligible effect on the linewidth, underlining the high quality of MCs that can be achieved with MBE growth. In good agreement with these observations the gradient of the cavity resonance energy leads to an inhomogeneous broadening of 80 μeV within the 60 μm spotsize, supporting the assumption that the measured cavity linewidth here is dominantly lifetime broadened.

As pointed out in the section 5.5 the reflectivity of the DBRs varies across the stop band. In the structure described above this is expected to lead to a dependence of the cavity linewidth on the cavity energy, because the cavity resonance effectively probes the reflectivity in different parts of the stop band. In Fig.5.10b the measured variation of the linewidth with energy is shown[100], and the dashed line shows a fit using Eq. 5.3 and 5.9, and E_0=1515 meV. The agreement with the measured values is good, and it is noted that in a region of $\approx$10 meV from the center of the stop band the linewidth is practically constant. In a couple of narrow spectral regions the linewidth is significantly higher than the modelled values, which is ascribed to background absorption in the structure, possibly from exciton states bound to defects.

5.3.4 Polariton energy levels.

In Fig.5.11a-d the measured polariton energies are plotted as a function of detuning for HCØ596, HCØ621, HCØ641 and HCØ642. The detuning is defined here as the difference between the bare cavity energy and the energy of the bare heavy-hole exciton, Δ=E_{cav}-E_{hh}, and in the following it will be described in detail how it is calculated. All the polariton energy levels show the avoided crossing behaviour around one or two resonances in the structures, similar to coupled harmonic oscillators. The polariton energies may be fitted in many ways, for instance by using TMM calculations with a special matrix describing the dielectric response of the exciton [81]. This is consistent with a quantum mechanical picture, where the polariton eigenstate is a superposition of the bare cavity photon state and the bare exciton state(s) [81][86]. In both cases the polariton energies are found by diagonalization of the Hamiltonian

$$\hbar \begin{bmatrix} \omega_{cav} & \Omega_{hh} & \Omega_{lh} \\ \Omega_{hh} & \omega_{hh} & 0 \\ \Omega_{lh} & 0 & \omega_{lh} \end{bmatrix} \cdot \begin{bmatrix} c_{ph} \\ c_{hh} \\ c_{lh} \end{bmatrix} = E \begin{bmatrix} c_{ph} \\ c_{hh} \\ c_{lh} \end{bmatrix} \tag{5.10}$$

where $\hbar\omega_{cav}$, $\hbar\omega_{hh}$ and $\hbar\omega_{lh}$ are the energies of the bare cavity resonance, and heavy- and light-hole excitons[89]. The *coupling strengths* of the excitons to the photons are given by $\hbar\Omega_{hh}$and $\hbar\Omega_{lh}$, whereas c_{ph}, c_{hh} and c_{lh} are the amplitudes of each of the uncoupled states in the eigenstates of the Hamiltonian.

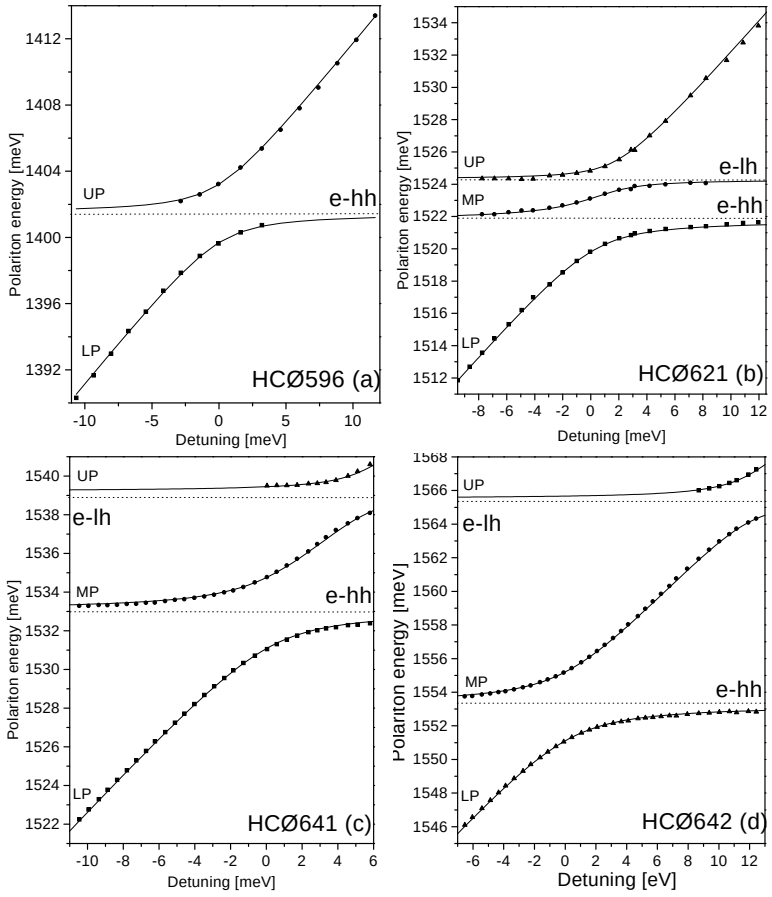

Figure 5.11: Measured (solid symbols) and fitted (solid lines) polariton energies as a function of detuning for HCØ596, HCØ621, HCØ641 and HCØ642. The dashed lines mark the energies of the uncoupled heavy-hole and light-hole exciton resonances.

Normalization of the eigenstates leads to $|c_{ph}|^2+|c_{hh}|^2 + |c_{lh}|^2=1$. Diagonalization of equation 5.10 leads to three eigenstates of the system, which are usually termed the lower, middle and upper polaritons (LP,MP and UP).

To fit the measured values the energies of the bare excitons were first deduced, using the polariton energies far from resonance. For instance in Fig.5.11d the energy of the heavy-hole is close to the average of the LP energy at high values of Δ and the MP energy at the lowest values of Δ. Next, the coupling strenghts were estimated, by calculating the minimum separation of two polaritons around an anticrossing point. This socalled Rabi-splitting, E_{Rabi}, is related to the coupling strenghts in the Hamiltonian by $E_{Rabi}=2\hbar\Omega_{hh/lh}$. Finally, the bare cavity energy was calculated using the

Sample	E_{hh} [meV]	$\hbar\Omega_{hh}$ [meV]	E_{lh} [meV]	$\hbar\Omega_{lh}$ [meV]
HCØ596	1401,45	1,75	-	-
HCØ621	1521,75	1,80	1524,3	1,1
HCØ641	1533,04	1,87	1539,2	1,21
HCØ642	1553,24	2,06	1565,5	1,43
HCØ634	1525,40	0,44	1529,3	0,25

Table 5.2: The fitted values of the heavy-hole and light-hole exciton energies, E_{hh} and E_{lh}, and the heavy-hole and light-hole exciton Rabi-splittings, $\hbar\Omega_{hh}$ and $\hbar\Omega_{lh}$ for the samples investigated here.

law of energy conservation that yields

$$E_{cav} + E_{hh} + E_{lh} = E_{LP} + E_{MP} + E_{UP} \tag{5.11}$$

With these values, listed in Table 5.2, equation 5.10 can be diagonalized, and the corresponding fits are shown with solid lines in Fig. 5.11a-d. The agreement between the measured and calculated values is very good, with typical differences on the order of 100 μeV, showing that the polariton energies are very well described by equation 5.10. Note, that in the case of HCØ596, which is a simpler two level system, a 2×2 matrix equation was used insted of equation 5.10.

The fitted energy levels of the excitons in HCØ621, HCØ641 and HCØ642 agree with the expected positions. As the quantum well thickness decreases the quantization energy increases, and hence the difference between E_{hh} and the bulk GaAs exciton energy at 1519 meV increases. Likewise, the heavy-light-hole splitting, E_{lh}-E_{hh}, increases because of the different hole masses. Since HCØ596 contains an InGaAs quantum well, E_{hh} is below the GaAs bandgap and due to the strain the heavy-light-hole splitting is very large, see section 2.1.2, and the light-hole exciton is not seen here.

The Rabi-energies in Table 5.2 measures the dipole interaction, $\mathbf{d}\cdot\mathbf{E}$, and are given by

$$\Omega = \sqrt{\frac{2\Gamma c}{n_{cav} L_{eff}}} \tag{5.12}$$

for a single quantum well placed at the antinode in a MC[81]. Γ is the radiative lifetime of the exciton, which is proportional to the exciton oscillator strength, f_{xy},and the parameters n_{cav} and L_{eff} are given in the previous section. The fitted values of $\hbar\Omega_{hh}$ and $\hbar\Omega_{lh}$ increase for the GaAs quantum wells

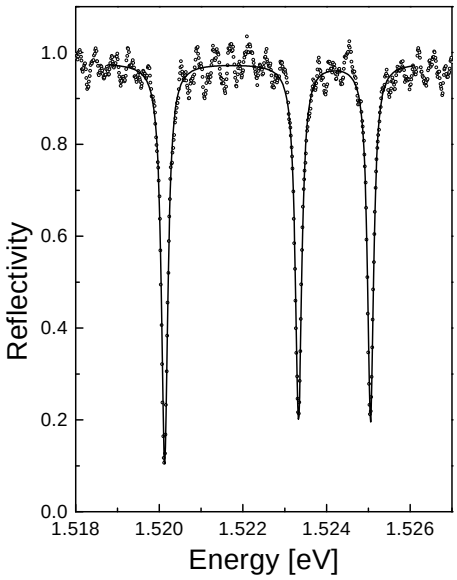

Figure 5.12: Reflectivity spectrum showing the ultra narrow polariton lines at zero detuning of HCØ621.

as the quantum well thickness decreases, which is the expected behaviour because of the increasing exciton binding energy [79]. The relative strengths of $\hbar\Omega_{hh}$ and $\hbar\Omega_{lh}$ are in good agreement with previously reported values [89], and corresonds to the oscillator strength of the heavy-hole exciton being 2.1-2.7 times larger than the light-hole exciton. For comparison a theoretical value of 2.3 was found previously [79].

5.3.5 Polariton linewidths.

As shown in Fig.5.12 the linewidths obtained in the optimised structures are very narrow. In fact the ratio between the Rabi-splitting and the linewidth is 19 at zero detuning of HCØ621 [100], which is likely to be the highest value obtained so far [87]. This is partly due to the negligible inhomogeneous broadening of the quantum well and the low density of trions, and partly due to the low cavity energy gradient ensuring a small photonic inhomogeneous broadening. The very narrow polaritons obtained in the optimised structures are promising for investigating finer details of the light-matter coupling than was possible before.

The measured linewidths of the samples HCØ621, HCØ641 and HCØ642 are shown in Fig.5.14a-c as a function of detuning. Before analysing their behaviour, a short review will be given of the current understandig of polariton linewidths.

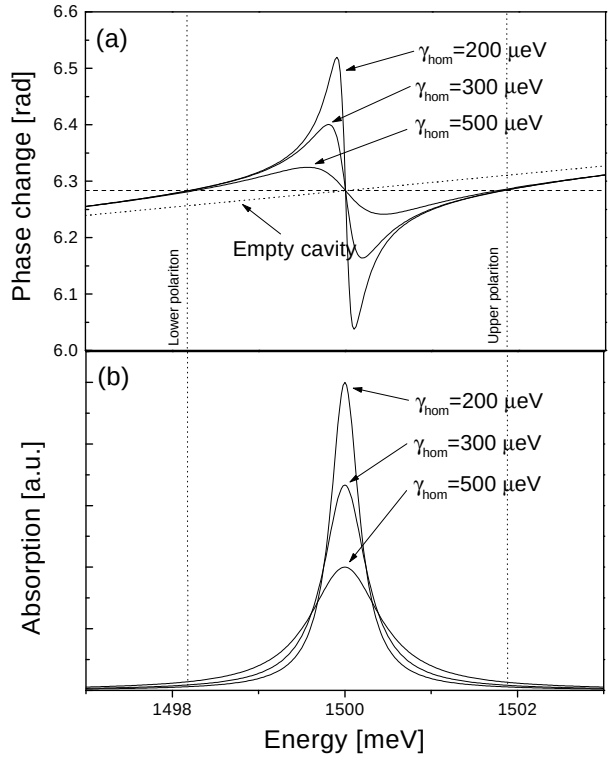

Figure 5.13: a): Phase change across the spacer layer of a microcavity containing an excitonic resonance. Three resonances are indicated with the same radiative line width of Γ=200 μeV, but different non-radiative broadenings, γ. The values given are the total homogeneous broadening $\Gamma+\gamma$. The dashed line is the phase change for an empty cavity. The vertical lines show the positions of the upper and lower polaritons. b): Absorption in the microcavity for the three different oscillators shown in a).

The simplest and most succesful explanation of the polariton linewidths so far that reproduces the measured values in the full detuning range was given by Ell et al. [91]. In this picture TMM calculations are used to model the MC response, where the experimentally measured dielectric function of the bare exciton has been used. The basic idea of this picture is shown in Fig.5.13a for a homogeneously broadened exciton in a cavity resonant at the same energy. Using equation 5.6, the phase change in a single cavity round trip was calculated, where the real part of the dielectric response of an exciton was added to the background refractive index of 3.6 in the cavity, yielding an energy dependent index, $n_{cav}(\hbar\omega)$. The exciton was treated as a Lorentzian oscillator with a radiative broadening of γ_{rad}=200μeV, and three different values of the non-radiative broadening was used, γ_{nonrad}=0, 100, 300μeV. Also shown in Fig.5.13a is the phase for an empty cavity (dashed

line).

Because the presence of the exciton increases the refractive index on the low energy side and decreases it on the high energy side, the resonance condition $\Delta\varphi$=m·2π is satisfied for two new energies on the low and high energy side of the cavity resonance corresponding to the polariton energies. It is noted that the positions of the polariton resonances are not changed as the non-radiative broadening is increased, because far from the exciton resonance the real part of the susceptibility does not depend on the non-radiative broadening. The absorptive part of the exciton response is peaked at the resonance energy, but extends to the polariton resonance energies with a value that depends on the amount of homogeneous broadening, see Fig.5.13b. As shown in Fig.5.13a a polariton at the exciton resonance also fulfills the resonance condition, but due to the high absorption here it is not stable.

In the case of a homogeneously broadened exciton the TMM approach is identical to diagonalizing the Hamiltonian in equation 5.10[81], and (in a two-level system) the linewidths of the polaritons are given by

$$\gamma_{pol} = \gamma_{cav} \left|c_{ph}\right|^2 + \gamma_x \left|c_x\right|^2 \tag{5.13}$$

where $|c_{ph}|^2$ and $|c_x|^2$ are the photon and exciton fractions, and γ_{cav} and γ_x are the bare cavity linewidth and the homogeneous exciton broadening. That is, at resonance the polariton linewidths are identical and given by the average $(\gamma_{cav}+\gamma_x)/2$. In a real exciton system however, some inhomogeneous broadening must be considered, and it was shown that for a symmetric Gaussian distribution with a width of σ, the polariton linewidths at resonance are still given by the homogeneous linewidth $(\gamma_{cav}+\gamma_x)/2$ [97], assuming that σ is smaller than the Rabi-splitting. That is, at resonance the polariton linewidths are not just the average of the bare cavity and exciton linewidths but in fact narrower because the inhomogeneous broadening is not seen in the tails of the exciton dielectric function. However, the assumption of a symmetric inhomogeneous broadening does not describe the dielectric response of a realistic exciton in a quantum well, which is typically asymmetric with a Gaussian absorption tail on the low energy side and an exponential absorption tail on the high energy side [43].

In the general approach by Ell et al. [91], where the realistic asymmetric exciton lineshape is used in the TMM calculations, it was found that the linewidth of a polariton is determined both by the local slope of the refractive index and the absorption at the polariton energy. In reference quantum wells similar to the ones used in HCØ621, HCØ641 and HCØ642, the FWHM of the exciton absorption peaks were measured to 200 μeV (HCØ621), 340 μeV (HCØ641) and 960 μeV (HCØ642). For the excitons in HCØ621 and

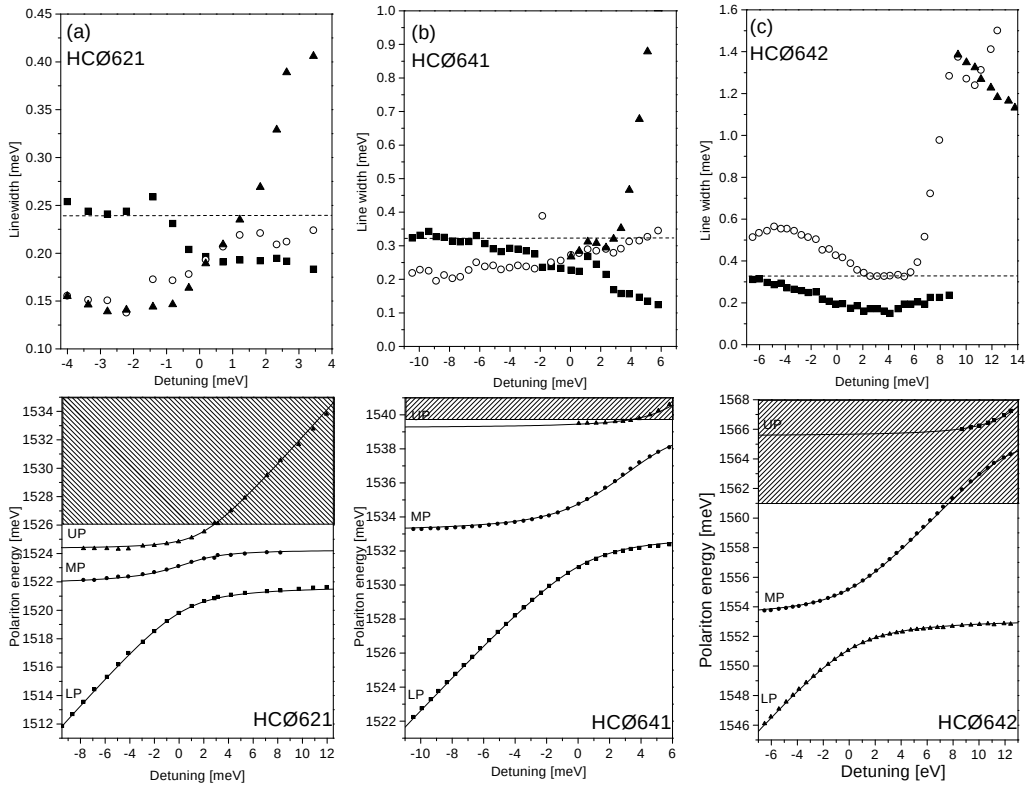

Figure 5.14: Top: Linewidths of polaritons in HCØ621, HCØ641 and HCØ642 at T=11K as a function of detuning. The solid squares, open circles and solid triangles are for the lower, middle and upper polaritons respectivily. The values have been corrected for the instrumental resolutions as discussed in section 5.3.2. Bottom: Corresponding energy level diagrams where the position of the heavy-hole continuum is indicated with a dashed reactangle.

HCØ641 the lineshapes were nearly symmetric, while a pronounced asymmetry was seen for HCØ642 [95]. From these observations combined with the results in the specific limits mentioned in the paragraph above, the measured linewidths plotted in Fig.5.14a-c may be explained. Also shown in the plot are the detuning curves, where the dashed area indicate the position of the heavy-hole continuum.

At large negative detuning the LP is photon like, so the linewidth should be given mainly by the nearly constant bare cavity linewidth, in good agreement with the measurements. The cavity linewidth is indicated in the plots with a dashed line. As the detuning is increased towards resonance and into the positive range $\Delta < 4$ meV, the LP linewidths decrease monotonically ending at a value less than 200 μeV, which should correspond approximately

to the homogeneous linewidth of the exciton [97] because the exciton has a Gaussian broadening on the low energy side. However, in HCØ642 the width eventually increases again for Δ >4 meV, which may be explained by the absorption tail of the exciton in HCØ642, that extends to lower energies than in HCØ621 and HCØ641 because of the larger inhomogeneous broadening.

Starting again from large negative detunings, the MP linewidths are initially at a nearly constant level and only close to resonance, $\Delta \approx$-2 meV, they start changing. The MP linewidths at large negative detuning follow the relation $\gamma_{MP621} < \gamma_{MP641} < \gamma_{cav} < \gamma_{MP642}$ which is explained by the increasing exciton absorption on the high energy side, as the inhomogeneous broadening increases. In the intermediate range, 2 meV< Δ <5 meV, where the cavity is tuned to the region between the heavy- and light-hole resonance in HCØ641 and HCØ642, the MP branch is photon-like, and as expected the linewidths approach the bare cavity linewidth here. Since $\gamma_{MP641} < \gamma_{cav}$ a crossing of the LP and MP linewidths is seen in HCØ641 for -2 meV< Δ <2 meV, in contrast to HCØ642 where they both decrease. In HCØ621 the photon-like behaviour is not clearly seen for the MP because the heavy- to light-hole splitting is smaller than the Rabi-splitting, so all three resonances are strongly coupled in the intermediate region. In HCØ642 the MP finally broadens significantly to γ_{meas} >1200 μeV for Δ >6 meV, whereas in HCØ641 this detuning range was not accessible but as the MP dip is very weak for Δ=6 meV it cannot be expected to be seen for much higher Δ. This difference is due to the position of the light-hole resonance compared to the heavy-hole continuum. In HCØ642 the light-hole resonance lies above the heavy-hole continuum edge, so the MP broadens because of the increased absorption in the continuum before it experiences the avoided crossing with the UP. In HCØ641 the avoided crossing between the MP and UP takes place below the continuum edge, so the MP energy stays below the continuum and the broadening is not seen.

Finally, for the UP the same behaviour is seen in HCØ621 and HCØ641, where the linewidth is initially below the bare cavity linewidth, similar to the MP in these two samples, but increases strongly at the end of the detuning range when it becomes photon-like and enters the continuum. In HCØ642, the UP is broad in the whole detuning range where it is detectable, because the corresponding light-hole resonance lies in the continuum.

The measured linewidths are hence in good qualitative agreement with the approach by Ell et al.[91], but the full TMM calculation should be made to verify the quantitative agreement. We note that at resonance in HCØ642 the average linewidth of $\approx$300 μeV clearly shows the small influence of the inhomogeneous broadening on the polariton linewidths at resonance, which should be $\approx$650 μeV if the average of the exciton and cavity linewidth is

taken. This effect was first reported by Whittaker et al. [93], and named *motional narrowing*, because it was explained as a result of the polariton mode averaging the quantum well disorder over a much larger area than the exciton. The smaller mass of the polariton was used to rewrite the exciton Hamiltonian, and through a rescaling argument it was shown to lead to a smaller inhomogeneous broadening. A similar quantum theory by Savona et al. [92] was able to explain the subaverage broadening at resonance, but for the full detuning range Ell et al. [91] obtained better results with the TMM calculations. Hence, it was concluded that only the quantum mechanical effects already included in the experimentally measured dielectric response of the bare exciton are needed to fully describe the linewidths of MC polaritons.

Finally, it is noted that Whittaker suggested a quantitative relation between the polariton line width and the background absorption at the polariton energy [94]. However, this is valid only when the polariton energy is in the tails of the exciton resonance. Using this relation Borri et al. recently made a quantitative analysis of the measured linewidths of HCØ621, HCØ641 and HCØ642 [95], and found a good overall agreement.

5.3.6 Advantages of reduced light-matter coupling.

In the preceding section it was found that many different parameters may influence the polariton linewidth, and it is difficult quantitatively to distinguish the effects of local absorption, local slope of the refractive index and the exciton homogeneous linewidth. Additonally, the sample with the sharpest and most ideal excitonic response used here, HCØ621, "suffer" from having two resonances close to the continuum edge with a separation less than the Rabi-splitting. Therefore in the resonant regime, -2 meV $< \Delta <$ 2 meV, all three polaritons are significantly mixed with both excitons and because of the level repulsion the UP quickly moves into the continuum and broadens. Thus, to see a more ideal polariton behaviour around each anticrossing and to reduce the contributions from local absorption it is advantageous to be able to design a structure with a reduced light-matter coupling. This may be achieved by placing the quantum well away from the antinode of the electromagnetic standing wave pattern. The energy level diagram of such a structure, HCØ634, is shown in Fig.5.15a and the fitting parameters are given in Table 5.2. Compared to HCØ621 and HCØ641, the values of the coupling strengths are reduced by a factor of ≈ 4, corresponding to a similar reduction of the electric field at the position of the quantum well. Hence an effective distance from a node in the standing wave pattern of $L_{cav}\sin^{-1}(0.25)/2\pi \approx 8$ nm, may be deduced. The level diagram shows that the two polariton anticrossings are much better isolated compared to Fig. 5.11b-c, because the

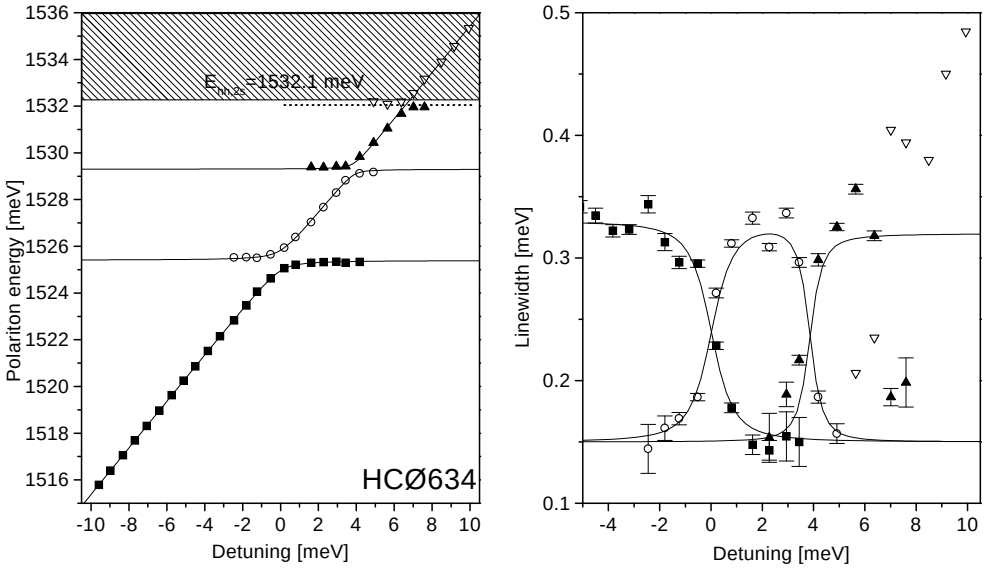

Figure 5.15: Left: Solid symbols show the measured polariton energies in HCØ634, and the solid lines are the fitted energies. Solid square: lower polariton, open circle: middle polariton, solid triangle: upper polariton, open triangle: "top" polariton branch. The dashed rectangle marks the heavy-hole continuum. Right: The solid symbols show the measured polariton linewidths as a function of detuning and the solid lines are fits obtained from equation 5.14.

ratio of the heavy-light-hole splitting to the heavy-hole Rabi-splitting is (E_{lh}-E_{hh})/$\hbar\Omega_{hh}$=4.4, in contrast to a ratio of 0.7 (1.6) in HCØ621 (HCØ641). In addition a new resonance at E=1532.1 meV is visible, which is ascribed to the 2s-state of the heavy-hole exciton, corresponding to an exciton binding energy of 6.7 meV.

The linewidths of the polaritons in HCØ634 are shown in Fig.5.15b. Compared to the linewidths of HCØ621 and HCØ641, the broadening of the UP when the cavity resonance is tuned into the continuum is significantly reduced, and because of the weaker level repulsion it is not clearly seen until Δ >7 meV. Furthermore, at the energy crossing points, Δ=0 meV and Δ=3.9 meV, the linewidths also cross and show a very symmetric behaviour. This is exactly what is expected for ideal homogeneously broadened polaritons in a microcavity where the asymmetry due to the exciton lineshape is negligible, and in fact the fit to the linewidth obtained from an extension of Eq.5.13

$$\gamma_{pol} = \gamma_{cav} \left|c_{ph}\right|^2 + \gamma_{hh} \left|c_{hh}\right|^2 + \gamma_{lh} \left|c_{lh}\right|^2 \qquad (5.14)$$

shows a very good agreement using γ_{cav}=320 μeV and $\gamma_{hh,\mathrm{hom}}$=$\gamma_{lh,\mathrm{hom}}$=150 μeV. Note, that the bare cavity linewidth and the bare exciton homogeneous

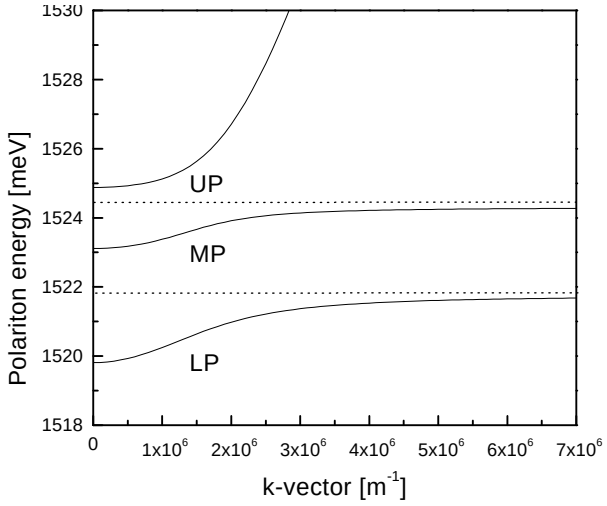

Figure 5.16: Dispersion of lower, middle and upper polaritons (LP, MP, UP) in HCØ621 for zero detuning at k=0. The dashed lines indicate the position of the uncoupled heavy- and light-hole excitons.

broadening are independent of the strength of the light-matter coupling, and correspond to the values found previously.

5.3.7 Reduced dynamic scattering.

The polaritons treated so far were assumed to be coupled to photons propagating in the growth direction perpendicular to the microcavity layers. However, light incident at an angle with respect to the growth direction also couples to the excitons, and in fact it was shown that the in-plane wave vector is a good quantum number for the polaritons [92]. In Fig. 5.16 the polariton energies of HCØ621 have been calculated as a function of the in-plane wave vector, by inserting equation 5.8 into equation 5.10 and solving for the eigenvalues. For the values chosen here, the empty cavity is resonant to the heavy-hole exciton at k=0.

At large k-vectors the lower and middle polariton energies tend to the energies of the uncoupled heavy- and light-hole excitons, while the upper polariton follows the bare cavity dispersion. However, at k-vectors close to zero the dispersion of the lower and middle polaritons is also large. It was predicted that due to the shape of the lower polariton dispersion, the phase space for acoustic phonon scattering is significantly reduced at k=0 [102]. This is due to the energy difference of approximately 2 meV between polaritons at k=0 and at high k values, that acts as a barrier against phonon scattering to high k-vectors. Only if an energy larger than 2 meV can be

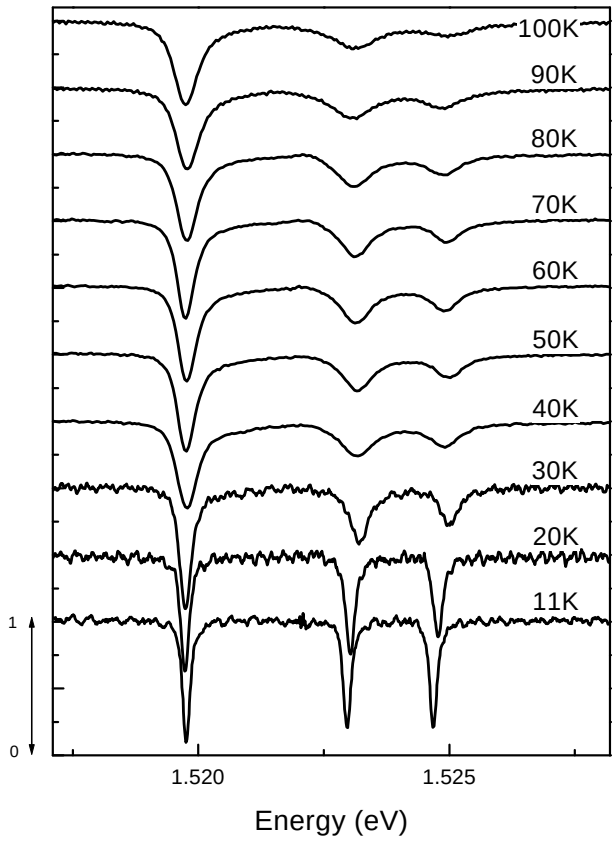

Figure 5.17: Reflectivity spectra of HCØ621 at zero detuning for different temperatures, from [96].

tranferred to the polariton in the phonon scattering process, the polariton can scatter to high k-vectors. However, due to the cutoff wavevector for exciton-phonon interaction it was estimated that only an energy of 1.24 meV can be transferred, which is not enough to overcome the barrier [96].

The prediction of the reduced scattering in the lower polariton branch was experimentally tested in sample HCØ621 [96]. The measured reflectivity spectra at normal incidence and zero detuning are shown in Fig.5.17 as a function of temperature. It is clearly seen that the lower polariton remains narrower than the middle and upper polaritons, as the temperature is increased. In Fig. 5.18 the measured values of the linewidths are shown as a function of temperature for a detuning of 0 meV and 1.2 meV. The solid line shows the linewidth expected from a bare exciton due to acoustic and optical phonon scattering.

It is believed that the reason for the polariton linewidths being broader than the bare exciton linewidth is due to additional scattering with the resid-

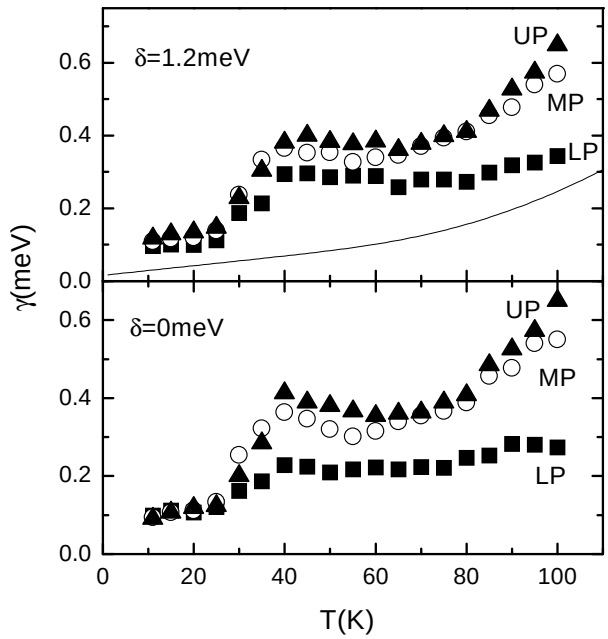

Figure 5.18: Measured linewidths as a function of temperature for HCØ621 at detuning of 0 meV and 1.2 meV, from [96].

ual trions in the structure, that were also visible in the PL-spectrum in Fig.5.6. Thus, the fact that the lower polariton is still narrower than the middle and upper indicates that the argument of reduced scattering phase space also holds for polariton-carrier scattering.

5.4 Secondary emission from microcavities.

When light is incident on a medium, emission may be observed in directions different from the direct reflection or transmission. This so-called secondary emission (SE), typically originates from photoluminescence and resonant Rayleigh scattering (RRS). Classically, the latter is an elastic scattering process on particles smaller than the wavelength of light, with a cross section proportional to λ^{-4}. Hence it is strongly dependent on the wavelength, and actually explains why the blue light from the sun is more efficiently scattered in the atmosphere than the red light [103].

The inevitable disorder in a quantum well leads to a spatially varying dielectric function of the exciton, that also causes RRS, and the intensity and time dependence of the scattered light is directly related to the nature of the disorder [104]. For a coherent excitation beam the RRS is also coherent, in contrast to the incoherent photoluminescence, and this property may be used

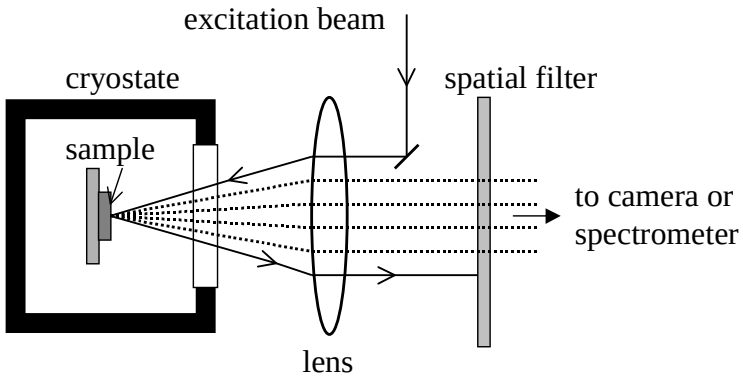

Figure 5.19: Illustration of the setup used for measuring the secondary emission from microcavitites. The solid lines with arrows show the beam path of the excitation beam and the direct reflection, and the dotted lines indicate the secondary emission.

to distinguish these two contributions to the resonant secondary emission (RSE) [105, 114].

Whereas RRS from bare quantum wells has been studied in great detail, the study of RRS from microcavities is only in its beginning and just a few experimental [109, 110, 111] and theoretical [112, 113] reports have been published. In this section, some very recent results [106] on the spectral and directional properties of SE from microcavities will be described.

5.4.1 Samples and experimental setup.

The samples used for the following measurements were HCØ621, HCØ641 and HCØ642, the details of which have been described in the previous sections. Here, it is just emphasised that the inhomogeneous broadening of the quantum well is smallest in HCØ621 and largest in HCØ642.

The experimental setup used in the following is shown in Fig. 5.19. The samples were kept in a He-cryostate at T = 5 K, and a mode-locked Ti:sapphire laser with a pulse duration of $\approx$ 100 fs and a spectral width of $\approx$ 16 meV, was used for the excitation. The laser was tuned during the experiments to ensure similar excitation intensities of the polariton resonances. The excitation was incident at an external angle of 11 degrees, ($k_{||} = 1.5 \cdot 10^6$ m^{-1}), focussed through a N.A.=0.24 lens, and the emission was collected with the same lens. The laser spot size was $\approx 50\mu$m, yielding an inhomogeneous broadening of the cavity resonance of $\approx 70\mu$eV, well below the measured line widths. In the far field apertures were inserted to filter out the reflection, leaving only SE, which was either imaged onto a CCD-chip or spectrally resolved in a grating spectrometer. A linear polarizer was used to analyse the

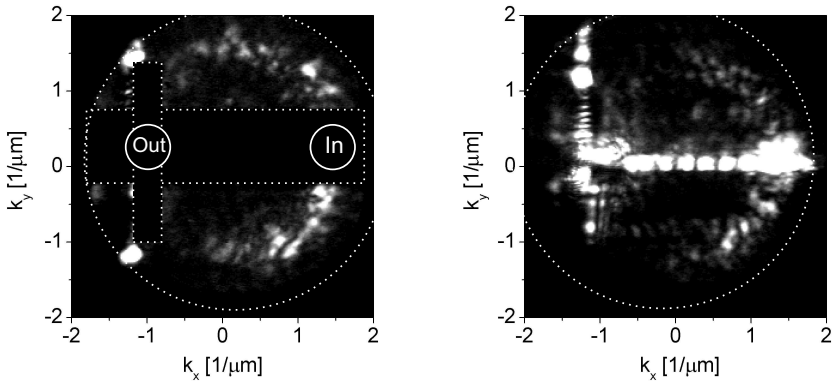

Figure 5.20: a) : Image of the secondary emission from HCØ621 in the far field at a detuning of $\Delta = -5.1$ meV. The dashed rectangles mark the positions of the blocking apertures, and the dashed circle is the aperture given by the lenses in the detection. The angular positions of the exciting (in) and reflected (out) beams are marked by solid circles. b) : Far field image for $\Delta = -7.7$ meV without the apertures so the pattern of spots in the plane of incidence is visible.

polarization state of the emitted light.

In Fig.5.20a, the SE from HCØ621 in the far field is shown, which corresponds to resolving the emission in coordinates of the in-plane wave vector, $\vec{k}_{||}$. The horizontal and vertical apertures block the reflected light as well as the light emission sometimes seen in the plane of incidence (as shown in Fig.5.20b). The outer circular aperture is determined by the diameter of the lenses in the setup. Fig.5.20a shows that the SE forms a ring in the far field, with a diameter determined by the angle of incidence of the exciting beam, in agreement with previous observations of RRS from a MC [110, 111]. Furthermore we note that the emission is distributed in speckles, indicating its coherent nature and thus dominance of RRS. As will be described in the following, the reason for the ring shaped emission is that the condition for elastic scattering, $\mathrm{E}_{pol}(\overline{k}_{out})=\mathrm{E}_{pol}(\overline{k}_{in})$, implies that the magnitudes of the $k_{||}$–vectors are practically identical, $|\overline{k}_{out}|=|\overline{k}_{in}|$, due to the steep lower polariton dispersion at negative detuning.

The apparently stronger emission in the backscattering direction seen in Fig.5.20 is currently not well understood, although effects such as coherent backscattering due to weak localization has been suggested [111]. It is also noted that the regularity of the bright spots visible in the plane of incidence in Fig. 5.20b, suggest that a periodic arrangement of scatterers is present in the structure. Since it was experimentally observed that the relation between

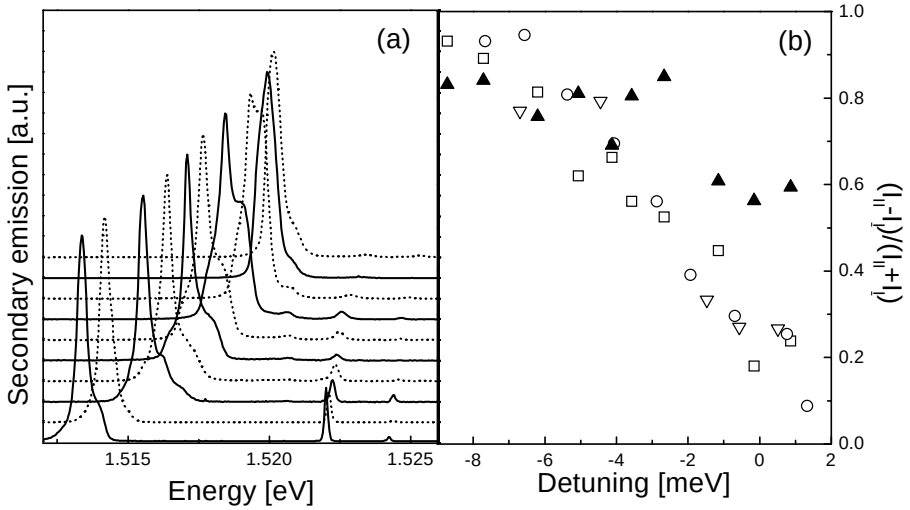

Figure 5.21: (a): Spectrally resolved secondary emission from HCØ621 for different values of the detuning. Starting from the bottom spectrum the detunings are (in meV): -8.7, -7.7, -6.2, -5.1, -4.1, -3.6, -2.7, -1.2, -0.2, 0.9. (b) : The degree of polarization shown as a function of detuning for the LP of HCØ621 (open squares), the LP of HCØ641 (open triangles), the LP of HCØ642 (open circles) and the MP of HCØ621 (solid triangles).

the $k_{||}$–vector and the energy of the emission of each spot coincides with the polariton dispersion relation, it is believed that the excitation at the surface is diffracted into a number of different directions, each exciting a different polariton mode of the MC. Due to the large spectral bandwidth of the exciting laser it covers the whole dispersion relation in the range of k-vectors imaged here, and the bright spots then correspond to the light emitted from each of the excited polariton modes. The spots are best observed at large negative detuning, where no photoluminescence is present in the center of the ring. However, the physical origin of the scatteres responsible for the spots is not known, but they could be due to regular steps at the interfaces of the Bragg reflectors or possibly dislocations.

For the rest of the measurements here, the geometry of the apertures shown in Fig.5.20a was maintained, blocking the diffraction spots described above.

5.4.2 Spectral properties of the secondary emission.

In Fig.5.21a, the total – both PL and RRS – spectrally resolved SE from HCØ621 is shown for different detunings. All spectra have been normalized to the same peak value. At the largest negative detuning, the spectrum shows three peaks corresponding to the LP, MP and UP, and the emission

is almost completely polarized parallel to the exciting laser beam showing the dominance of RRS. The width and center position of the peaks in the SE coincide with the dips seen in the reflection spectrum due to the elastic nature of the scattering. As the cavity is tuned closer to resonance a broad increasing emission is observed in addition to the spectrally sharp emission on the LP branch, accompanied by a decreasing degree of polarization (shown in Fig.5.21b). This demonstrates the increasing influence of unpolarized PL in the SE from the LP. A different behaviour is seen for the MP, which broadens and becomes less intense as the cavity is tuned closer to resonance. In addition, the RSE of the MP remains more than 60% polarized indicating less influence of PL. However, it is clear that in the range of detunings where the influence of PL in the RSE is negligible, the RRS on the MP increases compared to the RRS on the LP for increasing $|\Delta|$. This is the predicted behaviour according to the "filter" model of Shchegrov et al [113] for a MC with small inhomogeneous broadening compared to the bare cavity linewidth. The details of the filter model are not important here, but will be described in the next section.

It is noted that the absolute intensity of the RRS on the LP is only weakly dependent on detuning. It was observed that when increasing the detuning from -8.7 meV to -4.1 meV, the RRS on the LP was increasing continously by 30%. A similar weak dependence on detuning was observed in the other samples. This is in contradiction to the filter model [113, 112], where the RRS intensity is expected to be proportional to the square of both the exciton and photon fraction of the polariton. At these detunings the photon fraction is nearly constant while the exciton fraction increases approximately by a factor of 3. Moreover, for a MC with small inhomogeneous broadening compared to the cavity line width, the RRS is expected to be less intense on the LP than on the MP at negative detuning [113]. Both observations suggest that there is an additional scattering mechanism on the LP, which is attributed to scattering in the photonic part of the polariton due to dielectric inhomogeneties, e.g. originating from microroughness on the interfaces in the structure [118]. However, since the light is elastically scattered on a ring it is suggested that the scattering can still be described by a filter model which includes the dielectric disorder in addition to the static quantum well disorder.

To support the following discussion, Fig. 5.22 shows the dispersion of the polariton branches in HCØ621 for different detunings as well as the photon fraction of the lower polariton. For resonantly excited polaritons on the MP and UP branch, a dominating fast interband relaxation is expected to exciton-like polaritons at high k–values on the LP branch, forming a reservoir of incoherent polaritons [115, 116], explaining the low fraction of PL in the

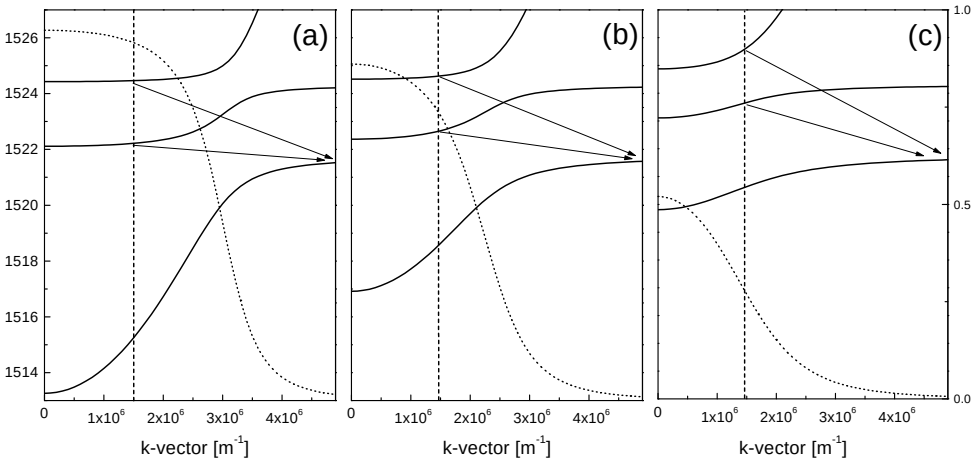

Figure 5.22: Dispersion of the polariton branches in HCØ621 for detunings at k=0 of -8 meV (a) -4 meV (b) and 0 meV (c), where the polariton energies are given on the left axis. The dotted lines show the photon fraction of the lower polariton on the right axis. The dashed vertical lines indicate the excitation k-vector used here, and the arrows indicate the fast interbranch scattering processes of the MP and UP polaritons.

RSE from the MP and UP. For the LP at zero and negative detuning, intraband relaxation via acoustic phonons from the exciton-like polaritons in the reservoir towards lower k–values becomes less likely for decreasing k–values, because of the decreasing density of final states [117]. This results in a bottleneck effect, and explains the behaviour of the degree of polarization and the spectra shown in Fig. 5.21b. For large negative detuning the excited polaritons are almost completely photon-like, and hence relaxation via phonons into these states is impossible. As the detuning is increased towards zero, the exciton fraction of the LP increases (the photon fraction decreases), giving rise to an increasing contribution from incoherently scattered polaritons and hence a decreasing degree of polarization. Since the incoherently scattered polaritons occupy a broad range of k–space compared to the excited polaritons they account for the spectrally broad emission contribution, seen in Fig. 5.21a. It is noted that the degree of polarization of the LP emission has an almost identical behaviour as a function of detuning for HCØ621, HCØ641 and HCØ642, showing that the presence of a polariton bottleneck has the same dependence on the detuning for the three samples. This is expected since the dispersion of the LP is very similar in the three samples, and the inhomogeneous broadening is so small that it does not significantly affect the possible scattering mechanisms.

To investigate the influence of inhomogeneous broadening on the spectral properties of RRS from MC's we show in Fig.5.23 the spectrally resolved

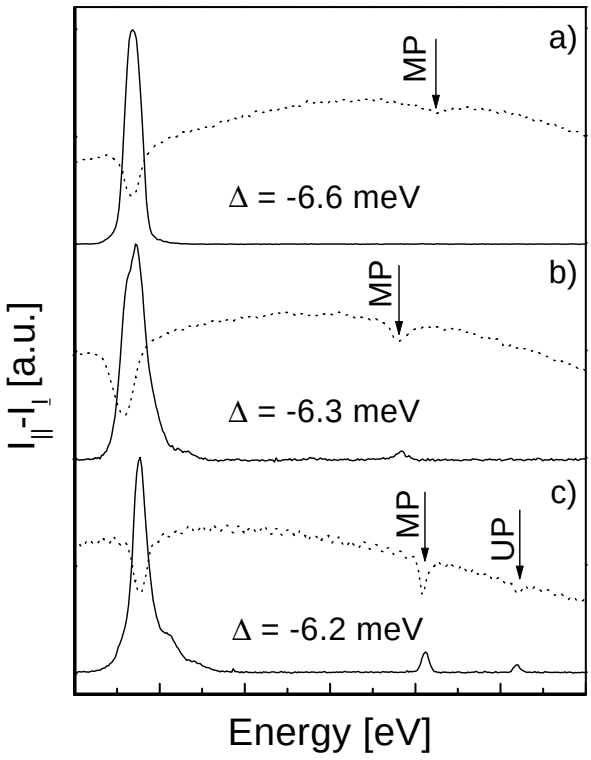

Figure 5.23: Solid (dotted) lines: Spectrally resolved RRS (reflection) for a) HCØ642, b) HCØ641 and c) HCØ621. The arrows indicate the reflectivity dips corresponding to the middle and upper polaritons. The spectra in a) and b) have been shifted to ease the comparison.

RSE from the three microcavities for the same ratio of the detuning to the Rabi-splitting, $\Delta/\hbar\Omega_{Rabi} = -1.6$ where the influence of PL is negligible. Also shown is the spectrum of the reflected light, indicating the spectral positions of the excited polaritons. It is noted that the emission intensity of the MP relative to the LP decreases as the static quantum well disorder increases. For HCØ621 the ratio of the integrated emission from the MP polariton to the LP is about 3%, decreasing to 1% for HCØ641, whereas no emission is observable on the MP in HCØ642. Again, this observation is in qualitative agreement with the theory of MC RRS by Shchegrov et al. [113], which predicts that for larger inhomogeneous broadening the MC RRS intensity is shifted towards the photonlike polaritons. However, a quantitative comparison is difficult, because relaxation effects are not treated in the theory [113] and as argued above the RRS from the LP has a significant contribution from photonic scattering at this detuning. The observation of decreasing MC RRS on the UP for increasing inhomogeneous broadening seems to be in contradiction to

the interpretation of the filter model by Whittaker [112], which emphasises the importance of a spectral overlap between the polariton and the bare exciton in order to get efficient MC RRS. Since the UP is spectrally very close to the bare exciton for $\Delta/\hbar\Omega_{Rabi} = -1.6$, this interpretation instead predicts an increasing MC RRS for increasing disorder.

5.4.3 Directional properties of the secondary emission.

In this section the directional properties of the RSE from the MC samples are described. Due to the coherent nature of the RRS component a pronounced speckle effect is seen in the emission images at negative detunings (se e.g. Fig.5.20). To obtain meaningfull statistical information the images are analysed by integration the RSE intensity over the azimutal angles. The integrated RSE intensity is calculated as:

$$I(k_{||}) = \int_{\theta}^{\theta+\Delta\theta} I(k_{||}, \phi) d\phi \tag{5.15}$$

where $I(k_{||}, \phi)$ is the intensity in a cylindrical coordinate system with the origin at the center of the emission ring. The integral is performed over a large range of azimutal angles, typically 90 degrees, averaging out the speckle structure in the image. The data from the CCD chip is converted into the cylindrical coordinate system such that a uniform illumination of the CCD chip results in a constant $I(k_{||})$. The intergrated RSE is shown in Fig.5.24 as a function of in-plane momentum for HCØ621 and HCØ641 for a range of different detunings. The arrows on the right side indicate the position of the circular aperture shown in Fig.5.20. Note that the intensity does not drop sharply to the right of the arrow, because the emission ring and the circular aperture are not concentric.

For the detunings used in Figs. 5.24a and 5.24b the RSE is dominated by RRS. Here a peaked emission is observed on a nearly constant background. The peak in the integrated RRS corresponds to the ring in the images of Fig.5.20 and is primarely due to RRS from the LP. The constant background is partly due to stray light and partly to RRS from the MP or UP, which is emitted in a broad range of directions because of the flat polariton dispersion, similar to a bare quantum well, see Fig. 5.22a. In Fig. 5.24c an additional contribution to the background emission is seen, gradually increasing for larger values of the in-plane momentum. In Fig. 5.24d, the emission is completely transformed into a broad distribution peaked at the outer aperture. This is exactly the shape expected for PL due to the polariton bottleneck [117]. The appearance of this incoherent contribution in the

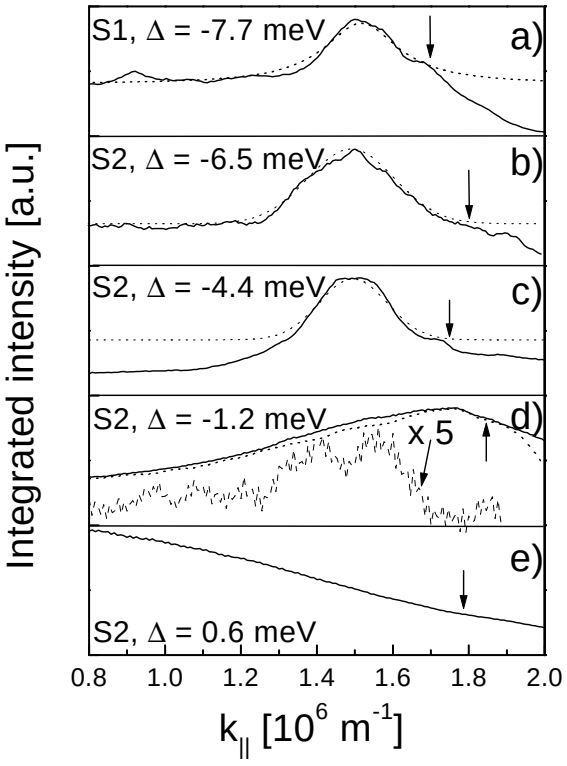

Figure 5.24: a)-e) : The solid lines show the measured distribution of emission in k-space, $I_{||}$, integrated over the in-plane angles. The dotted line in a) is the calculated distribution for a Lorentzian distribution using Eq.5.16, whereas the dotted lines in b) and c) are Gaussian fits as described in the text. d): The solid (dotted) lines show the distribution in k-space for polarization parallel (perpendicular) to the excitation. The dashed line shows the difference, $I_{||} - I_{\perp}$. S1 (S2) refers to HCØ621 (HCØ641).

integrated RSE for $\Delta \geq -4$meV matches the observation of the decreasing degree of polarization of the RSE from the LP. Comparison of $I_{||}$ and $I_{\perp}$ shows that an extra contribution is still seen in the $I_{||}$ emission originating from the Rayleigh scattering. Finally, for a small positive detuning, shown in Fig. 5.24e, the polaritons are completely relaxed to $k = 0$ with a decaying tail for increasing wavevectors, that is there is no bottleneck effect for this detuning.

The filter model predicts not only the presence of the ring shaped RRS emission but is also able to predict the width of the ring. Consider first a monochromatic plane wave of energy $\hbar\omega$ resonant to a polariton with a wave vector k'. Then the possible outscattering directions are given by the range of polaritons in k–space that has a spectral overlap with $\hbar\omega$. If the polariton line width is γ_p, the emission in k–space is centered at $|k'|$ and

has a width given by $\gamma_p \cdot (dE/dk|_{k'})^{-1}$, which defines the *output filter*. It is important to notice that even excitation with monochromatic light gives rise to a broadening of the ring and is already evidenced in the images of Houdré et al [111]. Exciting the polariton with a broad spectrum and a focussed beam give rise to additional broadening. To accurately account for the additional broadening the output filter must be convoluted with the spectrum of the excited polaritons. Under the assumption that a Lorentzian distribution of polariton energies of width γ_{exc} is excited, and that the output filter is Lorentzian, the width of the ring in k–space can be approximated by:

$$\Delta k = (dE/dk)^{-1}(\gamma_p + \gamma_{exc}). \tag{5.16}$$

The proportionality of the width with $(dE/dk)^{-1}$ has already been observed [110, 112], but here we distinguish between the contributions from the excitation and the output filter. To test this approach, Eq.5.16 was used to calculate the directional emission in Fig. 5.24a, where $\gamma_{\rm p} = 260$ μeV was assumed in agreement with the reflection measurements described previously, and the experimentally obtained spectrum of the emission was approximately Lorentzian with $\gamma_{\rm ext} = 420$ μeV. The dispersion was calculated using a three level model [100], and no fitting parameters have been used. As shown in Fig. 5.24a the agreement between the measured and the calculated distribution is very good.

Due to the polariton dispersion the spectral distribution of the excited polaritons depend on the range of k–vectors in the excitation beam. A tighter focus was used in Fig. 5.24b and 5.24c and a wider range of energies was consequently excited. From the RRS spectrum, $\gamma_{\rm ext} = 700$ μeV and $\gamma_{\rm ext} = 550$ μeV was obtained for Fig. 5.24b and 5.24c, respectively, and a spectral shape closer to a Gaussian than a Lorentzian. Hence, Eq. 5.16 is not strictly valid here. For these two curves a Gaussian with a spectral width of $\gamma_{\rm eff}^2 = \gamma_p^2 + \gamma_{\rm ext}^2$ was used and from the calculated inverse dispersion slopes of $0.353 \cdot 10^6 (\text{meV m})^{-1}$ and $0.376 \cdot 10^6 (\text{meV m})^{-1}$ the fits shown in Fig. 5.24b and 5.24c were obtained. Note that due to the tail of the bottleneck under the peak in Fig. 5.24c, the modelled distribution does not coincide with the background level on the left side. The good overall agreement supports the approach used here to describe the directional emission.

In summary, it was found that the proposed filter model of the RRS from MC's [113] is able to qualitatively reproduce most aspects of the measured RRS data. In agreement with the model an increasing RRS on the MP was observed for larger negative detuning in a sample with small inhomogeneous broadening, as well as a shift of the RRS toward the LP for increasing inhomogeneous broadening. The model is also able to correctly predict the width

of the emission in k–space and points to the importance of broadening in both the excitation and emission process. In addition, an RRS contribution on the LP was observed that was not related to the QW inhomogeneous broadening, and it was argued that this was due to dielectric roughness at the interfaces, which couples to the photonic part of the LP.

Chapter 6

Summary and conclusion

In this thesis the growth and the optical properties of semiconductor nanostructures with electronic and photonic confinements have been described.

The basic theory of semiconductor optics relevant for the work here has been reviewed, focussing especially on the influence of strain on the band structure, the properties of low-dimensional structures and the transfer matrix method for calculating the optical properties of straitified media.

The current understanding of molecular beam epitaxial growth of Arsenide-based III-V semiconductors has been summarized, both with regard to the different thermodynamic phases of the surface morphology and the surface reactions taking place on an atomic scale. For the surface morphology a qualitative distinction between uniform films, dislocated films and coherently strained islands has been made. The surface reactions on an atomic scale include both reactions in the plane of growth, that account for the roughness of the surface, and exchange reactions between monolayers that describe surface segregation. A smoothening of the interfaces in a quantum well due to a growth interrupt of 120s has been experimentally demonstrated, yielding monolayer flat islands larger than the exciton Bohr radius and showing that the amount of impurities incorporated into the surface during the interrupt is small enough not to affect the photoluminescence markedly.

Two other growth "tricks" have been experimentally demonstrated, digital alloying and controlled thickness variations. With digital alloying, several $Al_xGa_{1-x}As$ layers were grown for x-values between 0 and 0.257 with band gaps very close to continuously grown alloys and a high uniformity across the wafer. The thickness variations across the wafer when rotation was stopped during growth was determined to be $5\%cm^{-1}$ in the steepest direction, in agreement with a simple flux model assuming a point source. Based on the understanding gained here, digital alloying and intentional thickness and composition variations have been used in the rest of the work to make sample

design more flexible and add new functionalities to the structures.

A large part of the work has dealt with growth of low-dimensional structures, quantum wells, quantum wires and quantum dots, and the characterization of their basic optical properties at low temperatures, such as transition energies and linewidths. All of the structures have been grown using both ternary materials, AlGaAs and InGaAs, as well as the quaternary InAlGaAs.

Starting from the quantum wells, a detailed analysis of InAlGaAs based structures was made, using InGaAs reference samples to calibrate the In growth rate and to deduce the parameters describing surface segregation. Using a computer code to simulate the composition profile under the influence of surface segregation and a six band k·p-model to calculate the quaternary quantum well transition energies, an empirical band gap relation for InAlGaAs was found (Eq. 4.1). A simple linewidth analysis of the photoluminescence peaks revealed effective well width fluctuations of 1.1 ML in addition to the expected random alloy fluctuations. Hence, it is concluded that the growth conditions used here for the InAlGaAs quantum wells are optimal, avoiding clustering in the group-III sublattice and yielding very flat interfaces.

A number of InAlGaAs multi quantum well structures were grown using digital alloying, in order to be able to choose the Al mole fraction in the barriers independent of the Al and In mole fractions in the well. A comparison with continuously grown structures, yielded similar photoluminescence linewidths but the transition energies were 40-50 meV lower than the designed value. This difference was ascribed to the different methods used for calibrating the In growth rate. The uncertainty using the RHEED oscillations is larger compared to an In containing reference structure, because the growth rate depends on the position where the electron beam hits the calibration wafer. Thus it is suggested to use a GaAs piece as a "marker" on the center of the calibration wafer to reduce this uncertainty. Finally, the conditions for avoiding dislocations in InAlGaAs multi quantum well structures were analysed, yielding a value of the frictional strain in the range ϵ_{fric}=0.0017-0.0030.

The InAlGaAs multi quantum well structures were used for growing T-shaped quantum wires, with the so-called cleaved edge overgrowth technique. Because of the larger lattice constant of InAlGaAs than GaAs, the overgrown quantum well was under tensile strain in the T-shaped intersection. From a comparison with unstrained AlGaAs structures and theoretical calculations, a strain induced enhancement of the quantum wire confinement energy of 5-10 meV was found. However, the quality of the overgrown GaAs layers was found to decrease for increasing In content in the InAlGaAs quantum wells and for an In mole fraction of 0.2 no quantum wires were observed,

possibly due to defects or dislocations. In any case, the observation of a strain induced enhancement is promising for the realization of quantum wire structures with larger confinement energies than the record values obtained so far in asymmetric structures.

For the lowest dimensionality, quantum dot structures were grown both in InAs, InGaAs and InAlGaAs. The growth conditions were optimized for InAs quantum dots, where In desorption was found to be important for T_{sub}=515°C whereas for T_{sub}=480°C no significant change of the luminescence peak and linewidth was observed when introducing a 30s growth interrupt before covering the dots. To obtain higher transition energies a structure with 5-6 ML $In_{0.5}Al_xGa_{0.5-x}As$ quantum dots and $Al_{2x}Ga_{1-2x}As$ barriers was realized for x = 0, 0.04 and 0.08 using an 8s growth interrupt between the deposition of each monolayer of the quantum dots. In this way transition energies ranging from 1315 meV to 1490 meV were obtained, with typical linewidths of 50 meV. Compared to other reports using InAs quantum dots on AlGaAs barriers to increase the transition energies, the quantum dots in the structure used here are significantly more uniform.

In conclusion, the main difference between quaternary InAlGaAs compared to InGaAs for nanostructures is that strain effects can be used in structures with high transition energies, near the visible red part of the spectrum. Although the main motivation in the present work for growing quantum dots in this spectral range was to fit the transition energies to the requirements set by a specific detector or excitation laser, the understanding gained here of InAlGaAs quantum wells and quantum dots may also prove useful for future applications in semiconductor lasers [39]. Especially, the quantum dot structures with a low total Al content and narrow size distribution, could be advantageous as a gain medium in a waveguide structure, where a refractive index contrast to the cladding layers is needed to confine the light. Finally, the use of InAlGaAs instead of AlGaAs makes it possible to realize GaAs structures with strained barriers, as was shown for the strained T-shaped quantum wires. Although the applications of this effect may be limited, one may think of using InAlGaAs for strain-patterned structures, e.g. for spatial control of quantum dot nucleation.

Another large part of the work has focussed on growing semiconductor microcavities with narrow polariton resonances and characterising their optical properties. The growth of each part of the microcavity, the Bragg reflector, the spacer layer and the quantum well was analysed in detail and experimentally investigated. An optimized microcavity structure was developed, where both the bare cavity linewidth and the linewidth of the excitonic resonance was minimized. To minimize the cavity linewidth while still keeping the cavity energy tunable, the spacer layer was intentionally wedged, while the Bragg

reflector was grown without a thickness gradient. In this way a cavity energy gradient of 1.35 mm/meV was obtained, ensuring an inhomogeneous broadening of the cavity resonance much smaller than the homogeneous linewidth when probing a area of 50-75 μm. The linewidth of the exciton resonance was minimized using a broad GaAs quantum well where the influence of well width fluctuations on the inhomogeneous broadening is small. At the same time a special spacer layer design was used, leading to a low density of free carriers in the quantum well and a reduced homogeneous broadening of the exciton due to free carrier scattering. In such an optimized structure with a 25 nm quantum well, a record high ratio of the Rabi-splitting to the linewidth of 19 was obtained.

A number of different microcavity structures were grown with different inhomogeneous broadenings of the quantum well and different strengths of the exciton-photon coupling. Using reflection measurements at low temperature, the polariton energies and linewidths were investigated as a function of detuning. It was found that a simple coupled harmonic oscillator model was sufficient to precisely model the polariton energies, whereas the understanding of the linewidths was much more involved. Since the nature of the polaritons changes between photon-like and exciton-like as a function of detuning, the linewidths change because the homogeneous widths of the exciton and photon are different. Furthermore, the absorption in the quantum well at the polariton energy broadens the line, which is especially important in the tails of the excitonic absorption and in the continuum. This was clearly demonstrated in a structure where the exciton-photon coupling was reduced by placing the quantum well close to a node of the electromagnetic standing wave pattern. Because of the lower sensitivity to background absorption, an "ideal" behaviour was observed in this structure for a large detuning range, where the linewidth was given by an average of the cavity linewidth and the homogeneous exciton linewidth, weighted by the exciton and photon content of the polariton.

The polariton linewidths were also measured as a function of temperature, showing a narrower lower polariton resonance compared to the middle and upper polaritons. Since the broadening of the polaritons as a function of temperature is expected to be due to scattering of the exciton on phonons or free carriers, the narrow lower polariton is explained by a reduced scattering rate in this branch, in agreement with theoretical predictions. This is due to the steep dispersion of the lower polariton branch at k=0, which significantly reduces the density of final states compared to a bare exciton.

The secondary emission from microcavities was investigated as a function of detuning and quantum well disorder. A good qualitative agreement for the resonant Rayleigh scattering was found with the so-called filter model [113],

but the contributions from incoherently scattered polaritons (photoluminescence), which were not included in the model, made a quantitative agreement difficult. It was found that dielectric disorder is present in the Bragg reflectors of the microcavities, giving rise to elastic light scattering even at large negative detunings. Finally, a polariton bottleneck was experimentally observed in the directionally resolved photoluminescence, in agreement with theoretical predictions [117].

All considered, the control of the polariton resonance linewidth achieved in the structures developed in this work, is very promising for future research in the field of strong light-matter coupling. Generally, the narrow linewidths that have been obtained allow the investigation of finer details than was possible so far. But more specifically the understanding of this near-ideal planar structure may be important for the development of other structures with a strong light-matter coupling, e.g. utilizing photonic band gap components instead of a planar microcavity to localize the light.

Bibliography

[1] J.Faist, F.Capasso, D.L.Sivco, C.Sirtoni, A.L.Hutchinson, and A.Y.Cho, Science **264**, 553 (1994).

[2] D.C.Streit, T.R.Bloch, P.Chin, and M.Wojtowicz, "MBE production for Telecommunication Devices and Circuits", Eleventh International Conference on Molecular Beam Epitaxy, MBE-XI, Beijing, China, 2000.

[3] Y.Matsushima, and H.Gotoh, "MBE production for High Power Lasers for Submarine Applications", Eleventh International Conference on Molecular Beam Epitaxy, MBE-XI, Beijing, China, 2000.

[4] P.Y.Yu and M.Cardona, "Fundamentals of Semiconductors", Physics and Material Properties, Springer-Verlag, Berlin, 1996

[5] N.Peyhambarian, S.W.Koch and A.Mysyrowicz, "Introduction to Semiconductor Optics", Prentice Hall, New Jersey, 1993.

[6] T.Norris, "Excitons in strongly coupled semiconductor microcavities", in Semiconductor Quantum Optoelectronics, ed. A.Miller, M.Ebrahimzadeh and D.M.Finlayson, Proceedings of the Fiftieth Scottish Universities Summer School in Physics, St. Andrews, July 1998.

[7] Y.Arakawa, and H.Sakaki, Appl.Phys.Lett. **40** (11), 939 (1982).

[8] H.Haug and S.W.Koch, "Quantum Theory of the Optical and Electronic Properties of Semiconductors", World Scientific, Singapore, 3rd Edition, 1994.

[9] M.A.Herman, and H.Sitter, "Molecular Beam Epitaxy", Springer Series in Materials Science 7, Springer-Verlag Berlin Heidelberg (1989).

[10] A.Zangwill, "Physics at Surfaces", Cambridge University Press (1988).

[11] C.Kittel, "Introduction to Solid State Physics", 6th edition, John Wiley & Sons, Inc., New York, (1986).

[12] V.A.Shchukin, N.N.Ledentsov, P.S.Kop'ev, and D.Bimberg, Phys. Rev. Lett. **75** (16), 2968 (1995).

[13] V.A.Shchukin, and D.Bimberg, Rev. Mod. Phys. **71** (4), 1125 (1999).

[14] Ratsch, and A.Zangwill, Surf. Science. **293**, 123 (1993).

[15] F.Heinrichsdorff, A.Krost, M.Grundmann, D.Bimberg, A.Kosogov, P.Werner, F.Bertram, and J.Christen, Proceedings of The 23rd International conference on Semiconductor Physics, Berlin, 1996, p1321.

[16] E.Pehlke, N.Moll, and M.Scheffler, Proceedings of The 23rd International conference on Semiconductor Physics, Berlin, 1996, p1301.

[17] T.S.Jones, P.B.Joyce, T.J.Krzyzewski, G.R.Bell, S.Malik, D.Childs, and R.Murray, " ", Eleventh International Conference on Molecular Beam Epitaxy, MBE-XI, Beijing, China, 2000.

[18] B.A.Joyce, D.D.Vvedensky, and C.T.Foxon, Handbook of Semiconductors, volume 3, chapter 4, "Growth Mechanisms in MBE and CBE of III-V Compounds", edited by T.S.Moss, Elsevier Science B.V. (1994).

[19] M.Itoh, G.R.Bell, A.R.Avery, T.S.Jones, B.A.Joyce, and D.D.Vvedensky, Phys. Rev. Lett. **81** (3), 633 (1998).

[20] K.Leosson, J.R.Jensen, W.Langbein, and J.M.Hvam, Phys. Rev. B., **61** (15), 10322 (2000).

[21] W.Langbein, K.Leosson, J.R.Jensen, J.M.Hvam, and R.Zimmermann, Phys. Rev. B., **61** (16), R10555 (2000).

[22] L.Pavesi, and M.Guzzi, J.Appl.Phys., **75** (10), 4779 (1994).

[23] L.M.Smith, K.Leosson, J.Erland, J.R.Jensen, J.M.Hvam, and V.Zwiller, to appear in the proceedings of the International Conference on Semiconductor Quantum Dots, Munich,Germany, 2000.

[24] J.M.Moison, C.Guille, F.Houzay, F.Barthe, and M. Van Rompay, Phys. Rev. B **40** (9), 6149 (1989).

[25] J.M.Gerard and J.Y.Marzin, Phys. Rev. B **45** (11), 6313 (1992).

[26] N.Grandjean, J.Massies, and M.Leroux, Phys. Rev. B **53** (3), 998 (1996).

[27] J.M.Gerard and G. Le Roux, Appl. Phys. Lett., **62** (26), 3452 (1993).

[28] J.Massies, F.Turco, A.Saletes, and J.P.Contour, Jour. Cryst. Growth **80**, 307 (1987).

[29] S.S.Dosanjh, X.M.Zhang, D.Sansom, J.J.Harris, M.R.Fahy, B.A.Joyce, and J.B.Clegg, Jour. Appl. Phys. **74** (4), 2481 (1993).

[30] K.Muraki, S.Fukatsu, Y.Shiraki, and R.Ito, Appl. Phys. Lett. **61** (5), 557 (1992).

[31] J.M.Gerard, Appl. Phys. Lett. **61** (17), 2096 (1992).

[32] O.Dehaese, X.Wallart, and F.Mollot, Appl. Phys. Lett. **66** (1), 52 (1995).

[33] J.M.Gerard, Jour. Cryst. Growth **127**, 981 (1993).

[34] J.M.Gerard and C.d'Anterroches, Jour. Cryst. Growth **150**, 467 (1995).

[35] J.R.Jensen, J.M.Hvam, and W.Langbein, Jour. Appl. Phys. **86** (5), 2584 (1999).

[36] E.P.O'Reilly and A.R.Adams, IEEE Jour. Quantum. Elec. **30** (2), 366 (1994).

[37] H.Gislason, "Growth and Optical Characterization of GaAs Quantum Wires", Ph.D. Thesis, Mikroelektronik Centret, Oktober 1997.

[38] C.B.Sørensen, "MBE-growth, processing and characterization of low-dimensional GaAs/AlAs heterostructures", Ph.D. Thesis, Mikroelektronik Centret and Niels Bohr Institute f.AFG, November 1998.

[39] J.Ko, C.H.Chen, and L.A.Coldren, Elec. Lett. **32** (22), 2099 (1996).

[40] W.Langbein, "Vielteilcheneffekte und Ladungsträgerdynamik in Typ-II-Übergitterstrukturen", Ph.d.-thesis, Fakultät für Physik der Universität (TH) Karlsruhe, (1995).

[41] R.Atanasov, F.Bassani, A.D'Andrea, and N.Tomassini, Phys. Rev. B **50** (19), 14381 (1994).

[42] E.F.Schubert, E.O.Göbel, Y.Horikoshi, K.Ploog, and H.J.Queisser, Phys. Rev. B **30** (2), 813 (1984).

[43] R.F.Schnabel, R.Zimmermann, D.Bimberg, H.Nickel, R.Lösch, and W.Schlapp, Phys. Rev. B **46** (15), R9873 (1992).

[44] H.Yu, C.Roberts, and R.Murray, Appl. Phys. Lett. **66** (17), 2253 (1995).

[45] M.Ogasawara, H.Sugiura, M.Mitsuhara, M.Yamamoto, and M.Nakao, Jour. Appl. Phys. **84** (9), 4775 (1998).

[46] B.A.Fox, and W.A.Jesser, Jour. Appl. Phys. **68** (6), 2801 (1990).

[47] B.A.Fox, and W.A.Jesser, Jour. Cryst. Growth **109**, 252 (1991).

[48] A.R.Goñi, L.N.Pfeiffer, K.W.West, A.Pinczuk, H.U.Baranger, and H.L.Stormer, Appl. Phys. Lett. **61** (6), 1956 (1992).

[49] Y.Chang, L.L.Chang, and L.Esaki, Appl. Phys. Lett. **47** (12), 1324 (1985).

[50] D.Gershoni, J.S.Weiner, S.N.G.Chu, G.A.Baraff, J.M.Vandenberg, L.N.Pfeiffer, K.West, R.A.Logan, and T.Tanbun-Ek, Phys.Rev.Lett. **65** (13), 1631 (1990).

[51] H.Akiyama, T.Someya, M.Yoshita, T.Sasaki, and H.Sakaki, Phys. Rev. B. **57** (7), 3765 (1998).

[52] H.Akiyama, T.Someya, and H.Sakaki, Phys. Rev. B. **53** (16), R10520 (1996).

[53] H.Akiyama, T.Someya, and H.Sakaki, Phys. Rev. B. **53** (24), R16160 (1996).

[54] T.Someya, H.Akiyama, and H.Sakaki, Appl. Phys. Lett. **66** (26), 3672 (1995).

[55] T.Someya, H.Akiyama, and H.Sakaki, Phys. Rev. Lett. **76** (16), 2965 (1996).

[56] H.Akiyama, T.Someya, and H.Sakaki, Phys. Rev. B. **53** (8), R4229 (1996).

[57] T.Someya, H.Akiyama, and H.Sakaki, Jour. Appl. Phys. **79** (5), 2522 (1996).

[58] M.Yoshita, H.Akiyama, T.Someya, and H.Sakaki, Jour. Appl. Phys. **83** (7), 3777 (1998).

[59] H.Akiyama, J. Phys.: Condens. Matter **10** (1998), 3095-3139.

[60] T.Someya, H.Akiyama, and H.Sakaki, Phys. Rev. Lett. **74** (18), 3664 (1995).

[61] H.Gislason, W.Langbein, and J.M.Hvam, Appl. Phys. Lett. 69 (21), 3248 (1996).

[62] H.Gislason, "Growth and optical characterisation of GaAs quantum wires", Ph.D.-thesis, Mikroelektronik Centret, Technical University of Denmark (1997).

[63] W.Langbein, H.Gislason, and J.M.Hvam, Phys. Rev. B. **54** (20), 14595 (1996).

[64] W.Langbein, H.Gislason, and J.M.Hvam, Phys. Rev. B. **60** (24), 16667 (1999).

[65] W.Wegschieder, L.N.Pfeiffer, M.M.Dignam, A.Pinczuk, K.W.West, S.L.McCall, and R.Hull, Phys. Rev. Lett. **71** (24), 4071 (1993).

[66] K.Nishi, H.Saito, S.Sugou, and J.S.Lee, Appl.Phys.Lett. **74** (8), 1111 (1999).

[67] V.M.Ustinov, N.A.Maleev, A.E.Zhukov, A.R.Kovsh, A.Y.Egorov, A.V.Lunev, B.V.Volovik, I.L.Krestinov, Y.G.Musikhin, N.A.Bert, P.S.Kop'ev, Z.I.Alferov, N.N.Ledentsov, and D.Bimberg, Appl.Phys.Lett. **74** (19), 2815 (1999).

[68] A.Polimeni, A.PatanÚ, M.Henini, L.Eaves, and P.C.Main, Phys. Rev. B. **59** (7), 5064 (1999).

[69] M.Grundmann, O.Stier, and D.Bimberg, Phys. Rev. B **58** (16), 10557 (1998).

[70] K.Leosson, J.Erland, J.R.Jensen, and J.M.Hvam, Conference of Lasers and Electro-Optics (CLEO),San Francisco, 2000.

[71] K.Leosson, J.R.Jensen, J.M.Hvam, and W.Langbein, Non-linear Optics of Excitons in Confined Systems (NOEKS) Marburg, Germany, 2000.

[72] J.Oshinowo, M.Nishioka, S.Ishida, and Y.Arakawa, Appl.Phys.Lett. **65** (11), 1421 (1994).

[73] P.W.Fry et al., Phys. Rev. Lett., **84** (4), 733 (2000).

[74] J.Erland, S.I.Bozhevolnyi, K.Pedersen, J.R.Jensen, J.M.Hvam, Appl.Phys.Lett. **77** (6), 806 (2000).

[75] B.Vohnsen, S.I.Bozhevolnyi, K.Pedersen, J.Erland, J.R.Jensen, J.M.Hvam, submitted for Opt. Lett.

[76] J.Minch, S.H.Park, T.Keating, and S.L.Chuang, IEEE Jour. Quant. Elec. **35** (5), 771 (1999).

[77] J.R.Jensen, J.M.Hvam, and W.Langbein, accepted for MBE-XI, Beijing, China, 2000.

[78] D.S.Citrin, and T.B.Norris, IEEE J. Sel. Topics. Quant. Electron **2**, 401 (1996).

[79] L.C.Andreani, and A.Pasquarello, Phys. Rev. B, **42** (14), 8928 (1990).

[80] G. Panzarini, L.C.Andreani, A.Armitage, D.Baxter, M.S.Skolnick, V.N.Astratov, J.S.Roberts, A.V.Kavokin, M.R.Vladimirova, and M.A.Kaliteevski, Phys.Rev.B. **59** (7), 5082 (1999).

[81] V.Savona, L.C.Andreani, P.Schwendimann, and A.Quattropani, Sol.Stat.Comm. **93** (9), 733 (1995).

[82] D.I.Babic, and S.W.Corzine, IEEE J.Quantum.Elec. **28** (2), 514 (1992).

[83] K.Ujihara, Jap.J.Appl.Phys. **30** (5B), L901 (1991).

[84] R.P.Stanley, R.Houdré, U.Oesterle, M.Gailhanou, M.Ilegems, Appl.Phys.Lett. **65** (15), 1883 (1994).

[85] Data in Science and Technology, Semiconductors: group IV Elements and III-V Compounds, Editor: O.Madelung, Springer-Verlag Berlin Heidelberg 1991.

[86] V.Savona and F.Tassone, Sol.Stat.Comm. **95** (10), 673 (1995).

[87] M.S.Skolnick, T.A.Fisher, and D.M.Whittaker, Semicond.Sci.Technol. **13**, 645-669 (1998).

[88] C.Weisbuch, M.Nishioka, A.Ishikawa, and Y.Arakawa, Phys.Rev.Lett. **69** (23), 3314 (1992).

[89] H.Cao, S.Jiang, S.Machida, Y.Takiguchi, and Y.Yamamoto, Appl.Phys.Lett. **71** (11), 1461 (1997).

[90] R.P.Stanley, R.Houdré, C.Weisbuch, U.Oesterle, and M.Ilegems, Phys.Rev.B. **53** (16), 10995 (1996).

[91] C.Ell, J.Prineas, T.R.Nelson, Jr., S.Park, H.M.Gibbs, G.Khitrova, S.W.Koch, and R.Houdré, Phys.Rev.Lett. **80** (21), 4795 (1998).

[92] V.Savona, C.Piermarocchi, A.Quattropani, F.Tassone, and P.Schwendimann, Phys.Rev.Lett. **78** (23), 4470 (1997).

[93] D.M.Whittaker, P.Kinsler, T.A.Fisher, M.S.Skolnick, A.Armitage, A.M.Afshar, M.D.Sturge, and J.S.Roberts, Phys.Rev.Lett. **77** (23), 4792 (1996).

[94] D.M.Whittaker, Phys.Rev.Lett. **80** (21), 4791 (1998).

[95] P.Borri, W.Langbein, U.Woggon, J.R.Jensen, and J.M.Hvam, submitted to Phys.Rev.B.

[96] P.Borri, J.R.Jensen, W.Langbein, and J.M.Hvam, Phys.Rev.B, **61** (20), R13377 (2000).

[97] R.Houdré, R.P.Stanley, M.Ilegems, Phys.Rev.A **53** (4), 2711 (1996).

[98] G.Cassabois, A.L.C.Triques, D.Larousserie, C.Delalande, Ph.Roussignol, P.Senellart-Mardon, J.Bloch, V.Thierry-Mieg, and R.Planel, Phys.Rev.B. **59** (16), R10429 (1999).

[99] R.P.Stanley, R.Houdré, U.Oesterle, and M.Ilegems, Sol.Stat.Comm. **106** (8), 485 (1998).

[100] J.R. Jensen, P. Borri, W. Langbein, and J.M. Hvam, Appl. Phys. Lett. **76**, 3262 (2000).

[101] R.Houdré, C.Weisbuch, R.P.Stanley, U.Oesterle, P.Pellandini, and M.Ilegems, Phys.Rev.Lett. **73** (15), 2043 (1994).

[102] V.Savona, and C.Piermarocchi, phys.stat.sol. (a) **164**, 45 (1997).

[103] R.Loudon, "The Quantum Theory of Light", Oxford Science Publications, 2nd Edition, Clarendon Press, Oxford.

[104] H.Stoltz, "Time-Resolved Light Scattering from Excitons", Springer Tracts in Modern Physics, Vol. 130, Springer-Verlag, Berlin Heidelberg 1994.

[105] W.Langbein, J.M.Hvam, and R.Zimmermann, Phys.Rev.Lett., **82** (5), 1040 (1999).

[106] J.R.Jensen, D.Birkedal, and J.M.Hvam, submitted to Phys.Rev.B. rapid comm.

[107] C. Weisbuch, M. Nishioka, A. Ishikawa, and Y. Arakawa, Phys. Rev. Lett. **69**, 3314 (1992).

[108] D.M. Whittaker et al, Phys. Rev. Lett. **77**, 4792 (1996); V. Savona et al, Phys. Rev. Lett, **78**, 4470 (1997); D.M. Whittaker, Phys. Rev. Lett, **80,** 4791 (1998); C. Ell et al, Phys. Rev. Lett. **80**, 4795 (1998).

[109] G.R. Hayes et al, Phys. Rev. B **58**, R10175 (1998).

[110] T. Freixanet et al, Phys. Rev. B. **60**, R8509 (1999).

[111] R. Houdre et al, Phys. Rev. B **61**, R13333 (2000).

[112] D.M. Whittaker, Phys. Rev. B **61**, R2433 (2000).

[113] A.V. Shchegrov, J. Bloch, D. Birkedal, and J. Shah, Phys. Rev. Lett. **84**, 3478 (2000).

[114] D. Birkedal and J. Shah, Phys. Rev. Lett. **81**, 2372 (1998).

[115] J. Bloch and J.Y. Marzin, Phys. Rev. B **56**, 2103 (1997).

[116] B. Sermage et al, Phys. Rev. B **53**, 16516 (1996).

[117] F. Tassone et al, Phys. Rev. B **56**, 7554 (1997).

[118] R.P. Stanley et al, Appl. Phys. Lett. **65**, 1883 (1994).

Appendix 1

Borland C++ code for
"STRAITIFY.CPP"

```
#include <stdio.h>
#include <stdlib.h>
#include <complex.h>
#include <malloc.h>

#define pi 3.14159265359
#define hc 1239.8424  // value of hc for converting nm <-> eV

//
// Structure of inputfile:
// Number_of_layers: x
// Type p1 p2 p3 p4 p5
// x x x x x x
// --
// --
// x x x x x x
// Wavelength_start[nm]: x
// Wavelength_end[nm]: x
// Number_of_points: x
//
// Meaning of parameters:
//           DescriptionType           p1           p2           p3           p4           p5
// Dielec. layer           0           n_real       n_imag       d[nm]        0            0
// Right DBR               1           R_int        E(eV)        d(phi)/dE  n_left  n_right
// Left DBR   2            R_int       E(eV)        d(phi)/dE  n_left  n_right
// Quantum well            3           E_ex         G_rad        G_nonrad     d[nm]        n_back
// Interface  4            n_left      n_right      0            0            0
// Bragg period            5           n_left       n_right      d_left       d_right      0
//
// Waves are propagated from left to right.
//

// structure for defining geometry and materials in dielectric structure.

struct mediumlist
{
  int layers;
  int *typeno;
  double *p1, *p2, *p3, *p4, *p5;
};

// structure for holding the complex refractive index of the structure at
// a given wavelength.

struct optparlist
{
  int layers;
  double *m11_real, *m11_imag,
         *m12_real, *m12_imag,
         *m21_real, *m21_imag,
         *m22_real, *m22_imag;
};

// structure for holding the transfer matrix and reflectivity/transmittivity of
// a layered structure at a given wavelength.

struct optic
{
  struct complex m11,m12,m21,m22;
  struct complex amp_r,amp_t;
  double int_r,int_t;
};

// functions for calculating optical properties
// alloc_memory_mediumlist : allocates dynamic memory for the mediumlist structure
// load_medium : generates/loads the medium geometry/material list
// alloc_memory_optparlist : allocates dynamic memory for the optparlist structure
// calc_medium_n : calculates the layer refractive index at a given wavelength
// calc_medium_o : calculates the optical properties of the whole medium

struct mediumlist *alloc_memory_mediumlist(int n);
struct optparlist *alloc_memory_optparlist(struct mediumlist *);
```

```
void calc_medium_n(struct mediumlist *, struct optparlist *, double wl);
struct optic calc_medium_o(struct optparlist *);

// definition for the function for getting dielectric structure

struct mediumlist *alloc_memory_mediumlist(int n)
{
  struct mediumlist *m;
  if ((m=(struct mediumlist *) malloc(sizeof(struct mediumlist)))==NULL)
  { printf("Memory allocation error!\n"); };
  m->layers=n;
  m->typeno=(int *) malloc(n*sizeof(int));
  m->p1=(double *) malloc(n*sizeof(double));
  m->p2=(double *) malloc(n*sizeof(double));
  m->p3=(double *) malloc(n*sizeof(double));
  m->p4=(double *) malloc(n*sizeof(double));
  m->p5=(double *) malloc(n*sizeof(double));
  return(m);
}

struct optparlist * alloc_memory_optparlist(struct mediumlist * m)
{
  struct optparlist *m_n;
  m_n=(struct optparlist *) malloc(sizeof(struct optparlist));
  m_n->m11_real=(double *) malloc((m->layers-2)*sizeof(double));
  m_n->m11_imag=(double *) malloc((m->layers-2)*sizeof(double));
  m_n->m12_real=(double *) malloc((m->layers-2)*sizeof(double));
  m_n->m12_imag=(double *) malloc((m->layers-2)*sizeof(double));
  m_n->m21_real=(double *) malloc((m->layers-2)*sizeof(double));
  m_n->m21_imag=(double *) malloc((m->layers-2)*sizeof(double));
  m_n->m22_real=(double *) malloc((m->layers-2)*sizeof(double));
  m_n->m22_imag=(double *) malloc((m->layers-2)*sizeof(double));
  return (m_n);
}


void calc_medium_n(struct mediumlist * m, struct optparlist * m_n,double wl)
{
  // Transfer matrix evaluation corresponding to Savona et al. (Sol.Stat.Comm. 93 (9) p.733)
  struct complex iun,d0,t,r;
  double nratio,ph1,ph2,a;
  int i;

  iun=complex(0,1);
  m_n->layers=m->layers-2;
  for(i=0;i<(m_n->layers);i++)
  {
    switch(m->typeno[i+1])
    {
      // dielectric layer
      case 0: t=exp(iun*2*pi*m->p3[i+1]*(m->p1[i+1]+iun*m->p2[i+1])/wl);
              m_n->m11_real[i]=real(t);
              m_n->m11_imag[i]=imag(t);
              m_n->m12_real[i]=0;
              m_n->m12_imag[i]=0;
              m_n->m21_real[i]=0;
              m_n->m21_imag[i]=0;
              t=exp(-iun*2*pi*m->p3[i+1]*(m->p1[i+1]+iun*m->p2[i+1])/wl);
              m_n->m22_real[i]=real(t);
              m_n->m22_imag[i]=imag(t);
              break;
      // right DBR mirror
      case 1: r=sqrt(m->p1[i+1])*exp(iun*m->p3[i+1]*(hc/wl-m->p2[i+1]));
              t=1-r;
              nratio=m->p4[i+1]/m->p5[i+1];
              m_n->m11_real[i]=nratio*real(1/conj(t));
              m_n->m11_imag[i]=nratio*imag(1/conj(t));
              m_n->m12_real[i]=nratio*real(-conj(r/t));
              m_n->m12_imag[i]=nratio*imag(-conj(r/t));
              m_n->m21_real[i]=nratio*real(-r/t);
              m_n->m21_imag[i]=nratio*imag(-r/t);
              m_n->m22_real[i]=nratio*real(1/t);
```

```
            m_n->m22_imag[i]=nratio*imag(1/t);
            break;
      // left DBR mirror
      case 2: r=sqrt(m->p1[i+1])*exp(iun*m->p3[i+1]*(hc/wl-m->p2[i+1]));
            t=1-r;
            nratio=1;
            m_n->m11_real[i]=nratio*real(1/conj(t));
            m_n->m11_imag[i]=nratio*imag(1/conj(t));
            m_n->m12_real[i]=nratio*real(r/t);
            m_n->m12_imag[i]=nratio*imag(r/t);
            m_n->m21_real[i]=nratio*real(conj(r/t));
            m_n->m21_imag[i]=nratio*imag(conj(r/t));
            m_n->m22_real[i]=nratio*real(1/t);
            m_n->m22_imag[i]=nratio*imag(1/t);
            break;
      // quantum well
      case 3: d0=iun*m->p2[i+1]/(hc/wl-m->p1[i+1]+iun*m->p3[i+1]);
            m_n->m11_real[i]=real(exp(iun*2*pi*m->p4[i+1]*m->p5[i+1]/wl)*(1-d0));
            m_n->m11_imag[i]=imag(exp(iun*2*pi*m->p4[i+1]*m->p5[i+1]/wl)*(1-d0));
            m_n->m12_real[i]=real(-d0);
            m_n->m12_imag[i]=imag(-d0);
            m_n->m21_real[i]=real(d0);
            m_n->m21_imag[i]=imag(d0);
            m_n->m22_real[i]=real(exp(-iun*2*pi*m->p4[i+1]*m->p5[i+1]/wl)*(1+d0));
            m_n->m22_imag[i]=imag(exp(-iun*2*pi*m->p4[i+1]*m->p5[i+1]/wl)*(1+d0));
            break;
      // interface
      case 4: m_n->m11_real[i]=0.5*(m->p1[i+1]+m->p2[i+1])/(m->p2[i+1]);
            m_n->m11_imag[i]=0;
            m_n->m12_real[i]=-0.5*(m->p1[i+1]-m->p2[i+1])/(m->p2[i+1]);
            m_n->m12_imag[i]=0;
            m_n->m21_real[i]=-0.5*(m->p1[i+1]-m->p2[i+1])/(m->p2[i+1]);
            m_n->m21_imag[i]=0;
            m_n->m22_real[i]=0.5*(m->p1[i+1]+m->p2[i+1])/(m->p2[i+1]);
            m_n->m22_imag[i]=0;
            break;
      // Bragg period
      case 5: a=m->p2[i+1]/m->p1[i+1];
            ph1=2*pi*m->p1[i+1]*m->p3[i+1]/wl;
            ph2=2*pi*m->p2[i+1]*m->p4[i+1]/wl;
            m_n->m11_real[i]=0.25*(cos(ph1+ph2)*(2+a+1/a)+cos(ph2-ph1)*(2-a-1/a));
            m_n->m11_imag[i]=0.25*(sin(ph1+ph2)*(2+a+1/a)+sin(ph2-ph1)*(2-a-1/a));
            m_n->m12_real[i]=0.25*(cos(ph1+ph2)*(1/a-a)+cos(ph2-ph1)*(a-1/a));
            m_n->m12_imag[i]=0.25*(sin(ph1+ph2)*(1/a-a)+sin(ph2-ph1)*(a-1/a));
            m_n->m21_real[i]=0.25*(cos(ph1+ph2)*(1/a-a)+cos(ph1-ph2)*(a-1/a));
            m_n->m21_imag[i]=0.25*(-sin(ph1+ph2)*(1/a-a)+sin(ph1-ph2)*(a-1/a));
            m_n->m22_real[i]=0.25*(cos(ph1+ph2)*(2+a+1/a)+cos(ph1-ph2)*(2-a-1/a));
            m_n->m22_imag[i]=0.25*(-sin(ph1+ph2)*(2+a+1/a)+sin(ph1-ph2)*(2-a-1/a));
            break;
    }
  };
}

// function for calculating the transfer matrix/reflectance/transmittance of the
// medium at wavelength wl
struct optic calc_medium_o(struct optparlist *m)
{
  struct optic op;
  int i;
  struct complex a11,a12,a21,a22,iun,nc;
  iun=complex(0,1);
  op.m11=1;
  op.m12=0;
  op.m21=0;
  op.m22=1;
  for (i=0;i<=(m->layers-1);i++)
  {
      a11=(m->m11_real[i]+iun*m->m11_imag[i])*op.m11+(m->m12_real[i]+iun*m->m12_imag[i])*op.m21;
      a12=(m->m11_real[i]+iun*m->m11_imag[i])*op.m12+(m->m12_real[i]+iun*m->m12_imag[i])*op.m22;
      a21=(m->m21_real[i]+iun*m->m21_imag[i])*op.m11+(m->m22_real[i]+iun*m->m22_imag[i])*op.m21;
      a22=(m->m21_real[i]+iun*m->m21_imag[i])*op.m12+(m->m22_real[i]+iun*m->m22_imag[i])*op.m22;
      op.m11=a11;
```

```
      op.m12=a12;
      op.m21=a21;
      op.m22=a22;
  };
  op.amp_r=-op.m21/op.m22;
  op.amp_t=(op.m11*op.m22-op.m12*op.m21)/op.m22;
  op.int_r=abs(op.amp_r)*abs(op.amp_r);
  op.int_t=abs(op.amp_t)*abs(op.amp_t);
  return op;
}

// main program

void main(int argc, char *argv[])
{
  struct mediumlist * mucav;
  struct optparlist * mucav_n;
  struct optic muopt;
  char str[20];
  // struct field mufield;
  int i,j,no,nop,ns;
  double wl1,wl2,wl,d1,d2,d3,d4,d5,phasr,phast,l;
  struct complex prei,ei,preo,eo,iun;
  FILE *fout,*fin;

  iun=complex(0,1);

  if (argc!=2)
  {
    printf("Wrong number of input parameters\n");
    exit(1);
  };

  strcpy(str,argv[1]);
  strcat(str,".map");
  if ((fin=fopen(str,"r"))==NULL)
  {
    printf("Cannot open input file\n");
    exit(1);
  };
  printf("Opening file %s\n",str);
  fscanf(fin,"Number_of_layers: %d\n",&no);
  printf("Number of layers: %d\n",no);
  mucav=alloc_memory_mediumlist(no+2);
  mucav->layers=no+2;
  fscanf(fin,"Type p1 p2 p3 p4 p5\n");
  for (i=1;i<=no;i++)
  {
     fscanf(fin,"%d %lf %lf %lf %lf %lf\n",&mucav->typeno[i],&d1,&d2,&d3,&d4,&d5);
     mucav->p1[i]=d1;
     mucav->p2[i]=d2;
     mucav->p3[i]=d3;
     mucav->p4[i]=d4;
     mucav->p5[i]=d5;
  };
  fscanf(fin,"Wavelength_start[nm]: %lf\n",&wl1);
  fscanf(fin,"Wavelength_end[nm]: %lf\n",&wl2);
  fscanf(fin,"Number_of_points: %d\n",&nop);
  fclose(fin);
  for (i=1;i<(mucav->layers-1);i++)
  {
    printf("%d %f %f %f %f %f\n",mucav->typeno[i],mucav->p1[i],
    mucav->p2[i],mucav->p3[i],mucav->p4[i],mucav->p5[i]);
  };
  printf("WL: %f - %f in %d points\n",wl1,wl2,nop);

  switch (nop)
  // If number of points to be calculated are 1, the total field in the structure
  // is calculated instead, at the start wavelength
  {
    case 1: strcpy(str,argv[1]);
    strcat(str,".fld");
```

```
    printf("%s\n",str);
    if ((fout=fopen(str,"w"))==NULL)
    {
      printf("Error opening file!\n");
    };
    ei=complex(0.0,0.0);
    eo=complex(1.0,0.0);
    l=0;
    for (i=1;i<=no;i++)
    {
      switch (mucav->typeno[i])
      {
        // case of dielectric layer
        case 0: ns=(int) 40*mucav->p3[i]*mucav->p1[i]/wl1+1;
        fprintf(fout,"%lf %lf %lf %lf %lf %lf\n",l,mucav->p1[i],real(ei),imag(ei),real(eo),imag(eo));
        for (j=1;j<=ns;j++)
        {
          ei=exp(iun*2*pi*(mucav->p1[i]+iun*mucav->p2[i])/wl1*mucav->p3[i]/ns)*ei;
          eo=exp(-iun*2*pi*(mucav->p1[i]+iun*mucav->p2[i])/wl1*mucav->p3[i]/ns)*eo;
          l=l+mucav->p3[i]/ns;
          fprintf(fout,"%lf %lf %lf %lf %lf %lf\n",l,mucav->p1[i],real(ei),imag(ei),real(eo),imag(eo));
        };
        break;
        // case of interface
        case 4: prei=ei;
        preo=eo;
        ei=0.5*(1+(mucav->p1[i])/(mucav->p2[i]))*prei+0.5*(1-(mucav->p1[i])/(mucav->p2[i]))*preo;
        eo=0.5*(1-(mucav->p1[i])/(mucav->p2[i]))*prei+0.5*(1+(mucav->p1[i])/(mucav->p2[i]))*preo;
        fprintf(fout,"%lf %lf %lf %lf %lf %lf\n",l,0.0,real(ei),imag(ei),real(eo),imag(eo));
        break;
      };
    };
    fclose(fout);
    break;
    // if number of points are greater than 1, this part is carried out
    default: mucav_n=alloc_memory_optparlist(mucav);
    strcpy(str,argv[1]);
    strcat(str,".out");
    printf("%s\n",str);
    if ((fout=fopen(str,"w"))==NULL)
    {
      printf("Error opening file!\n");
    };
    for (i=1;i<=nop;i++)
    {
      wl=wl1+(wl2-wl1)*(i-1)/(nop-1);
      calc_medium_n(mucav,mucav_n,wl);
      muopt=calc_medium_o(mucav_n);
      printf("%5d\r",i);
      phasr=arg(muopt.amp_r);
      phast=arg(muopt.amp_t);
      if (phasr>0.5*pi) phasr=phasr-pi;
      if (phasr<-0.5*pi) phasr=phasr+pi;
      if (phast>0.5*pi) phast=phast-pi;
      if (phast<-0.5*pi) phast=phast+pi;
      fprintf(fout,"%12.8lf %12.8lf %12.8lf %12.8lf %12.8lf %12.8lf\n",hc/wl,wl,
      abs(muopt.amp_r),phasr,abs(muopt.amp_t),phast);
    };
    fclose(fout);
  }

}
```

Appendix 2

Borland C++ code for
project SEGSIM.IDE
with programs
"SEGSIM.H"
"SEGSIM.CPP"
"SEG_FUNC.CPP"

SEGSIM.H

```
#define a0 2.827
/*
#define E1 3133.2   // 0.27eV divided by k (Al-In system) //
#define E2 1972.8   // 0.17eV divided by k (Ga-In system) //
#define E3 1160.4   // 0.10eV divided by k (Al-Ga system) //
*/
#define JGaAs 8974  // J(GaAs)*Ang^3/k //
#define JAlAs 8916  // J(AlAs)*Ang^3/k //
#define JInAs 5744  // J(InAs)*Ang^3/k //
#define latGaAs 5.6533 // GaAs lattice constant in Angstrom //
#define latAlAs 5.660  // AlAs lattice constant in Angstrom //
#define latInAs 6.0583 // InAs lattice constant in Angstrom //

// definition of structures for input and output files //

struct growth_parameters
{
  int step_no;
  double *ga_growth, *al_growth, *in_growth, *shutter_time, *sub_temp;
};

struct monolayer_map
{
  int monolayer_no;
  double thick,Es1,Es2,Es3;
  double *gamole_nom, *almole_nom, *inmole_nom,
         *gamole_seg, *almole_seg, *inmole_seg, *sub_temp;
};

struct surf_bulk_molefrac
{
  double xs,xb,ys,yb;
};

struct surf_bulk_molefrac3
{
  double xs,xb,ys,yb,zs,zb;
};

struct filelist
{
  int no_energies;
  double *Es1, *Es2, *Es3;
  int no_files;
  char *filename[80];
};

// definition of functions used by segsim.cpp //

struct growth_parameters* load_growth_parameters(char *fname);
struct filelist * load_file_list(char *fname);
void seg_simul(struct surf_bulk_molefrac * p, double expon, double lat,
double mis, double J, double dJ);
void seg_simul3(struct surf_bulk_molefrac3 * p, double temp,double Es2,
double Es3);
void save_growth_sim(struct monolayer_map *p, char *fname);
void generate_output(struct monolayer_map *p, char *fname);
struct monolayer_map * growth_simul(struct growth_parameters * pin, double Es1,
double Es2,double Es3);
double * dvector(int nl, int nh);
void free_dvector(double * v, int nl, int nh);
void free_growth_parameters(struct growth_parameters *p);
void free_monolayer_map(struct monolayer_map * p);
void free_filelist(struct filelist *p);
```

SEGSIM.CPP

```
#include <stdio.h>
#include <stdlib>
#include <math.h>
#include <segsim.h>

main(int argc, char **argv)
{
  struct growth_parameters * sample_input;
  struct monolayer_map * sample_output;
  struct filelist * files;
  char str[80];
  int i,j;

  // test if the right number of input files have been specified //

  if (argc==1) {printf("\nNo input file specified!\n"); exit(0);}
  if (argc>2) {printf("\nToo many input files specified!\n"); exit(0);}
  if (argc==2) printf("\nSpecified input file : %s\n",argv[1]);

  files=load_file_list(argv[1]);

  for (i=1;i<=files->no_files;i++)
  {

    for (j=1;j<=files->no_energies;j++)
    {

      // load data from input file //

      sample_input=load_growth_parameters(files->filename[i]);
      printf("Growth recipy succesfully loaded!\n");


      // perform the growth simulation //

      sample_output=growth_simul(sample_input,files->Es1[j],files->Es2[j],
      files->Es3[j]);
      printf("Nominal molefractions succesfully calculated\n");

      // save the results of the growth simulation //

      sprintf(str,"%s%d",files->filename[i],j);
      save_growth_sim(sample_output,str);
      generate_output(sample_output,str);
      printf("Results saved\n\n");

      // free the memory used by the input and output structures //

      free_monolayer_map(sample_output);
      free_growth_parameters(sample_input);
    }
  }

  free_filelist(files);
  return(0);
}
```

SEG_FUNC.CPP

```
#include <stdio.h>
#include <stdlib.h>
#include <math.h>
#include <segsim.h>

struct monolayer_map * growth_simul(growth_parameters * pin,double Es1,
double Es2,double Es3)
{
  double tot_growth,x,y,z,rest=0,rest2=0,thickness=0,x0,y0,z0;
  int monolayers,i,j,k=1,layer,diskr;
  struct monolayer_map * p;
  struct surf_bulk_molefrac *top;
  struct surf_bulk_molefrac3 *top3;

  // allocate memory for monolayer_map output //

  if ((p=(monolayer_map *) malloc(sizeof(struct monolayer_map)))==NULL)
  {printf("Memory error!\n"); exit(0);}

  // calculate total thickness of the structure, and //
  // the corresponing number of monolayers //

  for (i=1;i<=(pin->step_no);i++)
  thickness+=pin->shutter_time[i]*((pin->ga_growth[i])+(pin->al_growth[i])+
  (pin->in_growth[i]));
  monolayers=floor(thickness/a0)+1;

  // allocate memory for monolayer_map //

  p->monolayer_no=monolayers;
  p->thick=thickness;
  p->Es1=Es1;
  p->Es2=Es2;
  p->Es3=Es3;
  p->gamole_nom=dvector(1,monolayers);
  p->almole_nom=dvector(1,monolayers);
  p->inmole_nom=dvector(1,monolayers);
  p->gamole_seg=dvector(1,monolayers);
  p->almole_seg=dvector(1,monolayers);
  p->inmole_seg=dvector(1,monolayers);
  p->sub_temp=dvector(1,monolayers);

  // step through growth recipy, and generate monolayer_map //
  // i: recipy step number, k:monolayer number              //
  // x,y,z : Ga,Al,In molefractions of growth step          //

  for (i=1;i<=(pin->step_no);i++)
  {
    // total growth rate and nominal molefractions during the i'th step //

    tot_growth=(pin->ga_growth[i])+(pin->al_growth[i])+(pin->in_growth[i]);
    x=(pin->ga_growth[i])/tot_growth;
    y=(pin->al_growth[i])/tot_growth;
    z=(pin->in_growth[i])/tot_growth;

    // if the previously grown atomic layer was not full, add the rest to //
    // layer from the i'th growth step, and adjust shutter_time for this  //
    // step //

    // case 1 : the i'th growth step CANNOT complete the monolayer //

    if ((rest>0) && (pin->shutter_time[i]*tot_growth<a0*rest))
    {
      rest2=pin->shutter_time[i]*tot_growth/a0;
      p->gamole_nom[k]+=rest2*x;
      p->almole_nom[k]+=rest2*y;
      p->inmole_nom[k]+=rest2*z;
      p->sub_temp[k]+=rest2*pin->sub_temp[i];
      pin->shutter_time[i]=0;
      rest-=rest2;
```

```
  }

  // case 2 : the i'th growth step CAN complete the monolayer //

  if ((rest>0) && (pin->shutter_time[i]*tot_growth>=a0*rest))
  {
    pin->shutter_time[i]=pin->shutter_time[i]-rest*a0/tot_growth;
    p->gamole_nom[k]+=rest*x;
    p->almole_nom[k]+=rest*y;
    p->inmole_nom[k]+=rest*z;
    p->sub_temp[k]+=rest*pin->sub_temp[i];
    k++;
  }

  // calculate the number of full monolayers grown in the i'th step, and //
  // add them to the monolayer map //

  layer=floor((pin->shutter_time[i])*tot_growth/a0);
  for (j=1;j<=layer;j++)
  {
    p->gamole_nom[k]=x;
    p->almole_nom[k]=y;
    p->inmole_nom[k]=z;
    p->sub_temp[k]=pin->sub_temp[i];
    pin->shutter_time[i]-=a0/tot_growth;
    k++;
  }

  // add initiated (but not completed) layer to the monolayer map //

  rest=0;
  if (pin->shutter_time[i]*tot_growth/a0>1e-3)
  {
    rest=(pin->shutter_time[i])*tot_growth/a0;
    p->gamole_nom[k]=rest*x;
    p->almole_nom[k]=rest*y;
    p->inmole_nom[k]=rest*z;
    p->sub_temp[k]=rest*pin->sub_temp[i];
    rest=1-rest;
  }
}

for(k=1;k<=monolayers;k++)
{
  if (p->gamole_nom[k]<=1e-4) p->gamole_nom[k]=0;
  if (p->almole_nom[k]<=1e-4) p->almole_nom[k]=0;
  if (p->inmole_nom[k]<=1e-4) p->inmole_nom[k]=0;
  p->gamole_seg[k]=p->gamole_nom[k];
  p->almole_seg[k]=p->almole_nom[k];
  p->inmole_seg[k]=p->inmole_nom[k];
}
// allocate memory for top variable //

if ((top=(surf_bulk_molefrac *) malloc(sizeof(struct surf_bulk_molefrac)))==NULL)
{printf("Memory error!\n"); exit(0);}

if ((top3=(surf_bulk_molefrac3 *) malloc(sizeof(struct surf_bulk_molefrac3)))==NULL)
{printf("Memory error!\n"); exit(0);}

for(k=2;k<=(monolayers-1);k++)
{
  x0=(p->gamole_seg[k-1])+(p->gamole_seg[k]);
  y0=(p->almole_seg[k-1])+(p->almole_seg[k]);
  z0=(p->inmole_seg[k-1])+(p->inmole_seg[k]);
  diskr=(z0!=0)+2*(y0!=0)+4*(x0!=0);
  switch(diskr)
  {
    case 0 : printf("Error in monolayer map - empty layers\n");
             exit(0);
    case 1 : break;
    case 2 : break;
    case 4 : break;
```

```
      case 3 : top->xs=p->almole_seg[k];
                                       top->xb=p->almole_seg[k-1];
               top->ys=p->inmole_seg[k];
               top->yb=p->inmole_seg[k-1];
               seg_simul(top,(double) (Es1/(p->sub_temp[k])),
               latAlAs, (latAlAs-latInAs)/latAlAs, JAlAs/(p->sub_temp[k]),
               (JInAs-JAlAs)/(p->sub_temp[k]));
               p->almole_seg[k]=top->xs;
               p->almole_seg[k-1]=top->xb;
               p->inmole_seg[k]=top->ys;
               p->inmole_seg[k-1]=top->yb;
               break;
      case 5 : top->xs=p->gamole_seg[k];
                                       top->xb=p->gamole_seg[k-1];
               top->ys=p->inmole_seg[k];
               top->yb=p->inmole_seg[k-1];
               seg_simul(top,(double) (Es2/(p->sub_temp[k])),
               latGaAs, (latGaAs-latInAs)/latGaAs, JGaAs/(p->sub_temp[k]),
               (JInAs-JGaAs)/(p->sub_temp[k]));
               p->gamole_seg[k]=top->xs;
               p->gamole_seg[k-1]=top->xb;
               p->inmole_seg[k]=top->ys;
               p->inmole_seg[k-1]=top->yb;
               break;
      case 6 : top->xs=p->almole_seg[k];
                                       top->xb=p->almole_seg[k-1];
               top->ys=p->gamole_seg[k];
               top->yb=p->gamole_seg[k-1];
               seg_simul(top,(double) (Es3/(p->sub_temp[k])),
               latAlAs, (latGaAs-latAlAs)/latAlAs, JAlAs/(p->sub_temp[k]),
               (JGaAs-JAlAs)/(p->sub_temp[k]));
               p->almole_seg[k]=top->xs;
               p->almole_seg[k-1]=top->xb;
               p->gamole_seg[k]=top->ys;
               p->gamole_seg[k-1]=top->yb;
               break;
      case 7 : top3->xs=p->inmole_seg[k];
               top3->xb=p->inmole_seg[k-1];
               top3->ys=p->almole_seg[k];
               top3->yb=p->almole_seg[k-1];
               top3->zs=p->gamole_seg[k];
               top3->zb=p->gamole_seg[k-1];
               seg_simul3(top3,p->sub_temp[k],Es2,Es3);
               p->inmole_seg[k]=top3->xs;
               p->inmole_seg[k-1]=top3->xb;
               p->almole_seg[k]=top3->ys;
               p->almole_seg[k-1]=top3->yb;
               p->gamole_seg[k]=top3->zs;
               p->gamole_seg[k-1]=top3->zb;
               break;
    }
  }

  free(top);
  free(top3);
  return(p);
}

void seg_simul(struct surf_bulk_molefrac * m, double expon, double lat,
double mis, double J, double dJ)
{
  double xtot,ytot,c1,a,b,c,d,ys,dys;
  xtot=(m->xs)+(m->xb);
  ytot=(m->ys)+(m->yb);
  d=lat*lat*lat*mis*mis*(J+1.5*dJ*ytot);
  ys=(m->ys);
  dys=1;
  while (dys*dys>1e-20)
  {
    c1=exp(expon)*exp(0.5*d*ytot)*exp(-d*ys);
    a=1-c1;
    b=1-ytot+c1*(1+ytot);
```

```
    c=-c1*ytot;
    dys=(a*ys*ys+b*ys+c)/(2*a*ys+b+d*c1*ys*ys-d*c1*(1+ytot)*ys+d*c1*ytot);
    ys-=dys;
    if ((ys>1) || (ys<0)) {printf("ys out of bounds : %lf - exiting",ys); exit(0);}
  }
  m->ys=ys;
  m->yb=ytot-(m->ys);
  m->xs=1-(m->ys);
  m->xb=xtot-(m->xs);
}

void seg_simul3(struct surf_bulk_molefrac3 * p, double temp,double Es2,double Es3)
{
  double c1,c2,d1,xtot,ytot,ztot,xs,zs,fx,fz,gx,gz,f,g,dxs=1,dzs=1;
  xs=p->xs;
  zs=p->zs;
  xtot=(p->xs)+(p->xb);
  ytot=(p->ys)+(p->yb);
  ztot=(p->zs)+(p->zb);
  while ((dxs*dxs+dzs*dzs)>1e-20)
  {
    d1=latGaAs*(latGaAs-latInAs)*(latGaAs-latInAs)*
    (JGaAs+1.5*(JInAs-JGaAs)*xtot)/temp;
    c1=exp(Es2/temp)*exp(-d1*(xs-0.5*xtot));
    c2=exp(Es3/temp);
    fx=(c1-1)*zs+ztot-d1*c1*xs*zs+d1*c1*xtot*zs;
    fz=(c1-1)*xs-c1*xtot;
    gx=(1-c2)*zs+ztot*c2;
    gz=2*(1-c2)*zs+(ytot-1+c2+c2*ztot)+(1-c2)*xs;
    f=(c1-1)*xs*zs+ztot*xs-c1*xtot*zs;
    g=(1-c2)*zs*zs+(ytot-1+c2+c2*ztot)*zs+(1-c2)*xs*zs+ztot*c2*xs-c2*ztot;
    dxs=(f*gz-g*fz)/(fx*gz-gx*fz);
    dzs=(g*fx-f*gx)/(fx*gz-gx*fz);
    xs-=dxs;
    zs-=dzs;
  }
  p->xs=xs;
  p->zs=zs;
  p->ys=1-xs-zs;
  p->xb=xtot-xs;
  p->zb=ztot-zs;
  p->yb=ytot-1+xs+zs;
}

struct filelist * load_file_list(char *fname)
{
  int i;
  char str[80];
  FILE *fp;
  struct filelist *p;

  // generate file name, and open file if possible //

  sprintf(str,"%s.com",fname);
  printf("Reading command file %s\n",str);
  if ((fp=fopen(str,"rt"))==NULL) {printf("Can't open file!"); exit(0);}

  // allocate memory for the pointer to the input structure //

  if ((p=(filelist *) malloc(sizeof(struct filelist)))==NULL)
  {printf("Memory error!"); exit(0);}

  // get number of segregation energies in file //

  if (fscanf(fp,"Number_of_energies %d\nEs1    Es2    Es3\n",&(p->no_energies))!=1)
  {printf("Wrong number of energies!"); exit(0);}
  printf("Number of energies : %d\n",p->no_energies);

  p->Es1 = dvector(1,p->no_energies);
  p->Es2 = dvector(1,p->no_energies);
  p->Es3 = dvector(1,p->no_energies);
```

```
  for (i=1;i<=p->no_energies;i++)
  {
    if (fscanf(fp,"%lf %lf %lf\n",&(p->Es1[i]),&(p->Es2[i]),&(p->Es3[i]))!=3)
    {printf("Error reading energies"); exit(0);}
    printf("Es1: %lf  Es2: %lf  Es3: %lf\n",p->Es1[i],p->Es2[i],p->Es3[i]);
  }

  // get number of filenames in command file //

  if (fscanf(fp,"Number_of_files %d\n",&(p->no_files))!=1)
  {printf("Wrong number of files!"); exit(0);}
  printf("Number of files : %d\n",p->no_files);

  for (i=1;i<=p->no_files;i++)
  {
    if ((p->filename[i]=(char *) malloc(81*sizeof(char)))==NULL)
    {printf("Error assigning memory for filename list!"); exit(0);}
    if (fscanf(fp,"%s\n",p->filename[i])!=1)
    {printf("Error reading file names\n"); exit(0);}
    printf("Filename no %d : %s\n",i,p->filename[i]);
  }
  fclose(fp);
  return(p);
}


struct growth_parameters * load_growth_parameters(char *fname)
{
  int i;
  char str[80];
  FILE *fp;
  struct growth_parameters *p;

  // generate file name, and open file if possible //

  sprintf(str,"%s.grw",fname);
  printf("Reading parameter file %s\n",str);
  if ((fp=fopen(str,"rt"))==NULL) {printf("Can't open file!"); exit(0);}

  // allocate memory for the pointer to the input structure //

  if ((p=(growth_parameters *) malloc(sizeof(struct growth_parameters)))==NULL)
  {printf("Memory error!"); exit(0);}

  // get number of steps in growth recipy //

  if (fscanf(fp,"Number_of_steps %d\n",&(p->step_no))!=1)
  {printf("Wrong number of steps!"); exit(0);}

  // allocate memory for arrays of growth rates, shutter opening times, and //
  // substrate temperature. //

  p->ga_growth = dvector(1,p->step_no);
  p->al_growth = dvector(1,p->step_no);
  p->in_growth = dvector(1,p->step_no);
  p->shutter_time = dvector(1,p->step_no);
  p->sub_temp=dvector(1,p->step_no);

  // scan file for growth parameters, and read them  //

  if (fscanf(fp,"Structure_parameters\nGa[ang/s] Al[ang/s] In[ang/s] Time[s] Temp[K]\n")!=0)
  { printf("Error in structure parameters!"); exit(0); }
  for (i=1;i<=(p->step_no);i++)
  {
    if (fscanf(fp,"%lf %lf %lf %lf %lf\n",&(p->ga_growth[i]),&(p->al_growth[i]),
    &(p->in_growth[i]),&(p->shutter_time[i]),&(p->sub_temp[i]))!=5)
    { printf("Error in structure parameter values!"); exit(0); }
  }
  fclose(fp);

  return(p);
}
```

```
void save_growth_sim(struct monolayer_map *p, char *fname)
{
  int i;
  char str[80];
  FILE *fp;

  // generate output file name, and open file //

  sprintf(str,"%s.out",fname);
  if ((fp=fopen(str,"w"))==NULL)
  { printf("\nCan't open output file\n"); exit(0); }

  // write number of monolayers, total thickness and nominal molefraction //
  // of each monolayer //

  fprintf(fp,"Number of monolayers in structure : %d\n",p->monolayer_no);
  fprintf(fp,"Thickness of structute : %lf[Ang]\n\n",p->thick);
  fprintf(fp,"Energies of segregation: Es1=%lf Es2=%lf Es3=%lf\n",p->Es1,p->Es2,p->Es3);
  fprintf(fp,"Molefraction of group III elements in structure:\n");
  fprintf(fp,"Monolayer  Nominal molefractions:        Simulated molefractions:  Temperature[K]:\n");
  fprintf(fp,"---------  ----------------------        ------------------------  ---------------\n");
  fprintf(fp,"           Ga       Al       In          Ga       Al       In\n");
  for (i=1;i<=((p->monolayer_no)-1);i++)
  fprintf(fp,"%4d       %lf %lf %lf    %lf %lf %lf    %lf\n",i,p->gamole_nom[i],
  p->almole_nom[i],p->inmole_nom[i],p->gamole_seg[i],p->almole_seg[i],
  p->inmole_seg[i],p->sub_temp[i]);

  fclose(fp);
}

void generate_output(struct monolayer_map *p, char *fname)
{
  int ok,i,numdigmon=0,monolay_left,monolay_step,monolay_number;
  double derivga,derival,derivin,slopega,slopeal,slopein,accga,accal,accin;
  char str[80];
  FILE *fp;

  // generate output file name, and open file //

  sprintf(str,"%s.tpm",fname);

  if ((fp=fopen(str,"w"))==NULL)
  { printf("\nCan't open output file\n"); exit(0); }

  // generate parameters for calculation details

  fprintf(fp,"number_of_points                  128\n");
  fprintf(fp,"number_of_trialstates[cbg,cbx,vb] 2  0 16\n");
  fprintf(fp,"number_of_eigenstates[cbg,cbx,vb] 1  0 3\n");
  fprintf(fp,"lattice_constant[nm]              0.5653\n");
  fprintf(fp,"growth_direction                  0 0 1\n");
  fprintf(fp,"in_plane_direction                1 -1 0\n");
  fprintf(fp,"number_of_momentum_steps          1 1 1\n");
  fprintf(fp,"superlattice_momentum[1/cm]       0e6 0e6 0e6\n");
  fprintf(fp,"momentum_symmetry                 s s s\n");
  fprintf(fp,"structure_inv_symmetry            s\n");


  monolay_left=p->monolayer_no-10;
  monolay_number=1;

  // repeat the following until there are no monolayers left

  while (monolay_left>0)
  {
    // set step size to 8 initially
    monolay_step=40;
    // if step size is greater than remaining number of steps, decrease
    if (monolay_step>monolay_left) {monolay_step=monolay_left;}
    ok=0;
    // repeat the following until step size is 1 monolayer or step size is OK
```

```
    while ((ok!=1) && (monolay_step>1))
    {
      derivga=0;
      derival=0;
      derivin=0;
      // calculate average slope of full step
      slopega=0;
      slopeal=0;
      slopein=0;
      // find largest slope between neighbouring layers
      for (i=monolay_number;i<monolay_number+monolay_step-1;i++)
      {
        slopega=max(slopega,fabs(p->gamole_seg[monolay_number]-p->gamole_seg[i+1]));
        slopeal=max(slopeal,fabs(p->almole_seg[monolay_number]-p->almole_seg[i+1]));
        slopein=max(slopein,fabs(p->inmole_seg[monolay_number]-p->inmole_seg[i+1]));
        derivga=max(derivga,
        fabs(p->gamole_seg[i]-p->gamole_seg[i+1]));
        derival=max(derival,
        fabs(p->almole_seg[i]-p->almole_seg[i+1]));
        derivin=max(derivin,
        fabs(p->inmole_seg[i]-p->inmole_seg[i+1]));
      }
      // if all slopes are less than 2% step size is OK, otherwise reduce step size
      if ((derivga>0.01) || (derival>0.01) || (derivin>0.01) || (slopega>0.01) ||
      (slopeal>0.01) || (slopein>0.01)) {monolay_step-=1;} else {ok=1;}
    }
    accga=0;
    accal=0;
    accin=0;
    // get average Ga/Al/In molefractions in step
    for (i=monolay_number;i<monolay_number+monolay_step;i++)
    {
      accga+=p->gamole_seg[i];
      accal+=p->almole_seg[i];
      accin+=p->inmole_seg[i];
    }
    monolay_number+=monolay_step;
    monolay_left-=monolay_step;
    numdigmon++;
    p->gamole_seg[numdigmon]=accga;
    p->almole_seg[numdigmon]=accal;
    p->inmole_seg[numdigmon]=accin;
  }
  // write layers into output file
  fprintf(fp,"number_of_layers             %d\n",numdigmon);
  fprintf(fp,"number_of_elements[c,a]      3  1\n");
  fprintf(fp,"cation_element_names         Ga  Al  In\n");
  fprintf(fp,"anion_element_names          As\n");
  fprintf(fp,"material_file_name           mat_par.dat\n");
  for (i=1;i<=numdigmon;i++)
  {
    accga=p->gamole_seg[i]+p->almole_seg[i]+p->inmole_seg[i];
    fprintf(fp,"structure_layer\n");
    fprintf(fp,"   length[nm]              %5.3lf\n",accga*0.283);
    fprintf(fp,"   cation_composition      %5.3lf %5.3lf %5.3lf\n",
    p->gamole_seg[i]/accga,p->almole_seg[i]/accga,p->inmole_seg[i]/accga);
    fprintf(fp,"   anion_composition       1\n");
  }
  // write end of output file
  fprintf(fp,"refractive_index           3.5\n");
  fprintf(fp,"energy_range_cb_gamma[eV]  1.5  1.8\n");
  fprintf(fp,"energy_steps_cb_gamma      0\n");
  fprintf(fp,"energy_range_cb_x[eV]      1.7  2.0\n");
  fprintf(fp,"energy_steps_cb_x          0\n");
  fprintf(fp,"energy_range_vb[eV]        -0.2 0.0\n");
  fprintf(fp,"energy_steps_vb            0\n");

  fclose(fp);
}


double * dvector(int nl, int nh)
```

```
{
  double * v;

  v=(double *) malloc((int) (nh-nl+1)*sizeof(double));
  if (!v) {printf("Allocation error in dvector()"); exit(0);}
  return v-nl;
}

void free_dvector(double * v, int nl, int nh)
{
  free((char *) (v+nl));
}

void free_growth_parameters(struct growth_parameters *p)
{
  free_dvector(p->ga_growth,1,p->step_no);
  free_dvector(p->al_growth,1,p->step_no);
  free_dvector(p->in_growth,1,p->step_no);
  free_dvector(p->shutter_time,1,p->step_no);
  free_dvector(p->sub_temp,1,p->step_no);
  free(p);
}

void free_monolayer_map(struct monolayer_map * p)
{
  free_dvector(p->gamole_nom,1,p->monolayer_no);
  free_dvector(p->almole_nom,1,p->monolayer_no);
  free_dvector(p->inmole_nom,1,p->monolayer_no);
  free_dvector(p->gamole_seg,1,p->monolayer_no);
  free_dvector(p->almole_seg,1,p->monolayer_no);
  free_dvector(p->inmole_seg,1,p->monolayer_no);
  free_dvector(p->sub_temp,1,p->monolayer_no);
  free(p);
}

void free_filelist(struct filelist *p)
{
  int i;
  free_dvector(p->Es1,1,p->no_energies);
  free_dvector(p->Es2,1,p->no_energies);
  free_dvector(p->Es3,1,p->no_energies);
  for (i=1;i<=p->no_files;i++)
  {
    free(p->filename[i]);
  }
  free(p);
}
```

Publications

Optical properties of InAlGaAs quantum wells: Influence of segregation and band bowing

J. R. Jensen[a] and J. M. Hvam
Mikroelektronik Centret, The Technical University of Denmark, Building 345 East, DK-2800 Lyngby, Denmark

W. Langbein
Experimentelle Physik EIIb, Universität Dortmund, Otto-Hahn Str.4, 44221 Dortmund, Germany

(Received 16 March 1999; accepted for publication 19 May 1999)

Knowledge of the quaternary InAlGaAs material system is very limited for the composition range relevant for growth on GaAs substrates. We report on the characterization and modeling of InAlGaAs quantum wells with AlGaAs barriers, grown pseudomorphically on a GaAs substrate with molecular beam epitaxy. The quantum wells are characterized with photoluminescence, and the measured transition energies are modeled taking into account the influence of In segregation on the shape of the well potential. From the modeling we deduce a relation for the low temperature band gap of unstrained $In_x(Al_yGa_{1-y})_{1-x}As$, for $0 \leqslant x,y \leqslant 0.20$. The measured linewidths of the luminescence peaks are in agreement with the broadening expected from random alloy fluctuations and well width fluctuations with an effective interface roughness of 1.1 ML. © *1999 American Institute of Physics.* [S0021-8979(99)00617-9]

I. INTRODUCTION

The ability to fabricate ternary and quaternary alloys of III-V semiconductors is of fundamental importance for applications in electronics and optoelectronics. Varying the alloy composition is the handle used to optimize the band gap, the effective masses, or the strain in a heterostructure layer.

Previously, different composition regions of the InAlGaAs material system have been studied in great detail. Especially the ternary subsystems of AlGaAs and InGaAs grown on GaAs are well characterized, due to their applications for devices in the wavelength range of 750–1000 nm. Also, band gap relations and effective masses for the quaternary InAlGaAs alloys, lattice matched to InP substrates, have been investigated,[1–8] since here the band gap range covers the important wavelengths around 1.55 μm for optical communication. However, little has been reported for InAlGaAs grown on GaAs substrates. This material system is important for low threshold multiple quantum well lasers at wavelengths shorter than 860 nm,[9,10] and for growth of certain self-organized quantum dot structures.[11] We also believe that the large flexibility of this system with respect to band gap and strain will prove useful for future designs of low-dimensional structures, e.g., realized by growth on cleaved edges.

For the properties of InAlGaAs on GaAs, two effects are especially important. First, due to the 7% lattice mismatch between InAs and AlGaAs, it is only possible to grow a few nanometers of pseudomorphic material. For a given In content there is a critical thickness above which misfit dislocations are formed in the InAlGaAs layer, and since AlAs has almost the same lattice constant as GaAs the critical thickness is expected to depend on the In mole fraction as in InGaAs.[12,13] For the relevant In contents from 0.05 to 0.20, the critical thickness ranges from several tens of nanometers to approximately 10 nm, which means that quantum confinement effects are inevitable in pseudomorphic InAlGaAs layers, except for the lowest In mole fractions. Second, it has been shown that In tends to surface segregate during growth,[14] smearing out the nominally sharp interfaces between a quantum well and its barriers. This leads to a blueshift of the transition energies compared to a perfectly square quantum well.[15] Therefore, in order to perform a physically meaningful analysis of InAlGaAs quantum well transition energies and deduce a band gap relation for the bulk material, it is necessary to prepare samples in a way that allows the effects of segregation and quantum confinement to be determined independently.

II. GROWTH OF STRUCTURES

The measurements described in the following were made on three samples, referred to as S1, S2, and S3, grown by molecular beam epitaxy (MBE) on undoped (100) GaAs substrates. S1 contains eight $In_xGa_{1-x}As/GaAs$ quantum wells of different nominal thicknesses and with a constant nominal In mole fraction of 0.10. S2 contains six $In_xGa_{1-x}As/GaAs$ quantum wells with a constant thickness of 5 nm, and In mole fractions varying from 0.05 to 0.30. Finally, S3 contains five $In_x(Al_{0.17}Ga_{0.83})_{1-x}As/Al_{0.17}Ga_{0.83}As$ quantum wells with constant thicknesses of 8 nm and In mole fractions varying from 0.05 to 0.25. The ratio of the Al to Ga mole fraction was kept constant during the growth of S3. In the following the five quantum wells in S3 will be referred to as QW1–QW5, QW1 being the quantum well with the lowest In content.

The growth rates were 0.7 μm/h for GaAs and 0.15 μm/h for AlAs with a standard V/III flux ratio of approxi-

[a]Electronic mail: jrj@com.dtu.dk

mately 10. Due to the large lattice mismatch between InAs and GaAs, reflection high energy electron diffraction (RHEED) oscillations cannot be obtained by growing InAs on a GaAs substrate. Instead, the InAs growth rate can be measured by subtracting the growth rate of GaAs from the growth rate of $In_xGa_{1-x}As$ for low x values. However, it was found that only an approximate calibration is possible in this way, since at low x values ($x<0.05$) the uncertainty on the InAs growth rate is large compared to the growth rate itself, and at high x values ($x>0.15$) the RHEED oscillations are strongly damped. We stress that the thicknesses and mole fractions stated above for S1, S2, and S3 are the *nominal* values obtained from the RHEED calibration, but as described in the following a better calibration of the In source was found using the photoluminescence (PL) peak positions of S2. All three samples were grown at $T_{sub}=530\,^{\circ}C$ during the same loading of the MBE system, and prior to each growth the GaAs and AlAs growth rates were carefully measured using RHEED oscillations.

III. MODELING OF SURFACE SEGREGATION AND TRANSITION ENERGIES

For the growth of III-V arsenide heterostructures, In surface segregation has been observed in both InGaAs and InAlAs, the tendency being strongest in InAlAs.[14,16,17] Ga also segregates in AlGaAs, but the effect is weaker than in any of the In systems. Surface segregation can be modeled as a chemical reaction interchanging a group III atom in the surface atomic layer (s) with a group III atom in the layer underneath (b):

$$\mathrm{Ga}(b)+\mathrm{Al}(s)\rightarrow\mathrm{Ga}(s)+\mathrm{Al}(b), \tag{1}$$

$$\mathrm{In}(b)+\mathrm{Ga}(s)\rightarrow\mathrm{In}(s)+\mathrm{Ga}(b), \tag{2}$$

$$\mathrm{In}(b)+\mathrm{Al}(s)\rightarrow\mathrm{In}(s)+\mathrm{Al}(b). \tag{3}$$

The energies gained in each of the reactions have been deduced from previous measurements[16,17] and consists of two terms, one corresponding to the change of chemical energy, E_s, and one corresponding to the change of elastic energy due to strain in the layers.[14]

To calculate the composition profile of the quantum wells investigated here, the growth was modeled in steps of one atomic layer. For each step the initial composition of the surface layer was calculated from the flux rates of the group III sources, and using the law of mass action the composition in thermal equilibrium with the layer underneath was found. For the segregation profiles of S1 and S2 only the equilibrium of Eq. (2) had to be considered, whereas for S3 the equilibrium of all three reactions was found restricting the solution to the one where the sum of group III mole fractions is 1 in the (s) and (b) layers, respectively.

From the composition profiles the potentials and effective masses in the quantum wells were calculated, taking into account the strain effects on the bandstructure.[18] The energies of the electron and hole states were found by solving the Schrödinger equation, using an isotropic conduction band model and a six-band $k\cdot p$ model for the valence band. For unstrained $In_xGa_{1-x}As$ the following relation was used for the low temperature band gap in eV:[19]

$$1.519-1.584x+0.475x^2 \tag{4}$$

and for $Al_yGa_{1-y}As$ in eV:[20]

$$1.519+1.36y+0.22y^2. \tag{5}$$

TABLE I. Values of the physical parameters used for calculating the potentials and effective masses of the electrons and holes.

Parameter	GaAs	AlAs	InAs
Lattice constant, d(Å)	5.6503[b]	5.6611[b]	6.0583[b]
Stiffness constant, $C_{11}(\times10^{10}\,\mathrm{Pa})$	11.88[a]	12.02[a]	8.329[b]
Stiffness constant, $C_{12}(\times10^{10}\,\mathrm{Pa})$	5.38[a]	5.70[a]	4.526[b]
Stiffness constant, $C_{44}(\times10^{10}\,\mathrm{Pa})$	5.94[a]	5.89[a]	3.959[b]
Relative electron mass, m_e/m_0	0.0667[a]	0.15[a]	0.0248[c]
Luttinger parameter, γ_1	7.1[a]	3.76[a]	19.7[b]
Luttinger parameter, γ_2	2.02[a]	0.9[a]	8.37[b]
Luttinger parameter, γ_3	2.91[a]	1.42[a]	9.29[b]
Hydrostatic deformation potential, a_g (eV)	−8.233[c]	−8.110[d]	−6.080[c]
Shear deformation potential, b_v (eV)	−1.824[c]	−1.7[d]	−1.8[b]
Spin-orbit splitting, V_{so} (meV)	340[b]	275[b]	380[b]

[a]Reference 21.
[b]Reference 22.
[c]Reference 23.
[d]Reference 24.

The values of the other physical parameters used here for the binary materials are given in Table I.[21–24] For the ternary and quaternary materials, the values have been found by linear interpolation, however for the electron masses the *inverse* values have been interpolated. The conduction band offset was set to 67% of the total band offset, and the conduction band deformation potential was set to 90% of a_g.[18] To account for Coulomb interactions a well-width dependent exciton binding energy was used for the InGaAs structures in S1 and S2.[19] Based on the binding energy for a heavy-hole exciton in an 8 nm InGaAs quantum well, the binding energies of the heavy- and light-hole excitons in S3 were taken as 7 and 8 meV. Since the contributions of the exciton binding energies to the transition energies calculated in the following are small, discrepancies of a few meV compared to the real values will not affect the results.

IV. TRANSITION ENERGIES

In Fig. 1 the photoluminescence (PL) spectrum of S1 at 10 K is shown, and the positions of the peaks are compared to the calculated transition energies with and without segregation. First, the In content of the wells was fitted to $x=0.092$, using a square well potential for the thickest well where the effect of surface segregation on the transition energy is negligible. Then a chemical energy of 0.34 eV for In segregation in InGaAs was found, yielding the best overall fit to the transition energies. This is about a factor of two larger than the value obtained by Gerard *et al.*,[16,17] but as pointed out by Grandjean *et al.*[25] the chemical energy itself depends on the temperature and can only be used as a fitting parameter. The tail of the segregation profile calculated for $E_s=0.34\,\mathrm{eV}$ shows an exponential decay length of 2.7 nm,

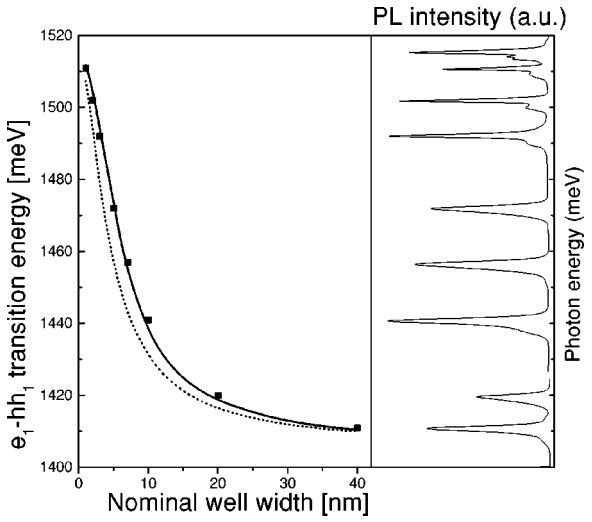

FIG. 1. Right: Photoluminescence spectrum of S1 at $T=10$ K. Left: Comparison of measured transition energies (squares) vs the nominal well thickness with calculated values for a square composition profile (dotted line) and a segregation profile with $E_s=0.34$ eV (solid line).

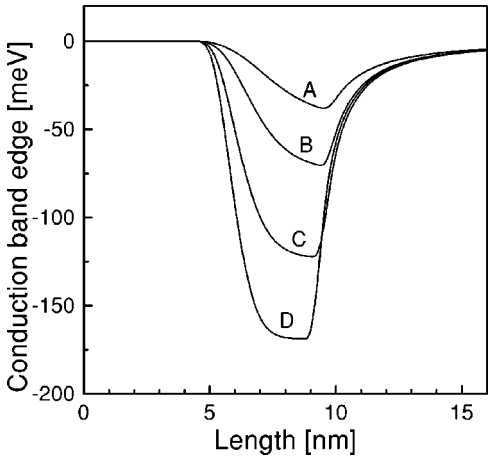

FIG. 3. The shape of the conduction band potential of four InGaAs/GaAs quantum wells in S2, with a nominal thickness of 5 nm and nominal (real) In contents of A: 5% (5.5%), B: 10% (9.2%), C: 20% (15.6%) and D: 30% (21.7%). The origin of the energy scale corresponds to the conduction band edge in GaAs.

in good agreement with a previous secondary-ion mass spectroscopy (SIMS) measurement yielding 2.9 nm for $T_{\mathrm{sub}}=520\,^{\circ}\mathrm{C}$.[15]

Using the value of the chemical energy found for S1, the transition energies of S2 were calculated, fitting only the dependence of the In mole fraction in the wells on the absolute In source temperature, T. It was assumed that the flux rate of In atoms from the source has an exponential dependence on T^{-1} in agreement with the vapor pressure dependence on the temperature, given by the Clausius-Clapeyron relation. In Fig. 2 the PL spectrum of S2 at 10 K is shown, and the measured transition energies are compared to the calculated values. For this fit, a maximum deviation of 2 meV for all six quantum wells was found. The difference between the nominal and the real In source calibration causes a change in the thickness of the wells, which has been taken into account in all the calculations described here. The shapes of the potentials in the quantum wells in S2 are shown in Fig. 3, represented by the energy of the conduction band edge. The deviation from an ideal square well potential is clear; however, for high In contents the first interface becomes more abrupt. This is due to the strain contribution to the reaction energy,[14] which tends to inhibit In segregation for high In contents. The growths of S1 and S2 can be compared using the PL peak position of the 5 nm well with a nominal In content of 0.10 included in both samples. Their transition energies differ by less than 0.2 meV, indicating identical growth conditions and assuring the comparability of all three samples investigated here. Furthermore, the sharp PL lines of S1 and S2 indicate a good crystal quality and that the critical thickness has not been exceeded.

In Fig. 4 the PL spectrum of S3 at $T=10K$ is shown. The In contents and widths of the wells according to the

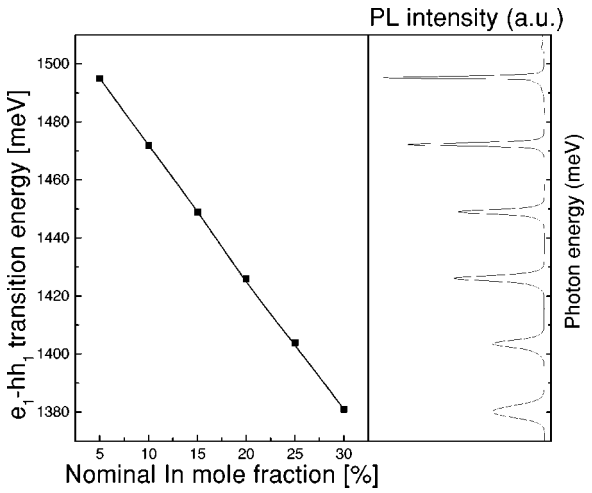

FIG. 2. Right: Photoluminescence spectrum of S2 at $T=10$ K. Left: Comparison of measured transition energies (squares) vs the nominal In mole fraction with calculated values for the best fit of the In source flux rates (solid line).

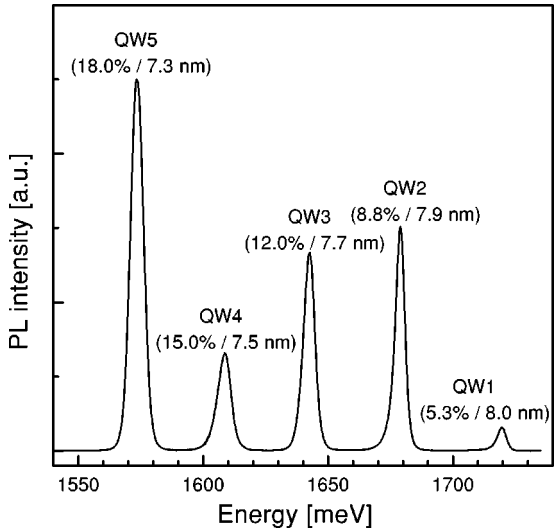

FIG. 4. Photoluminescence spectrum of S3 at $T=10$ K. The In content in the wells obtained by calibrating the In source with the PL peaks in S2, are stated in parenthesis.

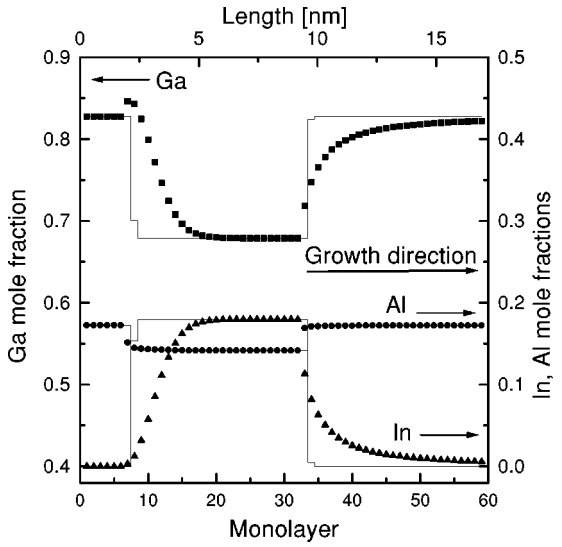

FIG. 5. Simulated composition profile of a 8-nm-thick quantum well with an In mole fraction of 0.18 (QW5 in S3), and $Al_{0.17}Ga_{0.83}As$ barriers. The calculated mole fractions of the group III elements are indicated with symbols (Ga: squares, Al: circles, In: triangles) and the composition profiles without segregation are shown with straight lines. Right axis: Al and In mole fractions, and left axis: Ga mole fraction.

calibration using the S2 PL-peak positions are indicated. The PL intensities of the quantum wells cannot be compared directly, since different excitation efficiencies and reabsorption effects in the structure should be considered. However, the PL-line shapes are identical; only the widths are different as will be addressed in Sec. V.

In order to model the composition profile of the quaternary quantum wells as described in Sec. III, knowledge of the chemical energy for each of the three reactions (1)–(3) is needed. Based on the value found from S1 we have used $E_s = 0.17\,\mathrm{eV}$ for Ga segregation in AlGaAs and $E_s = 0.52\,\mathrm{eV}$ for In segregation in InAlAs, according to the experimentally determined ratio of approximately 1:2:3 between these quantities.[16,17] The simulated composition profile for QW5 is shown in Fig. 5. Since Al is the nonsegregating element in the quaternary InAlGaAs system, the transients in the In mole fraction at the interfaces of the quantum well are accompanied by a change in the Ga mole fraction, whereas the Al mole fraction is almost constant. Before the growth of the InAlGaAs layer, the surface is Ga rich due to Ga segregation in the AlGaAs barrier. However, in the quaternary well material the segregation of In is strongest, and hence the Ga rich surface is ''pushed'' into the bulk giving rise to the Ga peak at the first interface in Fig. 5. This peak is also reflected in the shape of the potential energy in the wells, shown in Fig. 6, where the shoulder at the first interface is due to the increased Ga mole fraction compared to the barrier region.

Fitting the calculated transition energies to the measured values, allows us to obtain an empirical band gap relation for unstrained $In_x(Al_yGa_{1-y})_{1-x}As$, in the form of a second order expansion for low values of x and y. For this expansion the terms proportional to x, y, x^2, and y^2 are given by Eqs. (4) and (5), leaving only the term proportional to xy to be determined. The fit then yields:

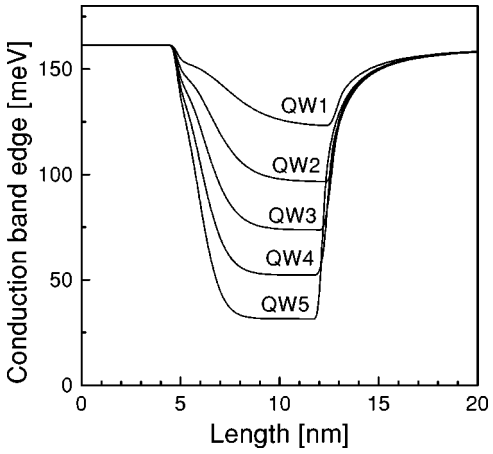

FIG. 6. The shape of the conduction band potential of the five 8 nm InAlGaAs/AlGaAs quantum wells in S3. The origin of the energy scale corresponds to the conduction band edge in GaAs.

$$1.519 + 1.36y - 1.584x + 0.55xy + 0.22y^2 + 0.475x^2. \quad (6)$$

The agreement between the measured e-hh and e-lh (measured with photoluminescence excitation spectroscopy) transition energies and the calculated values are shown in Fig. 7 and Table II. For the heavy holes the difference is less than 4 meV for all the wells, whereas for the light holes it is less than 5 meV for QW3–QW5 and 8 meV for QW1 and QW2. Since the valence band potential is very shallow for QW1 and QW2, the light-hole wave functions penetrate into the barrier. Hence, the enhancement of the exciton binding energy due to quantum confinement is overestimated here, partly explaining the difference.

Since the empirical band gap relation is based on the well established relations for the ternary compounds InGaAs and AlGaAs, the term proportional to xy could in principle have been determined by fitting the transition energy of a single InAlGaAs quantum well. However, the good agreement obtained for all the quantum wells in S3 where the In content is varied, further supports the band gap relation and the model for the In segregation used here.

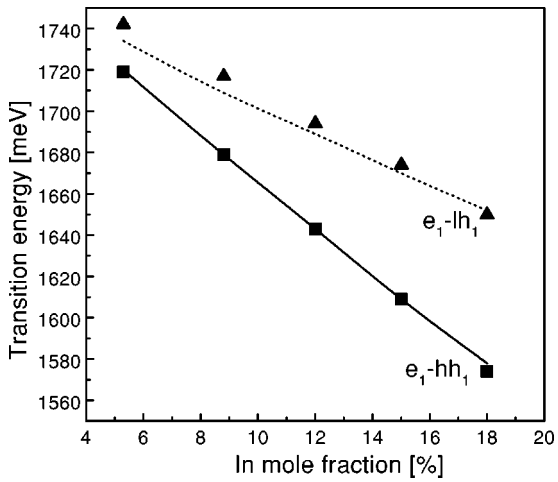

FIG. 7. Measured $e_1 - hh_1$ (squares) and $e_1 - lh_1$ (triangles) transition energies of S3, compared to calculated values for the heavy (solid line) and light hole (dotted line) using Eq. (6) for the band gap energy.

TABLE II. Calculated and measured values for the *e*-hh and *e*-lh transitions and PL linewidths of S3. L and x denote the values of well thickness and In content used in the calculations.

			$E_{e\text{-hh}}$ (eV)		$E_{e\text{-lh}}$ (eV)		FWHM (meV)	
	L (nm)	x	meas.	calc.	meas.	calc.	meas.	calc.
QW1	8.0	0.052	1.719	1.720	1.742	1.734	3.5	3.50
QW2	7.9	0.088	1.679	1.679	1.717	1.709	3.9	3.93
QW3	7.7	0.12	1.643	1.643	1.694	1.689	4.6	4.62
QW4	7.5	0.15	1.609	1.609	1.674	1.670	5.4	5.32
QW5	7.3	0.18	1.574	1.578	1.650	1.652	6.0	5.99

V. LINEWIDTH ANALYSIS

In Table II, the measured linewidths, full width at half maximum (FWHM), of the five InAlGaAs quantum wells are compared to the linewidths expected from random alloy fluctuations (RAF) and well width fluctuations (WWF). Based on a previous analysis for ternary bulk semiconductors,[26] the following relation was used to calculate the FWHM broadening due to the random distribution of In in a $In_x(Al_yGa_{1-y})_{1-x}As$ quantum well:

$$\Delta E_x = 2\sqrt{2\ln 2}\sqrt{\frac{x(1-x)}{N}}\frac{\partial E_{\text{gap}}}{\partial x}. \tag{7}$$

The same relation was used for the Al distribution. N is the number of atoms contained in the volume of the exciton, V. Here, we have used $V=\pi a_0^2 L_z$, where a_0 is the in plane exciton Bohr radius and L_z is the FWHM size of the electron wave function in the direction of growth. However, for QW1 and QW2, L_z was set to the well width, because the FWHM size is larger than the well width. The best fit was found for $a_0=13$ nm, which is smaller than the exciton Bohr radius in GaAs, due to the enhanced exciton binding energy in a quantum well compared to a bulk structure. The FWHM broadening due to WWF is given by:

$$\Delta E_{\text{WWF}} = \frac{\partial E_{e-hh}}{\partial L}\Delta L, \tag{8}$$

where L is the thickness of the well and ΔL is an effective interface roughness. The derivative of the transition energy with respect to the thickness was calculated for the quantum wells individually and for the effective roughness a value of 1.1 ML was obtained, which is comparable to typical values obtained for AlGaAs structures. Assuming that the three contributions to the broadening are independent, the total FWHM broadening is given by:

$$\Delta E_{\text{tot}} = \sqrt{(\Delta E_x)^2+(\Delta E_y)^2+(\Delta E_{\text{WWF}})^2}. \tag{9}$$

For QW1–QW5, E_{WWF} varies almost linearly with the In content from 0.77 to 3.85 meV, whereas E_x (E_y) varies sublinearly from 1.75 (2.93 meV) to 3.19 meV (3.29 meV). Since the dependencies of WWF and RAF on the In content in QW1–QW5 are different, the two broadening mechanisms can be distinguished in the measured line widths and hence the parameters in the model, a_0 and ΔL, are well determined.

Due to the good agreement between the measured and calculated linewidths, we conclude that the distribution of group III atoms in the InAlGaAs quantum wells does not show any signs of clustering, and is well described by random statistics.

VI. CONCLUSION

The transition energies and linewidths of several InAlGaAs/AlGaAs quantum wells grown on a GaAs substrate, have been measured and modeled. Using two reference samples with InGaAs/GaAs quantum wells grown under the same conditions, it was possible to make a calibration of the In growth rate and the chemical energies of the In segregation. A good fit to the *e*-hh and *e*-lh transitions was found using a band gap relation for $In_x(Al_yGa_{1-y})_{1-x}As$, Eq. (6), based on the well known relations for $In_xGa_{1-x}As$ and $Al_yGa_{1-y}As$, and adding a term $0.55xy$ to account for the simultaneous presence of In and Al. From the linewidths, an effective interface roughness of 1.1 ML was found, using a model that includes well width fluctuations and random alloy fluctuations. Hence, the linewidths do not show indications of clustering or dislocation formation in the InAlGaAs/AlGaAs structures.

ACKNOWLEDGMENTS

The authors would like to thank C. B. Sørensen at the III-V Nanolab for helpful discussions on the growth of the samples. This work was supported by the Danish Natural Science Research Council.

[1] D. Olego, T. Y. Chang, E. Silberg, E. A. Caridi, and A. Pinczuk, Appl. Phys. Lett. **41**, 476 (1982).
[2] J. C. Fan and Y. F. Chen, J. Appl. Phys. **80**, 1239 (1996).
[3] Y. F. Chen, Y. T. Dai, J. C. Fan, T. L. Lee, and H. H. Lin, Appl. Phys. Lett. **67**, 1256 (1995).
[4] H. Hillmer, R. Losch, and W. Schlapp, J. Appl. Phys. **77**, 5440 (1995).
[5] R. P. Leavitt and J. L. Bradshaw, J. Appl. Phys. **76**, 3429 (1994).
[6] L. A. Cury, J. Beerens, and J. P. Praseuth, Appl. Phys. Lett. **63**, 1804 (1993).
[7] R. F. Kopf, H. P. Wei, A. P. Perley, and G. Livescu, Appl. Phys. Lett. **60**, 2386 (1992).
[8] Y. Hirayama, W. Choi, L. H. Peng, and C. G. Fonstad, J. Appl. Phys. **74**, 570 (1993).
[9] J. Ko, C.-H. Chen, and L. A. Coldren, Electron. Lett. **32**, 2099 (1996).
[10] S. Bhargava, C. Zheng, J. Ko, M. A. Chin, L. A. Coldren, and V. Narayanamurti, Appl. Phys. Lett. **73**, 3271 (1998).
[11] R. Nötzel, Semicond. Sci. Technol. **11**, 1365 (1996).
[12] *Properties of Lattice-matched and Strained Indium Gallium Arsenide*, edited by P. Bhattacharya (INSPEC, London, 1993).
[13] T. G. Andersson, Z. G. Chen, V. D. Kulakovskii, A. Uddin, and J. T. Vallin, Appl. Phys. Lett. **51**, 752 (1987).
[14] J. M. Moison, C. Guille, F. Houzay, F. Barthe, and M. V. Rompay, Phys. Rev. B **40**, 6149 (1989).
[15] K. Muraki, S. Fukatsu, Y. Shiraki, and R. Ito, Appl. Phys. Lett. **61**, 557 (1992).
[16] J. M. Gerard and J. Y. Marzin, Phys. Rev. B **45**, 6313 (1992).
[17] J. M. Gerard, Appl. Phys. Lett. **61**, 2096 (1992).
[18] P. Y. Yu and M. Cardona, *Fundamentals of Semiconductors* (Springer, Berlin, 1996).
[19] R. Atanasov, F. Bassani, A. D'Andrea, and N. Tomassini, Phys. Rev. B **50**, 14381 (1994).
[20] L. Pavesi and M. Guzzi, J. Appl. Phys. **75**, 4779 (1994).
[21] *Properties of Aluminium Gallium Arsenide*, edited by S. Adachi (INSPEC, London, 1993).
[22] *Numerical Data and Functional Relationships in Science and Technology*,

Volume 17a, Semiconductors, edited by O. Madelung, M. Schulz, and H. Weiss (Springer, Berlin, 1982).
[23] *Physical Properties of III-V Semiconductor Compounds*, edited by S. Adachi (Wiley, New York, 1992).
[24] C. G. Van de Walle, Phys. Rev. B **39**, 1871 (1989).
[25] N. Grandjean, J. Massies, and M. Leroux, Phys. Rev. B **53**, 998 (1996).
[26] E. Schubert, E. O. Göbel, Y. Horikoshi, K. Ploog, and H. J. Queisser, Phys. Rev. B **30**, 813 (1984).

Exciton localization and interface roughness in growth-interrupted GaAs/AlAs quantum wells

K. Leosson, J. R. Jensen, W. Langbein,* and J. M. Hvam
Research Center COM, Technical University of Denmark, Building 349, DK-2800 Lyngby, Denmark
(Received 19 July 1999; revised manuscript received 19 November 1999)

We have used photoluminescence spectroscopy to investigate the influence of interface roughness in GaAs/AlAs quantum wells on their optical properties over a wide continuous range of well thicknesses. In order to compare different correlation lengths of the in-plane disorder potential, the wells were fabricated with growth interruption at both, one, or neither of the interfaces. Growth-interruption increases the correlation length of the monolayer-island structure on the surface, which gives rise to a long-range interface roughness after overgrowth. The relation between the correlation lengths of the in-plane disorder potential and the exciton localization length determines the spectral shape of the exciton luminescence. When the correlation length of the in-plane disorder potential is larger than the exciton localization length, the excitonic spectrum splits up into discrete peaks, stemming from regions differing in effective thickness by an integral number of monolayers. The energies of monolayers peaks, taking into account the in-plane localization energy, are found to be reproducible in wafers grown under similar conditions. We conclude that atomically smooth growth islands are formed on both AlAs and GaAs surfaces after growth interruption. During overgrowth, surface segregation leads to the generation of an atomic-scale disorder in the first overgrown monolayers. This results in an additional in-plane disorder potential with a much shorter correlation length than the original surface. It also modifies the shape of the well potential in the growth direction, as we have modelled by growth simulations, blueshifting the excitonic transition energies with respect to a square-well model.

I. INTRODUCTION

Interface roughness is an important parameter for the optical and electrical properties of quantum wells and, consequently, for quantum-well based devices. The observed photoluminescence (PL) spectrum of quantum wells with imperfect interfaces is largely determined by how the length scales of the interface roughness compare to the diameter, localization length and diffusion length of the quantum-well excitons. When quantum wells are grown with molecular-beam epitaxy (MBE), the interface roughness can be tailored to some extent by interrupting the growth at the heterointerfaces, allowing for a restructuring of the free surface, mainly by surface diffusion. It was realized early on that growth islands with sizes comparable to or larger than the exciton diameter can be created in this way, resulting in a splitting of the PL into several lines of reduced inhomogeneous linewidth.[1] Initially, such narrow luminescence lines were assigned to laterally extended quantum well regions with a well-defined monolayer (ML) thickness.[1,2]

More detailed investigations on these ''monolayer peaks'' in growth-interrupted (GI) quantum wells revealed, however, that narrow exciton luminescence was not necessarily indicative of quantum wells having perfect interfaces and integer monolayer widths. Gammon *et al.*[3] demonstrated a wafer-to-wafer variation in absolute energies of ML peaks in GI GaAs/AlAs wells grown under identical conditions. Warwick *et al.*[4] observed a significant variation in peak energy in $Al_{0.37}Ga_{0.63}As$/GaAs wells in a single sample, which could not be explained by alloy fluctuations. The simplest model which can account for this behavior is that of bimodal interface roughness.[4] It is now commonly accepted that discrete luminescence lines can originate from extended quantum well regions that differ in effective thickness by approximately one monolayer and exhibit nanoroughness on a length scale smaller than the exciton diameter. Optically, the presence of nanoroughness has been inferred from measurements of GI GaAs quantum wells with $Al_xGa_{1-x}As$ ($x \leqslant 0.4$) barriers[5–10] as well as pure AlAs barriers.[11,12]

Scanning tunneling microscopy studies indicate that the as-grown GaAs surface has atomically-flat islands which, after growth interruption, can reach lateral sizes of tens or hundreds of nanometers,[13] possibly with a distribution of ML-deep holes much smaller than the exciton diameter.[14] The as-grown AlAs surface exhibits a higher degree of roughness on the nanometer scale, even after growth interruption, due to the smaller surface mobility of Al.[12] Nevertheless, atomically smooth growth islands as large as 15 nm$\times$40 nm on an $Al_{0.35}Ga_{0.65}As$ surface have been reported.[13]

In order to clarify the relationship between surface roughness during growth and the final interface structure, we have used PL and microphotoluminescence (μ-PL) spectroscopy to characterize GaAs/AlAs quantum wells fabricated with growth interruption at one, both, or neither of the interfaces. The wells have a wide range of thicknesses, varying continuously between approximately 4 and 11 nm (for thicknesses under 4 nm, the indirect barrier material results in the formation of type-II quantum wells[12]). The use of binary barrier and well materials eliminates the effects of alloy disorder, making the results more reproducible. By interrupting the MBE growth, we tune the correlation length of the quantum well potential through several distinct regimes of interface roughness. Using recent theoretical results[15] we identify these regimes with approximate length scales. Contrary to previous work in the field, we demonstrate that when sufficiently large growth islands are formed, *reproducible* ML peak positions can be achieved over a large range of quan-

tum well thicknesses, consistent with the formation of monolayer-flat islands on both AlAs and GaAs surfaces after GI. From growth simulations, we deduce that segregation effects during overgrowth are generating atomic-scale interface roughness, resolving the apparent contradiction between atomically smooth as-grown surfaces and the observed nanoroughness of quantum well interfaces.

II. EXPERIMENT

Single GaAs quantum wells, nominally 10, 7, and 5 nm wide, were MBE grown at 630 °C on two-inch GaAs (100) wafers using pure AlAs barriers. One wafer (Wafer 1) was grown continuously, without growth interruption. Three wafers were grown with a 120 s GI before (Wafer 2), after (Wafer 3) and both before and after (Wafer 4) growing the wells. Short-period GaAs/AlAs superlattices (SPSL's) were grown between wells in order to trap impurities and improve the surface structure. Rotation of the substrate was stopped only during the growth of the wells in order to achieve a continuous variation in well thickness across the wafer while maintaining a constant barrier width. Growth rates were calibrated using reflectance high-energy electron diffraction (RHEED) on a reference wafer. The nominal growth rates were 0.8 ML/s and 0.3 ML/s for GaAs and AlAs, respectively, and a 30% variation in growth rate was observed across the wafer. A standard V/III flux ratio of 8–10 was used. For comparison, a wafer with four GaAs quantum wells, growth-interrupted at both interfaces, was fabricated in a later run, under similar growth conditions (Wafer 5). The nominal quantum well thicknesses were 11, 8.5, 6.5, and 5 nm. Wafer 5 was grown with narrow (8 nm) AlAs barriers and 50 nm GaAs spacers but no SPSL's between wells.

Conventional PL measurements were carried out at sample temperatures of 10–50 K. In addition, micro-PL spectra were measured at 10 K on selected samples. The samples were cooled in a closed-cycle He cryostat and excited with a He-Ne laser, focused to a 50 μm spot. The PL was dispersed in a spectrometer and detected with a cooled charge coupled device array. The spectral resolution of the detection system was ≈ 1 Å (0.2 meV). In μ-PL measurements, the excitation beam and PL were passed confocally through a 0.85 NA objective located inside the cryostat, giving an excitation spot diameter and a spatial resolution close to 0.5μm.

III. RESULTS

Figure 1 shows PL spectra from the three single quantum wells measured at similar positions on Wafers 1 to 4. The continuously grown Wafer 1 exhibits nearly Gaussian luminescence lines for all well widths. At first glance, no large difference is observed in Wafer 2, when MBE growth is interrupted only at the bottom (inverted) interface. However, as shown below, systematic variations in linewidth are observed when the PL is measured at different positions on the wafer. In the third case, where growth is interrupted only at the top (normal) interface, the PL peaks split into a doublet, most clearly seen in the 7 nm well. Only when growth is interrupted at both interfaces does the luminescence exhibit narrow peaks with discrete energies. Such a splitting of the

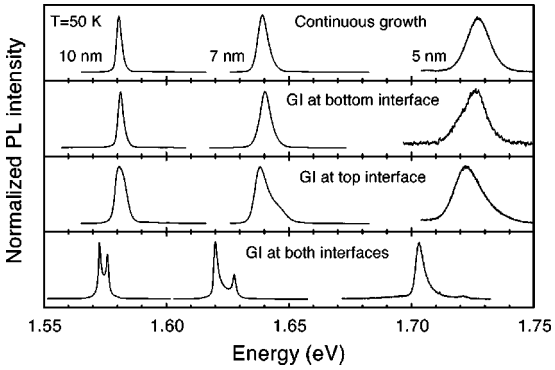

FIG. 1. PL, measured at 50 K, from quantum wells of equal thickness but grown with 120-s growth interrupts at neither, one, or both interfaces, as indicated. The spectra from each well have been normalized with respect to the peak height.

PL from each well into two or three peaks is observed on Wafer 4. The highest energy peak is well fitted by a Lorentzian function whereas the peaks at lower energies are asymmetric, with a tail on the high energy side. Identical results were obtained for Wafer 5 (not shown).

The variation of the PL from single quantum wells along a 5 mm section of each wafer is shown in Fig. 2. The spectra are taken at comparable positions on Wafers 1 to 4. The total scan distance corresponds to a quantum well thickness

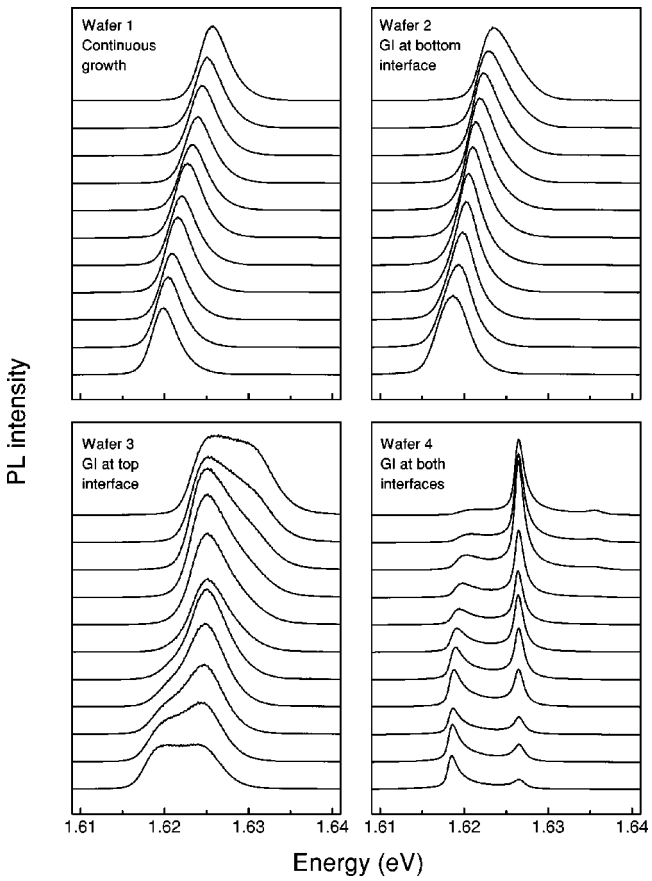

FIG. 2. Single quantum well PL spectra sampled over a 5 mm region on the wafers at 50 K. The total scan distance represents a thickness change of approximately one monolayer. The average well thickness is 6 nm.

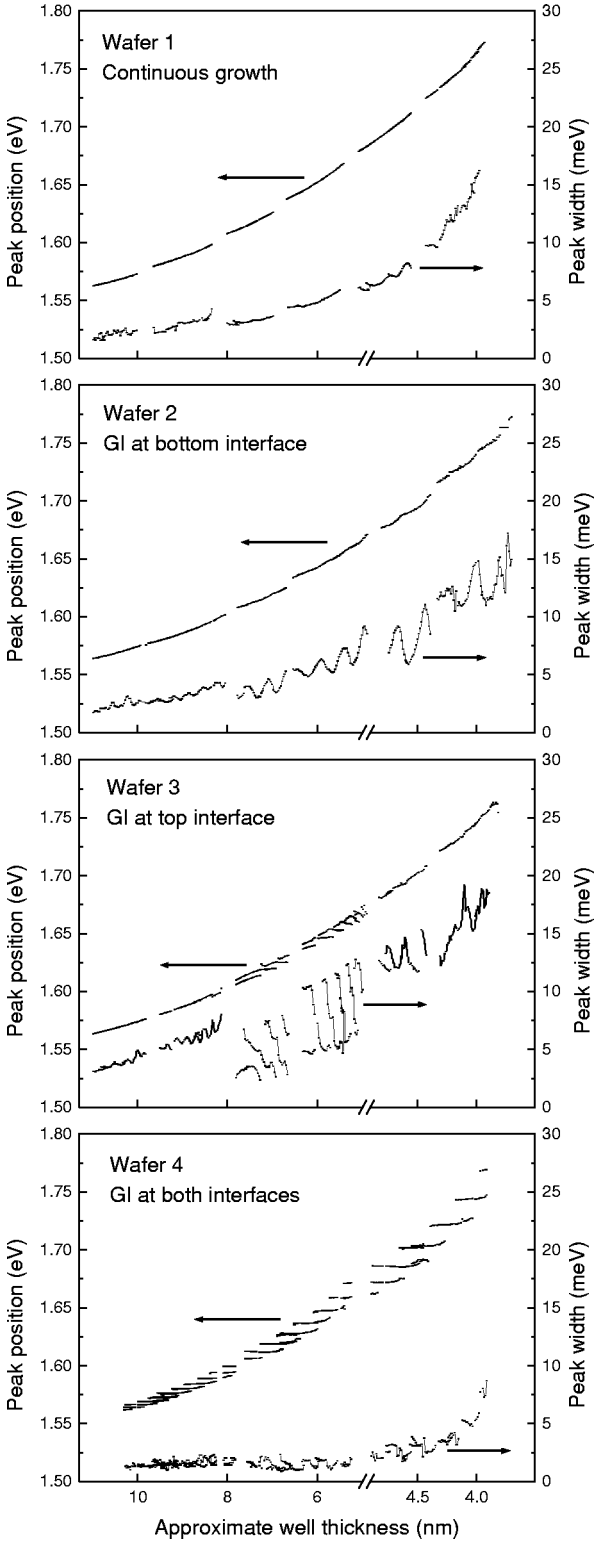

FIG. 3. PL peak positions (at 50 K) and widths (FWHM) measured at various points on the wafers. For clarity, results from the different wells have been shifted horizontally and the position on the wafer translated into an approximate well thickness scale.

change of approximately one monolayer. Similar spectra were recorded for all three wells at 0.5 mm intervals across the entire surface of the wafers in order to cover the full range of well widths. In Fig. 3, the position and width of the luminescence peaks are plotted as a function of distance

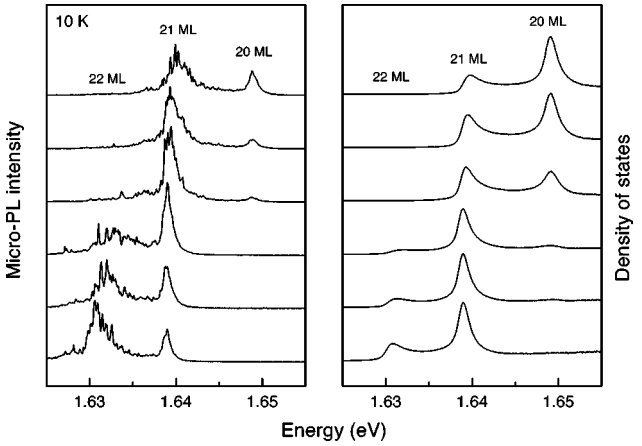

FIG. 4. Left: 10-K micro-PL spectra from a nominally 7 nm thick quantum well, growth-interrupted at both interfaces, at an excitation power of 0.3 μW. The spectra were recorded at 1 mm intervals along the sample surface and are displaced vertically for clarity. The total scan distance corresponds to a thickness change of one monolayer. Right: Optical density of states for the same positions on the sample, determined from 50-K PL spectra and corrected for the temperature dependence of the bandgap.

across the wafer. The position on the wafer has been converted into an approximate thickness scale. For Wafers 1 and 2, the PL signal was fitted with a single Gaussian peak. In the case of Wafer 3, the data was fitted with two Gaussian peaks for intermediate well thicknesses (5-8 nm). The position and full width at half maximum (FWHM) of each peak is indicated in this thickness range. For narrower and wider wells, the peaks could not be resolved and the position of the maximum luminescence and the FWHM of the total signal are given. For Wafer 4, where growth was interrupted at both interfaces, the positions and FWHM of the individually fitted Lorentzian peaks are shown.

The left graph in Fig. 4 shows μ-PL spectra measured at 10 K on the nominally 7 nm-thick quantum well in Wafer 4. The PL was excited and detected confocally, with a resolution of approximately 0.5 μm and the displayed spectra were recorded at 1 mm intervals along the sample surface. As the probe is scanned in the direction of decreasing well thickness, each ML peak in the μ-PL spectra first appears as a single unresolved peak with a FWHM around 1 meV, increasing in intensity to a maximum value without shifting in energy. As the maximum intensity drops, the peak splits up into narrow lines with widths below our resolution limit. The narrow-line pattern varies with position on the sample and individual lines arise from regions with sizes below our spatial resolution. As the well thickness decreases further, the single lines spread over a larger energy range, the center of the distribution shifts to higher energies and the total intensity drops. For μ-PL measurements an excitation power of 0.3 μW was used. A significant modification of the narrow-line spectrum due to saturation of states was observed when the excitation power exceeded 3 μW. Figure 4 also shows the exciton optical density of states (ODOS) for corresponding positions on the sample. The ODOS was obtained from the 50 K PL spectra assuming a Boltzmann distribution of carriers. The spectra were shifted in energy to compensate for the change in the GaAs bandgap with temperature. To

confirm that the excitons are in thermal equilibrium at 50 K, we performed a temperature dependent photoluminescence study of adjacent ML peaks (16 and 17 ML) with a relatively large splitting (around 11 meV at the position measured). The integrated intensity ratio of the two peaks essentially follows the form given by Melliti *et al.*[16] with a linear temperature dependence above 30 K characterized by an activation energy of around 8 meV.

Our main observations from the PL spectra can be summarized as follows:

(i) The continuously grown single quantum wells exhibit a smooth increase in transition energy and linewidth with decreasing well thickness. The inhomogeneous linewidth broadening corresponds to an exciton-averaged well thickness variation of less than a monolayer. Anomalously increased linewidth, along with a drop in luminescence efficiency, is observed close to the edges of the wafer. The line shape is discussed in more detail in the following section.

(ii) Growth interruption at the bottom interface introduces only a slight modulation of the peak position as a function of well width. The peak width, however, oscillates strongly with the well thickness, in some cases dropping below the corresponding linewidth of the continuously grown well. A reduction in PL excitation (PLE) linewidth in similarly prepared samples reported by Zhang *et al.*[17] is consistent with this observation.

(iii) In the case of growth interruption at the top interface, the PL is split into a doublet. The average PL energy increases continuously with a weak modulation, similar to the previously described case. However, when two peaks are resolved, each peak shifts to higher energy as it gains intensity and then stays pinned or moves to lower energies as the intensity drops again, with a decrease in peak width. Even more pronounced ''sawtooth'' behavior of this kind was reported by Gammon *et al.* in similar quantum wells and attributed to gradients in barrier thickness.[3] Our observations show, however, that the effect persists with AlAs layers of constant thickness. Furthermore, we note that in the ODOS calculated from the PL spectra each peak moves monotonically upwards in energy with decreasing well thickness.

(iv) When growth is interrupted at both top and bottom interfaces, two or three narrow PL lines are observed simultaneously. As the probe is scanned across the surface, the peak position is generally pinned within ± 0.2 meV until the peak has lost approximately half its maximum intensity, then it broadens and shifts gradually to higher energies. The minimum linewidths stay constant at around 1.3 meV, increasing to about 5 meV only for the narrowest wells, as also observed in Ref. 18. Similar discrete peaks were also measured in Wafer 5, with minimum linewidths around 0.8 meV. We attribute the smaller linewidth in these wells to reduced exciton-electron scattering,[19] confirmed by the observation of trionic PL in Wafer 4 at low temperatures. Due to the narrow barriers, charging effects are less important in the quantum wells of Wafer 5, which do not show trionic PL at low temperatures.

(v) Micro-PL spectroscopy reveals that the broadening and shifting of ML peaks is observed simultaneous to their further splitting into sharp PL lines, arising from spatially localized exciton states. When compared with the exciton ODOS, the μ-PL curves confirm the localization of the excitons into small islands, in which the in-plane quantization supersedes the effect of nanoroughness within the islands.

IV. ANALYSIS

To determine the degree of interface roughness and exciton localization in our continuously grown samples we use the line shape model of Schnabel *et al.*[20] to fit the PL peaks. This model takes into account the violation of wave-vector conservation due to partial localization of the exciton's center-of-mass wave function. For the ground state transition, the optical density for a disordered potential with a mean energy E_0 can be calculated to

$$\overline{\alpha}(E) \propto \frac{1}{2\eta}\left[1+\mathrm{erf}\left(\frac{E-E_0}{\sigma_E}-\frac{\sigma_E}{2\eta}\right)\right]\exp\left[\left(\frac{\sigma_E}{2\eta}\right)^2-\frac{E-E_0}{\eta}\right]. \tag{1}$$

We estimate $\overline{\alpha}$ by calculating the ODOS from our 50-K PL spectra, as previously described, and fit Eq. (1) to the result. The relevant fitting parameters are the standard deviation of the potential variation, σ_E, and a localization energy parameter, $\eta=\hbar^2\Delta K^2/2M$, derived from the wavevector uncertainty ΔK, with M being the exciton mass. For the narrowest continuously grown wells, we find a potential variation around 4 meV, decreasing to 1 meV for the widest wells. The localization energy parameter follows a similar dependence on well width, with the ratio σ_E/η being nearly constant for all wells and equal to 0.67 ± 0.03. The momentum uncertainty in the model can be converted to a minimum localization radius, ΔR, via the uncertainty relation, yielding lower limits for localization radii at 3.5 nm for the narrowest well, increasing to 8 nm for the widest.

Energies of ML peaks measured in Wafers 4 and 5 are plotted in Fig. 5(a). The measured data points correspond to the energies at which the PL peaks are pinned before blueshifting as the peaks lose intensity. Since the only periodic change over the different positions is the well thickness in monolayers, we assign the neighboring peak positions to quantum wells differing in thickness by one monolayer. This assignment is in agreement with the RHEED growth calibration. From Fig. 3 it is evident that due to the peak shift over the average well thickness, a submonolayer splitting between peaks is observed when comparing the positions of the different peaks for the same average thickness, i.e., in the PL measured at one position. Such submonolayer splitting (typically 0.8–0.9 ML) has been previously reported in literature.[2,4,6,8,10] In order to determine the absolute thickness of the wells, we find the position on the wafer where the thickness difference between wells (counted in ML steps in the PL spectra) matches exactly the RHEED-calibrated thickness difference. At this position, the actual well thickness equals the nominal thickness and, therefore, we can assign absolute quantum well thicknesses to the series of ML peaks, accurate to within 1 ML.

We find an excellent agreement between ML peak positions within each wafer and between wafers. Typical variations in peak position between Wafers 4 and 5 are of the same order as the variation within the wafers (under 0.5 meV). For intermediate well thicknesses, the agreement is better than 0.1 meV. For wells with thickness around 7 nm,

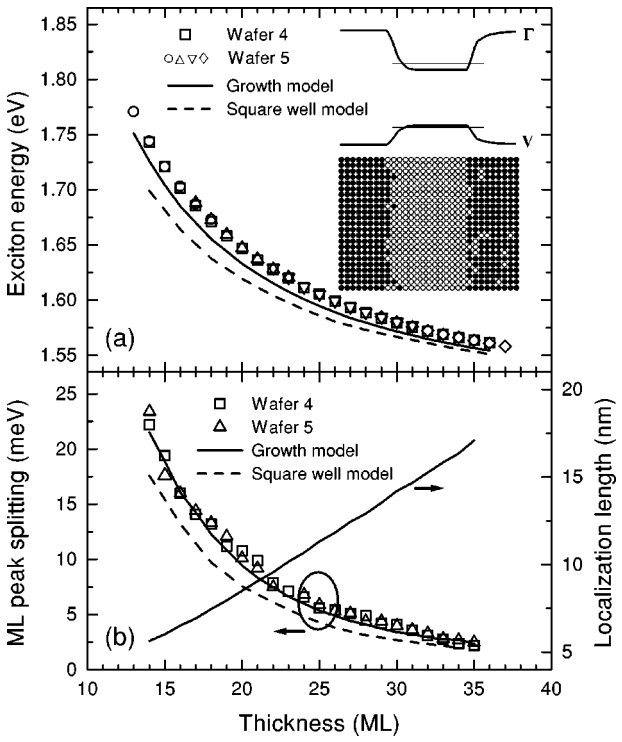

FIG. 5. (a) Discrete PL peak energies in growth-interrupted Wafer 4 (squares) and Wafer 5 (circles, diamonds, and triangles) demonstrating the reproducibility of peak positions measured in different wells and on different wafers. Also shown are calculated transition energies for a square well potential (dashed line) and a well potential where segregation effects are included (solid line). The diagram on the right schematically illustrates the calculated segregation in a 14 ML well with initially flat growth surfaces, along with the resulting well potential. (b) Experimental and theoretical values for the monolayer peak splitting. The calculated ML splitting is in excellent agreement with the measured values when segregation is included. The exciton localization length, determined from the peak splitting, is also shown.

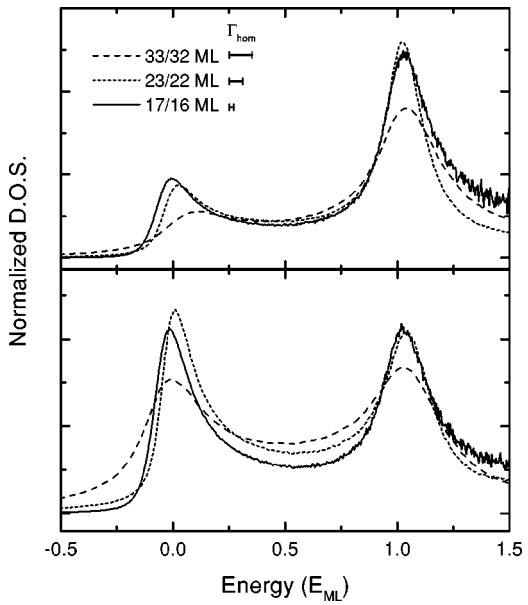

FIG. 6. Exciton optical density of states in wells of different thicknesses, plotted on a normalized energy scale. The graphs represent different island densities; 30% (top) and 50% (bottom). The spectra are normalized with respect to the total number of states. Horizontal bars indicate an upper limit of the homogeneous linewidth on each energy scale.

this corresponds to a maximum exciton-averaged thickness difference of less than 0.02 ML. It should be emphasized that several months passed between the growth of Wafers 4 and 5 and that the wafers have different barrier configurations and different nominal well thicknesses. The largest deviations (up to 0.3 ML) are observed for the narrowest wells (<16 ML) and for peaks measured close to the wafer edges.

In order to calculate the transition energies of our quantum wells we used an effective-mass model with two types of well potentials: (i) a simple finite-barrier square well potential with integral ML thickness and (ii) a nonabrupt potential obtained from a surface segregation model, where the possibility of cation interchange at the interfaces during overgrowth is taken into account. The calculation of the electronic states was carried out assuming an isotropic conduction band and using a six-band $\mathbf{k}\cdot\mathbf{p}$ approximation for the valence band. The physical parameters used in the calculation, along with a description of the segregation model, are provided elsewhere.[21] Well-width dependent heavy-hole exciton binding energies were calculated using the interpolation formula provided by Gurioli *et al.*[22] The variation of the GaAs band gap with temperature was determined from the shift in the near-bandgap luminescence of the GaAs substrate, giving $E_g(0\ \mathrm{K})-E_g(50\ \mathrm{K})=3.0$ meV. The results of the calculations are plotted in Fig. 5(a). We observe a significant blueshift of transition energies when segregation effects are included, up to 27 meV for 14 ML wells. Calculated ML peak splittings for the two types of well potential and measured values from Wafers 4 and 5 are plotted as a function of well thickness in Fig. 5(b). Excellent agreement between calculated and measured values of the peak splitting is obtained when segregation effects are taken into account. In Fig. 5(a) we also show schematically the calculated interface structure and resulting well potential for a 14 ML quantum well, assuming initially perfect growth surfaces. This clearly shows the importance of segregation, which introduces nanoroughness on the interface, even in the case of growth-interrupted QW's.

In Fig. 6, we show the ODOS for three different well widths from Wafer 4 on a monolayer energy scale. By carefully selecting the positions on the wafer, we compare spectra with average well widths of $(n+0.3)$ ML and $(n+0.5)$ ML, with $n=16$, 22, and 33. In the former case, the low-energy peak shifts to higher energy and becomes less defined with increasing well thickness while the position of the high-energy peak remains fixed. In the latter case, peak positions are unaffected but more states appear between the monolayer peaks. We note that this modification cannot be accounted for by the relative increase of the homogeneous linewidth $\Gamma_{\mathrm{hom}}\lesssim 0.7$ meV (Ref. 23), which is indicated for reference in the figure. We attribute the observed changes in the ODOS to the larger localization length in wider wells, as discussed in the following section.

V. DISCUSSION

In previous literature, simple quantitative models have generally been employed in order to explain the experimen-

tally observed ML peak splitting in the exciton luminescence from growth-interrupted quantum wells. These models assume that one or both interfaces consist of extended monolayer-high but atomically rough growth islands with sizes comparable to or larger than the exciton radius.[2–4,7,8,11–13] Sharp transition lines observed in micro-PL have furthermore been attributed to roughness-induced localization of exciton states.[24–27]

The case of a realistic well potential with a disorder correlation length smaller than the exciton radius has been treated theoretically in some detail.[28,29] Due to the small length scales of the disorder, these studies do not predict a splitting of the optical exciton density of states. In a recent work of Castella and Wilkins,[15] however, the problem is studied for a wider range of correlation lengths. Their analysis indicates (a) that the energy distribution of exciton states is mainly dependent on the ratio of island size (correlation length) to localization length, rather than the ratio of island size to exciton radius and (b) that ML peaks appear when the island size is similar to or larger than the localization length. The localization length represents the minimum lateral extension of a disk-shaped potential fluctuation which creates a bound state in the quantum-well plane,[15]

$$\xi_0 = \frac{\pi\hbar}{\sqrt{2MV_0}}. \tag{2}$$

V_0 is the strength of the confining potential, which is given by the monolayer peak spacing when the island size is larger than the exciton diameter. As a result, the localization length increases considerably with well thickness and larger growth islands are required in wider wells to observe ML splitting. In Fig. 5(b) we plot ξ_0 for the quantum wells of Wafers 4 and 5. The localization length varies from 6 nm to 18 nm, whereas the exciton radius $a_B = \hbar/\sqrt{2\mu E_b}$ only changes from 6 nm to 7 nm in the same well width range (calculated using values of exciton binding energies E_b from Ref. 22). We note that analysis based on the separation of the exciton wave function into relative and center-of-mass coordinates might not be valid in our narrowest wells (<16 ML), where the confinement potential exceeds the exciton binding energy.

The simulations of Castella and Wilkins[15] show that the shape of the exciton spectra is sensitive to the ratio between the correlation length scale ξ of the disordered quantum well potential and the localization length ξ_0. We note that a doublet structure in the exciton spectra is expected when the $\xi/\xi_0 \approx 1/2$ and a ML splitting occurs when $\xi/\xi_0 \approx 1$, with the splitting becoming gradually more defined as the ratio increases. By comparing the shape of our measured spectra (Figs. 2 and 6) with the simulations of Ref. 15 we can identify distinct regimes of potential fluctuations, corresponding to different ξ/ξ_0 ratios. Using localization lengths determined from Eq. (2) we can derive approximate length scales of interface roughness in our quantum wells.

(i) In the continuously grown quantum wells, the interface roughness is fully averaged over the exciton area and no splitting is observed in the PL spectra. By putting V_0 in Eq. (2) equal to the exciton-averaged potential variation, σ_E, determined from the lineshape fit presented in the previous section, we deduce that ξ_0 varies from 14 nm in narrow wells to 30 nm in wider wells. The degree of localization was also deduced independently via the localization energy parameter η in the lineshape fit. The relationship between the localization length and the localization radius is given by $\Delta R = (\xi_0/\pi)\sqrt{\sigma_E/\eta}$. We observe a constant σ_E/η ratio for all well widths, yielding a direct proportionality between ΔR and ξ_0. From the fact that we observe a single asymmetric ODOS peak, even in our narrowest wells where the localization length is shortest, we conclude, by comparison with simulations, that the typical correlation length in continuously grown wells is $\xi \lesssim \xi_0/4 \approx 3$ nm, much smaller than the localization length.

(ii) Interrupting growth at the bottom interface slightly changes the luminescence characteristics, most notably in wells under 7 nm thickness. We are therefore moving out of the small island regime, where the exciton in insensitive to the underlying potential fluctuation. Since no evidence of peak splitting is observed, the localization length in the narrow wells can still taken to be around 14 nm. The fact that no splitting is observed furthermore implies that $\xi_0/\xi < 1/2$ so we estimate the correlation length in this case to be 4–6 nm.

(iii) Wells with GI at the top interface show a weak splitting of the exciton peak, but no pinning of peak energies. The shape of the spectra agrees with simulation results in an intermediate regime, where island sizes approach half of the localization length, around 6–8 nm in this case. Here, the island size is also approaching the exciton diameter and the averaging of the potential becomes less important.

(iv) When growth is interrupted at both interfaces, islands become sufficiently large for the ODOS to split into discrete levels. From Fig. 6 we observe that the ML splitting is more pronounced in thinner wells, where the localization length is shorter. Comparison with simulations indicates that correlation lengths comparable to ξ_0 in thicker wells and up to $2\xi_0$ in thinner wells match our observations, giving a typical potential correlation length in all wells of 15–20 nm.

Growth-interruption is known to result in the formation of large growth islands on the GaAs surface, with sizes of more than 50 nm.[12,13] In samples with GI at both interfaces, we therefore attribute the observed 15–20 nm correlation length of the quantum well potential to the typical island size on the GI AlAs surface. When growth is not interrupted at the bottom interface (case iii), the island size is reduced to 6–8 nm. During GI, the AlAs surface therefore relaxes by enlarging the island size by a factor of 2–3, consistent with a slow surface diffusion of Al. Using GI only at the bottom interface (case ii), the observed potential correlation length is 4–6 nm. Knowing that typical island sizes on the GI AlAs surface are significantly larger, this length represents the island size on the non-GI GaAs surface. This is in agreement with STM studies on non-GI GaAs surfaces (grown at 580 °C) which have shown typical island sizes of 3–6 nm.[13] The deduced roughness length scales of 4–6 nm and 6–8 nm at non-GI top and bottom interfaces, respectively, are also consistent with the observed $\leqslant$3-nm combined potential correlation length in Wafer 1.

From the small variations in ML peak positions within each wafer and between wafers grown under similar conditions, we conclude that atomically smooth monolayer-high islands are formed on both AlAs and GaAs surfaces upon GI during MBE growth. A significant degree of nanoroughness on the growth islands would necessarily result in greater

fluctuations of the ML peak positions. Although atomically smooth AlAs surfaces can be formed during growth, atomic-scale nanoroughness still arises during overgrowth because of the segregation of Al atoms into the GaAs quantum well. This process results in an atomically rough interface, extending through approximately 2 ML, according to our simulations. Similarly, segregation of Ga atoms into the AlAs barrier also takes place at the top interface. The segregation length of Ga into AlAs is longer than that of Al in GaAs, but the effect of Ga segregation on transition energies is smaller since it occurs in the barrier rather than the quantum well. A higher degree of segregation might be responsible for a blue-shift of ML peaks observed with increasing growth temperatures.[11,18] The peak shift reported in these studies, however, is considerably larger than predicted by our simulations. The combination of surface diffusion during GI resulting in large atomically flat growth islands and atomic-scale segregation during overgrowth is the origin of the bimodal character of the interface roughness. In the case of non-GI quantum wells, the combined effects of small islands on as-grown surfaces and segregation will result in an nanorough interface of increased thickness and a smoother quantum well potential, consistent with a red-shift of luminescence upon GI, observed by us (Fig. 1) and others, e.g., Ref. 10.

VI. CONCLUSIONS

From the above discussion we stress the following points, frequently overlooked in the previous literature:

(i) Shifting of ML peaks and observation of sub-ML splitting in growth-interrupted quantum wells is due to the finite quantization energy of excitons localized in monolayer islands with sizes exceeding the exciton localization length. The localization length, which is determined by the monolayer splitting and the exciton mass, can be considerably larger than the exciton diameter. Positions of ML peaks for negligible in-plane quantization energy are reproducible in wafers grown under similar conditions.

(ii) Observation of interface nanoroughness in quantum wells does not imply nanoroughness on free as-grown surfaces. Instead, substantial interface roughness on the atomic scale is unavoidably introduced through surface segregation during growth, resulting in a bimodal distribution of the in-plane disorder potential correlation length, especially important in growth-interrupted quantum wells.

(iii) Surface segregation changes the shape of the quantum well potential, increasing ground-state transition energies as compared to a square quantum well potential with the same deposited thickness.

In summary, we have argued that atomically smooth growth islands can be formed on free AlAs and GaAs surfaces following growth interruption. The resulting correlation length of the well potential is sufficiently large, compared to the exciton localization length, to cause a monolayer splitting of the optical density of states. Segregation during the growth of the wells is responsible for formation of nanorough quantum well interfaces. A bimodal interface roughness therefore arises naturally when large atomically smooth islands are formed during growth. Furthermore, the segregation modifies the shape of the potential well, causing a blue-shift of transition energies.

ACKNOWLEDGMENTS

The samples were grown at III-V Nanolab, a joint laboratory between Research Center COM and the Niels Bohr Institute, Copenhagen University. The authors wish to thank Dr. C.B. Sørensen for his assistance with the MBE growth. This work was supported by the Danish Ministries of Industry and Research under the framework of CNAST (Center for Nanostructures).

*Present address: Lehrstuhl für Experimentelle Physik EIIb, Universität Dortmund, Otto-Hahn-Str. 4, 44227 Dortmund, Germany.

[1] A comprehensive review of luminescence studies of heterointerfaces until 1990 can be found in M. A. Herman, D. Bimberg, and J. Christen, J. Appl. Phys. **70**, R1 (1991).

[2] R.F. Kopf, E.F. Schubert, T.D. Harris, and R.S. Becker, Appl. Phys. Lett. **58**, 631 (1991).

[3] D. Gammon, B. V. Shanabrook, and D. S. Katzer, Appl. Phys. Lett. **57**, 2710 (1990).

[4] C.A. Warwick, W.Y. Jan, A. Ourmazd, and T.D. Harris, Appl. Phys. Lett. **56**, 2666 (1990).

[5] C.A. Warwick, R.F. Kopf, Appl. Phys. Lett. **60**, 386 (1992).

[6] B. Orschel, G. Oelgart, and R. Houdré, Appl. Phys. Lett. **62**, 843 (1993).

[7] J.C. Woo, S.J. Rhee, Y.M. Kim, H.S. Ko, W.S. Kim, and D.W. Kim, Appl. Phys. Lett. **66**, 338 (1995).

[8] Z.L. Yuan, Z.Y. Xu, B.Z. Zheng, C.P. Luo, J.Z. Xu, W. Ge, P.H. Zhang, X.P. Yang, J. Appl. Phys. **79**, 1073 (1996).

[9] K. Fujiwara, H.T. Grahn, and K.H. Ploog, Phys. Rev. B **56**, 1081 (1997).

[10] M.K. Chin and C.P. Luo, J. Lumin. **79**, 233 (1998).

[11] D. Gammon, B.V. Shanabrook, and D.S. Katzer, Phys. Rev. Lett. **67**, 1547 (1991).

[12] D. Bimberg, F. Heinrichsdorff, R.K. Bauer, D. Gerthsen, D. Stenkamp, D.E. Mars, and J.N. Miller, J. Vac. Sci. Technol. B **10**, 1793 (1992).

[13] R.F. Kopf, E.F. Schubert, T.D. Harris, R.S. Becker, and G.H. Gilmer, J. Appl. Phys. **74**, 6139 (1993).

[14] R. Grousson, V. Voliotis, N. Grandjean, J. Massies, M. Leroux, and C. Deparis, Phys. Rev. B **55**, 5253 (1997).

[15] H. Castella and J.W. Wilkins, Phys. Rev. B **58**, 16 186 (1998).

[16] A. Melliti, M.A. Maaref, and R. Planel, J. Lumin. **78**, 25 (1998).

[17] J. Zhang, P. Dawson, J.H. Neave, K.J. Hugill, I. Galbraith, P.N. Fawcett, and B.A. Joyce, J. Appl. Phys. **68**, 5595 (1990).

[18] D.S. Katzer, D. Gammon, B.V. Shanabrook, J. Vac. Sci. Technol. B **10**, 800 (1992).

[19] A. Manassen, E. Cohen, A. Ron, E. Linder, and L.N. Pfeiffer, Phys. Rev. B **54**, 10 609 (1996).

[20] R.F. Schnabel, R. Zimmermann, D. Bimberg, H. Nickel, R. Lösch, and W. Schlapp, Phys. Rev. B **46**, 9873 (1992).

[21] J.R. Jensen, J.M. Hvam, and W. Langbein, J. Appl. Phys. **86**, 2584 (1999).

[22] M. Gurioli, J. Martinez-Pastor, M. Colocci, A. Bosacchi, S. Franchi, and L.C. Andreani, Phys. Rev. B **47**, 15 755 (1993).

[23] T. Ruf, J. Spitzer, V.F. Sapega, V.I. Belitsky, M. Cardona, and K. Ploog, Phys. Rev. B **50**, 1792 (1994).

[24] K. Brunner, G. Abstreiter, G. Böhm, G. Tránkle, G. Weimann, and Appl. Phys. Lett. **64**, 3320 (1994).
[25] H.F. Hess, E. Betzig, T.D. Harris, L.N. Pfeiffer, and K.W. West, Science **264**, 1740 (1994).
[26] D. Gammon, E.S. Snow, and D.S. Katzer, Appl. Phys. Lett. **67**, 2391 (1995).
[27] U. Jahn, S.H. Kwok, M. Ramsteiner, R. Hey, H.T. Grahn, and E. Runge, Phys. Rev. B **54**, 2733 (1996).
[28] R. Zimmermann and E. Runge, J. Lumin. **60**, 320 (1994).
[29] Al.L. Efros, C. Wetzel, and J.M. Worlock, Phys. Rev. B **52**, 8384 (1995).

PHYSICAL REVIEW B VOLUME 61, NUMBER 16 15 APRIL 2000-II

Instantaneous Rayleigh scattering from excitons localized in monolayer islands

W. Langbein
Lehrstuhl für Experimentelle Physik EIIb, Universität Dortmund, Otto-Hahn Strasse 4, D-44227 Dortmund, Germany

K. Leosson, J. R. Jensen, and J. M. Hvam
Research Center COM, Technical University of Denmark, Building 349, DK-2800 Lyngby, Denmark

R. Zimmermann
Institut für Physik der Humboldt, Universität zu Berlin, Hausvogteiplatz 5-7, D-10117 Berlin, Germany

(Received 13 January 2000)

We show that the initial dynamics of Rayleigh scattering from excitons in quantum wells can be either instantaneous or delayed, depending on the exciton ensemble studied. For excitation of the entire exciton resonance, a finite rise time given by the inverse inhomogeneous broadening of the exciton resonance is observed. Instead, when exciting only a subsystem of the exciton resonance, in our case excitons localized in quantum well regions of a specific monolayer thickness, the rise has an instantaneous component. This is due to the spatial nonuniformity of the initially excited exciton polarization, which emits radiation also into nonspecular directions.

Light emission from resonantly excited excitons in semiconductor quantum wells (QW) receives continued interest. In particular, the emission dynamics after a short-pulse excitation is discussed.[1–4] The scattering of the excitation light into a nonspecular direction which differs from the transmitted or reflected directions is called secondary emission (SE), and involves scattering processes which are breaking the in-plane translational invariance of an ideal QW. The temporal coherence between the scattered and exciting light fields allows a distinction between scattering by static disorder, which preserves the coherence, and scattering by other quasiparticles, like phonons or excitons, which does not preserve the coherence. If static disorder dominates, the scattering is elastic and is called Rayleigh scattering. It was noticed early on[2] that excitons in QW's showed a delayed secondary emission, unlike what is observed in atomic vapors.[5] This is due to the fact that the spectrally integrated 1*s* excitonic oscillator strength is distributed uniformly in the QW plane. Scattering processes within the 1*s* exciton dispersion do not affect this property. Only when internally excited exciton states like the 2*s* or the continuum are mixed with the 1*s* state by the scattering, i.e., when the broadening of the exciton resonance is comparable to the exciton binding energy, this invariance is broken. Exciting the entire 1*s* exciton resonance only allows the initial macroscopic polarization to accommodate the incoming plane wave uniformly, and the initial emission occurs in specular directions only—no instantaneous SE is present. At finite times after excitation, the spatially varying time dynamics of the microscopic polarization, which is induced by the scattering processes, lead to a spatial disorder of the macroscopic polarization, and SE (into nonspecular directions) occurs. For static disorder scattering, a quadratic rise of the SE has been predicted[6,7] and observed.[3] For high exciton densities, exciton-exciton scattering was found to dominate the rise of the SE.[2,8] In this case, the initial dynamics is often described in the Markov-limit by a linear rise.

In the present work, we show that the delayed rise of the SE is relying on the excitation of the entire exciton resonance. When exciting only a part of the resonance, the in-plane uniformity of the initially excited polarization is broken, and an instantaneous rise of the SE is observed. For excitons in QW's, the experimental difficulty to measure such an instantaneous rise is to optically excite only a part of the exciton resonance with sufficient temporal resolution, i.e., with a pulse that is wider than the spectral width of the excited exciton distribution. This becomes possible when the exciton resonance is split into separated peaks, which can be achieved by growing QW's with a growth interrupt on both interfaces. The formation of growth islands larger than the exciton localization length[9,10] during the growth interrupt leads to a splitting of the excitonic absorption into distinct lines corresponding to regions of the QW differing in effective thickness by one monolayer (ML). To compare both cases of the initial SE dynamics, we investigate two different samples, grown with or without growth interruption. While the spectral widths of the excited excitonic distributions are similar in both samples, the SE rise is different, instantaneous for the monolayer peak of the growth interrupted sample, and delayed for the continuously grown sample.

The two investigated samples are GaAs single quantum wells (SQW's) grown on GaAs (100) wafers. The first sample (CG) was grown without growth interrupt, and contains a 12 nm thick GaAs well embedded in $Al_{0.3}Ga_{0.7}As$ barriers. In this sample, the surface growth islands are smaller than the exciton Bohr radius, and the segregation as well as the alloy disorder in the barriers introduce a disorder potential with an atomic scale correlation length. The sample shows an asymmetric excitonic absorption line shape (see Fig. 1). Such a line shape is typical for excitons localized by a potential with a correlation length much smaller than the exciton radius.[11]

The second sample (GI) contains a nominally 11 nm thick GaAs well embedded in AlAs barriers. The growth has been

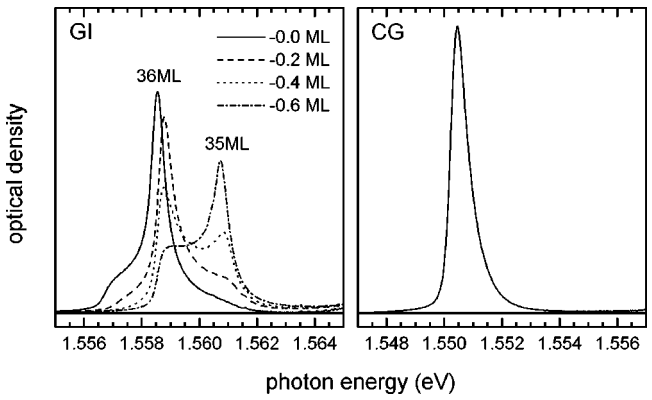

FIG. 1. Optical density of the excitonic resonance in the investigated SQW samples, deduced from the photoluminescence at 30 K lattice temperature. Left: sample GI, a growth interrupted 11 nm GaAs/AlAs well at several positions along the thickness gradient. The labels give the estimated differences in the average well thickness for the different positions. Right: sample CG, a continuously grown 12 nm GaAs/$Al_{0.3}Ga_{0.7}As$ well.

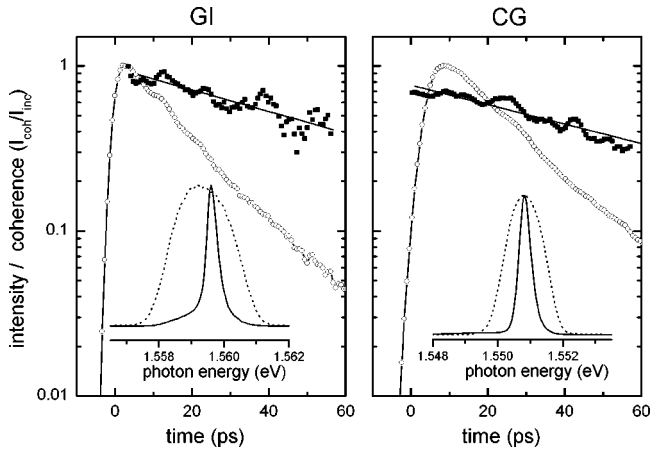

FIG. 2. Secondary emission intensity (open circles) and its coherence (closed squares) deduced from the speckle statistics. Left: sample GI for the -0.2 ML position. Right: sample CG. In the insets the intensity spectra of the respective exciting pulse (dotted line) and secondary emission (solid line) are shown.

interrupted for 120 s at each interface to enable the formation of larger monolayer islands on the respective surfaces. This results in a splitting of the exciton resonance into so-called monolayer peaks, which are related to excitons localized in QW regions with effective thicknesses differing by integer monolayers. The broadening of each monolayer peak is due to the finite size of the growth islands, leading to varying in-plane quantization energies, and due to an atomic-scale interface roughness formed by segregation during the overgrowth on the surfaces. We have chosen a rather wide GaAs well in order to reduce the spectral width of the monolayer peaks originating from the atomic-scale interface roughness. However, the monolayer splitting is reduced by the same factor, while the in-plane quantization energies are constant, and thus the monolayer peaks are not as well distinguished as for narrower wells. Rotation of the substrate was stopped during the growth of the well in order to achieve a continuous variation in well thickness across the wafer. This allows us to tune the well thickness for the best linewidth. More details about the growth and characterization are given in Ref. 9. In the following experiments we choose the sample position -0.2 ML in Fig. 1. The samples are placed in a helium cryostat at a temperature of 5 K. The exciton resonance is excited by optical pulses from a mode-locked Ti:sapphire laser spectrally shaped to about 1 ps Fourier-limited pulse width. The SE in various directions is spectrally filtered by a monochromator and detected by a synchroscan streak camera with a time resolution of about 3 ps. The angular resolution achieved by the second dimension of the streak camera was adjusted to the speckle size, i.e., to the diffraction limit of the emission from the excited area on the sample.[12] The spectral resolution of about 1 meV rejects nonresonant emission, but does not deteriorate the temporal resolution. All presented data were taken with excitation in Brewster angle and detection normal to the sample, through an analyzer parallel to the linear excitation polarization.

From the temporally and directionally resolved emission intensity $I(t,\vec{q})$, the speckle analysis technique[12–15] can deduce the average emission intensity $\overline{I(t)}$, and the average coherence $c=\overline{I_{\rm coh}}/\overline{I}$ where the average is taken over the scattering directions $\vec{q}$ at fixed time, and $I_{\rm coh}$ is the SE intensity which is coherent to the excitation (RRS). A simple model[12] for localized 1*s* excitons in a SQW is a spatially homogeneous distribution of oscillators with Gaussian distributed, spatially uncorrelated transition frequencies of variance σ. Each state has the same polarization decay rate due to radiative loss and phonon dephasing, $\Gamma=\Gamma_{\rm rad}+\Gamma_{\rm phon}$. For the emitted intensity $\overline{I(t)}$ after a δ-like excitation pulse at $t=0$ one gets[12]

$$\overline{I}(t)\propto e^{-2\Gamma_{\rm rad}t}(1-e^{-\sigma^2t^2-2\Gamma_{\rm phon}t}), \tag{1}$$

$$c(t)=(1-e^{-\sigma^2t^2})/(e^{2\Gamma_{\rm phon}t}-e^{-\sigma^2t^2}).$$

The measured $\overline{I(t)}$ and $c(t)$ are displayed in Fig. 2 for the two investigated samples. The corresponding SE spectra are shown in the inset together with the exciting laser pulse. The full width at half maximum (FWHM) of the SE spectra are 0.42 (0.4) meV for the sample GI (CG), corresponding to $\sigma^{-1}=3$ ps (3.3 ps). The laser spectra are of 2.3 meV (1.4 meV) FWHM, corresponding to 0.8 ps (1.3 ps) long pulses. Both samples show, after the initial transient, an exponential decay of the secondary emission intensity with 16 ps (19 ps) decay time, and of the emission coherence with 66 ps (74 ps) decay time, respectively. From the decay we deduce according to Eq. (1) a $\Gamma_{\rm rad}$ of 21 μeV (17 μeV), and a $\Gamma_{\rm phon}$ of 5 μeV (4.5 μeV). Both the lifetime and the dephasing times are thus much longer than the inverse inhomogeneous broadening, which implies that the initial dynamics is dominated by the inhomogeneous broadening and that the initial SE is dominantly RRS.

The initial dynamics for both samples is displayed on a linear scale in Fig. 3 together with the response function of the streak camera. The dynamics according to Eq. (1), convoluted with the streak response, is given by the solid lines ($\alpha=1$), using the parameters given above. The data for the GI sample show a much faster rise than this calculation, while the data from the CG sample are in full agreement.

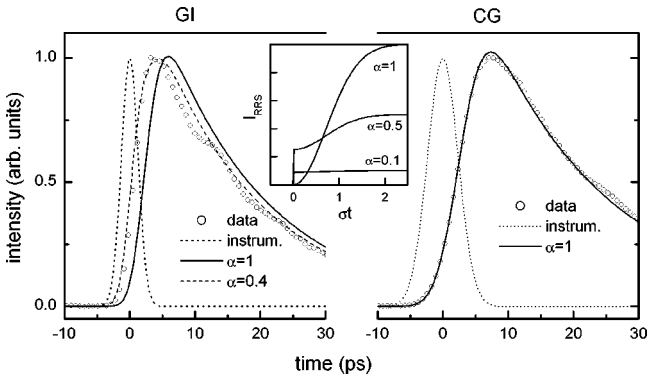

FIG. 3. Initial secondary emission intensity dynamics (circles), compared with the prediction of Eq. (1) (solid) and Eq. (2) for $\alpha = 0.4$ (dashed), and the instrument response (dotted). Left: sample GI for the -0.2 ML position. Right: sample CG. The inset shows $\overline{I}(t)$ from Eq. (2) for various values of α and $\Gamma_{rad}=\Gamma_{phon}=0$.

The dynamics in the GI sample thus do not show the quadratic rise given by the inhomogeneous broadening as predicted by Eq. (1), but a much faster response, indicating an instantaneous contribution to the RRS.

To include the influence of growth islands into the model of Eq. (1), we can assign to each exciton a monolayer thickness, where the spatial distribution of the monolayers is random on a length scale of the light wavelength. Only excitons belonging to the selected monolayer are optically excited, and are thus contributing to the SE. With the probability α of an exciton to belong to the excited monolayer, we get

$$\overline{I}(t) \propto \alpha e^{-2\Gamma_{rad}t}(1-\alpha e^{-\sigma^2 t^2 - 2\Gamma_{phon}t}), \qquad (2)$$

$$c(t) = (1-\alpha e^{-\sigma^2 t^2})/(e^{2\Gamma_{phon}t} - \alpha e^{-\sigma^2 t^2}).$$

The calculated initial dynamic for different α and neglecting Γ_{rad} and Γ_{phon} is shown in the inset of Fig. 3. The SE intensity acquires an instantaneous contribution of a fraction $1-\alpha$ of the total signal. For a small concentration of excited resonances, as it is the case in atomic vapors or for impurity-bound excitons in bulk semiconductors, the predicted RRS rise is thus completely instantaneous. For the present case of excitons localized in monolayer islands, typically 2–3 different monolayer thicknesses exist for a given average thickness,[9,16,17] which is compatible with $\alpha \approx 0.4$. In this case, both an instantaneous and a delayed component is expected. The calculation using Eq. (2) convoluted with the streak camera response is given as a dashed line in Fig. 3. It agrees with the data on the GI sample. We thus conclude that the dynamics of the CG sample is well described by the model with a spatially homogeneous distribution of the optically excited excitons. In contrast, the GI sample shows a faster rise, which is instantaneous within our time resolution. We assign this instantaneous RRS contribution to the spatial nonuniformity of the excitons belonging to one monolayer thickness. This behavior is illustrated in Fig. 4.

In the CG sample (upper row), the initially excited polarization is constant ($\sigma t = 0$), while in the GI sample, only the regions of the selected monolayer thickness are excited, and the polarization has a corresponding spatial pattern, which implies that RRS is present already at $\sigma t = 0$. For a finite time

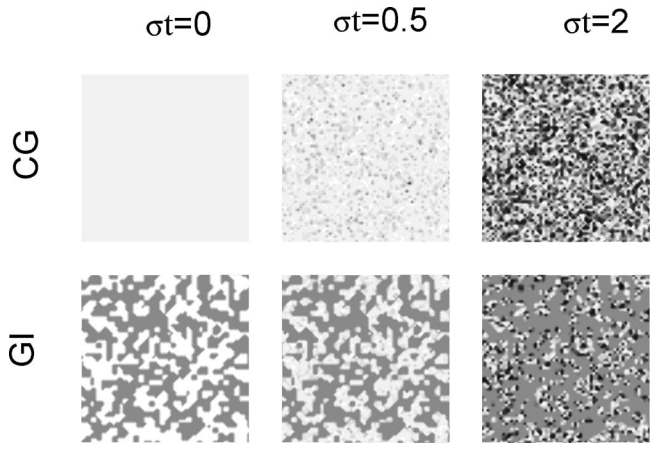

FIG. 4. Illustration of the spatial dynamics of the macroscopic polarization following excitation of the whole exciton resonance (top) or only one monolayer peak (bottom). The grayscale is linear, and centered at zero. The pictures have been generated from a 64 $\times$ 64 array of resonances with Gaussian-distributed eigenenergies, excited at $t=0$ by a δ pulse. In the case of the GI, the resonances are only active at the positions given by the pattern visible at $\sigma t = 0$, for which $\alpha = 0.5$.

after excitation ($\sigma t = 0.5$), the initially in-phase excited polarization from the individual localized excitons becomes out of phase, due to their different eigenenergies, which leads to a spatially varying macroscopic polarization. After the initial transient ($\sigma t = 2$), the phases of the individual excitons are fully random, and strong SE occurs. This is equivalent in the GI structure, but here, the initial spatial variation is only weakly increasing at later times.

The length scale of the monolayer islands is about[9] 20 nm, significantly lower than the wavelength of the emitted light. The SE is thus emitted isotropically in all directions. Since the growth islands are rather small, typically only one localized exciton state is situated in each island, and the phase of the macroscopic polarization has a common time evolution within one island. On a length scale of 10 nm, the spatial pattern of the macroscopic polarization is thus markedly different for the two investigated structures, which might be important in modelling the long-term RRS dynamics by microscopic models for QW's with large correlation lengths of the disorder potential.[18]

In conclusion, we have demonstrated that the initial dynamics of the SE from excitons in QWs can acquire an instantaneous contribution in a situation where the excited exciton polarizability is spatially nonuniform. This is expected not only to be important in the investigated case of a monolayer peak, but also for samples of larger disorder, in which internally excited states of the exciton are mixed into the broadened $1s$ excitonic resonance.

The samples were grown at III-V Nanolab, a joint laboratory between Research Center COM and the Niels Bohr Institute, Copenhagen University. The authors wish to thank Dr. C.B. Sørensen for his assistance with the MBE growth, P. Borri for stimulating discussions, and Tele Danmark R/D for the donation of experimental equipment. This work was supported by the German Science Foundation (DFG) within the ''Schwerpunktprogramm Quantenkohärenz in Halbleitern.''

[1] H. Stolz, D. Schwarze, W. von der Osten, and G. Weimann, Phys. Rev. B **47**, 9669 (1993).
[2] H. Wang, J. Shah, T. Damen, and L. Pfeiffer, Phys. Rev. Lett. **74**, 3065 (1995).
[3] S. Haacke, R. Taylor, R. Zimmermann, I. Bar-Joseph, and B. Deveaud, Phys. Rev. Lett. **78**, 2228 (1997).
[4] D. Birkedal and J. Shah, Phys. Rev. Lett. **81**, 2372 (1998).
[5] S. Haroche, in *High Resolution Laser Spectroscopy*, Vol. 13 of *Topics in Applied Physics* (Springer, Berlin, 1976), pp. 253–313.
[6] R. Zimmermann, Nuovo Cimento D **17D**, 1801 (1995).
[7] D. S. Citrin, Phys. Rev. B **54**, 14 572 (1996).
[8] S. Haacke, G. Hayes, R. A. Taylor, B. Deveaud, R. Zimmermann, and I. Bar-Joseph, Phys. Status Solidi B **204**, 35 (1997).
[9] K. Leosson, J. R. Jensen, W. Langbein, and J. M. Hvam, Phys. Rev. B **61**, 10 322 (2000).
[10] H. Castella and J. W. Wilkins, Phys. Rev. B **58**, 16 186 (1998).
[11] R. Zimmermann and E. Runge, J. Lumin. **60-61**, 320 (1994).
[12] W. Langbein, J. M. Hvam, and R. Zimmermann, Phys. Rev. Lett. **82**, 1040 (1999).
[13] W. Langbein and J. M. Hvam, in *Advances in Solid State Physics*, edited by B. Kramer (Vieweg, Braunschweig, 1999), Vol. 39, pp. 463–472.
[14] E. Runge and R. Zimmermann, in *Advances in Solid-State Physics*, edited by B. Kramer (Vieweg, Braunschweig, 1999), Vol. 39, pp. 423–432.
[15] W. Langbein and J. M. Hvam, Phys. Status Solidi A. (to be published).
[16] D. Gammon, B. V. Shanabrook, and D. S. Katzer, Phys. Rev. Lett. **67**, 1547 (1991).
[17] R. F. Kopf, E. F. Schubert, T. D. Harris, and R. S. Becker, Appl. Phys. Lett. **58**, 631 (1991).
[18] V. Savona, S. Haacke, and B. Deveaud, Phys. Rev. Lett. **84**, 183 (2000).

Second-harmonic imaging of semiconductor quantum dots

John Erland[a)]
Research Center COM, Technical University of Denmark, Building 349, DK-2800 Lyngby, Denmark

Sergey I. Bozhevolnyi and Kjeld Pedersen
Institute of Physics, Aalborg University, Pontoppidanstræde 103, DK-9220 Aalborg, Denmark

Jacob R. Jensen and Jørn M. Hvam
Research Center COM, Technical University of Denmark, Building 349, DK-2800 Lyngby, Denmark

(Received 30 March 2000; accepted for publication 12 June 2000)

Resonant second-harmonic generation is observed at room temperature in reflection from self-assembled InAlGaAs quantum dots grown on a GaAs (001) substrate. The detected second-harmonic signal peaks at a pump wavelength of ~885 nm corresponding to the quantum-dot photoluminescence maximum. In addition, the second-harmonic spectrum exhibits another smaller but well-pronounced peak at 765 nm not found in the linear experiments. We attribute this peak to the generation of second-harmonic radiation in the AlGaAs spacer layer enhanced by the local symmetry at the quantum-dot interface. We further observe that second-harmonic images of the quantum-dot surface structure show wavelength-dependent spatial variations. Imaging at different wavelength is used to demonstrate second-harmonic generation from the semiconductor quantum dots. © *2000 American Institute of Physics.* [S0003-6951(00)00932-3]

Second-harmonic generation (SHG) is extremely sensitive to the symmetry of materials[1] and is widely used as a nondestructive and noncontact probe of surfaces and interfaces.[2] Furthermore, starting with the first experiments on spatially resolved SHG from a dye monolayer,[3] SHG microscopy has appeared as a very useful characterization tool for *inhomogeneous* surfaces. It has recently been applied to imaging of periodically poled ferroelectric domains,[4] poled silica waveguides,[5] and domain walls,[6] domain structures in epitaxially grown magnetic garnet films[7] and polymer monolayers,[8] and polar orientational distribution in thin polymer films.[9] Semiconductor quantum dots (QDs), whose unique properties promise wide applications in optoelectronics,[10] is yet another interesting object for SHG microscopy. The electronic eigenstates of the QDs are strongly influenced by their sizes and shapes as well as by strain and piezoelectric fields.[11] Self-assembled InAs/GaAs QDs have been extensively studied with various methods,[10] however, the wealth of information encoded in the *nonlinear* optical coefficients is still largely unexplored. As far as SHG is concerned, the main problem is related to the fact that GaAs possesses very large second-order susceptibilities,[12] so that any second harmonic (SH) radiation from the QDs has to be distinguished from the SH generated in GaAs. Our idea is to use SHG in configurations where the bulk and surface contributions are forbidden for a homogeneous sample, so that the only source of SHG is associated with nanostructures embedded in the host material.[13]

In this letter, we demonstrate that, for normal incidence of resonant pump radiation, SHG in reflection from a sample containing selfassembled $In_{0.50}Al_{0.08}Ga_{0.42}As$ QDs grown on a GaAs (001) substrate is dominated by the SH radiation from the QDs. The spectral analysis shows correspondence to the energy eigenstates characterized by photoluminescence (PL) measurements. The wavelength dependence of the SH signal is found to exhibit another peak at 765 nm, which is related to the interface between the QD layer and the AlGaAs spacer layer. Furthermore, we present preliminary results on wavelength resolved SH imaging of QDs conducted for different linear polarizations of the SH radiation. Transformation of the SH images when changing the pump wavelength is observed and attributed to the spatially varying conditions for SHG generation at the inhomogeneous surface and therefore essential for the identification of the SH radiation from the QDs.

The QD sample used in this work was fabricated by molecular beam epitaxy, where 6 monolayers of $In_{0.50}Al_{0.08}Ga_{0.42}As$ were grown with 100 (20) nm $Al_{0.16}Ga_{0.84}As$ bottom (top) spacer layer and 8 nm $Al_{0.40}Ga_{0.60}As$ barriers terminated with a GaAs cap layer of 20 nm. The molefractions of the QD material was chosen to fit the energies of the QD states into a wavelength range accessible with the Ti:sapphire laser used for the SHG, see the following. The Stranski–Krastanow formation of the QDs was evident from the reflection high energy electron diffraction spectrum during growth as well as from atomic force microscope studies of uncapped QD samples grown under similar conditions indicating typical QD distances of 50 nm. To remove possible influences from the semi-insulating (001) GaAs substrate on the SHG experiments, a 500 nm GaAs buffer layer was grown on top of an etch layer of 50 nm AlAs. After etching with 10% hydroflouric acid and lift-off using a wax, the QD sample was mounted on a high optical quality sapphire substrate using only van der Waals forces to avoid any additional strain in the sample.

The mounted QD sample was characterized by measuring the PL spectrum at room temperature [Fig. 1(a)]. The PL spectrum, after excitation with a HeNe laser over two de-

a)Author to whom all correspondence should be addressed; electronic mail: jeo@com.dtu.dk

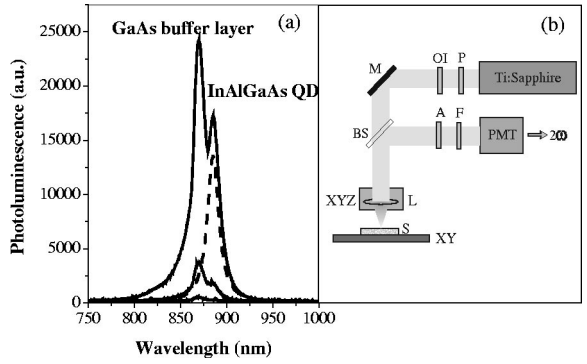

FIG. 1. (a) Photoluminescence characterization of the QD sample for three different HeNe (632.8 nm) laser light intensities (solid) revealing the GaAs buffer layer at 870 nm and the QD resonance at the design wavelength of 885 nm. The extracted QD resonance with a linewidth of 15 nm from line shape analysis is shown as a dashed line. (b) The second-harmonic imaging setup in reflection with a PMT: photomultiplier, BS: beam splitter, S: sample, M: mirror, L: focusing lense, OI: optical isolator, F: filter, A: analyzer, and P: polarizer.

cades of cw power up to 1 mW focused to a spot of $\sim 40\,\mu$m, shows two strong resonances: the PL from the GaAs buffer layer at 870 nm (1.42 eV) and from the QDs at the design wavelength of 885 nm (1.40 eV). From the spectra we estimate an inhomogeneous broadening of the QDs of 15 nm (24 meV), i.e., the QD eigenstates are well separated from the GaAs absorption band edge. The InAlGaAs wetting layer resonance appeared as a small shoulder on the GaAs PL signal at ~ 810 nm, but was not directly observable in the SHG experiments.

The experimental setup for SHG microscopy represents a scanning optical microscope in reflection geometry [Fig. 1(b)]. The linearly polarized light beam from a mode-locked Ti-sapphire laser ($P_{\omega}^{\mathrm{av}} \approx 50$ mW, repetition rate $f \approx 80$ MHz, pulse duration $\tau \sim 200$ fs) was focused on the sample surface at normal incidence with a $\times 40$ microscope objective (the spot size $\sim 2\,\mu$m), and the sample was scanned along the surface plane by a stepper-motor driven xy stage. The reflected SH radiation was detected with a photomultiplier, whose output was recorded as a function of the scanning coordinate (with the step length of 0.25 μm). Note that only at normal incidence is the SHG from the *bulk* and the *surface* forbidden by symmetry. Our first measurements in GaAs showed that the SHG in reflection (at carefully adjusted normal incidence) from a (001) substrate was negligibly small, and the SH signal was more than three orders of magnitude weaker than that from a (111) substrate.[13] We have used an optical isolator to avoid the reflected pump beam coupling back into the laser cavity [Fig. 1(b)]. The incident pump beam was linearly polarized either along the x or y axis in the experimental setup, and we detected the SH radiation at two orthogonal linear polarizations x and y. Because of the lift-off of the sample, the crystal axis of the sample was unknown. However, in the investigations of the SH signals for the four different combinations of linear polarizations between the incident pump and the detected SHG signal, the SH signal in the yy configuration was on average one order of magnitude larger than that in the other combinations (data not shown). With the investigated QD sample and the polarization configuration with the best SHG yield, a resonant pump power of about 50 mW at the sample resulted in SH

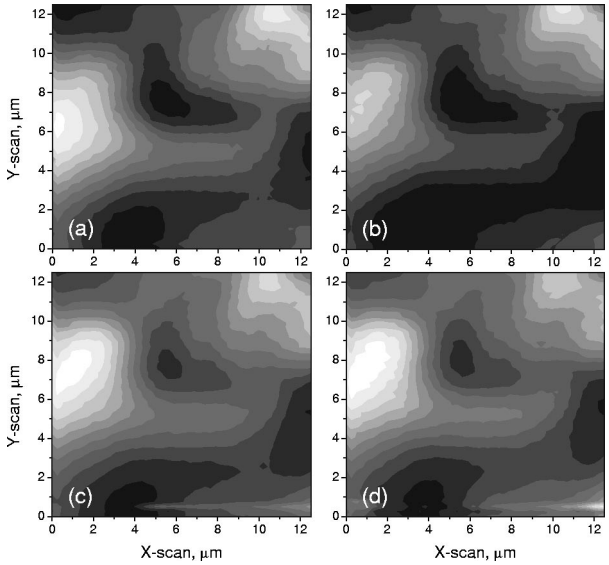

FIG. 2. Room temperature second-harmonic images recorded at pump wavelengths of: (a) 896 nm, (b) 885 nm, (c) 879 nm, and (d) 875 nm.

signals in the range $10^3 - 10^4$ counts/s. This signal level allowed us to use a count time of 0.1 s and to record SH images containing 100×100 points within ~ 16 min.

The main features observed in our experiment are (i) the spatial dependence of the SH signal, (ii) the transformation of the SH image with the wavelength (Fig. 2), and (iii) the wavelength dependence of the average SH signal (Fig. 3). Strong enhancement of the average SH signal at ~ 885 nm with the width of the enhancement (< 20 nm) being comparable to the linear QD PL spectrum is observed [cf. Figs. 3 and 1(a)]. This indicates that the detected SH radiation originates from QDs, whose energy states are inhomogeneously broadened. With the spot size obtainable in far-field microscopy, the incident beam interacts with a large ($\sim 10^4$) number of QDs and the SH signal averages out the responses of individual QDs. However, we have observed that the SH images show strong variation in the SH signal (Fig. 2). This feature can be attributed to variations mainly due to the local

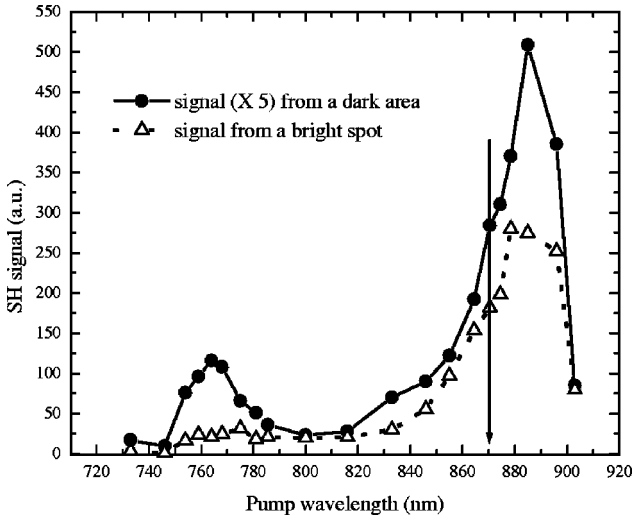

FIG. 3. The spectral changes of the SHG signal recorded at the darker spot (open circles) in the center (dark area) and at the brighter spot to the left (open triangles) of the images in Fig. 2. The vertical arrow indicates the absorption band edge for GaAs at 870 nm.

surface orientation since the large number of QDs average their spatial variation and their individual optical response. Since the positions of bright and dark spots were found to be stable with respect to the pump wavelength, we believe that bright spots represent the areas that are locally tilted with respect to the average surface plane. Such a tilt would break the symmetry and allow SHG from the bulk, i.e., from the GaAs buffer layer. Therefore, one should expect that the SH signal from bright spots may contain a substantial contribution from the bulk SHG. Indeed, the main peak in the SHG spectrum obtained at the bright spot is shifted toward lower wavelengths (in comparison with the peak from the dark spot) and exhibits a pronounced shoulder at the wavelength of 870 nm corresponding to the maximum of PL from the GaAs buffer layer (Fig. 3). Actually, a similar (but less pronounced) shoulder is also seen in the main peak obtained at the dark spot indicating that, even at normal incidence, there is a (relatively weak) bulk contribution to SHG. This contribution can be accounted for by the fact that the pump light is scattered by the embedded nanostructures so that the local normal incidence condition is not fulfilled for the *scattered* light. The same reasoning can be used to explain a second peak in the SHG spectrum at 765 nm (Fig. 3), which corresponds to the room temperature band gap of the $Al_{0.16}Ga_{0.84}As$ spacer layer.[14] Finally, let us notice that the *shape* of the dark spot depends on the pump wavelength (Fig. 2). We believe that this modification can be related to the interplay between the SHG response from the dark and bright areas with different spatial and spectral SHG response. The observed features demonstrate that the wavelength resolved SHG microscopy is a very sensitive tool for investigation of nanostructured semiconductors.

In conclusion, we have demonstrated SHG from semiconductor QDs at room temperature using resonant sample illumination at normal incidence. In this configuration, the second-order nonlinear optical susceptibility $\chi^{(2)}$ due to bulk and surface contributions from the different semiconductor layers composing the structure is ideally zero. The SHG spectrum is peaked at 885 nm in accordance with the InAlGaAs QD spectrum of the PL. Scanning over the sample surface was used to map the strength of SHG over a surface area of $12.5\times12.5\,\mu m^2$. The SH imaging was used to separate the SH signals from the QDs and the GaAs bulk, whose contribution notably increases when the normal incidence condition deteriorates. This furthermore enabled the observation of a second peak in the SHG spectrum at 765 nm resulting from light scattering at the interface between the QD layer and the AlGaAs spacer layer. Finally, we would like to stress that, contrary to the PL characterization technique, the SHG microscopy in reflection used in this work is *inherently insensitive* to the presence of a GaAs substrate even at *room temperature*. It can therefore be successfully used at room temperature to study embedded nanostructures without etching away a substrate.[13] This is normally a complicated procedure which makes subsequent characterization, e.g., determination of the orientation of the crystal axis, very difficult because of reduced sample quality. We believe that further exploration of this technique would enable us to investigate various fascinating phenomena such as the influence of strain and piezoelectric fields on the QD characteristics.[11]

The authors gratefully acknowledge financial support from the Danish Natural Science Research Council under Contracts 9901971 and 9903131.

[1] R. W. Boyd, *Nonlinear Optics* (Academic, London, 1992).
[2] T. F. Heinz, in *Nonlinear Surface Electromagnetic Phenomena*, edited by H. Ponath and G. Stegeman (Elsevier, Amsterdam, 1991), p. 353.
[3] G. T. Boyd, Y. R. Shen, and T. W. Hänsch, Opt. Lett. **11**, 97 (1986).
[4] S. Kurimura and Y. Uesu, J. Appl. Phys. **81**, 369 (1997); Y. Uesu, S. Kurimura, and Y. Yamamoto, Appl. Phys. Lett. **66**, 2165 (1995).
[5] J. Arentoft, K. Pedersen, S. I. Bozhevolnyi, M. Kristensen, P. Yu, and C. B. Nielsen, Appl. Phys. Lett. **76**, 25 (2000).
[6] S. I. Bozhevolnyi, J. M. Hvam, K. Pedersen, F. Laurell, H. Karlsson, T. Skettrup, and M. Belmonte, Appl. Phys. Lett. **73**, 1814 (1998).
[7] V. Kirilyuk, A. Kirilyuk, and Th. Rasing, Appl. Phys. Lett. **70**, 2306 (1997).
[8] M. Flörsheimer, Phys. Status Solidi A **173**, 15 (1999).
[9] J. Vidra and M. Eich, Appl. Phys. Lett. **72**, 275 (1998).
[10] D. Bimberg, M. Grundmann, and N. N. Ledentsov, *Quantum Dot Heterostructures* (Wiley, Chichester, 1998).
[11] O. Stier, M. Grundmann, and D. Bimberg, Phys. Rev. B **59**, 5688 (1999).
[12] D. N. Nikogosyan, *Properties of Optical and Laser-Related Materials: A Handbook* (Wiley, Chichester, 1997).
[13] J. Erland, P. Yu, S. I. Bozhevolnyi, J. M. Hvam, and N. N. Ledentsov, *Technical Digest QELS'99* (Baltimore, Maryland, May 1999), p. 233.
[14] L. Pavesi and M. Guzzi, J. Appl. Phys. **75**, 4779 (1994).

phys. stat. sol. (b) **221**, 49 (2000)

Subject classification: 71.35.Cc; 78.55.Cr; 78.66.Fd; S7.12

Linewidth Statistics of Single InGaAs Quantum Dot Photoluminescence Lines

K. LEOSSON[1]) (a), J. R. JENSEN (a), J. M. HVAM (a), and W. LANGBEIN (b)

(a) Research Center COM, Technical University of Denmark, Bldg. 345v, DK-2800 Kgs. Lyngby, Denmark

(b) Lehrstuhl für Experimentelle Physik EIIb, Universität Dortmund, Otto-Hahn-Str. 4, D-44227 Dortmund, Germany

(Received April 10, 2000)

We have used photoluminescence spectroscopy with high spatial and spectral resolution to measure the linewidths of single emission lines from $In_{0.5}Ga_{0.5}As$/GaAs self-assembled quantum dots. At 10 K, we find a broad, asymmetric distribution of linewidths with a maximum at 50 μeV. The distribution of linewidths is not significantly influenced by small variations in the quantum dot confinement potential. We claim that the wider transition lines are broadened by local electric field fluctuations while narrower lines are homogeneously broadened by acoustic-phonon interactions. The width of narrow single-dot luminescence lines depends only weakly on temperature up to 50 K, showing a broadening of 0.4 μeV/K. Above 50 K, a thermally activated behavior of the linewidth is observed. This temperature dependence is consistent with the discrete energy level structure of the dots.

Probing of photoluminescence (PL) with a high spatial resolution has become a standard tool for optical characterization of semiconductor nanostructures [1]. Initial high-resolution studies of excitons localized at width fluctuations in quantum wells [2] and in self-assembled quantum dots [3] demonstrated that the inhomogeneously broadened photoluminescence could be resolved into sharp (<100 μeV FWHM) luminescence lines. A combination of high spatial and spectral resolution can thus be used to directly determine the intrinsic linewidth of individual optical transitions within an inhomogeneously broadened ensemble. The natural linewidth is a parameter of interest, both fundamentally and for device applications, and provides information about the homogeneous broadening mechanisms in the system. The transition linewidth and its dependence on temperature has been investigated for localized excitons in GaAs/AlGaAs by several authors [4 to 6] and for InAs and AlInAs self-assembled quantum dots embedded in $Al_{0.3}Ga_{0.7}As$ by Ota et al. [6]. In the present work, we report a statistical analysis of the linewidths of individual transitions in self-assembled $In_{0.5}Ga_{0.5}As$ quantum dots (QDs). Furthermore, we discuss the temperature dependence of single emission lines, which we have observed up to 95 K. $In_{0.5}Ga_{0.5}As$ quantum dots are a suitable gain material for low-threshold quantum-dot lasers [7] and their homogeneous linewidth at room temperature has been reported [8] to be about 5 meV.

The quantum dot heterostructures were grown by molecular beam epitaxy on GaAs (001) substrates. Five monolayers of $In_{0.5}Ga_{0.5}As$ were grown at 520 °C, one monolayer

[1]) Corresponding author: Tel.: +45 4525 6352; Fax: +45 4593 6581; e-mail: kl@com.dtu.dk

at a time with growth interrupts of 8 s between the monolayers, and sandwiched between GaAs barriers. Growth was interrupted for additional 60 s after growth of the quantum dot layer. 8 nm AlAs layers were placed 100 nm below and 20 nm above the $In_{0.5}Ga_{0.5}As$ layer to confine carriers to the quantum dot region. Atomic force microscope investigation of uncapped samples revealed a dot density of approximately 2×10^{10} cm^{-2}.

For photoluminescence measurements, the sample was excited over the GaAs barrier bandgap using a He–Ne laser or below the barrier bandgap with a tunable cw Ti:sapphire laser. The excitation and detection were done confocally through a 0.85 NA microscope objective located inside a closed-cycle He cryostat. The luminescence was dispersed in a spectrometer and detected by a Peltier-cooled coupled-charge-device array. For high-resolution measurements, a 2 m Littrow spectrometer with a resolution better than 20 μeV was used. In order to further improve the spatial resolution of our measurement and to be able to relocate specific areas on the sample, the photoluminescence was collected through sub-micron sized apertures in an 80 nm Au film on the sample. The apertures were fabricated with electron-beam lithography.

In conventional (macroscopic) PL measurements, we observe a Gaussian luminescence peak with a width (FWHM) of 39 meV, centered at 1.325 eV, as shown in Fig. 1a. A micro-photoluminescence spectrum recorded through a single 250 nm diameter aperture is also plotted in the figure. The latter spectrum clearly shows isolated sharp photoluminescence lines corresponding to transitions between individual localized states. One of the single emission lines is shown at different temperatures in Fig. 1b, illustrating the temperature broadening. The shown emission line is in all cases well described by a Lorentzian function, indicating a homogeneously broadened transition.

Spectral linewidths of several hundred single emission lines were determined from micro-PL spectra measured with a 17 μeV spectral resolution at 100 W/cm^2 of non-reso-

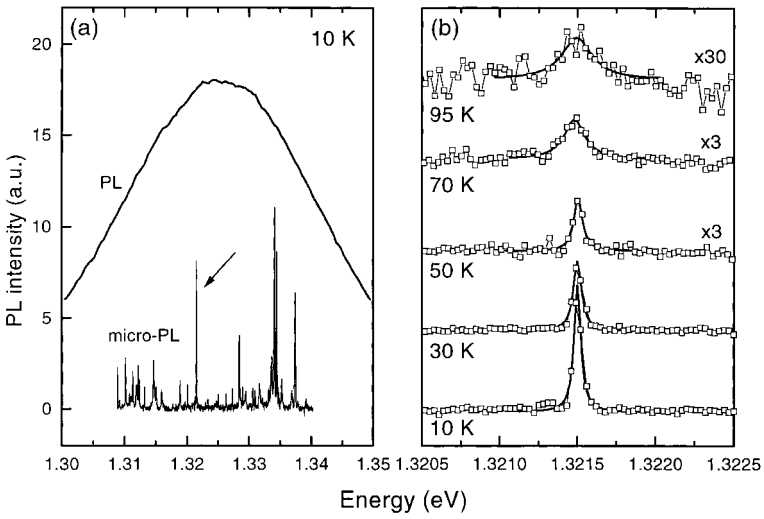

Fig. 1. a) Photoluminescence and micro-photoluminescence spectra of $In_{0.5}Ga_{0.5}As$ quantum dots. b) A single PL line (marked with an arrow in (a)) measured at different temperatures. The spectra have been vertically displaced for clarity and horizontally shifted for $T > 10$ K to compensate for the change in bandgap

nant (632.8 nm) excitation. The intensity of single lines observed in low-power spectra saturates at about 1 kW/cm^2 of excitation power. Simultaneously, additional narrow PL lines appear in the same energy range, indicating the onset of emission involving multi-exciton states. We do not observe a significant variation in linewidth when exciting below the barrier bandgap, in contrast to the observations of, e.g., Ref. [9], although the relative intensities of the single lines change significantly when the excitation wavelength is tuned across the barrier bandgap.

The histogram in Fig. 2 shows the statistical distribution of linewidths in the QD spectra. Three energy ranges were investigated, as shown in the inset, corresponding to the central part of the macroscopic PL peak and to its high and low energy tails. The maximum of the linewidth distribution occurs at 50 μeV, with the majority of lines lying in the 20 to 120 μeV range. In Fig. 2 we also plot individually the distribution of linewidths for each energy interval, revealing only minor differences in the linewidth distribution for different energies. Since a similar distribution of linewidths is observed for all transition energies we conclude that small changes of the quantum dot confinement potential, due to variations in shape, size and composition of the dots, are not significantly influencing the measured linewidth. Furthermore, time-resolved photoluminescence measurements on similar samples reveal that individual spectral components decay with a single time constant of several hundred ps [10], corresponding to a homogeneous linewidth broadening of only a few μeV. We therefore exclude any significant linewidth variations linked to radiative lifetime broadening.

The spectral width of narrow ($<$80 μeV at 100 W/cm^2) PL lines increases by approximately 10 μeV per decade of excitation intensity, even above the saturation power. Broader lines ($>$80 μeV at 0.1 kW/cm^2) deviate from Lorentzian shape and their width depends more strongly on excitation intensity, with power broadening up to an order of magnitude higher than for the narrower lines. Apparent broadening due to fine-struc-

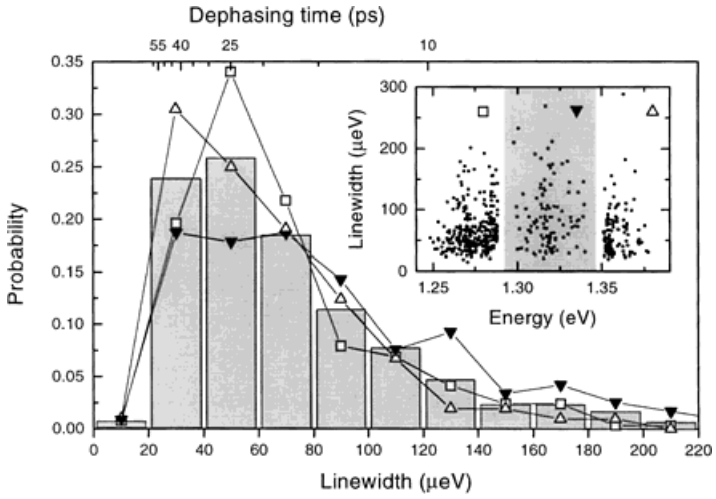

Fig. 2. Histogram of the emission linewidths in $In_{0.5}Ga_{0.5}As$ quantum dots (columns). Linewidth distributions for low (open squares), intermediate (filled triangles), and high transition energies (open triangles) within the inhomogeneous ensemble are also plotted individually. Inset: The three energy intervals investigated and the measured linewidths

ture splitting of the ground state or accidental overlapping of individual spectral lines below our resolution limit will contribute to the linewidth distribution but cannot explain the increased power broadening. We therefore attribute the appearance of broad lines in the micro-PL spectra to single transitions, broadened by local electric field fluctuations induced by photoexcited carriers, while we argue that narrower lines are homogeneously broadened by dephasing through acoustic-phonon interactions. In the latter case, the measured linewidths can be expressed in terms of a dephasing time of 15 to 60 ps.

Several of the homogeneously broadened PL lines were investigated at different temperatures. Below 50 K, we find that the linewidth increases linearly with temperature by about 0.4 μeV/K. This is significantly lower than the 1.6 to 3 μeV/K increase in homogeneous linewidth reported for narrow InGaAs quantum wells [11]. Above 50 K, we observe a thermally activated behavior with a 20 to 30 meV activation energy. Theoretical calculations of optical linewidths in single quantum dots predict a linear temperature dependence at low temperatures and a finite zero-temperature linewidth due to diagonal electron–phonon interactions involving only the exciton ground state and low-energy acoustic phonons [12]. At higher temperatures, off-diagonal contributions from excited states become important, as well as contributions from optical phonons, with an energy spectrum broadened by alloying and strain effects in the dots [13]. We therefore conclude that the weak linear dependence of the homogeneous linewidth below 50 K and the zero-temperature offset results from the elastic phonon interaction enhanced by the strong confinement [12], while acoustic phonon scattering to excited states is inhibited due to the large energy separation. Furthermore, our measured activation energies are close to the expected level splitting and the optical phonon energy.

In summary, we have measured a statistical variation in the spectral width of individual photoluminescence lines from $In_{0.5}Ga_{0.5}As/GaAs$ quantum dots. This variation is not related to differences in the confinement potential of the dots but can be partly explained by local electric-field fluctuations. The temperature dependent linewidth of homogeneously broadened PL lines is in agreement with theoretical predictions and reflects the discrete energy level structure of the quantum dots.

Acknowledgement The samples were grown at III–V Nanolab, a joint laboratory between Research Center COM and the Niels Bohr Institute at Copenhagen University.

References

[1] A. GUSTAFSSON, M.-E. PISTOL, L. MONTELIUS, and L. SAMUELSON, J. Appl. Phys. **84**, 1715 (1998).
[2] K. BRUNNER, G. ABSTREITER, G. BÖHM, G. TRÄNKLE, and G. WEIMANN, Appl. Phys. Lett. **64**, 3320 (1994).
[3] J.-Y. MARZIN, J.-M. GÉRARD, A. IZRAËL, D. BARRIER, and G. BASTARD, Phys. Rev. Lett. **73**, 716 (1994).
[4] D. GAMMON, E.S. SNOW, B.V. SHANABROOK, D.S. KATZER, and D. PARK, Science **273**, 87 (1996).
[5] U. BOCKELMANN, W. HELLER, A. FILORAMO, PH. ROUSSIGNOL, and G. ABSTREITER, phys. stat. sol. (a) **164**, 281 (1997).
[6] K. OTA, N. USAMI, and Y. SHIRAKI, Physica **2E**, 573 (1998).
[7] D. BIMBERG, N. KIRSTAEDTER, N.N. LEDENTSOV, ZH. I. ALFEROV, P.S. KOPEV, and V.M. USTINOV, IEEE J. Selected Topics in Quantum Electronics **3**, 196 (1997).
[8] P. BORRI, W. LANGBEIN, J. MØRK, J.M. HVAM, F. HEINRICHSDORFF, M.-H. MAO, and D. BIMBERG, Phys. Rev. B **60**, 7784 (1999).
K. MATSUDA, T. SAIKI, H. SAITO, and K. NISHI, Appl. Phys. Lett. **76**, 73 (2000).

[9] H. KAMADA, J. TEMMYO, M. NOTOMI, T. FURUTA, and T. TAMAMURA, Jpn. J. Appl. Phys. **36**, 4194 (1998).
[10] L.M. SMITH, K. LEOSSON, J.E. ØSTERGAARD, J.R. JENSEN, J.M. HVAM, and V. ZWILLER, unpublished.
[11] P. BORRI, W. LANGBEIN, J.M. HVAM, and F. MARTELLI, Phys. Rev. B **59**, 2215 (1999).
[12] X.-Q. LI and Y. ARAKAWA, Phys. Rev. B **60**, 1915 (1999).
T. TAKAGAHARA, Phys. Rev. B **60**, 2638 (1999).
[13] M. GRUNDMANN, O. STIER, and D. BIMBERG, Phys. Rev. B **52**, 11969 (1995).

Ultranarrow polaritons in a semiconductor microcavity

J. R. Jensen,[a] P. Borri,[b] W. Langbein,[b] and J. M. Hvam
Research Center COM, The Technical University of Denmark, Building 349, DK-2800 Kgs. Lyngby, Denmark

(Received 26 January 2000; accepted for publication 4 April 2000)

We have achieved a record high ratio (19) of the Rabi splitting (3.6 meV) to the polariton linewidth (190 μeV), in a semiconductor λ microcavity with a single 25 nm GaAs quantum well at the antinode. The narrow polariton lines are obtained with a special cavity design which reduces the exciton broadening due to scattering with free charges and has a very low spatial gradient of the cavity resonance energy. Since the static quantum-well disorder is very small, the polariton broadening is dominantly homogeneous. Still, the measured linewidths close to zero detuning cannot be correctly predicted using the linewidth averaging model. © *2000 American Institute of Physics.* [S0003-6951(00)02922-3]

Since the first realization of a semiconductor microcavity (MC) structure showing a Rabi splitting of the cavity polaritons (CP),[1] the strong-coupling regime of excitons and photons in this two-dimensional system has been studied intensely. Much work has been focused on understanding the behavior of the CP linewidth as a function of detuning, and it is still debated if the linewidths can be fully described using linear dispersion theory or if additional effects such as motional narrowing have to be taken into account.[2,3] However, little progress has been reported on realizing MCs with CP lines narrower than 0.5 meV, which is interesting, e.g., for bistable devices.[4]

Stanley *et al.*[5] have reported a very narrow bare cavity linewidth of 120 μeV obtained in a structure grown by molecular-beam epitaxy (MBE). They conclude that the width is limited by the curvature of the thickness of the epitaxial layers across the sample. Bare excitonic resonances of the same width may also be obtained in wide $GaAs/Al_{0.3}Ga_{0.7}As$ quantum wells at low temperatures,[6] where the influence of quantum-well disorder is negligible and the homogeneous broadening due to phonon scattering is small. Yet, for a wide GaAs quantum well in a MC, the CP linewidths that have been obtained are much broader than expected from the bare linewidths.[7] Instead, the narrowest CPs have been obtained using a shallow InGaAs/GaAs quantum well where the excitonic resonance is broadened by quantum-well disorder.[8]

In this letter, we demonstrate that ultranarrow CP lines can be obtained using a single 25 nm GaAs quantum well confined by a low barrier potential, similar to shallow InGaAs/GaAs quantum wells. Two samples with different barriers, in the following labeled S1 and S2, were grown by MBE for comparison. Both samples consist of a 25 nm $GaAs/Al_{0.3}Ga_{0.7}As$ quantum well placed at the antinode of a λ cavity, with a 25 (16) period $AlAs/Al_{0.15}Ga_{0.85}As$ Bragg reflector at the bottom (top). In S1 the quantum well is surrounded by $Al_{0.3}Ga_{0.7}As$ barriers forming the spacer layer of the cavity, whereas in S2 the quantum well has 5-nm-wide $Al_{0.3}Ga_{0.7}As$ barriers and the rest of the spacer layer consists of digitally alloyed $Al_{0.05}Ga_{0.95}As$. Both structures were grown with a V/III flux ratio of approximately 8, a substrate temperature of 630 °C, and a growth rate of 1 μm/h. The samples were rotated during growth of the Bragg reflectors and the quantum well but stopped at a specific angle for the growth of the spacer layers on each side of the quantum well, generating a thickness gradient across the sample.

The photoluminescence (PL) spectra of S1 and S2, shown in Fig. 1, were obtained by exciting the quantum wells with a Ti:sapphire laser through the cavity resonance, which was tuned to an energy more than 30 meV above the exciton resonance. The power density of the laser was 0.3-0.9 W/cm^2. Both the heavy-hole exciton (X_{hh}) and the light-hole exciton (X_{lh}) are visible, as well as a low-energy shoulder on the X_{hh} peak. This resonance is ascribed to excitons bound to free carriers (trions), in agreement with measurements showing a constant intensity ratio of the low-energy shoulder to the X_{hh} peak over two orders of magnitude of the excitation power. The full width at half maximum (FWHM) of the heavy-hole exciton peak in S1 (S2) is 440 μeV (220 μeV). From the PL spectra we conclude that a significantly larger free-carrier density is present in S1 than in S2, giving rise to a more intense trion peak and

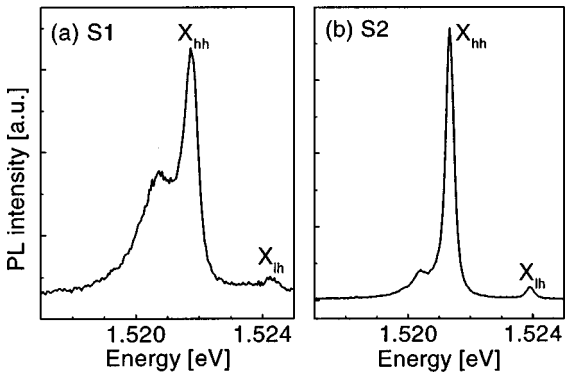

FIG. 1. Photoluminescence spectra of (a) S1 and (b) S2 at $T=11$ K. The labeled peaks correspond to the heavy-hole (X_{hh}) and light-hole (X_{lh}) excitons.

[a]Electronic mail: jrj@com.dtu.dk
[b]Present address: Lehrstuhl für Experimentelle Physik EIIb, Universität Dortmund, Otto-Hahn Str. 4,D-44221 Dortmund, Germany.

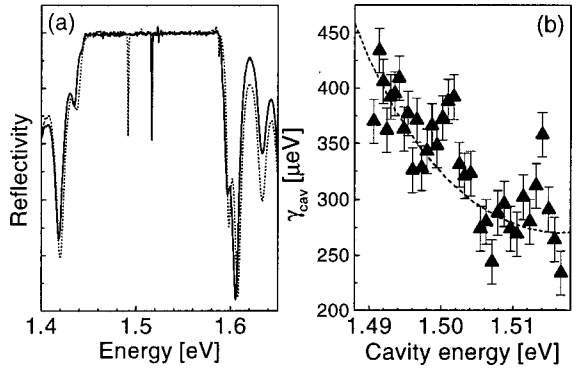

FIG. 2. (a) Reflection spectra of S2 ($T=11$ K) at two different positions on the sample, where the cavity resonance is tuned below the excitonic resonance. (b) The measured (triangles) and calculated (dashed line) Lorentzian cavity linewidths (FWHM) as a function of the cavity resonance energy.

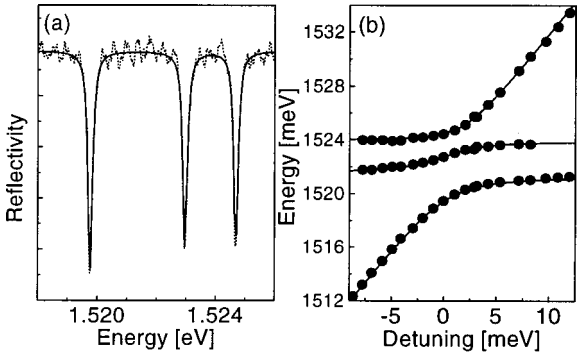

FIG. 3. (a) Measured reflection spectrum (dashed line) of S2 at zero detuning, and best fit obtained with three Lorentzian lines (solid line). (b) Measured (circles) and fitted (solid lines) energies of the polaritons as a function of detuning.

larger homogeneous broadening due to a higher free-carrier scattering rate. A broadening of the excitonic resonance due to charged states has also been reported for other MC structures.[9]

Since S1 and S2 are nominally undoped, the charges in the structures most likely originate from background p doping, due to carbon incorporation during growth. The largest contribution is expected from the AlAs Bragg layers, since previous experiments have shown that the background doping concentration increases with the Al molefraction in AlGaAs.[10] Hence, the total concentration of dopants is approximately the same in S1 and S2, but due to the lower band gap of the spacer layer in S2 a smaller density of free charges can accumulate in the quantum well before band-bending makes it energetically favorable to tunnel out into the spacer layer.

In Fig. 2 the broadband reflectivity spectrum is shown for two positions on S2 18 mm apart. For all the reflectivity measurements reported here, white light was focused to a diffraction-limited spot size of 75 μm (NA=0.0065) on the sample at normal incidence. For this value of the numerical aperture, the angle of the light cone is small enough to avoid a broadening of the cavity linewidth[5] due to the k dispersion, and at the same time the spot size is so small that the shift of the cavity energy within the probe spot is always significantly less than the cavity linewidth. The measurements shown in Fig. 2 were obtained for the cavity energy tuned below the exciton resonance, where the properties of the bare cavity can be obtained. As expected, the position of the stop band is the same since the Bragg reflectors have a uniform thickness, but due to the wedge of the spacer layer the cavity resonance energy is shifted. The gradient of the cavity resonance energy is 1.5 meV/mm, which is a factor of 5 lower than what is obtained with our MBE system if the whole MC is wedged. This large reduction of the gradient is in agreement with theoretical calculations showing that the cavity resonance energy is more dependent on the penetration depth into the Bragg reflectors than the spacer layer thickness.[11]

The low gradient of the cavity energy achieved here is very important in order to avoid a broadening of the cavity linewidth due to the shift of the cavity energy within the optimal probe spot area.[5] However, with this design the width of the cavity resonance is not constant across the structure, as shown in Fig. 2. Since the reflectivity of a Bragg reflector is highest in the middle of the stop band, the cavity linewidth increases when it is detuned from the center due to a reduced photon lifetime in the cavity. The dashed line indicates the calculated cavity linewidths for S2 obtained from a tranfer matrix model. Except for two regions, where the measured linewidths are significantly larger than the calculated values, the agreement is very good. We attribute the increased linewidth to absorption features below the exciton resonance in the quantum well, probably due to defect states. We conclude that within a region of 15 meV from the center of the stop band the measured cavity linewidth is practically constant in such a structure, and theoretically it only increases by 10%.

The reflection spectrum of S2 for the cavity resonance tuned to the energy of the heavy-hole exciton is shown in Fig. 3. The three CP lines correspond to the mixed states between the bare cavity, and the heavy- and light-hole excitons. All three lines are well fitted by Lorentzian line having the same width of $\gamma=190\,\mu$eV, indicating a dominating homogeneous broadening. Indeed, for the 25 nm quantum well, an inhomogeneous broadening well below 60 μeV has been measured,[6] leaving mostly homogeneous broadening mechanisms for the polaritons, e.g., their radiative decay, and exciton dephasing due to phonon scattering and free-carrier scattering. For these measurements a high-resolution spectrometer was used with a resolution of 30 μeV. Note that in S1 the measured reflectivity spectrum showed a much bigger CP linewidth of ≈ 1 meV. The fit of the CP energies as a function of detuning was obtained by diagonalizing the Hamiltonian of the system,

$$\begin{bmatrix} E_{\mathrm{hh}} & 0 & \hbar\Omega_{\mathrm{hh}} \\ 0 & E_{\mathrm{lh}} & \hbar\Omega_{\mathrm{lh}} \\ \hbar\Omega_{\mathrm{hh}} & \hbar\Omega_{\mathrm{lh}} & E_{\mathrm{cav}} \end{bmatrix} \begin{bmatrix} c_1 \\ c_2 \\ c_3 \end{bmatrix} = E \begin{bmatrix} c_1 \\ c_2 \\ c_3 \end{bmatrix}, \tag{1}$$

where E_{cav}, E_{hh} and E_{lh} are the energies of the bare cavity resonance, heavy-hole exciton, and light-hole exciton, and the detuning is $E_{\mathrm{cav}}-E_{\mathrm{hh}}$. $\hbar\Omega_{\mathrm{hh}}$ and $\hbar\Omega_{\mathrm{lh}}$ are the coupling strengths of the photon to the heavy-hole and light-hole excitons, and correspond to half the Rabi splittings. For the fit, the values of E_{hh} and E_{lh} were fixed to the transition energies obtained from the PL measurement, and we found $\hbar\Omega_{\mathrm{hh}}=1.8$ meV and $\hbar\Omega_{\mathrm{lh}}=1.1$ meV, in good agreement with previous measurements.[12] The ratio of the heavy-hole Rabi

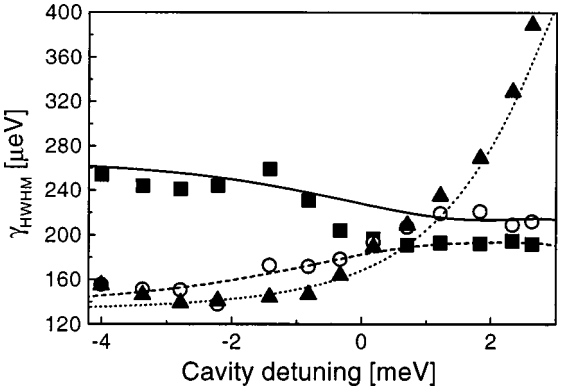

FIG. 4. Comparison of the measured linewidths (FWHM) with the linewidth averaging model [Eq. (2)]. The symbols show the measured values and the lines show the calculated values for the lower polariton (filled squares/solid line), the middle polariton (open circles/dashed line), and the upper polariton (filled triangles/dotted line).

splitting to the linewidth in this sample is $2\hbar\Omega_{hh}/\gamma=19$, which is approximately a factor of 2 better than the highest value reported so far.[8]

In Fig. 4, the measured linewidths of the CP branches are shown as a function of detuning at $T=11$ K. Due to the shallow reflectivity dips obtained for the exciton-like polaritons at large detunings, precise fits of all the linewidths could not be obtained over the full detuning range shown in Fig. 3. For negative detuning the mixing of the three bare states is weak, and we observe almost constant linewidths of the CPs. In this region, the width of the lower CP corresponds to the bare cavity, and the value is in good agreement with the measurements described previously. The widths of the middle and upper CPs correspond to the nonradiative broadening of the heavy- and light-hole excitons,[13] however, they are 60–80 μeV below the values obtained from PL. This difference is attributed to the different experimental conditions of the two measurements, e.g., the exciton resonance observed in the PL may be broadened due to photoinduced charges in the quantum well. Around zero detuning the linewidths cross, as the excitonic and photonic contents of the polaritons change due to the strong mixing. For positive detuning, the upper polariton has a dominating photonic content, so the abrupt increase in the linewidth observed here is explained by increased absorption in the cavity resonance due to the proximity of the continuum edge of the quantum well.

In order to compare the measurements with theory, we have calculated the CP linewidths using the linewidth averaging model,

$$\gamma_{pol}=|c_1|^2\gamma_{hh}+|c_2|^2\gamma_{lh}+|c_3|^2\gamma_{cav}. \quad (2)$$

Here, the nonradiative linewidths of the excitonic states were assumed to be constant, $\gamma_{hh}=\gamma_{lh}=130\,\mu$eV. The change of γ_{cav} due to absorption was empirically modeled using the tail of a Lorentzian, and assuming a constant 270 μeV linewidth in the absence of absorption.

We note two important differences between the measured and calculated values. First, the measured lower CP linewidth drops more steeply close to zero detuning than the calculated value, and second, the crossing of the upper and lower CP linewidths is shifted about 1 meV below the calculated crossing point. Both the steepness and the crossing point are practically insensitive to variations in γ_{hh}, γ_{lh}, and γ_{cav}, and almost entirely determined by the values of c_1, c_2, and c_3. However, the accurate fit of the eigenvalues in Fig. 3 show that c_1, c_2, and c_3 are well determined. We emphasize that our structure is a three-level system while most other structures studied both experimentally and theoretically are two-level systems, which implies that zero detuning in our definition ($E_{hh}=E_{cav}$) is not directly comparable to zero detuning in other structures. It is more relevant to compare with the detuning for which the upper and lower polaritons have equal excitonic and photonic contents, which is at 1.2 meV in S2. Indeed, at this value of the detuning, the lower CP is narrower than the upper CP, as predicted in Ref. 14. Temperature-dependent measurements have been carried out in order to investigate this effect further, which are described elsewhere.[15]

In conclusion, we have shown that MCs with ultranarrow homogeneously broadened polariton lines can be realized with a GaAs quantum well if a cavity design with shallow energy levels is used, reducing the density of free carriers in the well. Wedging only the spacer layer during growth ensures a low gradient of the cavity energy, and we have experimentally verified that for such a structure the variation of the cavity linewidth is negligible in a range of 15 meV from the center of the stop band, in agreement with transfer matrix calculations. Finally, we observe that close to zero detuning the polariton linewidths are not well predicted by the linewidth averaging model, indicating that additional narrowing of the lower polariton is taking place.

The authors would like to thank K. Leosson and N. A. Mortensen for help on the high-resolution measurements and parts of the numerical calculations. Also, the fruitful discussions with C. B. Sørensen at the III-V Nanolab on the MBE growth are acknowledged. This work was supported by the Danish Natural Science Research Council.

[1] C. Weisbuch, M. Nishioka, A. Ishikawa, and Y. Arakawa, Phys. Rev. Lett. **69**, 3314 (1992).
[2] C. Ell, J. Prineas, Jr., S. Park, H. M. Gibbs, G. Khitrova, S. W. Koch, and R. Houdre, Phys. Rev. Lett. **80**, 4795 (1998).
[3] D. M. Whittaker, P. Kinsler, T. A. Fisher, M. S. Skolnick, A. Armitage, A. M. Afshar, M. D. Sturge, and J. S. Roberts, Phys. Rev. Lett. **77**, 4792 (1996).
[4] D. Citrin and T. B. Norris, IEEE J. Sel. Top. Quantum Electron. **2**, 401 (1996).
[5] R. P. Stanley, R. Houdre, U. Oesterle, M. Gailhanou, and M. Ilegems, Appl. Phys. Lett. **65**, 1883 (1994).
[6] W. Langbein and J. M. Hvam, Phys. Rev. B **61**, 1692 (2000).
[7] S. Pau, G. Björk, H. Cao, F. Tassone, R. Huang, and Y. Yamamoto, Phys. Rev. B **55**, R1942 (1997).
[8] J. D. Berger, O. Lyngnes, H. M. Gibbs, G. Khitrova, T. R. Nelson, E. K. Lindmark, A. V. Kavokin, M. A. Kaliteevski, and V. V. Zapasskii, Phys. Rev. B **54**, 1975 (1996).
[9] R. P. Stanley, R. Houdre, U. Oesterle, and M. Ilegems, Solid State Commun. **106**, 485 (1998).
[10] C. B. Sørensen (private communications).
[11] G. Panzarini, L. C. Andreani, A. Armitage, D. Baxter, M. S. Skolnick, V. N. Astratov, J. S. Roberts, A. V. Kavokin, M. R. Vladimirova, and M. Kaliteevski, Phys. Rev. B **59**, 5082 (1999).
[12] H. Cao, S. Jiang, S. Machida, Y. Takiguchi, and Y. Yamamoto, Appl. Phys. Lett. **71**, 1461 (1997).
[13] V. Savona, L. C. Andreani, P. Schwendimann, and A. Quattropani, Solid State Commun. **93**, 733 (1995).
[14] V. Savona and C. Piermarocchi, Phys. Status Solidi A **164**, 45 (1997).
[15] P. Borri, J. R. Jensen, W. Langbein, and J. M. Hvam, Phys. Rev. B (to be published).

PHYSICAL REVIEW B VOLUME 61, NUMBER 20 15 MAY 2000-II

Direct evidence of reduced dynamic scattering in the lower polariton of a semiconductor microcavity

P. Borri,* J. R. Jensen, W. Langbein,* and J. M. Hvam
Research Center COM, The Technical University of Denmark, Building 349, DK-2800 Kgs. Lyngby, Denmark
(Received 21 December 1999; revised manuscript received 7 February 2000)

The temperature dependent linewidths of *homogeneously* broadened GaAs/$Al_xGa_{1-x}As$ microcavity polaritons are investigated. The linewidths of the lower, middle, and upper polariton resonances are measured directly from reflection spectra at normal incidence ($k_\parallel = 0$). The linewidth of the lower polariton is found to be smaller than the linewidths of the middle and upper polaritons at all investigated temperatures ranging from 11 to 100 K. The results clearly show the reduction of dynamic scattering processes in the lower polariton compared to the middle and upper polaritons, in agreement with theoretical predictions in literature. A nontrivial temperature dependence of the linewidth is found and its physical origin is discussed.

The optical linewidth of polariton resonances in semiconductor quantum-well microcavities has been the subject of intense theoretical and experimental work in recent years. Particular attention has been devoted to the role of the static structural disorder in the optical response of semiconductor microcavities in the strong coupling regime. This regime occurs when the damping mechanisms are weak compared to the exciton-photon coupling, resulting in a normal mode energy splitting when the cavity mode is close to the exciton resonance. It has been found experimentally[1,2] that at resonance the *inhomogeneous* linewidth of the lower polariton is narrower than that of the upper polariton. This has been explained by a spatial averaging over the disorder potential in the lower polariton[1,3,4] (motional narrowing) or by a linear dispersion theory together with an asymmetric lineshape of the bare quantum well (QW) excitonic absorption.[2] The role of phonon scattering and polariton-polariton scattering in the *homogeneous* polariton linewidth has also been recently discussed. Polariton-polariton scattering is predicted to be inhibited in the lower polariton resonance at $k_\parallel = 0$ as long as the scattering involves only the small region of k space, where the polariton effective mass is very light due to the photon coupling, resulting in a very small density of states.[5] This leads to a threshold density for the polariton-polariton scattering in the lower polariton branch.[5] Experimental results confirming this prediction have been reported.[6,7] However, due to the inhomogeneous broadening of the investigated samples, the homogeneous linewidth of the polaritons had to be inferred from nontrivial nonlinear experiments. Polariton-acoustic phonon scattering is also predicted to be strongly quenched in the lower polariton branch, as long as the temperature is low enough to limit the interaction to the zone where the density of states is very small.[8] Indications of this behavior have been experimentally shown[9,10] but again using indirect techniques, based on interferometric time-correlated secondary emission on inhomogeneously broadened samples. Moreover, no direct comparison between the lower and upper polariton homogeneous broadenings was presented.

In this work we have investigated the temperature-dependent linewidth of homogeneously broadened microcavity polaritons in the strong coupling regime using white-light reflection spectra at normal incidence ($k_\parallel = 0$). The sample consists of an MBE-grown 25 nm GaAs/$Al_{0.3}Ga_{0.7}As$ single quantum well placed in the center of a λ cavity. An AlAs/$Al_{0.15}Ga_{0.85}As$ Bragg reflector of 25 (16) periods was grown at the bottom (top) of the cavity. The $Al_{0.3}Ga_{0.7}As$ barriers are 5 nm thick and the rest of the spacer layer consists of $Al_{0.05}Ga_{0.95}As$. The spacer layer is wedged, in order to tune the cavity mode along the position on the sample. Details on the growth conditions and sample design can be found in Ref. 11. The white-light source was focused on the sample with a spot diameter of 75 μm, resulting in a variation of the cavity resonance over the spot size of only 100 μeV, due to the wedged geometry. This variation is more than a factor of 2 smaller than the cavity linewidth, as shown in the following. Smaller spot diameters resulted in an increased cavity linewidth due to larger incident k vectors. The sample was held in an exchange gas cryostat, at temperatures from $T = 11$ to 100 K. For $T < 40$ K, the spectra were detected using a high resolution spectrometer and a CCD camera, with a spectral resolution of 15 μeV half width at half maximum (HWHM). Above 40 K, a normal resolution spectrometer was used resulting in 50 μeV HWHM resolution. All the linewidths will be given in the paper as HWHM.

The use of a wide GaAs quantum well leads to a homogeneously broadened QW exciton absorption resonance, as experimentally shown in Ref. 12, due to the small effect of interface roughness on the confined excitons. An absorption linewidth of 60 μeV at 5 K is found at the 1s heavy-hole exciton, dominated by radiative decay.[12] The exciton-photon coupling in the microcavity structure leads to three polariton resonances, arising from the mixing of the heavy-hole (HH) exciton, light-hole (LH) exciton, and cavity modes. Measurements at 11 K of the polariton resonances at different detuning between the cavity mode and the HH exciton can be fitted by a three coupled-oscillator model from which we have inferred a Rabi splitting of 3.6 meV for the HH and 2.2 meV for the LH excitons.[11] The temperature dependence of the reflectivity spectra for a tuning of the cavity mode approximately in resonance with the HH exciton is shown in Fig. 1. The spectra have been corrected for the temperature induced band-gap shifts by aligning the reflectivity minima of the lower polariton (LP), for better clarity. It can be clearly seen that the middle (MP) and upper polariton (UP)

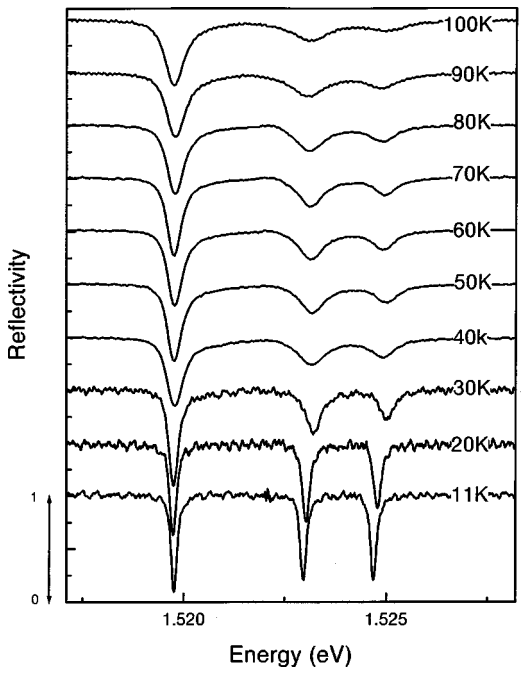

FIG. 1. Reflectivity spectra near zero detuning at different temperatures as indicated. The energy positions are shifted to overlap at the LP resonance for better clarity.

linewidths are strongly broadened by increasing the temperature, while the LP *is narrower* than MP and UP for $T>11$ K. The reflectivity spectrum at 11 K is fitted with a Lorentzian lineshape at each resonance, as shown in Fig. 2. A linewidth of 95 μeV at each of the resonances is found. At higher temperatures, the linewidth broadening leads to a partial merging of the polariton line shapes, especially for the MP and UP. In this case we have fitted the reflectivity spectrum using a triple-correlated Lorentzian function, according to the following expression:

$$R=1-\left|\sum_{n=1}^{3}\frac{A_n}{(E-E_n)+i\gamma_n}e^{i\delta_n}\right|^2, \qquad (1)$$

where E_n $(n=1,2,3)$ are the three polariton energy resonances and γ_n are the corresponding linewidths. A_n are amplitude fit parameters, and δ_n are the relative phases.

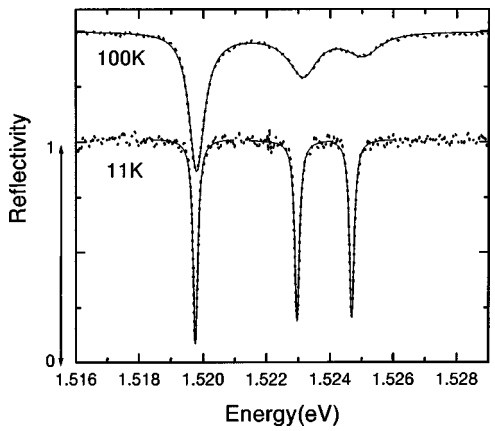

FIG. 2. Reflectivity spectra (dotted line) and fits (solid lines) at 11 and 100 K. The fit at 11 K is a Lorentzian function at each resonance. The fit at 100 K is obtained using a triple-correlated Lorentzian function.

The validity of this expression to fit the data has been checked by simulating the reflectivity spectrum in the microcavity with transfer matrix calculations. A perfect agreement between the numerical simulations and the formula used was found. The physical meaning of Eq. (1) is that the *total electric field* associated with the structure has to be calculated, by summing over the amplitude transmission coefficients of each resonance, to give rise to the reflectivity spectrum.[13] The use of this formula to fit the spectrum at 100 K is shown in Fig. 2. An excellent agreement between the data and the fit is found.

Savona and Piermarocchi[8] pointed out that a strong reduction in the temperature-dependent broadening of the LP linewidth compared to the UP is expected when calculating the scattering rate by acoustic-phonon absorption of the lower polariton at $k_\parallel=0$. In their work, the difference between the detuning dependence of the homogeneous linewidth resulting from the calculation and from linewidth averaging is also pointed out. The linewidth averaging approach is obtained by solving the complex eigenvalue problem of the exciton-photon coupled system[8] at $k_\parallel=0$. This approach is questionable when the broadening mechanisms are related to scattering between different $k_\parallel$, and thus influenced by the different dispersion in the microcavity compared to the bare QW.[8] The linewidth averaging predicts that LP and UP linewidths are equal at resonance (zero detuning) for two coupled oscillators. The calculation of Savona and Piermarocchi shows that the LP linewidth is *smaller* than the UP one at zero detuning. Consequently, the crossing point between the LP and UP linewidths is shifted towards negative detuning, i.e., when the cavity resonance is below the exciton resonance, assuming $\gamma_{\mathrm{HH}}<\gamma_{\mathrm{c}}$ where γ_{HH} and γ_{c} are the bare HH and cavity linewidths, respectively.

In Fig. 3 we show the measured detuning dependence of the linewidths for the three polariton resonances at three different temperatures, as indicated, and we compare it with the linewidth averaging in a three-coupled oscillators system. The detuning is defined as $\delta=E_{\mathrm{c}}-E_{\mathrm{HH}}$ with E_{c} and E_{HH} being the cavity and bare HH exciton energies. At 11 K, a cavity linewidth of 130 μeV and a bare exciton linewidth of 75 μeV is deduced from the large negative detuning data. The corresponding detuning dependence expected by linewidth averaging is shown in the lower part of the figure. Due to the presence of three resonances, the calculated crossing point is not at $\delta=0$, and does not correspond to 0.5 photonic and excitonic content, as in the two-coupled oscillators model.[8] Instead, the crossing point between LP and UP occurs at $\delta=1.2$ meV where the photonic content is 0.37 and the total (HH+LH) exciton content is 0.63 both in the LP and UP eigenstate.[11] From our measurements at 11 K, the crossing between the linewidths is obtained at $\delta\sim0$. For large positive detunings, the UP linewidth, which is cavity-like, is increased by the absorption from the QW continuum. At 20 K a larger bare-exciton linewidth of about 90 μeV is measured at negative detuning, as expected from enhanced scattering mechanisms at higher T on the bare exciton. The crossing point between the LP and UP occurs at a slight *negative* detuning. At 70 K the bare exciton linewidth is above the cavity linewidth, and no crossing between the LP and UP occurs at any detuning. Therefore, the simple line-

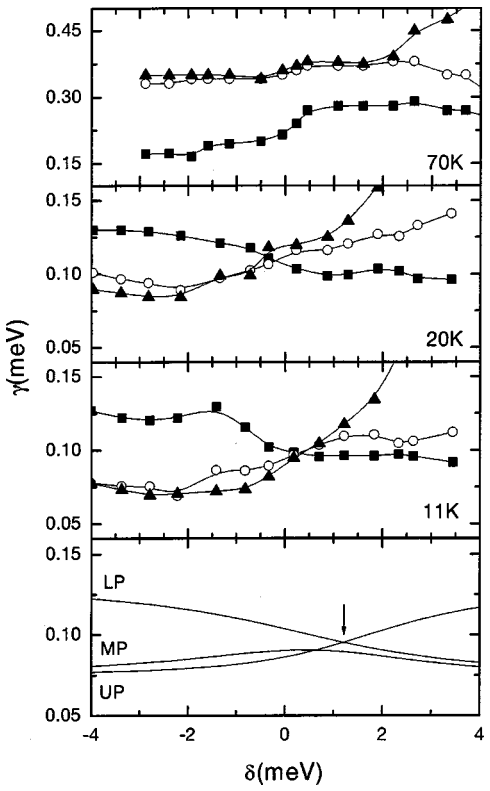

FIG. 3. LP (squares), MP (circles), and UP (triangles) linewidth versus detuning at three different temperatures as indicated. In the lower part, the detuning dependence as expected by linewidth averaging at 11 K is shown.

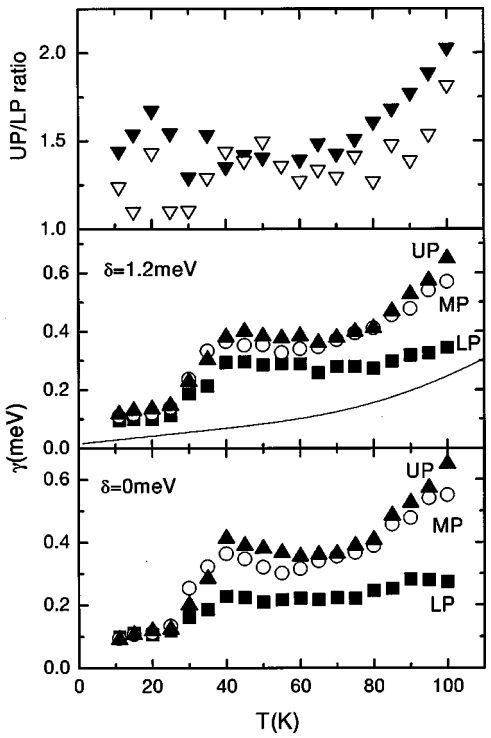

FIG. 4. Temperature dependence of the polariton linewidths for zero and 1.2 meV detuning. The solid line is the expected linewidth dependence due to phonon absorption in the bare exciton, weighted by the excitonic content at 1.2 meV detuning. In the top part, the ratio between the UP and LP linewidth, after subtraction of the cavity contribution, is shown at zero (open symbols) and 1.2 meV detuning (closed symbols).

width averaging is not verified by our experimental findings at any temperature, in agreement with the discussion in Ref. 8.

The physical quantities of interest in the reduced acoustic-phonon absorption of the LP branch at $k_{\|}=0$ are the energy separation ΔE, between the LP resonance at $k_{\|}=0$ and the HH bare exciton, and the cutoff (q_c) in the wave vector exchanged between the acoustic phonon and the exciton in the QW.[8,5,10] The k dispersion of the LP branch approaches the HH bare exciton for $k_{\|} \gg 0$, where a flat dispersion is recovered due to the large exciton mass. Therefore, ΔE is the energy barrier to overcome in order that the excitonlike part of the LP dispersion becomes available as final states for scattering via phonon absorption. As long as $k_B T < \Delta E$, only a small scattering phase space is available and the broadening in the LP is negligible.[8] When $k_B T > \Delta E$, the scattering rate depends on the comparison between the acoustic phonon energy associated with q_c (i.e., $\hbar v q_c$ with the sound velocity v) and ΔE. When $\hbar v q_c < \Delta E$, the phonon scattering of the lower polariton branch is expected to be several orders of magnitude smaller than for the bare exciton.[10,5] We estimate $\hbar v q_c = 1.24$ meV, with $v = 5000$ ms^{-1} and[10] $q_c = 3\pi/L$, where L is the width of the quantum well. At $\delta = 0$ we have $\Delta E = 2$ meV and at $\delta = 1.2$ meV, $\Delta E = 1.43$ meV. We therefore expect in our structure a strong reduction in the acoustic-phonon absorption rate of the LP, corresponding to a nearly constant LP linewidth versus temperature until the LO-phonon absorption becomes active. The MP and UP linewidths, instead, should almost follow the temperature dependence of the bare QW exciton.[8]

In Fig. 4 the LP, MP, and UP linewidths versus T are shown at $\delta = 0$ and $\delta = 1.2$ meV. The temperature dependence of the linewidth of the bare exciton, as expected from acoustic and optical phonon scattering is also shown (solid line), weighted by the excitonic content at $\delta = 1.2$ meV. An acoustic phonon coefficient of 2.1 μeV/K, and an optical phonon coefficient of 10 meV are used, in agreement with the measured dependence in the bare QW,[12] and a small inhomogeneous broadening of 25 μeV, which is realistic for the investigated quantum well, is also included. The measured temperature dependence in the MP and UP is surprisingly quite different from the one expected by phonon scattering (even at large negative detuning where the MP and UP tend to the bare HH and LH exciton). In particular, the linewidth of MP and UP is always higher than expected, indicating that *additional* scattering mechanisms are taking place. We believe that an excess of free carriers in the microcavity structure, possibly due to unintentional doping of the Bragg reflectors, is responsible for a polariton scattering additional to the phonon interaction. The nonlinear increase of the linewidth up to 40 K could be due to an increased kinetic energy of the free carriers with temperature. Above 40 K, the linewidth is slightly reduced up to 65 K. This could be explained by phonon assisted escape of the excess of carriers from the QW, via tunnelling through the shallow barriers, and consequent reduction of the free carrier concentration in the well. Finally, above 65 K an increased linewidth versus T, with a similar trend as the one due to LO-phonon absorption in the bare exciton, is found.

We would like to point out that the investigated sample is one of the highest qualities shown up to now, with a ratio of 19 between the HH Rabi splitting and the linewidth at zero detuning. We believe that the presence of free carriers is a common problem in microcavities, often simply masked by a dominant inhomogeneous broadening. Note that Cassabois *et al.*[10] use an acoustic phonon coefficient of 11 μeV/K to explain their results, much too high compared to what is reported in good-quality $In_xGa_{1-x}As$ quantum wells,[14] and possibly overestimated due to free carrier scattering. Anomalous photoinduced quenching of the polariton linewidth has been reported in $In_xGa_{1-x}As$ quantum well microcavities,[15] which could be also explained by a reduction of the free carrier density via recombination with the photoinduced carriers.

The measured temperature dependence of the polariton linewidths yields higher values than expected from pure phonon scattering, due to the additional free carrier scattering. However, we do observe a narrower linewidth in the LP compared to the MP and UP at all the investigated temperatures. It is actually reasonable that also free carrier scattering is quenched in the low polariton branch due to the general argument of a small density of states at small $k_{\|}$ in the LP dispersion, which also explains a reduced polariton-polariton scattering.[5,16]

In the top part of Fig. 4, the ratio between the UP and LP linewidth, after subtracting the cavity linewidth weighted by the photonic content, is shown versus temperature for $\delta=0$ and 1.2 meV. At $\delta=0$, the LP and UP do not have the same excitonic content, and the ratio has been multiplied with the ratio of the LP and UP excitonic content. According to the average linewidth model, this ratio should be 1 at all temperatures, as long as the correction to the Rabi splitting due to the broadening is negligible,[17] which is applicable in our case up to 100 K as experimentally verified. We clearly observe that the ratio is always above 1 and tends to 2 at 100 K. A ratio of 2 is obtained when the UP is broadened by acoustic and optical phonons of equal scattering rates, as is the case at $\sim$100 K, while the LP is only broadened by the LO-phonon scattering. This indicates that a phonon-scattering picture tends to be recovered at high temperatures when the LO-phonon scattering dominates over the free carrier scattering.[18]

In conclusion, we have experimentally demonstrated that the LP homogeneous linewidth is narrower than the MP and UP linewidths in the strong-coupling regime and at all temperatures from 11 to 100 K. We presented, to the best of our knowledge, the first *direct evidence* of reduced scattering processes in the homogeneous broadening of the LP compared to the UP. The measured temperature dependence of the linewidth shows a surprising behavior, that cannot be simply attributed to phonon scattering, and is assigned to a temperature dependent additional scattering from excess free carriers in the investigated structure.

The authors thank K. Leosson for the use of the high resolution spectrometer.

*Present address: Lehrstuhl für Experimentelle Physik EIIb, Universität Dortmund, Otto-Hahn Str.4, 44227 Dortmund, Germany.

[1] D. M. Whittaker, P. Kinsler, T. A. Fisher, M. S. Skolnick, A. Armitage, A. M. Afshar, M. D. Sturge, and J. S. Roberts, Phys. Rev. Lett. **77**, 4792 (1996).

[2] C. Ell, J. Prineas, T. R. Nelson, S. Park, H. M. Gibbs, G. Khitrova, S. W. Koch, and R. Houdré, Phys. Rev. Lett. **80**, 4795 (1998).

[3] D. M. Whittaker, Phys. Rev. Lett. **80**, 4791 (1998).

[4] V. Savona, C. Piermarocchi, A. Quattropani, F. Tassone, and P. Schwendimann, Phys. Rev. Lett. **78**, 4470 (1997).

[5] C. Ciuti, V. Savona, C. Piermarocchi, A. Quattropani, and P. Schwendimann, Phys. Rev. B **58**, R10 123 (1998).

[6] J. J. Baumberg, A. Armitage, M. S. Skolnick, and J. S. Roberts, Phys. Rev. Lett. **81**, 661 (1998).

[7] T. Baars, M. Bayer, A. Forchel, F. Schäfer, and J. P. Reithmaier, Phys. Rev. B **61**, R2409 (2000).

[8] V. Savona and C. Piermarocchi, Phys. Status Solidi A **164**, 45 (1997).

[9] X. Marie, P. Renucci, S. Dubourg, T. Amand, P. LeJeune, J. Barrau, J. Bloch, and R. Planel, Phys. Rev. B **59**, R2494 (1999).

[10] G. Cassabois, A. L. Triques, F. Bogani, C. Delalande, P. Roussignol, and C. Piermarocchi, Phys. Rev. B **61**, 1696 (2000).

[11] J. R. Jensen, P. Borri, W. Langbein, and J. M. Hvam, Appl. Phys. Lett. (to be published).

[12] W. Langbein and J. M. Hvam, Phys. Rev. B **61**, 1692 (2000).

[13] E. L. Ivchenko, M. A. Kaliteevski, A. V. Kavokin, and A. I. Nesvizhskii, J. Opt. Soc. Am. B **13**, 1061 (1996).

[14] P. Borri, W. Langbein, J. M. Hvam, and F. Martelli, Phys. Rev. B **60**, 4505 (1999).

[15] R. P. Stanley, R. Houdré, U. Oesterle, and M. Ilegems, Solid State Commun. **106**, 485 (1998).

[16] Due to the additional free carrier scattering, an absolute comparison between the line broadening in the microcavity and in the bare QW is difficult, and would require an accurate estimation of the free carrier density.

[17] V. Savona, L. C. Andreani, P. Schwendimann, and A. Quattropani, Solid State Commun. **93**, 733 (1995).

[18] One could speculate that the absorption from the QW continuum results in an increased cavity linewidth at positive detunings, which should be included when calculating the ratio in the top part of Fig. 4. We estimated this correction and no significant changes in the trend shown in Fig. 4 were found above 25 K. Only at lower temperatures the ratio is significantly increased by this correction and confirms the reduction of scattering processes in the LP.

Microcavity polariton linewidths in the weak-disorder regime

P. Borri, W. Langbein, and U. Woggon
Experimentelle Physik EIIb, Universität Dortmund, Otto-Hahn Strasse 4, 44227 Dortmund, Germany

J. R. Jensen and J. M. Hvam
Research Center COM, The Technical University of Denmark, Building 349, DK-2800 Kgs. Lyngby, Denmark
(Received 14 June 2000; revised manuscript received 11 October 2000; published 27 December 2000)

Polariton linewidths have been measured in a series of high-quality microcavities with different excitonic inhomogeneous broadening in the weak-disorder regime. We show experimentally that the influence of the disorder on the polariton linewidths is canceled when the polariton energies are far in the tail of the excitonic absorption. The measured linewidths are quantitatively compared with an estimation using the measured excitonic absorption spectrum of the bare quantum wells, and good agreement is found.

DOI: 10.1103/PhysRevB.63.035307 PACS number(s): 78.66.−w, 78.66.Fd, 71.36.+c

The role of static disorder in the linewidth of cavity polaritons has been intensively discussed in recent years, experimentally and theoretically. In 1996, Whittaker *et al.*[1] reported reflectivity spectra measured on a GaAs semiconductor microcavity (MC) containing three InGaAs quantum wells (QW's). They observed that when the cavity mode is in resonance with the bare heavy-hole (HH) exciton transition the linewidth of the lower polariton (LP) is smaller than expected by averaging the bare exciton and cavity linewidths. Moreover, the lower-polariton linewidth is narrower than that of the upper polariton. They explained the subaverage broadening with a scaling theory based on a motional narrowing argument: When a quantum particle of finite size moves in a disordered potential with correlation length smaller in size, the spectral linewidth is reduced compared to that of a classical particle due to spatial averaging over the disorder. However, their model, which neglected interbranch scattering and nonparabolicity of the polariton dispersion, failed in explaining the different linewidths of the lower and upper branches near resonance. In 1997, Savona *et al.*[2] proposed a one-dimensional microscopic model of disordered quantum wells embedded in a microcavity where exciton-photon coupling and exciton-disorder interaction are treated nonperturbatively. This model was able to reproduce both the subaverage broadening due to motional narrowing, and the larger linewidth in the upper polariton due to additional interbranch scattering. In 1998, Ell *et al.*[3] showed that all these features were reproduced by using the measured optical absorption of the bare QW together with linear dispersion theory. They concluded that the disorder-averaged excitonic response in the bare QW fully determines the optical properties of the well embedded in a microcavity, and in particular that the asymmetric line shape of an inhomogeneously broadened exciton absorption[4] is responsible for the narrower LP linewidth compared to that of the upper polariton. At the same time Whittaker[5] proposed a unified picture where numerical calculations using a microscopic two-dimensional model were in good agreement with a simpler model describing the polariton to exciton scattering in terms of an absorption picture. In this model, the polariton linewidth is given by the photon lifetime due to escape through the mirrors and by the loss of photons due to absorption into exciton states. In other words, the photonic fraction of the upper and lower polaritons is resonant with states in the tails of the exciton absorption that are in the weak-coupling regime and simply act as a source of absorption in the cavity. Therefore, in this model the difference between the widths of the two polariton branches is a consequence of the asymmetry of the inhomogeneously broadened exciton line shape, with larger absorption on the high-energy side.[4] This absorption model is thus a simplified version of the model of Ell *et al.*,[3] but in essence also agrees with the suggestion of Savona *et al.*[2] that the large width of the upper branch is caused by scattering of polaritons into higher-momentum exciton states. It is emphasized by Whittaker[5] that this simple model is justified because motional narrowing effectively eliminates the contribution to the linewidth due to disorder-induced scattering between low-momentum polaritons in the same branch, and the only important contribution is the polariton to exciton scattering. Thus a very intriguing feature of this absorption model is the prediction that the disorder contribution to the polariton linewidth should *disappear* in structures with small but finite exciton inhomogeneous broadening, when polariton to exciton scattering becomes impossible because the polariton energies are too far in the tails of the excitonic absorption (see Fig. 3 in Ref. 5). More precisely, the disorder contribution to the polariton linewidth should disappear, especially in the lower polariton, when the exciton inhomogeneous broadening is much narrower than the Rabi splitting in the microcavity (weak-disorder limit). However, this point was not experimentally verified in these previous works, also due to the significant exciton inhomogeneous broadening in the samples investigated. Recent achievements in growth of high-quality microcavities[6,7] now open the possibility of experimentally verifying this prediction.

In this article we report a detailed investigation of the polariton linewidths in a series of semiconductor microcavities with variable exciton inhomogeneous broadening, in the weak-disorder regime. We have used molecular beam epitaxy grown GaAs single QW's embedded in AlGaAs microcavities, with three different well widths of 25 nm, 15 nm, and 10 nm. With decreasing well width, the exciton becomes more sensitive to the interface and alloy disorder due to the larger wave function overlap with the interface region. The

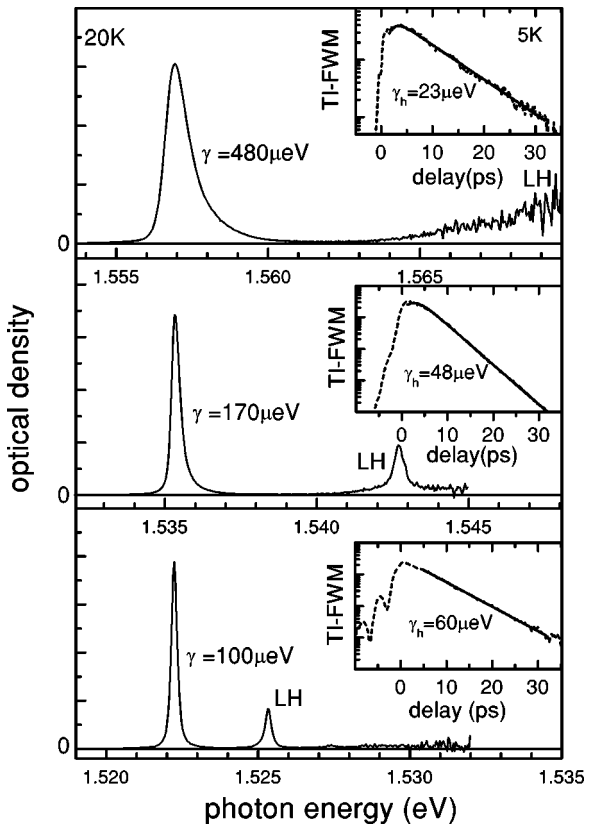

FIG. 1. Absorption profile, as deduced from the photoluminescence spectrum at 20 K corrected by a Boltzmann population factor, for a 25 nm (bottom), a 15 nm (middle), and a 10 nm (top) $GaAs/Al_{0.3}Ga_{0.7}As$ single quantum well. In the insets, four-wave mixing (FWM) traces at 5 K are given with the corresponding fits of the homogeneous broadening.

optical properties of bare $GaAs/Al_{0.3}Ga_{0.7}As$ QW's of the same nominal thicknesses and grown under similar conditions are shown in Fig. 1. The excitonic absorption spectrum is deduced from the photoluminescence spectrum, measured at 20 K at resonant excitation and low intensity, divided by the Boltzmann population factor, assuming an exciton population in thermal equilibrium at the lattice temperature as described in Ref. 8. This procedure is already a good approximation at 20 K in the samples investigated as we have experimentally verified by comparison with higher temperatures. The corresponding half widths at half maximum (HWHM's) of the HH excitonic absorption are indicated. All the linewidths will be given in the following as HWHM's. In order to estimate the exciton inhomogeneous broadening we have compared these linewidths with measurements of the homogeneous broadening by degenerate four-wave mixing (FWM). Details of the experimental setup can be found in Ref. 9. In the inset, the time-integrated FWM for collinearly polarized pulses is shown versus their relative delay time at 5 K close to the low-density regime ($\sim 10^9$ excitons/cm^2). For the 25 nm wide QW (bottom plot) the decay is monoexponential and the FWM is a free-polarization decay, indicating the absence of disorder probed by the exciton.[9] The corresponding homogeneous broadening agrees well with the absorption linewidth at 20 K, when we take into account 2.1 μeV/K linewidth broadening by acoustic-phonon absorption.[9] Thus, the exciton absorption in the 25 nm QW is predominantly homogeneously broadened. In the 15 nm wide QW (middle plot) signatures of exciton inhomogeneous broadening appear in the absorption line shape, which is broader and slightly asymmetric.[4] The FWM is now a photon echo with a delayed maximum, and its decay was fitted as proposed by Erland *et al.*[10] An acoustic-phonon coefficient of ~ 2 μeV/K was also measured in this QW, resulting in a homogeneous broadening contribution of ~ 80 μeV at 20 K. Thus the total linewidth of the 15 nm wide QW is an interplay of comparable homogeneous and inhomogeneous broadenings. Finally, the absorption profile of the 10 nm QW (top plot) is strongly inhomogeneously broadened, with a negligible contribution due to the homogeneous broadening as deduced by FWM, and largely asymmetric.

We have recently reported on the optical properties of a microcavity formed by embedding a 25 nm GaAs single QW inside an AlGaAs λ cavity.[6,11] An $AlAs/Al_{0.15}Ga_{0.85}As$ Bragg reflector of 25 (16) periods was grown at the bottom (top) of the cavity. A special design of the $Al_{0.3}Ga_{0.7}As$ barriers and the spacer layer was shown to be successful in reducing excess free-carrier densities in the microcavity compared to more conventional designs.[11] We obtained a Rabi splitting to linewidth ratio of 19 at 11 K, one of the best reported until now to our knowledge for single QW microcavities. With the same design, we have grown two new microcavities containing, respectively, a 15 nm and a 10 nm wide single GaAs QW, which are investigated in this work in comparison with the MC containing the 25 nm QW. The energy of the polaritons versus the energy distance between the cavity resonance and the bare HH exciton (detuning) is shown in Fig. 2 for these two microcavities at low temperature (5 K). A good fit to the data is obtained by solving a three-coupled-oscillator model including the light-hole (LH) exciton.[11] The coupling to the LH exciton results in the appearance of three polariton modes, the lower, middle, and upper polaritons. From the fits we deduced 3.8 meV HH Rabi splitting (2.4 meV LH Rabi splitting) for the MC containing the 15 nm QW, and 4.15 meV HH Rabi splitting (2.8 meV LH Rabi splitting) for the MC containing the 10 nm QW. Thus, in all the microcavities investigated the HH exciton inhomogeneous broadening is smaller than one-half the HH Rabi splitting, i.e., the structures are in the weak-disorder regime.[5] Note that for smaller well widths the stronger quantization of the LH exciton leads to a smaller mixing of this state in the LP and middle polariton (MP) resonances around zero detuning.

In the inset, the reflectivity spectrum measured with white light near normal incidence ($\sim 1°$) is shown for both MC's at zero detuning. The white-light source was focused on the sample with a spot diameter of 70 μm resulting in a small energy broadening of the cavity mode from the wedge gradient and the incident wave vector spread.[11] The spectra were detected using a spectrometer and an intensified multichannel analyzer, with a total spectral resolution close to a Lorentzian line shape of 65 μeV HWHM. It can be seen from the insets of Fig. 2 that the LP linewidth is narrower

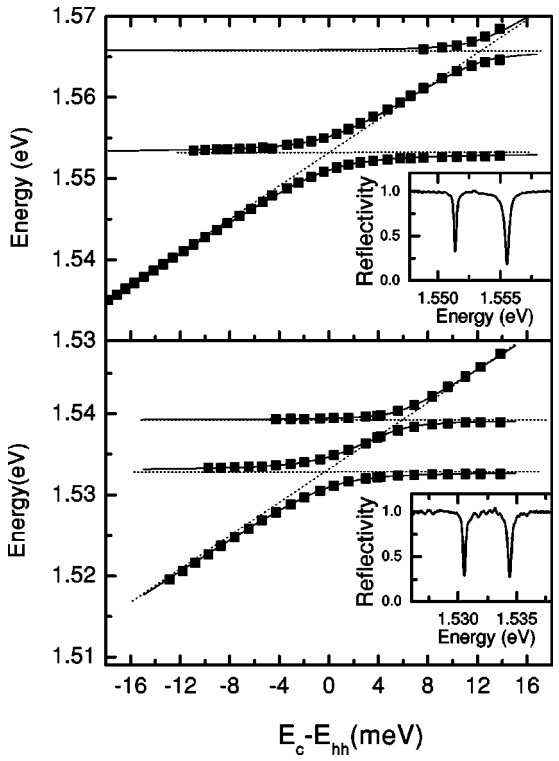

FIG. 2. Polariton energies versus detuning for the 10 nm (upper) and the 15 nm (lower) GaAs quantum well microcavity at 5 K. The solid lines are fits to the data. The insets show the reflectivity spectrum of the microcavity at zero detuning.

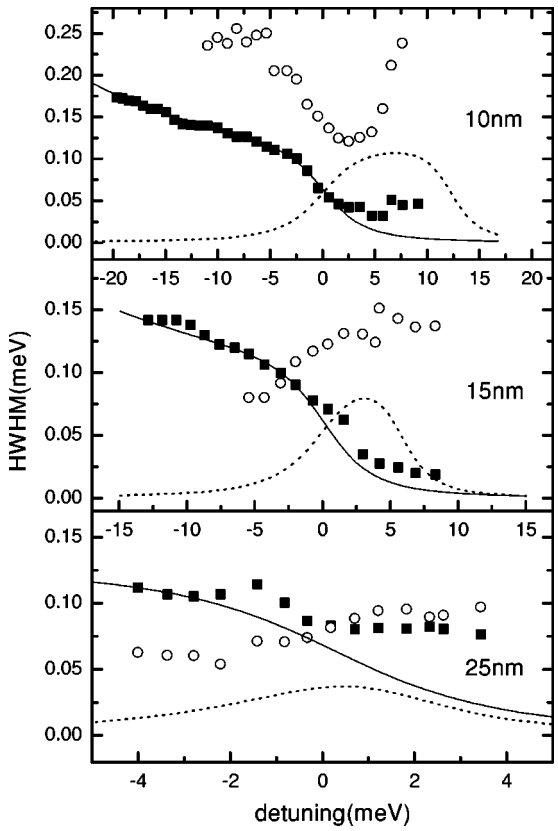

FIG. 3. Linewidths versus detuning of the lower (closed squares) and middle (open circles) polaritons, for the different microcavity samples as indicated. The solid (dotted) lines are the calculated photonic linewidths of the lower (middle) polaritons.

than that of the MP and its value is subaverage, in agreement with previous observations on the effect of disorder on the polariton linewidths.[1]

In order to investigate in detail the role of the disorder in the polariton linewidths, we have measured the detuning dependence of the LP and MP linewidths, as shown in Fig. 3. The measured linewidths, well fitted with Lorentzian profiles, have been corrected by subtracting the spectral resolution. The closed squares are the LP linewidths while the open circles are the MP linewidths. The solid (dotted) lines are the cavity linewidths, due to the finite transmission of the Bragg mirrors, multiplied by the calculated photonic content in the lower (middle) polariton. The cavity linewidth was calculated taking into account the change of the linewidth with energy position in our specially designed structure with uniform Bragg mirrors and a wedged spacer layer,[11] and agrees well with the measured LP linewidth at large negative detunings. Uncertainties in the fit of the cavity linewidths are less than 10%. Comparable LP broadenings are measured at large negative detuning in all the samples, consistent with the fact that all the samples have nominally equal Bragg mirror reflectivities. It can be clearly seen from Fig. 3 that close to zero detuning the 15 and 10 nm QW MC's show a LP linewidth narrower than that of the MP. Moreover, from the comparison with the calculated photonic part the LP linewidth is subaverage and given *only by the cavity contribution*. In the 25 nm QW MC, instead, the LP and MP linewidths are almost equal at zero detuning, and the LP linewidth is larger than the cavity linewidth contribution.

In order to give a physical picture of the observed results, we have plotted in Fig. 4 the polariton linewidths versus the distance $E_P - E_{HH}$ of the polariton energy from that of the HH bare exciton. According to the simple absorption model of Whittaker,[5] the polariton linewidth is the sum of the cavity contribution and an excitonic part. This excitonic part γ_e of the linewidth should be related to the strength of the exciton absorption probed by the polariton resonances. We have quantitatively performed this comparison. The measured absorption spectra in Fig. 1 have been scaled in order to represent the absorption probability in the QW.[12] The area of the absorption probability $\alpha(\omega)$ in a QW is proportional to the oscillator strength per unit area[13] f:

$$\int \alpha(\omega) d(\hbar\omega) = \frac{2\pi^2 \hbar e^2}{n m_0 c} f \tag{1}$$

with the refractive index n, the electron charge e and mass m_0, and the speed of light c. The oscillator strength per unit area is proportional to the exciton radiative linewidth,[13] which is related to the Rabi splitting $\hbar\Omega$ in the microcavity,[14] and one gets

$$f = \frac{(\hbar\Omega)^2 n^2 m_0 L_{\text{eff}}}{8\pi e^2 \hbar^2} \tag{2}$$

with L_{eff} the effective length in the microcavity due to the penetration length into the Bragg mirrors. The absorption probability is a loss in the cavity that gives rise to a photon

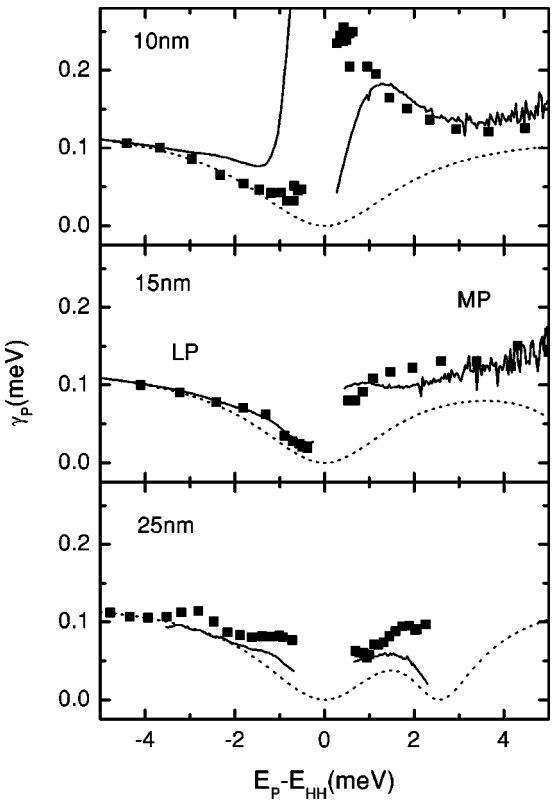

FIG. 4. Measured (symbols) and calculated (lines) polariton linewidths versus the energy distance of the polariton from the bare HH exciton. The dotted lines are the estimated cavity contributions in the polariton linewidths.

decay rate $\alpha(\omega)c(nL_{\text{eff}})^{-1}$ additional to the transmission losses from the Bragg mirrors. Thus, finally, the measured absorption spectrum with an integral over the energy normalized to 1, $s(\omega)$, is related to γ_e by

$$\gamma_e = |c_l|^2 s(\omega) \frac{\pi(\hbar\Omega)^2}{8} \tag{3}$$

with $|c_l|^2$ being the photonic content of the polariton at the energy $\hbar\omega$. This formula is a valid approximation when $|c_l|^2$ is not too small; otherwise it predicts that the polariton linewidth tends to zero when the photonic content tends to zero, while the true value tends to the exciton linewidth.[5]

The solid lines in Fig. 4 are the calculated polariton linewidths $\gamma_P = |c_l|^2\gamma_c + \gamma_e$ with γ_c the cavity linewidth (see Fig. 3) and γ_e calculated using Eq. (3) and the absorption spectra in Fig. 1. For comparison, the isolated cavity linewidth contribution $|c_l|^2\gamma_c$ is plotted as dotted lines. The overall quantitative agreement between calculated and measured linewidths is quite good for $|E_P - E_{HH}| > 1$ meV, where the absorption model holds, i.e., when the photonic content is not too small and when the polariton energies are resonant with excitonic states far enough in the tail of the absorption to be in the weak-coupling regime.[5] In particular, it appears clearly that when the excitonic absorption profile is asymmetric the contribution to the polariton linewidth from the excitonic absorption is bigger for $E_P - E_{HH} > 0$, i.e., for the MP, than for $E_P - E_{HH} < 0$, i.e., for the LP, in agreement with the measurements. Moreover, in the LP the disorder-induced broadening is *absent* when the polariton energies are far in the tail of the excitonic absorption.

Some small discrepancies between calculation and measurements are also evidenced. A parameter not under control in this comparison is the density of excess free carriers in the samples, resulting in trion resonances in the low-energy tail of the excitonic absorption. In the upper part of Fig. 4 a trion resonance ~ 2 meV below the exciton seems to be present in the 10 nm bare QW, which is not observed in the microcavity sample. The opposite occurs in the 25 nm QW (lower figure), where a trion resonance is evidenced in the microcavity sample, approximately 1 meV below the HH exciton, also in agreement with photoluminescence measurements on this structure,[11] while it is less present in the bare QW sample. Additionally, in the 15 nm and 25 nm QW MC's, the MP linewidths appear to be slightly higher (by a few tens of μeV) than the calculated ones in the region where the photonic content is not very small. Even if this difference is at the limit of our accuracy, it is reasonable that when the disorder-induced broadening is very small the MP linewidths are affected by other scattering processes, such as phonon or free-carrier interactions, not included in the simple absorption model of Whittaker.[5] In fact, the observed difference is on the order of what is calculated from additional homogeneous broadening of the upper polariton due to acoustic phonon scattering,[15] which is inhibited in the lower polariton. As a general comment, note that the polariton linewidths shown in this work are very small, well below those reported in previous work investigating the role of disorder in cavity polaritons.[3,5] Thus it is not surprising that small features such as trion/free carriers and phonon effects are affecting the measured linewidths in our samples.

In conclusion, we have shown experimentally that the influence of disorder on the polariton linewidth of microcavities in the weak-disorder regime can be canceled when the polariton energies are far in the tail of the excitonic absorption, in agreement with predictions in the literature.[5,2] The measured linewidths have been *quantitatively* compared with those estimated from the measured excitonic absorption in the bare quantum wells, following the simple absorption model proposed by Whittaker.[5] A generally good agreement is found.

[1] D.M. Whittaker, P. Kinsler, T.A. Fisher, M.S. Skolnick, A. Armitage, A.M. Afshar, M.D. Sturge, and J.S. Roberts, Phys. Rev. Lett. **77**, 4792 (1996).

[2] V. Savona, C. Piermarocchi, A. Quattropani, F. Tassone, and P. Schwendimann, Phys. Rev. Lett. **78**, 4470 (1997).

[3] C. Ell, J. Prineas, T.R. Nelson, S. Park, H.M. Gibbs, G. Khitrova, S.W. Koch, and R. Houdré, Phys. Rev. Lett. **80**, 4795 (1998).

[4] R.F. Schnabel, R. Zimmermann, D. Bimberg, H. Nickel, R. Lösch, and W. Schlapp, Phys. Rev. B **46**, 9873 (1992).

[5] D.M. Whittaker, Phys. Rev. Lett. **80**, 4791 (1998).

[6] P. Borri, J.R. Jensen, W. Langbein, and J.M. Hvam, Phys. Rev. B **61**, R13 377 (2000).
[7] M. Saba, F. Quochi, U. Oestersle, J.L. Staehli, B. Deveaud, G. Bongiovanni, and A. Mura, Phys. Status Solidi A **178**, 149 (2000).
[8] M. Gurioli, A. Vinattieri, J. Martinez-Pastor, and M. Colocci, Phys. Rev. B **50**, 11 817 (1994).
[9] W. Langbein and J.M. Hvam, Phys. Rev. B **61**, 1692 (2000).
[10] J. Erland, K.H. Pantke, V. Mizeikis, V.G. Lyssenko, and J.M. Hvam, Phys. Rev. B **50**, 15 047 (1994).
[11] J.R. Jensen, P. Borri, W. Langbein, and J.M. Hvam, Appl. Phys. Lett. **76**, 3262 (2000).
[12] Note that, from the comparison of the bare HH energy positions measured in the spectra of Fig. 1 and deduced by the fits of the polariton energies in Fig. 2, we actually found a small deviation in the effective well width inside the microcavity, which is $\sim 5\%$ larger compared to the bare sample. Thus the absorption spectra have been corrected by rescaling the energy axis in order to fit the exciton quantization energy of the quantum well in the microcavity sample.
[13] L. C. Andreani, in *Confined Electrons and Photons: New Physics and Applications*, Vol. 340 of *NATO Advanced Study Institute, Series B: Physics*, edited by E. Burstein and C. Weisbuch (Plenum Press, New York, 1995), pp. 57–112.
[14] M.S. Skolnick, T.A. Fisher, and D.M. Whittaker, Semicond. Sci. Technol. **13**, 645 (1998).
[15] V. Savona and C. Piermarocchi, Phys. Status Solidi A **164**, 45 (1997).